Université Paris Cité

en cotutelle avec Università degli Studi di Firenze

École doctorale Sciences de la Terre et de l'environnement et physique de l'Univers (STEP'UP n°560)

Institut de Physique du Globe de Paris, Équipe de Sismologie

Volcanic hazard monitoring using distributed acoustic sensing at Stromboli Volcano

Par Francesco BIAGIOLI

Thèse de doctorat de Sciences de la Terre et de l'environnement

Dirigée par Jean-Philippe MÉTAXIAN

& Giorgio LACANNA

& Eléonore STUTZMANN

Présentée et soutenue publiquement le 19 decembre 2024

Devant un jury composé de:

Charlotte KRAWCZYK, Prof.	GFZ	Rapportrice
Nicola PIANA AGOSTINETTI, Prof.	Université de Milano-Bicocca	Rapporteur
Valérie CAYOL, DR-CNRS	LMV/UCA	Examinatrice
Gilda CURRENTI, Chercheuse	INGV	Examinatrice
François BEAUDUCEL, Physicien	Université Paris Cité/IPGP	Examinateur
Eléonore STUTZMANN, Physicienne	Université Paris Cité/IPGP	Membre invité
Maurizio RIPEPE, Chercheur	Université de Firenze	Membre invité
Jean-Philippe MÉTAXIAN, DR-IRD	IPGP/IRD	Directeur de thèse
Giorgio LACANNA, Chercheur	Université de Firenze	Co-directeur de thèse

À Benedetta,
qui nous a accompagnés pour trop peu de temps,
mais qui nous éclairera pour toujours

Abstract

Title: Volcanic hazard monitoring using Distributed Acoustic Sensing at Stromboli volcano.

Keywords: seismology; volcano seismology; distributed acoustic sensing; volcanic monitoring; optical fibres.

Understanding the geophysical signatures of volcanic activity is crucial for eruption forecasting. However, hazardous and harsh volcanic environments often challenge continuous monitoring. Distributed Acoustic Sensing (DAS) offers a safer, cost-effective solution for long-term volcanic surveys. DAS probes fibre-optic cables to provide highly detailed spatial (metre-scale) and temporal (up to kHz) sampling of the seismic wavefield, measuring the dynamic fibre strain via Rayleigh backscatter interferometry.

As part of the ANR MONIDAS project, we deployed 4 km of optical fibre on the north-eastern flank of Stromboli volcano (Italy). A Febus A1-R DAS interrogator monitored volcanic activity during several experiments between 2020 and 2023, capturing around five months of data. To validate the DAS measurements, we installed nodal seismometers along the fibre. We also gathered data from the permanent monitoring network of the University of Firenze (Italy), comprising seismic stations, tiltmeters, infrasonic sensors, tsunami gauges, and visual/thermal cameras.

Our main objectives are (1) to assess the accuracy of DAS in detecting volcanic seismic signals and (2) to gain insights into the dynamics and locations of these events. We analyse DAS strain rate waveforms from several volcanic processes, primarily focusing on ordinary activity, including mild, frequent explosions (~10 events/hour) alongside volcanic tremor. Strain rate signals from Strombolian explosions typically fall in the 2-10 Hz range. Moreover, DAS measurements comprise very long-period seismic signals between 0.03-0.3 Hz. Additionally, we examine strain rate signals from more violent (major) explosions and pyroclastic density currents (PDCs).

To evaluate DAS accuracy, we compare its strain rate data with those of co-located nodes using two methods: converting seismic velocity from nodes into strain rate and converting DAS strain rate into velocity. Using the first method, we observe an almost perfect match in phase between the two datasets. The second method yields similar outcomes. However, DAS amplitudes are 1.5 to 5 times smaller than those recorded by nodes, likely due to inefficient strain transfer between the ground, cable, and fibre.

Finally, array processing techniques help us pinpoint stationary sources (tremor and explosions) and track moving sources (PDCs). The back-azimuths obtained with the DAS reveal dominant seismic sources located near the active craters during explosions and tremor, coherent with outcomes from co-located nodal arrays. DAS data also enable us to track two PDCs propagating from the craters to the sea with velocities from ~30 to 70 m/s. These outcomes match those obtained via seismo-acoustic data and with the images recorded by the monitoring cameras. Although further research is needed, these findings demonstrate the potential of this new technology in monitoring volcanic areas.

Résumé

Titre: Volcanic hazard monitoring using Distributed Acoustic Sensing at Stromboli volcano.

Mots-clefs: sismologie; sismologie volcanique; surveillance volcanique; distributed acoustic sensing; fibres optiques.

Comprendre les signatures géophysiques de l'activité volcanique est crucial pour la prévision des éruptions. Cependant, les environnements volcaniques dangereux et difficiles compliquent souvent la surveillance continue des volcans. La technologie de détection acoustique distribuée (DAS, *distributed acoustic sensing*) offre une solution plus sûre et économique pour des relevés de longue durée dans les applications sismo-volcaniques. Le DAS sonde les câbles de fibre optique avec un échantillonnage spatial (échelle métrique) et temporel (jusqu'au kHz) très détaillé du champ sismique, en mesurant la déformation dynamique des fibres grâce à l'interférométrie des rayons rétrodiffusés.

Dans le cadre du projet ANR MONIDAS, nous avons déployé 4 km de fibre optique sur le flanc nord-est du volcan Stromboli (Italie). Un interrogateur DAS Febus A1-R a enregistré l'activité volcanique lors de plusieurs expériences entre 2020 et 2023, capturant environ cinq mois de données. Pour valider les mesures DAS, nous avons installé des sismomètres le long de la fibre. Nous avons également collecté des données du réseau de surveillance permanent de l'Université de Florence (Italie), qui comprend des stations sismiques, des inclinomètres, des capteurs infrasons, des gauges de tsunamis, ainsi que des caméras visibles et thermiques.

Nos objectifs principaux sont (1) d'évaluer la précision du DAS pour la détection des signaux sismiques volcaniques et (2) d'obtenir des informations sur la dynamique et la localisation de ces événements. Nous analysons les formes d'onde DAS en *strain rate* (taux de déformation) provenant de plusieurs processus volcaniques, en nous concentrant principalement sur l'activité ordinaire, y compris les explosions modérées et fréquentes (~10 événements/heure) ainsi que le trémor volcanique. Les signaux de *strain rate* des explosions stromboliennes ont généralement des fréquences comprises entre 2 et 10 Hz. De plus, les mesures DAS comprennent des signaux sismiques à très longue période entre 0,03 et 0,3 Hz. Nous examinons également les signaux générès par des explosions plus violentes (majeures) et des coulées pyroclastiques.

Pour évaluer la précision du DAS, nous comparons les données de taux de déformation avec celles des sismomètres co-localisés en utilisant deux méthodes : la conversion de la vitesse sismique des sismomètres en *strain rate* et la conversion du *strain rate* DAS en vitesse. En utilisant la première méthode, nous observons un accord de phase presque parfait entre les deux ensembles de données. La seconde méthode donne des résultats similaires. Cependant, les amplitudes DAS sont de 1.5 à 5 fois plus faibles que celles enregistrées par les sismomètres, probablement en raison d'un transfert de déformation inefficace entre le sol, le câble et la fibre.

Enfin, les techniques de traitement de réseaux nous aident à localiser les sources stationnaires (tremor et explosions) et à suivre les sources mobiles (coulées pyroclastiques). Les back-azimuths obtenus avec le DAS révèlent que les principales sources sismiques sont situées près des cratères actifs lors des explosions et du tremor, ce qui est cohérent avec les résultats obtenus avec les réseaux sismiques co-localisés. Les données DAS nous permettent également de suivre deux coulées pyroclastiques se déplaçant des cratères vers la mer

avec des vitesses allant de ~40 à 70 m/s. Ces résultats correspondent à ceux obtenus via les données séismo-acoustiques et les images enregistrées par les caméras de surveillance. Bien que des recherches supplémentaires soient nécessaires, ces résultats démontrent le potentiel de cette nouvelle technologie dans la surveillance des zones volcaniques.

Riassunto

Titolo: Volcanic hazard monitoring using Distributed Acoustic Sensing at Stromboli volcano.

Parole chiave: sismologia; sismologia vulcanica; monitoraggio vulcanico; distributed acoustic sensing; fibre ottiche.

Comprendere i segnali geofisici prodotti dai vulcani è essenziale per monitorare e prevenire eventuali eruzioni. Tuttavia, le condizioni ambientali ostiche e gli elevati rischi possono complicare il monitoraggio continuo dei vulcani. La Tecnologia di rilevamento acustico distribuito (DAS, *Distributed acoustic sensing*) offre una soluzione più sicura ed economica per il monitoraggio vulcanico a lungo termine. Il DAS analizza i cavi in fibra ottica per fornire campionamenti spaziali (a scala metrica) e temporali (fino a kHz) molto dettagliati del campo d'onda sismico, misurando la deformazione dinamica delle fibre tramite interferometria della radiazione retrodiffusa (scattering di Rayleigh).

Nel progetto ANR MONIDAS, abbiamo installato 4 km di fibra ottica sul fianco nord-orientale del vulcano Stromboli (Italia). Un interrogatore DAS Febus A1-R ha monitorato l'attività vulcanica durante vari esperimenti tra il 2020 e il 2023, raccogliendo circa cinque mesi di dati. Per validare le misurazioni DAS, abbiamo posizionato numerosi sismometri lungo la fibra e raccolto dati dalla rete di monitoraggio permanente dell'Università di Firenze (Italia), che include stazioni sismiche, inclinometri, sensori infrasonici, gauge di tsunami e telecamere visibili e termiche.

I nostri obiettivi principali sono (1) valutare la precisione del DAS nella rilevazione dei segnali sismici vulcanici e (2) ottenere informazioni sulle dinamiche e le localizzazioni di questi eventi. Analizziamo le forme d'onda ottenute dal DAS in *strain rate* (tasso di deformazione) associate a vari processi vulcanici, focalizzandoci principalmente sull'attività ordinaria. Quest'ultima comprende esplosioni moderate e frequenti (~10 eventi/ora) e tremore vulcanico. I segnali di *strain rate* delle esplosioni stromboliane hanno frequenze principalmente tra 2-10 Hz e includono anche fase a lungo periodo, tra 0.03 e 0,3 Hz. Esaminiamo inoltre i segnali generati da esplosioni più violente e da flussi piroclastici.

Per valutare la precisione del DAS, ne confrontiamo i dati con quelli registrati dai sismometri co-localizzati utilizzando due metodi: convertendo la velocità sismica dei sismometri in *strain rate* e e convertendo lo *strain rate* DAS in velocità. Con il primo metodo, osserviamo un'ottima corrispondenza di fase tra i due dataset. Il secondo metodo fornisce risultati simili. Tuttavia, le ampiezze DAS sono da 1.5 a 5 volte più piccole rispetto a quelle registrate dai sismometri, probabilmente a causa di un trasferimento inefficiente di deformazione tra il suolo, il cavo e la fibra.

Infine, le tecniche di analisi di *array* ci permettono di localizzare sorgenti sismiche stazionarie (es. tremore ed esplosioni) e in movimento (es. flussi piroclastici). I back-azimuth ottenuti tramite i segnali DAS rivelano sorgenti sismiche dominanti vicino ai crateri attivi durante esplosioni e tremore, coerenti con i risultati degli *array* sismici co-localizzati. I dati DAS ci permettono anche di seguire lo spostamento di due flussi pircolastici dai crateri fino al mare con velocità comprese tra ~30 e 70 m/s. Questi risultati corrispondono a quelli ottenuti tramite dati sismo-acustici e con le immagini registrate dalle telecamere di monitoraggio. Sebbene siano necessarie ulteriori ricerche, questi risultati dimostrano il potenziale di questa nuova tecnologia nella sorveglianza delle aree vulcaniche.

Résumé long

Près de 800 millions de personnes sont potentiellement exposées aux risques volcaniques, une menace accrue par la croissance démographique rapide et l'urbanisation (Auker et al., 2013; Brown et al., 2017). L'activité volcanique affecte la vie humaine, causant des victimes, des pertes économiques considérables et perturbant les infrastructures ainsi que les réseaux de transport, en particulier le trafic aérien (Petersen et al., 2012; Takebayashi et al., 2021). Comprendre les signatures géophysiques de l'activité volcanique est crucial pour la prévision des éruptions. Parmi plusieurs approches, la sismologie volcanique est aujourd'hui un outil de surveillance essentiel et la pierre angulaire de nombreux observatoires (Chouet & Matoza, 2013; McNutt & Roman, 2015; McNutt, Thompson, et al., 2015). Cependant, les environnements volcaniques dangereux, corrosifs et difficiles d'accès compliquent souvent la surveillance continue des volcans.

La technologie de détection acoustique distribuée (DAS, *distributed acoustic sensing*) offre une solution sûre et économique pour des relevés de longue durée dans les applications sismo-volcaniques (Jousset et al., 2024). La technologie DAS fait partie d'une gamme plus large de méthodologies appelées détection distribuée par fibre optique (DOFS, i.e. *distributed optical fibre sensing*). Les systèmes DOFS utilisent la propagation de la lumière dans les fibres optiques pour mesurer des variables environnementales telles que la déformation et la température en plusieurs points le long des fibres, plutôt qu'à un seul emplacement (Lu et al., 2019; Fernández-Ruiz et al., 2020; Jousset et al., 2024).

Les fibres optiques sont de fins fils de verre qui guident les impulsions lumineuses sur de longues distances par réflexion totale interne. Elles contiennent naturellement des fluctuations de densité aléatoires, modifiant l'indice de réfraction du verre (Hartog, 2017; Lindsey, Rademacher, & Ajo-Franklin, 2020). Ces anomalies perturbent la propagation de la lumière dans les fibres, entraînant une rétrodiffusion de Rayleigh (Hartog, 2017). La signature de la lumière rétrodiffusée reste stable lorsque la fibre est stationnaire, mais varie en raison des déformations causées par des processus physiques tels que les perturbations élastiques ou les variations de température (Hartog, 2017; Williams et al., 2019; Fernández-Ruiz et al., 2020; Lindsey, Rademacher, & Ajo-Franklin, 2020). La technologie DAS mesure la deformation (*strain*) dynamique (ou le taux de deformation, i.e. le *strain rate*) des fibres optiques causée par les ondes sismiques.

Les mesures DAS nécessitent l'utilisation d'une unité d'interrogation, un dispositif

optoélectronique comprenant une source laser et un photodétecteur. Cette unité injecte des impulsions laser cohérentes dans la fibre et mesure la lumière rétrodiffusée. Grâce à l'interférométrie optique, le DAS exploite les variations de phase de la lumière rétrodiffusée dues aux changements de longueur de parcours des photons pour mesurer la contrainte longitudinale de la fibre (Hartog, 2017; Fernández-Ruiz et al., 2020). Une seule unité DAS peut sonder simultanément des dizaines de km de câbles de fibres optiques, les transformant en réseaux sismiques denses (échelle métrique) de milliers de capteurs de *strain* pouvant échantillonner jusqu'à des fréquences de plusieurs kHz.

Le DAS a établi un nouveau paradigme dans les analyses sismologiques. Il a été appliquée avec succès dans divers domaines géophysiques, tels que l'industrie pétrolière et gazière (Daley et al., 2013; Mateeva et al., 2014; Bakku, 2015), la sismologie des tremblements de terre (Lindsey et al., 2017; Jousset et al., 2018; Wang et al., 2018; Ajo-Franklin et al., 2019; Lindsey, Rademacher, & Ajo-Franklin, 2020; Li et al., 2023), la caractérisation de la sismicité sous-marine (Cheng et al., 2021; Taweesintananon et al., 2023; Shen & Wu, 2024), ainsi que dans le suivi de l'activité anthropique en milieu urbain, du comportement mécanique des infrastructures, de l'activité des glaciers, des systèmes géothermiques et des volcans (Fang et al., 2020; Lindsey, Yuan, et al., 2020; Spica et al., 2020; Walter et al., 2020; Hudson et al., 2021; Zhu et al., 2021; Jousset et al., 2022; Zhu et al., 2022; Azzola et al., 2023; Ehsaninezhad et al., 2024; Rahman et al., 2024).

Les expériences de DAS dans les zones volcaniques ont produit des résultats prometteurs. Jousset et al. (2018) a utilisé le DAS pour cartographier les structures dans la péninsule de Reykjanes (Islande). Nishimura et al. (2021) a localisé les hypocentres de séismes volcaniques superficiels du volcan Azuma (Japon), et Klaasen et al. (2021) a révélé une sismicité intense et de faible magnitude au Mont Meager (Canada). À l'Etna (Italie), des signaux sismo-acoustiques liés aux explosions volcaniques et au dégazage ont été enregistrés (Currenti et al., 2021). D'autres études ont observé des signaux de trémor volcanique sur le volcan Grímsvötn (Islande; Fichtner, Klaasen, et al., 2022) et analysé des épisodes de sismicité de très basse fréquence (VLP, i.e. *very long period*) sur l'île de Vulcano (Italie; Currenti et al., 2023).

Le DAS montre un potentiel pour analyser les fréquences VLP, qui fournissent des informations cruciales sur la dynamique des conduits volcaniques, bien que ses capacités restent encore à explorer (Currenti et al., 2023). Les techniques de traitement en réseau, telles que le *delay-and-sum beamforming* ou le *Multiple Signal Classification* (MUSIC), permettent de localiser précisément les événements qui n'ont pas d'arrivées claires d'ondes P ou S, comme de nombreux signaux sismo-volcaniques tels que les VEQs et le trémor (e.g., Capon, 1969; Schmidt, 1986; Goldstein & Archuleta, 1987; Furumoto et al., 1990; Almendros et al., 1997; Métaxian et al., 1997; Saccorotti et al., 1998; Métaxian et al., 2002; La Rocca, Saccorotti, et al., 2004; Inza et al., 2011; Schweitzer et al., 2012; Hansen & Schmandt, 2015; Eibl et al., 2017; Glasgow et al., 2018). Ces méthodes permettent notamment de déduire la vitesse apparente et le *back-azimuth* des ondes sismiques qui atteignent un réseau de capteurs. Diverses techniques de traitement d'antenne adaptées au DAS ont été proposées (Näsholm et al., 2022), mais elles ne sont pas encore standardisées. De plus, les mesures de *strain* distribuées pourraient améliorer la compréhension des structures volcaniques, en offrant un échantillonnage spatial dense du champ d'ondes pour une imagerie de haute résolution du sous-sol volcanique (Jousset et al., 2022; O'Brien et al., 2023).

Dans le cadre du projet ANR MONIDAS, nous avons déployé 4 km de fibre optique

sur le flanc nord-est du volcan Stromboli (Italie). Un interrogateur DAS Febus A1-R a enregistré l'activité volcanique lors de plusieurs expériences entre 2020 et 2023, enregistrant environ cinq mois de données comprenant des signaux sismiques générés par divers processus volcaniques. Pour valider les mesures DAS, nous avons installé des sismomètres le long de la fibre. Nous avons également utilisé les données du réseau de surveillance permanent de l'Université de Florence (Italie), qui comprend des stations sismiques, des inclinomètres, des capteurs infrasons, des gauges de tsunamis, ainsi que des caméras visibles et thermiques.

Stromboli présente une activité volcanique persistante (Rosi et al., 2000), avec des explosions fréquentes (~13 événements/heure; Ripepe et al., 2008) et un dégazage continu. Les signaux sismiques produits par les explosions couvrent une large gamme de fréquences (10^{-2} – 10 Hz; Neuberg et al., 1994; Chouet et al., 1997, 2003). De plus, un trémor volcanique est toujours présent dans les enregistrements sismiques, principalement entre ~1−5 Hz (Nappi, 1976; Langer & Falsaperla, 1996; Ripepe et al., 1996; Wassermann, 1997). Cependant, des phénomènes plus fascinants et dangereux peuvent interrompre ou accompagner ce régime d'activité relativement prévisible, tels que les coulées de lave et les explosions violentes, qualifiées de "majeures" et "paroxysmiques" selon leur intensité (Métrich et al., 2021; Ripepe, Lacanna, et al., 2021). Ces dernières représentent la manifestation la plus violente et la plus dangereuse de la dynamique explosive strombolienne, posant une menace significative pour les habitants. Les explosions majeures et paroxysmiques projettent des projectiles volcaniques à grande distance et peuvent générer des coulées pyroclastiques (PDCs) (Rosi et al., 2013). L'impact de grandes PDCs et de glissements de terrain dans la mer peut produire des vagues de tsunami, mettant en danger les côtes voisines (La Rocca, Galluzzo, et al., 2004; Ripepe & Lacanna, 2024). Ces caractéristiques font de Stromboli un site de test idéal pour mesurer les signaux de *strain rate* dynamique sur les volcans.

Nous analysons les formes d'onde DAS en *strain rate* provenant de plusieurs processus volcaniques, en nous concentrant principalement sur l'activité ordinaire, comprenant les explosions modérées et le trémor volcanique. Les signaux de *strain rate* des explosions stromboliennes ont généralement des fréquences comprises entre 2 et 10 Hz. De plus, les mesures DAS comprennent des signaux sismiques de très longue période entre 0.03 et 0.3 Hz. Nous examinons également les signaux générès par des explosions plus violentes (majeures) et des coulées pyroclastiques. Cette thèse explore le potentiel de le DAS comme outil de surveillance de l'activité volcanique du Stromboli. Nous souhaitons déterminer si le DAS peut offrir une meilleure compréhension des phénomènes volcaniques et si elle peut être utilisée conjointement avec l'instrumentation classique. Nos objectifs principaux sont (1) d'évaluer la précision du DAS pour la détection des signaux sismiques volcaniques et (2) d'obtenir des informations sur la dynamique et la localisation de ces événements.

Pour évaluer la précision du DAS, nous comparons les données en *strain rate* avec celles des sismomètres co-localisés. Nous avons appliqué deux méthodologies: La première, bien documentée (Bakku, 2015; Wang et al., 2018), a permis d'obtenir des signaux de *strain rate* par la différence finie des traces de vitesse sismique de deux sismomètres alignés sur une section de fibre. Ces résultats montrent une correspondance de phase quasi parfaite avec des coefficients de corrélation allant jusqu'à 0.99. Cependant, les signaux DAS sont souvent de 1.5 à 5 fois plus faibles que ceux des sismomètres, probablement à cause du couplage variable entre le câble et le sol, et d'un transfert de déformation inefficace dans la fibre. La seconde méthode, développée en collaboration avec l'Université Côte d'Azur

et l'Université de Naples, permet de récupérer les déplacements longitudinaux le long de la fibre sans sismomètres en intégrant numériquement les signaux du DAS. Elle montre que les traces de vitesse des particules obtenues avec le DAS correspondent bien à celles des sismomètres co-localisés (corrélations de 0.7 à 0.9), bien que les amplitudes soient plus faibles.

Nous appliquons des techniques de traitement d'antenne aux données en *strain rate* pour analyser l'activité volcanique et localiser les sources sismiques de différents signaux. En utilisant la méthode de Métaxian et al. (2002) pour estimer les délais entre paires de capteurs, nous analysons les signaux de trémor, d'explosions et de coulées pyroclastiques. Les résultats sont validés par des données de réseaux sismiques, d'infrasons et d'observations visuelles. Nous déterminons la vitesse apparente et l'azimut des ondes générées par l'activité ordinaire du Stromboli. Les signaux de trémor et d'explosions en *strain rate* indiquent des ondes sismiques se propageant depuis le sommet du volcan, à environ 200 m des cratères actifs, avec des vitesses apparentes d'environ 600 m/s, en accord avec les valeurs rapportées dans la littérature et avec les résultats obtenus avec les réseaux sismiques co-localisés.

Ensuite, nous étendons l'analyse aux signaux sismo-acoustiques générés par les coulées pyroclastiques qui ont eu lieu en octobre et décembre 2022 pour suivre leur propagation vers la mer. Une fois arrivés en mer, les deux PDCs ont généré des vagues de tsunami d'amplitude centimétrique (événement d'octobre 2022) et métrique (événement de décembre 2022), ce qui montre l'importance d'étudier et d'analyser ces phénomènes en profondeur. Les valeurs de *back-azimuth* obtenues à partir des signaux DAS, sismiques et infrasoniques montrent la migration des sources sismo-acoustiques des cratères jusqu'à la mer, correspondant aux observations visuelles. Ces informations permettent d'estimer les vitesses moyennes de propagation des coulées entre 33 et 73 m/s. Ces vitesses, ainsi que les estimations des volumes des deux coulées obtenues grâce aux images thermiques et aux énergies sismiques des signaux générés, nous permettent de simuler numériquement ces événements. Les simulations montrent que les angles de frottement de Coulomb diminuent avec l'augmentation du volume, reflétant un comportement observé dans d'autres processus gravitaires, sur Terre et sur d'autres corps planétaires (Lucas et al., 2014; Levy et al., 2015). Les paramètres rhéologiques des PDC sont essentiels pour modéliser leur dynamique, leur vitesse et leur distance de propagation. Bien que des recherches supplémentaires soient nécessaires, ces résultats démontrent le potentiel de cette nouvelle technologie dans la surveillance des zones volcaniques.

Contents

Abstract ii

Résumé iii

Riassunto v

Résumé long vi

List of Figures xiii

List of Tables xxix

Acronyms and Abbreviations xxxi

Introduction 1
About volcano seismology . . . 1
Distributed acoustic sensing and its use in geophyisical applications . . . 3
Aims of the thesis . . . 5
Thesis overview . . . 7

1 Properties of DAS measurements 9
1.1 Abstract . . . 9
1.2 Introduction . . . 9
1.3 Light propagation in optical fibres . . . 10
1.3.1 Scattering processes and losses within a fibre . . . 11
1.4 Basic principles of DAS measurements and response . . . 13
1.4.1 Retrieving the fibre strain from optical phase changes (ϕ-OTDR . . . 14
1.4.2 Gauge length effects . . . 15
1.4.3 DAS theoretical response . . . 16

2 Stromboli eruptive activity 20
2.1 Abstract . . . 20
2.2 Introduction . . . 20
2.3 Ordinary explosions . . . 24
2.3.1 VLP seismicity at Stromboli . . . 25
2.4 Violent explosions . . . 27
2.5 Lava flows . . . 28
2.6 Rapid mass movements and tsunamis . . . 29

3 DAS experiments at Stromboli volcano: from cable installation to analysis of seismo-volcanic signals **30**
3.1 Abstract . . . 30
3.2 Introduction . . . 31
3.3 Experimental setup . . . 33
3.3.1 Optical cable deployment . . . 33
3.3.2 DAS measurements and parametrisation . . . 35
3.3.3 Co-located instruments . . . 36
3.3.4 Permanent monitoring network . . . 36
3.4 Sensitivity patterns for wavelenghts observed at stromboli . . . 40
3.5 Geolocating the DAS channels . . . 41
3.6 Data overview . . . 43
3.6.1 Volcanic tremor . . . 43
3.6.2 Ordinary explosion . . . 47
3.6.3 Major explosion . . . 47
3.6.4 Rapid gravity-driven mass movements . . . 48
3.7 DAS measurements of VLP signals . . . 52
3.7.1 Principal strain axis . . . 56
3.8 Discussion and conclusions . . . 60

4 Empirical calibration of DAS measurements at Stromboli **62**
Preface . . . 62
4.1 Abstract . . . 63
4.2 introduction . . . 63
4.3 Converting node seismic-velocity to strain rate: finite-difference method . . . 65
4.3.1 Theoretical background . . . 65
4.3.2 Application to DAS measurements: ordinary and major explosions . . . 66
4.4 Converting DAS strain rate to velocity: spatial-integration approach . . . 72
4.4.1 Theoretical background . . . 76
4.4.2 Removing non-local signals . . . 77
4.4.3 Additional note on DAS sensitivity to displacement . . . 78
4.4.4 Application to DAS measurements: ordinary explosion . . . 80
4.5 Discussion and conclusions . . . 82

5 Array Analysis of Seismo-Volcanic Activity with Distributed Acoustic Sensing **84**
Preface . . . 84
5.1 Abstract . . . 85
5.2 Introduction . . . 85
5.3 Field experiment and data . . . 89
5.3.1 Description of the field-work . . . 89
5.3.2 Pre-processing . . . 90
5.4 Data . . . 90
5.5 DAS data calibration . . . 95
5.6 Slowness vector estimation . . . 96
5.6.1 Methodology . . . 96
5.6.2 Data selection . . . 98
5.6.3 Slowness vector estimation with the nodal array . . . 100

5.6.4 Slowness vector estimation with DAS arrays . . . 101
5.7 Discussion . . . 101
5.8 Conclusion . . . 104
5.9 Supplementary Information for: Array Analysis of Seismo-Volcanic Activity with Distributed Acoustic Sensing . . . 110
5.9.1 Supplementary Note A: Loss of strain sensitivity for a loose fibre bundle in a cable . . . 110

6 Tracking and characterising pyroclastic density currents with DAS and seismo-acoustic observations 115
Preface . . . 115
6.1 Abstract . . . 116
6.2 Introduction . . . 116
6.3 Methods . . . 120
6.3.1 Stromboli monitoring network and DAS deployment . . . 120
6.3.2 Array techniques . . . 121
6.3.3 Estimating seismic energies . . . 122
6.3.4 Numerical simulations . . . 123
6.4 Results . . . 124
6.4.1 Observed PDCs and seismo-acoustic signals . . . 124
6.4.2 Tracking PDCs . . . 125
6.4.3 PDCs Simulations . . . 127
6.5 Discussion . . . 130
6.6 Supplementary Information for: Tracking and characterising pyroclastic density currents with DAS and seismo-acoustic observations . . . 133
6.6.1 Supplementary Note 1: Stromboli activity . . . 133
6.6.2 Supplementary Note 2: Camera Analysis . . . 133
6.6.3 Supplementary Note 3: DAS data calibration . . . 133

Conclusions 147
Most significant achievements . . . 147
First track: assessing DAS data quality . . . 148
Second track: locating and characterising volcanic phenomena . . . 149
Ideas for further research . . . 149
DAS as a complementary volcano monitoring tool . . . 150

References 172

Acknowledgements 173

List of Figures

1.1 (a) Typical internal structure of an optical fibre; (b) scheme of major features regarding light propagation within the core of an optical fibre and the phenomenon of total internal reflection. The angle α in (b) is also known as angle of acceptance and is the angle of a light ray propagating in the air before entering the optical fibre, i.e. an input angle. (a) Is adapted and redrawn from Cabral (2016), while (b) from the following technical note. . 11

1.2 Summary of three types of scattering processes, Rayleigh, Brillouin and Raman together with their dependancy on physical parameters such as strain (ε) or temperature (T). Adapted from Muanenda et al. (2019). . . . 12

1.3 Illustration of DAS working principle. A DAS interrogator sends coherent optical pulses (in red) into the fibre and captures the radiation backscattered from random heterogeneites within the fibre glass (in green). Redrawn from Bakku (2015), Lindsey, Rademacher, and Ajo-Franklin (2020), and Al Hasani (2024). 13

1.4 Amplitude response for several gauge lengths L_G as a function of both frequency (bottom x-axis) and wavelength (top x-axis) considering a wave velocity of 1000 m/s. 15

1.5 (a) Change of the reference system towards fibre direction θ. (b) Seismic wave propagating horizontally along a direction ϕ and reaching an optical fibre having an orientation θ. (c) Sensitivity to P/SV/Rayleigh-waves of particle velocity (orange) and axial fibre strain (blue) under the assumption of a long wavelength with respect to the gauge length. Same as (c) but for SH/Love-waves. (b) Is redrawn from Martin (2018), while (c,d) are redrawn from Trabattoni et al. (2022). 16

1.6 Axial strain rate sensitivity along a horizontal fibre oriented at that angle ϑ from the direction of propagation of P (a,b) and S (c,d) waves. We present two cases with waves reaching the surface at an angle γ of 90° and 45° from the vertical. We consider different wavenumbers k (0.1, 0.5, 1, 4 and 16) and a gauge length L_G=10 m. Except for the case of small wavenumbers (i.e. large wavelengths compared to L_G), we observe a significant variation of the strain rate sensitivity with several notches appearing at various angles. Recalculated and redrawn from Martin (2018). 18

2.1 (a) Location of Stromboli volcano in the Southern Tyrrhenian Sea. (b) Hillshaded DEM of Stromboli island. The SdF and the active craters are indicated. Stromboli and Ginostra villages are marked as dark grey areas. Isolines in (b) are every 100 m. (c) Close-up view of the crater area with the NE, C and SW sectors. The DEM is computed from images taken in 2014 and courtesy of Italian Civil Protection. 21

2.2 3-D view (from NW) of Stromboli DEM comprising topography and bathymetry (vertical exaggeration 1.5x). 22

2.3 Examples of different processes occurring at Stromboli, such as (a) ordinary explosions, (b) major explosions, (c) paroxysmal explosions, (d) lava flows or overflows, and (e) PDCs, landslides and rockfalls. Credits are in the bottom left of each picture. (c) Is taken from Bevilacqua et al., 2020. . . . 23

2.4 Model of the plumbing system of Stromboli based on literature findings (Bertagnini et al., 2003; Parfitt, 2004; Francalanci et al., 2005; Métrich et al., 2005; Burton et al., 2007; Métrich et al., 2010; Calvari et al., 2011; Métrich et al., 2021; Ripepe, Lacanna, et al., 2021; Petrone et al., 2022; Pichavant et al., 2022). Redrawn from Métrich et al. (2010), Calvari et al. (2011), Petrone et al. (2022), and Ishikawa (2023). Vertical exaggeration of the 3D DEM is 2x. 24

2.5 Drumplot of six hours of seismic signals recorded at Stromboli (STR station, component E) between 04:00 and 10:00 UTC on 11 November 2022. We observe 45 explosive events, generating both high frequency (left) and VLP (0.03-0.3 Hz, right) signals. 25

2.6 (a) Thermal images of one ordinary explosion linked with its (b) thermal, (c) infrasound and (d) seismic signals. The VLP component of the seismic wavefield is visible in (d) with periods of ~10 s. (e) 2.5 hr long traces showing the ground tilt (top), VLP signals (middle) and thermal flux (bottom) associated with each explosion. Adapted from Ripepe, Delle Donne, et al. (2021). 26

2.7 (a) Log-log plot linking the typical plume heights with the erupted mass of ordinary (black), major (blue), and paroxysmal (red) explosions. (b) Ground tilt traces exhibit the exponential inflation (on a log scale) preceding ordinary (black), major (blue), and paroxysmal (red) explosions. The bold blue and red lines represent the stacking of several major explosions and paroxysms, respectively. (a) Is adapted from Voloschina et al. (2023), while (b) from (Ripepe, Lacanna, et al., 2021). 28

3.1 Pictures capturing the various stages of optical cable installation at Stromboli. (a-b) trench digging. (c) cable deployment in the trench. (d) Ensuring good contact between the cable and the ground and geolocation of the cable layout with differential GPS. (e) Covering the trench. (f) Performing tap tests. (g-h) Eventual fibre reparation and splicing. 32

3.2 (a) Map of Stromboli volcano with the DAS fibre layout (white, yellow and blue lines) and the permanent UniFi monitoring network, comprising broadband seismometers (white triangles), borehole tiltmeters (black circle), infrasound sensors (white diamond) and thermal (ROC) and visible (LBZ) cameras. The UniFi geophysical observatory is marked by a red star. (b-e) Show the various DAS arrays, i.e. NT (b), CT (c), ST (d), and GR (e). 34

3.3 Fibre layout and node deployment during each experiment. 37

3.4 Theoretical sensitivity patterns of seismometers (a) and DAS with a gauge length of 5 m (b) and 10 m (c) for P (blue), SV (purple), and SH (yellow) waves with velocities V_P = 2000 m/s and V_S = 1140 m/s and a frequency of 2 Hz. The vertical incidence angle of the waves is 45°. 39

3.5 Theoretical sensitivity patterns of particle velocity (a,d) and DAS strain rate with a gauge length of 5 m (b,e) and 10 m (c,g) for Rayleigh (blue) and Love (purple) waves. In the first row (a-c), we use velocities of Rayleigh and Love waves of V_R = 1000 m/s and V_L = 800 m/s, respectively, at 2 Hz. In the second row (d-f), we use velocities V_R = 350 m/s and V_L = 400 m/s at 9 Hz. 40

3.6 Workflow describing the several steps to locate the DAS channels. (a) Geolocation of the fibre layout with a differential GPS. Approximately every 10 m (red dots), we measure the incremental distance along the fibre later used to validate the tap-test locations The solid grey line is the final fibre layout, while the dashed black line is the raw differential GPS track. (b,c) Tap-test location of several DAS channels along the fibre. (c) Shows the strain rate waveforms of one tap recorded at ten DAS channels. The red trace in (c) indicates the channel that we identify as the closest to the tap. (d) Final 3D location of all the DAS channels. 42

3.7 (a) 3D location of the lowest branch of our fibre deployment, along the path to the summit. (b) Distance between subsequent DAS channels (in black) and standard deviation (blue interval). With a channel spacing of Δx = 2 m along the fibre, we measure Δx = 1.98 ± 0.03 m. Additionally, the interpolated channel spacing is consistently less than 2 m, likely due to bends and loops reducing the actual 3D distance between channels. 43

3.8 Data availability of the DAS measurements (in green) during the (a) 2020, (b) 2021, (c) 2022, and (d) 2023 experiments at Stromboli. The red vertical lines indicate major explosions that occurred on 2021/10/06, 2022/09/29, and 2023/01/30. The orange vertical lines indicate lava overflows on 2022/10/09, 2022/11/16, 2022/12/04, 2022/12/13, 2023/09/27, 2023/10/03, and 2023/10/06. The purple vertical lines indicate PDCs that occurred on 2022/10/09, 2022/10/10 and 2022/12/04. 44

3.9 (a) Seismic velocity trace (Z component, blue) of 15 seconds of volcanic tremor recorded by the broadband seismometer STR (Fig. 3.2a) on 2022/10/05 at approximately 22:13 UTC. (b) Power spectral density (PSD) of the ground velocity from (a). (c) Infrasonic pressure trace (black) recorded by the STR station. We observe several pressure transients (puffing) repeating every 1-2 s. (d) PSD of the pressure trace in (c). (e) DAS strain rate trace (red) recorded at channel 912. (f) PSD of the strain rate in (e). (g) Strain rate record along the entire 6 km fibre. The vertical dotted line in (g) indicates the position of channel 912 shown in (e). Black triangles above (g) indicate offsets where fibre segments (indicated by grey numbers from 1 to 6) are connected. (h) Frequency domain representation below 15 Hz of the strain rate in (g). (i) Map of the 2022 fibre layout showing the direction of light travel in the cable. (j) Snapshot from the ROC thermal camera during the event, with a white arrow pointing to the active vent in the NE crater area responsible for the puffing activity observed in (c). . . . 45

3.10 (a) 15 s seismic velocity trace (Z component, blue) recorded by the broadband seismometer STR (Fig. 3.2a) during a volcanic explosion on 2022/11/28 at approximately 03:26 UTC. (b) Power spectral density (PSD) of the ground velocity from (a). (c) Infrasonic pressure trace (black) recorded by the STR station. (d) PSD of the pressure trace in (c). (e) DAS strain rate trace (red) recorded at channel 912. (f) PSD of the strain rate in (e). (g) Strain rate record along the entire 6 km fibre. The vertical dotted line in (g) indicates the position of channel 912 shown in (e). Black triangles above (g) indicate offsets where fibre segments (indicated by grey numbers from 1 to 6) are connected. (h) Frequency domain representation below 15 Hz of the strain rate in (g). (i) Map of the 2022 fibre layout showing the direction of light travel in the cable. (j) Snapshot from the ROC thermal camera during the event, with a white arrow pointing to the explosion. . . 46

3.11 (a) 15 s seismic velocity trace (Z component, blue) recorded by the broadband seismometer STR (Fig. 3.2a) during a major explosion on 2021/10/06 at approximately 14:17 UTC. (b) Power spectral density (PSD) of the ground velocity from (a). (c) Infrasonic pressure trace (black) recorded by the STR station. (d) PSD of the pressure trace in (c). (e) DAS strain rate trace (red) recorded at channel 912. (f) PSD of the strain rate in (e). (g) Strain rate record along the entire 6 km fibre. The dashed yellow line in (g) marks the theoretical arrival times at the several channels of an infrasonic pressure wave propagating from the active craters at 340 m/s. The vertical dotted line in (g) indicates the position of channel 912 shown in (e). Black triangles above (g) indicate offsets where fibre segments (indicated by grey numbers from 1 to 6) are connected. (h) Frequency domain representation below 15 Hz of the strain rate in (g). (i) Map of the 2021 fibre layout showing the direction of light travel in the cable. (j) Snapshot from the ROC thermal camera during the event. 49

3.12 (a) 2 minutes of seismic velocity traces (Z component) recorded by the broadband seismometers STR (blue) and SCI (teal) (Fig. 3.2a) during a rockfall that occurred on 2022/10/25 at approximately 12:20 UTC. (b) Power spectral density (PSD) of the ground velocities from (a). (c) Infrasonic pressure trace (black) recorded by the STR station. (d) PSD of the pressure trace in (c). (e) DAS strain rate trace (red) recorded at channel 912. (f) PSD of the strain rate in (e). (g) 15 s strain rate record along the entire 6 km fibre. The vertical dotted line in (g) indicates the position of channel 912 shown in (e). Black triangles above (g) indicate offsets where fibre segments (indicated by grey numbers from 1 to 6) are connected. (h) Frequency domain representation below 15 Hz of the strain rate in (g). (i) Map of the 2022 fibre layout showing the direction of light travel in the cable. (j) Snapshot from the LBZ visible camera during the event, with a black arrow indicating the rockfall along the SdF. 50

3.13 (a) 3 minutes of seismic velocity traces (Z component) recorded by the broadband seismometers STR (blue) and SCI (teal) (Fig. 3.2a) during a rockfall that occurred on 2022/10/25 at approximately 12:20 UTC. (b) Power spectral density (PSD) of the ground velocities from (a). (c) Infrasonic pressure trace (black) recorded by the STR station. (d) PSD of the pressure trace in (c). (e) DAS strain rate trace (red) recorded at channel 912. (f) PSD of the strain rate in (e). (g) 15 s strain rate record along the entire 6 km fibre. The vertical dotted line in (g) indicates the position of channel 912 shown in (e). Black triangles above (g) indicate offsets where fibre segments (indicated by grey numbers from 1 to 6) are connected. (h) Frequency domain representation below 15 Hz of the strain rate in (g). (i) Map of the 2022 fibre layout showing the direction of light travel in the cable. (j) Snapshot from the LBZ visible camera during the event showing the PDC propagating along the SdF. 51

3.14 From 2022/09/15 to 2023/02/01, VLP amplitudes (in seismic displacement) recorded at the UniFi STR broadband station (Fig. 3.2a) reach maximum values between approximately November 10 and 20, 2022. 52

3.15 (Top row) 2 minutes strain measurements of an explosion occurred on 2022/11/13 at 04:47 UTC filtered between 1-10 Hz recorded by (a) single DAS channel (offset 1730 m) and (b) along the entire fibre. (Bottom row) Same as in (a,b) but filtered between 0.04-0.1 Hz. The grey curve in (c) shows the raw strain waveform at channel 1730. Vertical lines in (b,d) indicate DAS channels corresponding to changes in cable orientation. (e) Frame recorded by the thermal camera during the explosion. 53

3.16 (a) 180 s traces of DAS strain recorded at channel 1730 (ST array) during the 13 November 2022 explosion at 04:45:20 UTC. We show both raw (grey) and filtered in the VLP band between 0.04-0.1 Hz (red). (b) Same as (a) but considering the DAS channel 1910. (c) 180 s particle velocity traces recorded at the UniFi STR station (Fig. 3.17) along the direction (~263°) of the DAS channel 1730 (a). The grey and red traces respectively indicate raw and VLP (0.04-0.1 Hz) signals. (d) Same as (c) but considering the seismic signal along the direction of the DAS channel 1910 (~161°). (e) Normalised VLP strain traces recorded at channels 1700-1780 (red), overlaid with normalised seismic velocity records from the STR and RND broadband stations (Fig. 3.17) rotated along the same direction (black). (f) Same as (e) but considering the traces recorded at channels 1876-1920 and the seismic components of the STR and RND stations along the same direction. The maps within (a, b, e, f) show the position of the DAS channels in the ST array (grey line) as red circles. 54

3.17 Hillshaded view of Stromboli volcano showing the optical fibre layout. Each DAS channel is coloured with respect to the amplitude of the VLP strain signal in Fig. 3.15 at 04:47:25 UTC, i.e. at the midpoint of the waveform. The blue and red colors indicate negative and positive polarities, respectively. White squares represent the permanent UniFi broadband stations. Black lines indicate the horizontal particle displacement of the explosion in Fig. 3.15 in the VLP band. The red area indicate the crater terrace. The yellow and teal stars indicate the position of the VLP source centroid according to Ripepe, Delle Donne, et al. (2021) and Chouet et al. (2003), respectively. The black star indicates the location of the explosion as seen by the thermal camera. The dotted lines are altitude contours every 200 m. 55

3.18 Stack (in red, green, and blue) of 95 different VLP strain waveforms (in grey) recorded on 2022/11/13 at three different channels of the ST array: 1750 (a), 1820 (b), and 1890 (c). 56

3.19 (a) Stack of 95 different VLP strain waveforms recorded on 2022/11/13 at the offset 1730 m. (b) VLP strain measurements along 2.8 km of fibre resulting from the stack of 95 VLP signals recorded on 2022/11/13. The vertical dashed lines in (b) indicate changes in fibre direction. 57

3.20 Schematic drawing of the two principal unknown strains ε_{11} and ε_{22} (with ε_{11} having an unknown direction α with respect to the East) and the three known linear strains (e_1, e_2, and e_3) along three different directions (θ_1, θ_2, θ_3). 58

3.21 Stack (in black) of the VLP strain waveforms generated by the explosion at 04:45:20 UTC on 2022/11/13 and recorded at several channels along three different segments of the ST array (ST1, ST2, ST3) having different orientations (indicated on top of each plot relative to the East). 59

3.22 Determinant $D(\alpha)$ of the coefficient matrix in Eq. (3.7) considering different angles α from 0° to 180°. The red dots indicate the angles α for which $D(\alpha) = 0$, i.e., 1.82° and 91.82°. 59

3.23 Principal strain axes obtained from the explosion at 04:45:20 UTC on 2022/11/13. The red and blue colours respectively indicate positive and negative strains. Values of ε_{11} and ε_{22} are in nanostrain. 60

4.1 Geometries of the NT, ST and GR arrays. The fibre optic segments we use are coloured in red. Black triangles indicate the 3C nodes. The top row shows the deployment of nodes in 2021 at the NT (a) and ST (b) arrays. The bottom row shows the installation in 2022 at the NT (c) and GR (d) arrays. 67

4.2 Comparison between 20 s strain rate traces of an ordinary explosion occurred on 2021/09/26 recorded by DAS (red) and obtained from nodes (black) using Eq. (4.3). We consider six cable segments, corresponding to the three sides of both NT (N2-N3, N3-N4 and N5-N6) and the ST (S4-S5, S6-S7, S7-S8) arrays (Fig. 4.1). We compare DAS and node measurements both in time (left column) and frequency (right column) domains. The ratios (R) between the RMS amplitudes of node and DAS traces, and the maximum cross-correlation coefficients (CC) between the two waveforms are shown in the top right in the left column. To enhance clarity, we rescale DAS strain rate traces by multiplying them with the ratio R. Waveforms are filtered between 0.5-15 Hz. 69

4.3 Same as Fig. 4.2, but considering a Major explosion occurred on 2021/10/06 (same explosions as in Fig. 3.11). 70

4.4 Comparison between strain rate traces of ordinary (left column) and major (right column) explosion occurred in 2021 (top row) and 2022 (bottom row) recorded by DAS (red) and obtained from nodes (black) using Eq. (4.3) along the segment N2-N3. Normal explosions occurred on (a,c) 2021/09/26 (same event as in Fig. 4.8) and (e,g) 2022/10/09. Major explosions occurred on (b,d) 2021/10/06 (same event as in Fig. 3.11) and (f,h) 2022/09/29. The ratios (R) between the RMS amplitudes of node and DAS traces, and the maximum cross-correlation coefficients (CC) between the two waveforms are shown in the top right in the left column. To enhance clarity, we rescale DAS strain rate traces by multiplying them with the ratio R. (c,d) Show a 5 s zoom on the signals of ordinary explosions, while (g,h) show a 10 s zoom on the signals of major explosions. Waveforms in Fig. 4.4 are filtered between 0.5-15 Hz. 71

4.5 (a) A rectilinear fibre-optic cable (grey line) at rest with reference markers (black ticks) placed at regular intervals from the DAS interrogator (orange ruler). Three snapshots (b-d) show a zero-average localized impulsive wavelet moving through the cable from left to right. (b) As the wavelet reaches the start of the cable, ground displacement occurs, with blue indicating elongation and red indicating contraction. The displacement of the DAS interrogator causes a contraction at the beginning of the cable. This contraction reduces the distance to all subsequent points, adding a constant deformation $\delta(s,t) = -u(0,t)$ along the entire cable. (c) The deformation becomes confined within the linear section. Since shortening on one side balances elongation on the other, the integrated strain cancels out, leaving subsequent points unaffected. With a stationary reference point (the DAS interrogator) stationary, the measurement is local: $\delta(s,t) = u(s,t)$. (d) When the impulse reaches the end of the rectilinear section, and if the cable bends (e.g., with a 180° kink), the elongation is no longer balanced by an equal contraction, which occurs outside the cable. In this case, the backward part of the kink elongates by the same amount, increasing the arc length to points beyond the kink by twice the displacement: $\delta(s,t) = 2u(s,t)$. This illustrates that integration cannot be applied directly across a kink due to geometric effects. 74

4.6 Illustrative simulation. (a) An impulsive plane P wave propagating along the x-axis produces a horizontal displacement wavefield (blue–green–yellow background raster). A fibre-optic cable (red line) records the deformation along a given geometry. Deformation (b) is the sum of (d) the true displacement and (c) a reference term (also referred to as 'non-local effects') that must be estimated and removed. We observe non-local effects as horizontal features. They are space invariant signals starting at a given offset. The origin is either the beginning of the cable (marker A), a kink (markers B, C, D and E), a perturbation of the rectilinear segment (section CD), the curvature of the cable (section DE), or a nonlinear effect, here produced by a 50-m hanging section at the middle of the segment EF. (f) Segment-wise method in which we remove the averaged deformation (e) on each segment. Sliding-window method: an alternative solution is to remove (h) a sliding average (we use a 500 m long window with a Hann tapering) to get (i). Spatial differentiation of the deformation gives (g) strain, which is a local measurement. The red vertical dotted lines in (b-i) indicate linear cable segments. 75

4.7 Sensitivity characteristics of deformation-recovered displacement. (a) The sensitivity is a function of the product between the apparent wavenumber and the length of the rectilinear section (kL); and the shape of the window (here rectangular and Hann windows are shown). (b–e) Directivity patterns for P (b,d) and S (c,e) waves using the rectangular and the Hann windows for different kL values ranging from 1 to 16 (see legend on the right). The horizontal black lines in (b-e) indicate the cable direction. From Trabattoni et al. (2023). 79

4.8 Comparison between velocities recovered from DAS and co-located seismometers. (a) Deployment of the fibre-optic cable on the Stromboli's NE flank, with a detail of the fibre section (NT) considered in this comparison (solid red line). Six nodes were deployed (#1-6) at the midpoints of the straight segments (black inverted triangles). Letters from A (i.e., the beginning of the cable section) to E (its end) mark the sharp changes in orientation. (b) Strain rate recorded along the NT cable segment. Dashed black lines indicate the changes in cable direction marked in (a). Red dotted lines represent the offsets of the DAS channel closest to each node. (c) Deformation rate without any processing. (d) Velocity recovered with the segment-wise approach using the A-E markers as segment limits. (e) Velocity recovered with the sliding-window approach with a 250 m Hann window. (f-g) Comparison between the velocity waveforms from the seismometers (in black) and recovered from DAS (in red), described using correlation coefficient (CC) and RMS ratio (R), for the segment-wise and sliding-window approaches respectively. 81

4.9 Search of the optimal window length L^*. We compare DAS-recovered velocity computed with different window lengths using the sliding-window approach with the ground velocity recorded at the six co-located seismometers (nos 1–6). We use the CCs metric. Circles mark the optimal values for each channel. We find a correlation between the segment lengths and the value of L^*. Channel no. 5 is located on the smaller segment (DE) and has the smallest L^*. Its L^* is twice its segment length because the effective length of the Hann window is half its size. Channel no. 3 is in the middle of the longest section (BC) and exhibits the longer L^* of 450 m. The distance to the closest edge seems to be the main factor dictating L^*. We chose a fixed value of 250 m (vertical dashed line) as the global L^* (Figs 4.8e and g). 82

5.1 High-resolution digital elevation model (DEM) of Stromboli Northeast flank. The fibre-optic cable (yellow line), the 22 SmartSolo nodes numbered from N1 to N22 (blue triangles), the broadband station BB1 (black triangle) are displayed. Some node names are omitted for visual reasons, however they are named from N1 to N22 in a progressive manner starting from the Geophysical Observatory (OSV, red star). Green triangles mark the location of the seismic (ROC, STR), infrasonic (MIC5), and tiltmeter (LHR) stations of the Laboratory of Experimental Geophysics (LGS, University of Florence). (Bottom right) Magnified view of the triangle-shaped DAS and seismic arrays, with DAS channels colored according to their azimuth with respect to the North. The DAS interrogator was hosted inside the OSV. The DEM is computed from images taken in 2014 and courtesy of Italian Civil Protection. 86

5.2 (a) Velocity recorded by the L component of node N16 on 09/22/2020 from 19:34 to 20:34. (blue). (b) strain rate at co-located DAS channel d902.4 for the same time interval (red). Green circles in (a) mark the explosive events detected with a recursive STA/LTA algorithm (Beyreuther et al., 2010). The green star marks the largest event. (c) strain rate record at each of the 362 DAS channels ordered according to their offset from the DAS interrogator. The black horizontal segment marks the DAS channel d902.4. Data are filtered between 1 – 10 Hz in this figure. 87

5.3 PSDs computed during the hour-long time series (09/22/2020 19:34 – 20:34 UTC) for different unfiltered records: (a) PSD of DAS channel d902.4 (brown) and stack of the PSDs calculated for the channels d892.8-912.0 (red), in strain rate. (b) and (c) PSDs of the 3 components of co-located node N16 and broadband seismometer BB1, in acceleration. (d) PSDs of the DAS channel d902.4 and the DAS d892.8-912.0 channel stack converted to acceleration using Eq. (5.1), and the L components of N16 and BB1, in acceleration. 88

5.4 (a) velocity measurement of the L component of node N16 (blue) during an explosive event occurred at 20:14:30 UTC on 2020/09/22 (green star in Fig. 5.2). (b) strain rate of the same event at co-located DAS channel d902.4 (red). (c) strain rate record at each of the 362 DAS channels ordered according to their offset from the DAS interrogator. Black horizontal line in (c) marks the location of DAS channel d902.4 along the cable. (d) Zoom-in of the frame in (c). Dashed lines in (a–d) mark the theoretical arrival times at the several sensors of waves with velocities of 660 and 340 m/s starting from the onset of the acoustic wave at the source as recorded by the MIC5 infrasonic station (Fig. 5.1). (e) Frequency domain representation of the strain rate record below 25 Hz along the fibre for the 20 s of the explosion. 89

5.5 Comparison between the strain rate traces recorded by DAS (red) and obtained from nodes (blue) using Eq. (5.2) across the segment N18–19 (DAS channels d938.4-d967.2) for one explosive event (top row) and 20 s of volcanic tremor (bottom row), in both time (left column) and frequency (right column) domains. The ratios (R) between the RMS amplitudes of node and DAS traces, and the maximum cross-correlation coefficients (CC) between the two waveforms are shown in the bottom right of (a) and (c). To enhance clarity, we rescale DAS strain rate traces by multiplying them with the ratio R. 91

5.6 (a) Ratios (R) between the RMS amplitudes of strain rate obtained from nodes and DAS along segment N18-19 are calculated for various time windows throughout the entire hour shown in Fig. 5.2. This includes 17 volcanic explosions detected using an STA/LTA algorithm (green circles) and 20 windows containing volcanic tremor signals each with a length of 20 seconds (gray diamonds). The green dashed line in (a) represents the median value of the ratios R_{expl} calculated from explosion signals. The gray dotted line in (a) represents the median value of the ratios R_{tr} calculated from tremor signals. (b) DAS cumulative strain rate trace along the segment. (c) Node-derived strain rate trace along the segment. In (a) and (b), green circles indicate the detected explosions and gray vertical bars represent the 20-second long tremor windows used to compute R in (a). . . 92

5.7 Geometry of the nodal array N15–19 (a) and of the DAS-L (b) and DAS-T (c) arrays. The black arrow in (a-c) indicates the back-azimuth (251°) of the central part of the active craters with respect to the centroid of each array. (d-n) show the traces for an explosive event (same as in Fig. 5.4). (d, g, l) show the 3 components of the 5 nodes. (e, h, m) show the 10 DAS channels along the 3 segments of the DAS-L array. (f, i, n) show the 10 DAS channels along the 3 segments of the DAS-T array. Traces are band-pass filtered in the 3–5 Hz frequency range. 93

5.8 In red, average coherence computed during the unfiltered 1 hr long strain rate time series (09/22/2020 19:34–20:34) between all of the 135 channel pairs in the 3 segments of the DAS-L array. Coherence traces of each pair are also shown as dotted lines (with colors relative to the distance between the two channels). In blue, average coherence between the N component of each node pair in the array N15–19 during the same period of time. Grey vertical dashed lines mark the values of 1, 3 and 5 Hz, that are the limits of the two frequency bands (i.e. 1–3 and 3–5 Hz) for which we compare array analysis results with strain rate and seismic velocity data. 94

5.9 (a) 1-hr seismic velocity trace of the N component of node N16 band-pass filtered between 3–5 Hz. Green circles in (a) mark the detected explosive events. Array processing results obtained with the nodal N15–19 array are in b-f considering one hour of signals. (b) mean coherence between traces in each time window. (c) back-azimuths and (d) apparent velocities obtained with the method described in Section 5.6. Corresponding PDFs are shown in (e) and (f). Pink dashed lines in (c) and (e) indicate the back-azimuth of the central point of the active craters with respect to the array centroid. 96

5.10 PDF results of back-azimuth (left column) and apparent velocity (right column) in the frequency bands of 1–3 (blue), 3–5 (red), 5–7 (green) Hz for the Z, N, and E components of the nodal array N15-19 during the analysed 1-hr time series (09/22/2020 19:34–20:34 UTC). The dashed lines in the left column represent the direction of the central part of the active craters (251°). 97

5.11 strain rate traces corresponding to channels (a) d741.6 (in red) and (c) d902.4 (in blue) arrays, normalized and band-pass filtered between 3–5 Hz. Green circles in (a) and (c) mark the detected explosive events, while the green star marks the most intense event during the time period considered. (b) and (d) show the geometries of the DAS-L and DAS-T arrays. White circles in (b) and (d) mark the location of channels d741.6 and d902.4 along the cable. Black arrows in (b) and (d) represent the back-azimuth of the central part of the crater area (251°) with respect to the array centroids. Array processing results are in e-i for the DAS-L (red) and DAS-T (blue) arrays and for the N component of the nodal N15–19 array (black). (e) mean coherence between traces in each time window. (c) back-azimuths and (d) apparent velocities obtained with the method described in Section 5.6.1. Corresponding PDFs are shown in (h) and (i). Dashed lines in (f) and (h) indicate the direction of the active craters. 100

5.12 PDFs of back-azimuth (left column) and apparent velocity (right column) in the 3–5 Hz frequency band for the N component of the nodal N15-19 array (top row, in black) and for the DAS-L (red), the DAS-T (blue), and the DAS-TL (green) arrays (bottom row). The dashed lines in the left column represent the direction of the central part of the active craters (251°). 102

S5.1 (a) DEM of the North-east flank of Stromboli volcano showing the fibre-optic cable (white line). (b) Topographic profile along the A–A' line, approximately corresponding to the cable path. (c) Topographic profiles along the 150 m long B–B' and C–C' sections respectively below and above the position of node N06 (red star). From N06 to A', higher strain rate amplitudes (up to an order of magnitude) are recorded. 105

S5.2 (top row) Geometries of the (a) N15–19 and (b) N15–22 nodal arrays. (bottom row) Array response patterns for the (c) N15–19 and (d) N15–22 nodal arrays. 106

S5.3 DAS array response functions. First row: geometries of the (a) DAS-L, (b) DAS-T and (c) DAS-TL fibre-optic arrays. The black arrow represents the back-azimuth (250°) of a plane wave impinging on the array with a frequency of 5 Hz and an apparent velocity of 500 m/s. Second row: (d-f) are the array responses for the three different geometries calculated without taking into account the DAS polarization pattern. The red star indicates the true location of the considered wave. Third row: (g) polarization pattern of the strain rate (red) and seismic velocity (blue) for P/SV/Rayleigh waves propagating along the black arrow. Solid and dashed lines indicate positive and negative amplitudes, respectively. Modified after Trabattoni et al., 2022. (h-l) are the array responses for the three different geometries shown in a-c calculated by taking into account the strain rate polarization for P/SV/Rayleigh waves. Fourth row: (m-p) same as third row for SH/Love waves. Magnified views between -0.003 and 0.003 s/m are exhibited in (n) and (p), for clarity. This figure shows that an incident wave coming from the active craters at Stromboli can be recovered with our DAS array geometries. 107

S5.4 Same as Fig. S5.3 for a plane wave impinging on the DAS arrays with a back-azimuth of 160°, a frequency of 5 Hz and an apparent velocity of 500 m/s. 108

S5.5 (a) 1-hr seismic velocity trace of the N component of node N16 band-pass filtered between 3–5 Hz. Array processing results are in b-f for the array N15-N19 (black) and N15-N22 (red) considering 1 hr of signals. (b) mean coherence between traces in each time window. (c) back-azimuths and (d) apparent velocities obtained with the method described in Section 5.1. Corresponding PDFs are shown in (e) and (f). Dashed lines in (c) and (e) indicate the back-azimuth of the central point of the active craters with respect to the array centroids. 109

S5.6 (a) Representation of the fibre-optic cable deployed at Stromboli. (b) detail of one single fibre within the fibre bundle. (c) Scheme of the fibre in (b). . 110

S5.7 strain rate waveforms generated in the laboratory by three different types of energisation and recorded at co-located channels d38.4 (in black) and d125.6 (in red), respectively situated in the optical cable installed at Stromboli, and in the single cable without jacket secured to the previous one. (a) hit close to the cables; (b) tap on the jacketed cable; (c) hit on hanging cable. RMSA between each couple of waveforms are reported in the figure. Waveforms are bandpass-filtered between 1-10 Hz. 113

6.1 (a) Map of Stromboli Volcano showing the monitoring network of the University of Florence, Italy (UniFi) consisting of e.g. broadband seismo-acoustic stations (white triangles), infrasonic pressure sensors (white diamonds), tsunami gauges (blue circles), and the LBZ (visible) and ROC (thermal) cameras. Continues in the next page. 118

6.1 Continued from previous page. The yellow line represents the 4 km long DAS cable exhibiting four sub-arrays (i.e., D-NT, D-CT, D-ST and D-GR). The DAS interrogator is hosted in the UniFi Geophysical Observatory (OSV). Black triangles are three-component nodes deployed in two arrays (N-NT and N-GR). Blue and red stars in (a) respectively mark the location of PDC1 and PDC2 flow fronts obtained by LBZ georeferenced frames every 2s (Supplementary Note 1). (b) and (c) show two snapshots recorded by the LBZ camera during PDC1 and PDC2, respectively. Blue and red stars mark the position of the pyroclastic front in the visible images every 2s. tf_1 (07:23:08 UTC) and tf_2 (15:18:12 UTC) in (b) and (c) are the frame times from which PDC1 and PDC2 can be well located. te_1 (07:23:30 UTC) and te_2 (15:18:24 UTC) indicate the arrival times at sea of the two PDCs. (d) Exhibit time vs. distance plot for PDC1 (blue) and PDC2 (red) with the corresponding average front velocities. The DEM is computed from images taken in 2014 and courtesy of Italian Civil Protection. 119

6.2 4-minutes-long traces, spectrograms and corresponding back-azimuths of PDC1 (left column) and PDC2 (right column). (a,d) Show the DAS strain rate at the D-CT array. (b,e) Show the seismic velocity (vertical component) recorded by the T3 node (b) and the ROC seismometer (e). (c,f) Show the acoustic pressure recorded by the MIC5 infrasonic sensor. Back-azimuths are calculated using the D-CT, N-NT and EAR arrays. Supplementary Fig. S6.4 shows the results obtained with the remaining DAS and nodal arrays. The blue and red vertical lines indicate the onsets (ts_1 = 07:22:40 and ts_2 = 15:17:46 UTC) and arrival at sea (te_1 = 07:23:30 and te_2 = 15:18:24 UTC) of PDC1 and PDC2, respectively, as observed by the thermal and visible cameras (Supplementary Fig. S6.1, Supplementary Movies 1,2). Back-azimuths obtained with D-CT and N-NT arrays in (a,b,d) are filtered for coherencies> 0.4 and errors< 10° while being smoothed with a 3 s-long window. Back-azimuths obtained with EAR array are filtered for time residuals < 0.1 s (Section 6.3.2). Black arrows in (d,f) indicate the back-azimuths obtained for an explosion that occurred at the NECs at 15:16:45 UTC. (g-i) Show the geometries of D-CT, N-NT and EAR arrays. 126

6.3 Snapshots of the simulations that best fit the observed front velocities of PDC1 (left column, a-c) and PDC2 (right column, d-f). (a) and (d) show the thickness of the initial mass. (b, c) and (e, f) show the velocity of PDC1 and PDC2 at different times, i.e. when the flows are halfway down and reach the shoreline, respectively. Volumes V and friction coefficients δ of PDC1 ($V_1 = 23 \times 10^3\ m^3$, $\delta_1 = 25°$) and PDC2 ($V_2 = 81 \times 10^3\ m^3$, $\delta_2 = 21°$) are shown in (a) and (d) respectively. (g) shows the average front velocity of PDC1 (blue) and PDC2 (red) calculated at every time step for flow thickness > 0.5 m and different friction angles δ. The average front velocity is calculated in a radius of 100 m from the flow front. Blue and red stars in (g) are the front velocities calculated from each georeferenced frame (Fig. 6.1d). 128

6.4 (a) DAS strain rate traces (offset 900m) between 08:00–07:00 UTC on 2022/10/09. (b) back-azimuth results obtained with the D-CT array smoothed with a 5 s window. (c) Seismic velocity trace (node T3, Z component) during the same period. (d) back-azimuth results obtained from N-NT array smoothed with a 5 s window. (e-g) Three snapshots of the LBZ visible camera during the three events (Evs. 1-3). Event 1 corresponds to PDC1, while Events 2 and 3 are landslides along the SdF. 129

6.5 (a) Cumulative strain rate time series along offsets 890-910 between 13:50–15:40 UTC on 2022/12/04. The three colours represent three distinct phases of increasing volcanic activity observed from video, spectrogram and back-azimuth results. (b) Spectrogram of (a). (c) Back-azimuth results obtained with the D-CT array. The grey and blue horizontal bands in (c) represent the back-azimuths of the craters and the shoreline, respectively. The black vertical lines in (b) and (c) represent the two times when a change in activity is observed (i.e., ~14:25 and ~15:18 UTC). (d-f) Three snapshots of the LBZ camera during the 3 phases of activity. 131

S6.1 (a-d) Thermal images recorded by the ROC camera (top), and georeferenced visible images recorded by the LBZ camera (bottom) during PDC1. In (a), white lines represent the contour lines of the DEM projected onto the image (Supplementary Note 2). (e-h) Same as the top line, but for PDC2. In (e), we can observe the dimensions of the mass that generated PDC2, having a height of ~ 35 m and a width of ~ 47 m. White arrows in (b-d) and (f-h) point towards the location of PDC1 and PDC2 along the SdF. (i) Coordinates of the front position of PDC1 (blue) and PDC2 (red) obtained from visible images at three different times. 134

S6.2 Comparison between the strain rate traces recorded by DAS (red) and obtained from nodes (black) using Eq.(5.2) with six segments of the NT array (a-g) and five segments of the GR array (h-l). Traces are filtered between $1 - 15$ Hz. The ratios between the RMSA of node and DAS traces and the maximum cross-correlation coefficients (CC) between the two waveforms appear in the bottom left of each plot. (g) and (m) show the geometry of the NT and GR arrays. The fibre optic segments we use are coloured in red. Black triangles indicate the 3C nodes. 136

S6.3 (a) Strain rate, (b) seismic velocity, and (c) infrasonic pressure traces generated by one volcanic explosion (occurred on 2022/10/09 at ~07:05 UTC) recorded by D-CT (d), N-NT (e) and EAR arrays (f). DAS and node traces are filtered between $1 - 5$ Hz, while infrasound traces are filtered between $1 - 10$ Hz. 137

S6.4 (left column) 20 s-long traces and back-azimuth results obtained with D-CT (a), N-NT (b) and infrasound EAR (c) arrays during an explosive event (2022/10/09 at 07 : 05 UTC). (d) Map of Stromboli volcano with rose diagrams of the back-azimuth results obtained with D-CT (red), N-NT (blue) and EAR (black) arrays. (e) Zoom on the crater area. The red circle, blue triangle, and black diamond in (d,e) represent the D-CT, N-NT and EAR array centroids. The red and blue lines in (e) are the back-azimuths obtained using D-CT and N-NT that exhibit the highest coherence. The white dashed circle in (e) represent the total extent of the crater area, while the red one corresponds to the area of highest temperature at the summit(Revil et al., 2023). The red star in (d,e) is the location of the explosive event as seen from ROC thermal camera (f). 138

S6.5 (a) 15-second strain rate traces of the explosion occurred at 07:05 UTC on 2022/10/09 (same as Supplementary Figs. S6.2, S6.7, S6.6) recorded along the entire fibre-optic cable. (b) Zoom on the last portion of the fibre between offsets 4000 and 5600 (comprising the D-NT array). Several spurious signals due to high noise levels are visible at different (and varying) offsets as vertical features. (c) Individual strain rate traces between offsets 5200-5500 m. We observe the same features due to high noise levels. (d) Map of the fibre location of D-NT with offsets 5200-5500 m highlighted in red. Arrows in (b) and (c) indicate the spurious signals. 139

S6.6 (left column) Seismic velocity traces of ROC broadband seismometer (Z component) of PDC1 (a) and PDC2 (b) used to compute seismic energies. The onsets correspond to t_{s1} and t_{s2}, respectively. Signals are truncated 4 s after the entrance of the PDCs in the sea (at t_{e1} and t_{e2}. (right column) Power spectral densities of PDC signals recorded by STR, ROC and SCI broadband seismometers (Z components). 140

S6.7 Seismic velocity traces of ROC Z component (top row) and spectrograms (bottom row) for both PDC1 and PDC2. Same as Fig. 2b,e, but maintaining ROC as station for both PDCs for a better comparison. 140

S6.8 4-minutes-long traces and corresponding back-azimuths of PDC1 (left column) and PDC2 (right column) of the DAS strain rate (a,c), the seismic velocity (b). Blue and red vertical dotted lines indicate the onsets ($_{ts1}$ and t_{s2}) and arrival at sea (t_{e1} and t_{e2}) of PDC1 and PDC2, respectively, as observed by the thermal and visible cameras (Supplementary Fig. S6.1, Supplementary Movies 1,2). Back-azimuths are calculated using D-NT, D-ST, D-GR (a,c) and N-GR (b) arrays. Back-azimuths are filtered for coherencies> 0.4 and smoothed with a 3 s-long window. Black arrows in (c) indicate the back-azimuths obtained for an explosion that occurred at the NECs at 15:16:45 UTC (Fig. 2f). (d-g) Array geometries of DAS and nodal arrays. Red triangles in (g) indicate the nodes used for the analysis, while grey ones are unused. 141

S6.9 (a) Cumulative strain rate time series along offsets 890-910 between 13 : 50 and 15 : 40 UTC on 2022/12/04. (b) and (d) are the back-azimuths and apparent velocities obtained with D-CT during the entire time series. (c) and (e) are 4-minute zooms over PDC2. The colour grading of (b) and (c) is related to the apparent velocity, while that of (d) and (e) is concerning the back-azimuth. We observe that, right after PDC2, apparent velocities suddenly increase to ~ 6 km/s with errors up to ~ 3 km/s. Back-azimuths are further south than the craters with errors of up to ~ 30°. Horizontal bands in (b) and (c) mark the crater and coastline back-azimuths. Vertical dotted lines in (c) indicate the onset (ts_2 = 15:17:46 UTC) and the arrival at sea (te_2 = 15:18:24 UTC) of PDC2. 142

S6.10(a) GoogleEarth satellite imagery of Stromboli volcano showing the DAS cable (yellow) and UniFi monitoring stations (white squares). (b) Zoom on the Stromboli craters (satellite image dated 2022/07). (c) Same as (b), but with a satellite image taken about 9 months later (2023/04). We can observe traces of the partial collapse of the northeast crater rim, also clearly visible in drone images (d) immediately after PDC2 (2022/12/06). Drone image is courtesy of Sebastiano Cannavò. 144

S6.11Ratios between seismic energies of PDC2 and PDC1 calculated using each DAS channel. Seismic energies are calculated via Eq. (6) (Methods, Estimating seismic energies) considering strain rate traces between $1 - 20$ Hz. Dashed line represent the mean value of the ratios. 145

List of Tables

3.1 Overview of all the DAS experiments that have been performed at Stromboli between 2020 and 2023. Dx denotes the DAS channel spacing and f denotes the sampling frequency. 38

4.1 Metrics obtained by comparing DAS and node strain rate signals (between 0.5-15 Hz) obtained using Eq. (4.3) along 10 linear fibre segments and considering one ordinary and one major explosion that occurred in 2021. CC is the maximum cross-correlation coefficient between the two waveforms. R is the ratio between the RMS amplitudes of node and DAS traces. . . . 72

4.2 Metrics obtained by comparing DAS and node strain rate signals (between 0.5-15 Hz) obtained using Eq. (4.3) along 11 linear fibre segments and considering one ordinary and one major explosion that occurred in 2022. CC is the maximum cross-correlation coefficient between the two waveforms. R is the ratio between the RMS amplitudes of node and DAS traces. . . . 72

5.1 Maximum values and confidence intervals of the PDFs of both back-azimuth and apparent velocity computed during 1 hr of data for Z, N, and E components of the nodal array (N15–19). The craters' back-azimuth with respect to the centroid of the nodal array ranges between 246-256°. 98

5.2 Maximum values and confidence intervals of the PDFs of both back-azimuth and apparent velocity computed during one hour of data for the DAS-L, DAS-T, and DAS-TL configurations. The craters' back-azimuth with respect to the centroid of the three arrays ranges between 246-256°. 103

6.1 Average velocities (m/s) of PDC1 and PDC2 estimated with the back-azimuth results from D-CT and N-NT (seismic) and EAR (infrasonic) arrays and from frames of the LBZ visible camera. PDC1 was not deteced (N.D.) with EAR infrasound array. Node data were not available (N.A.) during PDC2 127

S6.1 Stations and channels used for array analyses considering node (N-NT, N-GR), infrasound (EAR) and DAS (D-NT, D-CT, D-ST and D-GR) arrays. 143

S6.2 Seismic energies Es computed for PDC1 and PDC2 using Eq. (6) for the E, N and Z components of STR, ROC and SCI broadband seismometers (Fig. 1 145

S6.3 Ratios $R_{Es} = Es_{PDC2}/Es_{PDC1}$ between the seismic energies Es of PDC2 and PDC1 for the E, N and Z components of STR, ROC and SCI broadband seismometers (Fig. 1). 145

Acronyms and Abbreviations

ARF Array Response Function

CC Cross Correlation

CT Central Triangle

DAS Distributed Acoustic Sensing

DEM Digital Earth Model

DOFS Distributed Optical Fibre Sensing

DTS Distributed Temperature Sensing

DVS Distributed Vibration Sensing

FIR Finite Impulse Response

GPS Global Positioning System

GR Grid

HPM High-Porphyritic Magma

LG Gauge Length

LP Long Period

LPM Low-Porphyritic Magma

MCCA Multi Channel Correlation Analysis

MUSIC MUltiple SIgnal Classification

NA Numerical Aperture

NEC North-East Crater

NT North Triangle

OFDR Optical Frequency Domain Reflectometry

OTDR Optical Time Domain Reflectometry

P-OTDR Polarization-Sensitive OTDR

PDC Pyroclastic Density Current

PDF Probability Density Function

PSD Power Spectral Density

RGMM Rapid Gravity-driven Mass Movement

RMSA Root Mean Square Amplitude

SdF Sciara del Fuoco

SNR Signal-to-Noise Ratio

ST South Triangle

STA/LTA Short-Term Average/Long-Term Average

UTC Coordinated Universal Time

UTM Universal Transverse Mercator

VEI Volcanic Explosivity Index

VEQ Volcanic Explosion Quake

VLP Very Long Period

VT Volcano-Tectonic

ϕ-OTDR Phase-Sensitive OTDR

3C Three-Component

Introduction

Up to ~800 million people face potential volcanic threats, and rapid population growth and urbanisation increase the exposure to these hazards (Auker et al., 2013; Brown et al., 2017). Volcanic activity significantly impacts human life, claiming victims and disrupting infrastructure and transportation networks, notably air traffic (Petersen et al., 2012; Takebayashi et al., 2021). In the 20th century alone, volcanic eruptions caused nearly 90,000 deaths (Witham, 2005; Baxter & Horwell, 2015). However, over the past two centuries, advances in science, monitoring, and hazard management have steadily reduced society's vulnerability to volcanic threats (Auker et al., 2013).

These improvements were made possible by volcano monitoring, which aims to enhance our understanding of volcanic structures and processes, thereby improving our ability to predict the timing and magnitude of eruptions. Multi-parametric volcanic observations allow the detection and characterisation of volcanic phenomena and the monitoring of potential destabilisation in ordinary activity (Jousset et al., 2022). Measurements of geophysical and geochemical parameters, alongside volcanological studies, provide a better understanding and modelling of complex magma and fluid transport processes driving eruptions. Among several approaches, volcano seismology is nowadays an essential monitoring tool and the cornerstone of many observatories (Chouet & Matoza, 2013; McNutt & Roman, 2015; McNutt, Thompson, et al., 2015).

About volcano seismology

Volcanoes generate various seismic signals in a broad frequency range. Moreover, seismic anomalies have preceded almost all recorded eruptions (McNutt & Roman, 2015; Saccorotti & Lokmer, 2021). Volcano seismicity can significantly change at different volcanoes, although some common features allow subdivision into distinct categories (Chouet, 1996b; Saccorotti & Lokmer, 2021; Jousset et al., 2022). These include volcanic tremor (having frequencies mainly between $\sim 0.1 - 10$ Hz), volcano-tectonic events (VTs; $\sim 2 - 20$ Hz), volcanic explosion-quakes (VEQs; $1 - 10$ Hz) together with long-period (LP; $1 - 5$ Hz) and very-long-period (VLP; $0.01 - 0.2$ Hz) signals (Chouet et al., 2003; Chouet & Matoza, 2013; Jousset et al., 2018; Ripepe, Delle Donne, et al., 2021; Saccorotti & Lokmer, 2021).

Other surficial and highly hazardous volcanic features such as rockfalls, pyroclastic density currents (PDCs) and lahars also generate seismic signals having distinctive properties (Allstadt et al., 2018).

Seismic signals at volcanoes carry insights into the physical mechanisms that produced them. The sources of this seismicity are numerous and driven by magmatic and hydrothermal processes (Wassermann, 2012; McNutt & Roman, 2015; Saccorotti & Lokmer, 2021). For example, VT events are due to shear fracture resulting from magma intrusion, hydrofracturing, or pore pressure effects coupled with tectonic stress and gravitational loading (McNutt, 2005). Conversely, multi-phase fluid dynamics and their interaction with host rocks are the sources of volcanic tremor and LP events (Chouet, 1996b; Ripepe & Gordeev, 1999; Chouet & Matoza, 2013; Saccorotti & Lokmer, 2021; Kumagai, 2022).

Seismometers should be installed close to the source because of low amplitudes and signal-to-noise ratios (SNRs) of seismo-volcanic signals. This can partly be due to persistent tremor at several volcanoes (Saccorotti & Lokmer, 2021). Furthermore, faint LP and VLP signals are sometimes only visible in near-field conditions (Wassermann, 2012). Additionally, heterogeneous volcanic structures can attenuate and scatter seismic waves as they propagate, distorting the wavefield (Métaxian et al., 1997; Clarke et al., 2021; Nishimura et al., 2021; Saccorotti & Lokmer, 2021). Single stations deployed on volcanoes may provide valid information about changes in volcanic activity and imminent eruptions. Variations in tremor frequencies (Cosentino et al., 1989; Hotovec et al., 2013) or amplitudes (McNutt et al., 1995) can be due to changes in pre-eruptive conduit dynamics. Particle motion of VLP and LP signals obtained with three-component (3C) broadband sensors can indicate the azimuth and dip of the respective sources (Wassermann, 2012; Ripepe, Delle Donne, et al., 2021). However, thorough interpretation of seismo-volcanic activity mostly comes from analysing data collected with seismic networks and arrays (Chouet, 2003; Wassermann, 2012).

Modern networks generally consist of four or more stations located within ~ 15 km of active craters and at different azimuths (Wassermann, 2012; McNutt, Thompson, et al., 2015). Seismic waves recorded by several stations provide constrain on source mechanisms of e.g. volcanic explosions and landslides (e.g., Kanamori et al., 1984; Nishimura, 1995; Chouet et al., 1997; Nishimura et al., 2000; Chouet et al., 2003; Zobin, 2017; Kumagai, 2022). Seismic networks also provide hypocenter location of signals with clear phase onsets, such as VTs (e.g., Power et al., 1994; Wassermann, 2012; White & McCausland, 2016; D'Auria et al., 2022). In the absence of clear onsets, amplitude location methods make it possible to approximately estimate source areas, taking care of correcting for site effects (Battaglia et al., 2005). Source location may also shed light on the geometries of magmatic pathways feeding the eruptions (e.g., Ryan et al., 1981; Lahr et al., 1994; Chouet, 1996a; Wright & Klein, 2006; D'Auria et al., 2022). Additionally, seismic tomography makes it possible to delineate deep magmatic bodies beneath volcanoes (e.g., Iyer, 1992; Lees, 2007; Koulakov et al., 2011; Koulakov & Shapiro, 2014). Denser seismic networks or arrays provide complementary information.

Seismic arrays are nowadays one fundamental tool in volcano seismology (Chouet, 1996a; Wassermann, 2012). Stations forming an array are separated by distances depending on the frequency/wavelength of the signals of interest (Rost & Thomas, 2002; Schweitzer et al., 2012). Station spacing is generally short, ranging between $10^1 - 10^2$ m (Wassermann, 2012). Seismic arrays allow the separation from incoherent noise of coherent waves crossing an array even of faint amplitudes (Rost & Thomas, 2002; McNutt,

Thompson, et al., 2015). Array processing techniques, such as delay-and-sum beamforming or Multiple Signal Classification (Capon, 1969; Schmidt, 1986; Goldstein & Archuleta, 1987; Schweitzer et al., 2012), provide precise locations of events that lack clear P- or S-wave arrivals, as are many seismo-volcanic signals such as VEQs and tremor (e.g., Furumoto et al., 1990; Almendros et al., 1997; Métaxian et al., 1997; Saccorotti et al., 1998; Métaxian et al., 2002; La Rocca, Saccorotti, et al., 2004; Inza et al., 2011; Hansen & Schmandt, 2015; Eibl et al., 2017; Glasgow et al., 2018). Dense and large-N arrays also improve the knowledge of volcanic structures and their spatial and temporal changes (Chouet et al., 1998; Petrosino et al., 2002; Bruno et al., 2017; Takano et al., 2020; Yeh et al., 2021).

However, of all the estimated ~1500 active volcanoes in the world (of which a third have erupted in historical times), less than 50% are currently monitored with ground-based instrumentation and only ~200 are equipped with seismometers (Brown et al., 2015; McNutt & Roman, 2015; Valade et al., 2019). Continuous seismic monitoring of volcanoes is challenging due to harsh environments and associated hazards. Installing and maintaining seismometers at short distances from active craters and under different environmental/weather conditions can be demanding from an economic and manpower perspective (Wassermann, 2012). The greater the number of stations, the greater the difficulties. Therefore, long-term use of seismic arrays for volcano monitoring is generally foreclosed (Wassermann, 2012; Allstadt et al., 2018). Additionally, severe logistical difficulties hamper long-term (and real-time) geophysical observations of currently unmonitored submarine volcanoes (Nakano et al., 2024). The emerging Distributed Acoustic Sensing (DAS) technology represents a suitable option for these purposes.

Distributed acoustic sensing and its use in geophyisical applications

DAS is part of a broader range of methodologies described as Distributed Optical Fibre Sensing (DOFS). DOFS exploits light propagating in optical fibres to measure environmental variables such as strain and temperature at multiple locations along the fibres rather than at a single point (Lu et al., 2019; Fernández-Ruiz et al., 2020)(Jousset et al., 2024). Optical fibres are thin glass threads that guide light pulses over long distances through total internal reflection. The fibres naturally contain randomly distributed density fluctuations, which alter the glass refractive index (Hartog, 2017; Lindsey, Rademacher, & Ajo-Franklin, 2020). These anomalies perturb the light propagation through the fibres, leading to Rayleigh backscattering (Hartog, 2017). The signature of the backscattered light remains stable when the fibre is at rest. Conversely, it varies due to fibre deformations caused by physical processes such as elastic perturbations or temperature changes (Hartog, 2017; Williams et al., 2019; Fernández-Ruiz et al., 2020; Lindsey, Rademacher, & Ajo-Franklin, 2020). DAS measures the dynamic strain (or strain rate) of optical fibres caused by seismic waves.

DAS measurements require the use of an interrogation unit, i.e. an optoelectronic device comprising a laser source and a photodetector. The unit interrogates the fibre by injecting coherent laser pulses and measuring the backscattered radiation. Using optical interferometry, DAS exploits phase changes in the backscattered light due to changes in

the photon path length to measure the longitudinal fibre strain (Hartog, 2017; Fernández-Ruiz et al., 2020). A single DAS unit can simultaneously probe tens of km of fibre-optic cables, turning them into dense (down to metres) arrays of thousands single-component strain sensors sampling at rates up to kHz.

Fibre-optic-based technologies present some advantages over inertial sensors. DAS may reduce the effort of installing and collecting an equal number (i.e., up to thousands) of seismometers. Additionally, DAS allows using existing fibre networks for monitoring purposes with relatively low costs and simplified logistics (Hartog, 2017; Lu et al., 2019; Williams, 2023). In particular, these networks can serve as the basis for continuous seismic monitoring of urban (Dou et al., 2017; Zhu et al., 2021) or oceanic (Williams et al., 2019) areas. Both environments are challenging for constant and long-term seismic surveys (Fernández-Ruiz et al., 2020). Moreover, battery life can represent a limit for inertial sensors, possibly reducing the lifespan of surveys employing seismic arrays. Conversely, as long as an electrical source is available, DAS allows for long recording campaigns. On volcanoes, for example, the cable can be installed at close distances from the source and interrogated remotely and safely (Nishimura, 1995; Jousset et al., 2022; Biagioli et al., 2024). Recording can also continue during explosive events that cause massive ash fallout, which may cover solar panels and thus limit the operation of seismic stations. Burying the cable deep enough protects it from pyroclastic fallout that may instead damage monitoring sites, notably solar pannels and batteries (Nishimura et al., 2021). DAS also guarantees telemetry. Data transmission occurs at the speed of light, and the recording points along the fibre are synchronised. Moreover, optical fibres are flexible, lightweight, long-living and relatively easy to handle, install and maintain (Jousset et al., 2024). Fibre-optic cables are also immune to electromagnetic interference and resistant to high temperatures or corrosive substances, therefore apt for deployments in harsh environments (Rogers, 1999; Lu et al., 2019; Jousset et al., 2024).

However, DAS recordings come with some features that can complicate processing. First, DAS only records the longitudinal deformation of optical cables. This represents a loss of information compared to 3C seismometers. Furthermore, this leads to a directional response of DAS measurements depending on the wave type. For example, DAS is blind to broadside P-waves or to S-waves propagating along the cable direction (Näsholm et al., 2022). Moreover, DAS averages the strain rate along a given gauge length. The gauge length corresponds to the effective sensor length for the strain estimation (Näsholm et al., 2022) and represents the lower boundary of spatial resolution (Williams, 2023), significantly influencing the measurements (Hartog, 2017). Another issue arises in the ground-to-fibre coupling. Sufficient coupling between the medium and the fibre is necessary for an efficient strain transfer. However, the coupling may be spatially heterogeneous, and its effect on the resulting measurements is still partially overlooked (Celli et al., 2024). This effect poses a problem for DAS usage in many seismological applications requiring true ground motion measurements (Lindsey, Rademacher, & Ajo-Franklin, 2020; Celli et al., 2024). On top of that, DAS produces large amounts of data, challenging storage and analysis.

Nevertheless, DAS is establishing a paradigm in seismological analyses. It has been used successfully in several geophysical applications, such as oil and gas (Daley et al., 2013; Mateeva et al., 2014; Bakku, 2015), earthquake seismology (Lindsey et al., 2017; Jousset et al., 2018; Wang et al., 2018; Ajo-Franklin et al., 2019; Lindsey, Rademacher, & Ajo-Franklin, 2020; Li et al., 2023), and submarine seismicity characterisation (Cheng

et al., 2021; Taweesintananon et al., 2023; Shen & Wu, 2024) alongside urban (Fang et al., 2020; Spica et al., 2020; Zhu et al., 2021; Ehsaninezhad et al., 2024), infrastructure (Lindsey, Yuan, et al., 2020; Zhu et al., 2022; Rahman et al., 2024), glacial (Walter et al., 2020; Hudson et al., 2021), geothermal (Azzola et al., 2023) and volcanic (Jousset et al., 2024) monitoring.

DAS experiments in volcanic areas reported promising outcomes. Jousset et al. (2018) used DAS to image structural features in the Reykjanes peninsula (Iceland). Nishimura et al. (2021) located the hypocenters of shallow volcanic earthquakes and estimated site effects at Azuma volcano (Japan). Klaasen et al. (2021) unveiled a surprisingly intense and low-magnitude seismicity at Mount Meager, British Columbia. At Mount Etna (Italy), Currenti et al. (2021) and Jousset et al. (2022) recorded seismo-acoustic signals generated by volcanic explosions and degassing events alongside mapping of shallow structural features. Fichtner, Klaasen, et al. (2022) observed the presence of volcanic tremor signals propagating through the ice sheet covering Grímsvötn volcano (Iceland). Currenti et al. (2023) investigated the presence of VLP seismicity during a volcanic unrest phase at Volcano Island (Italy). Biondi et al. (2023) highlighted the presence of a cap separating the shallow hydrothermal system from the deep magma chamber at Long Valley Caldera (USA). Finally, Nakano et al. (2024) used a submarine cable to detect and locate seismicity in the Tongan volcanic chain (Tonga).

However, much more has to be investigated. Key information about conduit dynamics comes from the analysis of VLP seismicity (Chouet, 1996b; Chouet et al., 2003; Ripepe, Delle Donne, et al., 2021). The capability of DAS to resolve such frequencies in volcanic environments is promising but yet to be fully understood (Currenti et al., 2023). Array analysis is often necessary to locate signals lacking clear onsets, such as VEQs and tremor. Various array processing techniques designed for DAS measurements have been proposed in the literature (Klaasen et al., 2021; Nayak et al., 2021; van den Ende & Ampuero, 2021; Näsholm et al., 2022). However, these applications are not yet standardised, requiring further research. Additionally, distributed strain measurements at volcanoes may enhance understanding of their behaviours and structures. Heterogeneous volcanic structures modify seismic wavefields through scattering processes (O'Brien et al., 2023). Dense spatial sampling of the wavefield obtained with DAS may provide high-resolution imaging of the volcanic subsurface, representing a more solid base for numerical waveform simulation, hypocenter location and source mechanisms comprehension (Nishimura et al., 2021; Jousset et al., 2022; O'Brien et al., 2023).

Aims of the thesis

To tackle these challenges, we performed DAS measurements at Stromboli volcano (Italy) within the framework of the ANR MONIDAS[1] project. Stromboli exhibits a persistent volcanic activity (Rosi et al., 2000) with frequent (~13 events/hour; Ripepe et al., 2008) and mild explosions alongside continuous degassing. Signals produced by the explosions show a broad frequency range (10^{-2} – 10 Hz; Neuberg et al., 1994; Chouet et al., 1997, 2003). Furthermore, volcanic tremor is always present in the seismic traces mainly between ~1 – 5 Hz (Nappi, 1976; Langer & Falsaperla, 1996; Ripepe et al., 1996; Wasser-

[1] https://anr.fr/Project-ANR-19-CE04-0011

mann, 1997). In addition, more fascinating and hazardous phenomena may interrupt or accompany this relatively predictable activity regime. These are lava flows and violent explosions, referred to as "major" and "paroxysmal" based on their intensity. (Métrich et al., 2021; Ripepe, Lacanna, et al., 2021). These latter are the most violent and dangerous manifestation of Strombolian explosive dynamics, representing a significant threat to the inhabitants. Both major and paroxysmal explosions eject volcanic ballistic projectiles at great distances and may generate PDCs (Rosi et al., 2013). The impact with the sea of large PDCs and landslides can produce tsunami waves, endangering nearby coastlines (La Rocca, Galluzzo, et al., 2004; Ripepe & Lacanna, 2024). These characteristics make Stromboli an ideal test site for measuring dynamic strain rate signals on volcanoes.

This thesis explores the potential of DAS as a tool for monitoring the volcanic activity at Stromboli. Our main objectives are: (i) recording and investigating dynamic strain rate signals produced by various eruptive phenomena such as ordinary explosions and validating their accuracy; (ii) extracting information about volcanic phenomena from strain rate signals by e.g. locating seismic sources of volcanic tremor, explosions and PDCs; (iii) lastly, we aim to compare the outcomes with those obtained with the permanent monitoring network to assess DAS capabilities as a volcanic monitoring tool. We want to investigate whether DAS could provide a better understanding of volcanic phenomena and whether we can use it jointly with classical instrumentation.

To these aims, we use DAS data recorded along 4 km of fibre-optic cable deployed on the volcanic flanks between 2020 and 2022. We buried the cable at 30 cm depth and designed the layout geometry to provide a broad coverage while constrained by natural obstacles and topographical features. We interrogated the cable with the FEBUS A1-R unit during multiple campaigns between 2020 and 2023. Survey durations vary from 7 days up to 4 months. We also deployed several 3C 5 Hz nodal seismometers and broadband (30 s) seismic stations co-located with the cable during each experiment. These instruments serve as a basis for calibrating the strain rate recordings. To investigate how DAS can interlock within a monitoring network, we also use data collected by the permanent monitoring network operated by the University of Firenze (UniFi, Italy). The multi-parametric network consists of broadband seismometers, infrasonic pressure sensors, borehole tiltmeters, thermal and visible cameras, and tsunami gauges at sea.

We recorded several types of strain rate signals. These include volcanic tremor and VEQs generated by both ordinary and major explosions. Furthermore, we also recorded signals generated by PDCs propagating from the craters to the sea. We observe ground-coupled infrasonic pressure waves excited by major and ordinary explosions. Furthermore, we examine the VLP component of explosive phenomena. We investigate several features of strain rate signals recorded at Stromboli: (i) we empirically calibrate DAS data by comparing them with those obtained from nodes or broadband seismometers; (ii) we develop an innovative method to retrieve the seismic velocity along the cable direction by numerical spatial integration of strain rate signals; (iii) we investigate the VLP component of the seismic wavefield generated by the explosions; (iv) we apply array technologies to strain rate data to obtain information on the location of seismic sources. By doing so, we analyse explosive sources and track the downslope propagation of seismic moving sources such as PDCs. The results are then compared with those obtained by node and infrasonic arrays.

Thesis overview

This thesis is organised as follows. Each chapter exhibits an abstract and an introduction to allow for independent reading. In Chapter 1, we provide a short overview of the theory behind DAS measurements and the main features of the recorded signals. Since each volcano has its own characteristics, we consider it important to provide a summary of Stromboli's eruptive style. Therefore, in Chapter 2, we report the principal volcanological information regarding its activity and the geophysical evidence of the dynamic processes taking place inside and outside the volcano. While the Introduction provides essential information concerning the main features of DAS measurements and Stromboli's eruptive dynamics, we encourage readers to refer to these two chapters for a more in-depth understanding.

Starting from Chapter 3, we delineate our DAS experiments at Stromboli and their outcomes. In Chapter 3, we describe the several experiments carried out between 2020 and 2023. We illustrate the deployment of the optical cable and inertial seismometers on the volcanic flanks and the parametrisation of the DAS interrogator. Furthermore, we present the workflow to geolocate the fibre-optic cable and the DAS channels. We show strain rate signals produced by several volcanic phenomena, such as tremor, ordinary and major explosions, and PDCs in both time and frequency domains. We also show examples of VLP signals generated by the explosive activity and recorded by DAS. About this latter subject, we are currently preparing a publication with the following preliminary title:

F. Biagioli, E. Stutzmann, M. Ripepe, J.-P. Métaxian, P. Bernard, **Distributed fibre-optic observations of very long period seismicity at Stromboli volcano, Italy**, *in prep.*

Furthermore, in Chapter 4, we empirically calibrate our DAS measurements by comparing them with signals recorded by co-located nodes. To do so, we apply two different methods. First, we compare the DAS strain rate with the strain rate retrieved from the finite difference of seismic velocity signals. Similar comparisons are also performed in Chapters 5 and 6. We also apply the opposite approach. We convert the DAS strain rate to velocity by numerical integration in space. The outcomes are then compared with co-located seismic measurements. These latter results are adapted from a paper published in *Geophysical Journal International* in December 2023:

A. Trabattoni, F. Biagioli, C. Strumia, M. van den Ende, F. Scotto di Uccio, G. Festa, D. Rivet, A. Sladen, J.P. Ampuero, J.-P. Métaxian, E. Stutzmann, **From strain to displacement: using deformation to enhance distributed acoustic sensing applications**, *Geophysical Journal International*, Volume 235, Issue 3, December 2023, Pages 2372–2384, https://doi.org/10.1093/gji/ggad365.

Both methods provide valid results. We observe excellent phase agreement between DAS and node traces. Nevertheless, we emphasise that the DAS has generally lower amplitudes than the nodes.

In Chapter 5, we apply array analysis techniques to DAS strain rate signals of volcanic tremor and VEQs to retrieve both apparent velocities and back-azimuth of seismic waves. We estimate the slowness vector by inversion of delay times computed between sensor pairs with a linear interpolation of the cross-spectrum phase. The results obtained with

the DAS arrays are coherent with waves propagating from the active craters. Moreover, these outcomes are consistent with those obtained with a co-located seismic array and with previous findings. Chapter 5 is adapted from a manuscript published in *Geophysical Journal International* in January 2024:

F. Biagioli, J.-P. Métaxian, E. Stutzmann, M. Ripepe, P. Bernard, A. Trabattoni, R. Longo, M.-P. Bouin, **Array analysis of seismo-volcanic activity with distributed acoustic sensing**, *Geophysical Journal International*, Volume 236, Issue 1, January 2024, Pages 607–620, https://doi.org/10.1093/gji/ggad427.

In Chapter 6, we expand the array analysis to moving volcanic sources. We analyse the seismo-acoustic signals produced by two PDCs in Stromboli in October and December 2022. The two flows propagated from the craters to the sea at an average velocity ranging between ~40-60 m/s, as observed by a visible camera. Array analyses of DAS, seismic and infrasonic arrays allow us to track the downslope movement of the two PDCs, providing valuable outcomes consistent with visual observation. We then use numerical modelling to improve our understanding of granular flow dynamics. This chapter is adapted after a publication in preparation having the following title and authors:

F. Biagioli, J.-P. Métaxian, M. Ripepe, E. Stutzmann, P. Bernard, G. Lacanna, A. Mangeney, G. Ulivieri, G. Risica, A. Trabattoni, M. Peruzzetto, and L. Innocenti, **Tracking and characterising pyroclastic density currents with DAS, seismo-acoustic and visual observations**, *in prep.*

We then reach the Conclusions , in which we lay out concluding remarks and research perspectives.

Chapter 1

Properties of DAS measurements

1.1 Abstract

Distributed acoustic sensing (DAS) is a relatively recent but rapidly growing technology in various geophysical applications such as earthquake, glacial and volcano seismology. Using coherent Rayleigh backscattering, DAS converts tens of km of optical fibres into cost-effective and dense arrays of single-component sensors that measure the longitudinal fibre strain (or strain rate) induced by elastic perturbations. These recordings bring with them some advantages over point measurements made with inertial seismometers, first and foremost the high spatial sampling of the wavefield. However, certain peculiarities of DAS measurements must be taken into account. DAS measures the horizontal projection of the strain tensor along the cable direction, thus limiting the wavefield reconstruction. The averaging of the strain over a certain gauge length may affect the records especially at wavelengths that are integer multiples of the gauge length. Furthermore, DAS exhibits more extreme sensitivity patterns than inertial sensors and is more susceptible to slow and shallow waves. In this chapter we provide a concise review of the characteristics of DAS systems and measurements. This will serve as a basis for a better understanding of our DAS data (and their processing) in the remainder of the thesis.

1.2 Introduction

DAS is one of the most known examples of a wide range of methodologies addressed to as Distributed Optical Fibre Sensing (DOFS). DOFSs exploit the characteristics of light propagation in optical fibres to measure environmental variables acting on optical fibres (e.g., strain or temperature) at several locations rather than at a single point (Hartog, 2017; Jousset et al., 2024). Optical fibres can transmit light pulses at long distances with small attenuation, ensuring distributed measurements up to tens of km from the fibre start.

DAS, also known as DVS (distributed vibration sensing) or DSSS (distributed dynamic strain sensing), is a generic term defining a technology that probes an optical fibre to measure the dynamic strain induced by seismic waves via Rayleigh backscattered light interferometry (Hartog, 2017; Lindsey, Rademacher, & Ajo-Franklin, 2020; Diaz-Meza et al., 2023). It can turn optical fibres into dense arrays of single-component strain sensors, providing significant advantages, such as enhanced spatial sampling for detailed seismic wavefield mapping. Over the past decades, it has increasingly become an essential tool in several geophysical applications due to its versatility and cost-efficiency.

While traditional seismometers measure translational ground motion (displacement, velocity, or acceleration), DAS directly measures fibre strain (or strain rate) over a finite gauge length. These two types of measurements differ in several ways. First, strain measurements have directional sensitivity, depending on the propagation direction and particle motion of seismic waves, resulting in narrower sensitivity to P-waves and increased blind angles to S-waves (Martin, 2018; Trabattoni et al., 2022). Second, strain measurements are averaged over the gauge length, leading to spectral notches in the DAS response at integer multiples of the apparent phase velocity divided by the gauge length (Hartog, 2017; Yang et al., 2022). Finally, strain measurements are more sensitive to slow, highly scattered waves, making their analysis more complex (Trabattoni et al., 2022).

Other factors may significantly affect DAS records, including the installation conditions of the sensing fibres and their physical properties. Studies have shown that ground-to-fibre coupling and strain transfer from the outer cable coating to the inner fibres are crucial aspects that affect measurement accuracy (Mateeva et al., 2014; Reinsch et al., 2017; Lindsey, Rademacher, & Ajo-Franklin, 2020; Jousset et al., 2022). These characteristics can vary between deployments, adding complexity to the interpretation of DAS data. Moreover, DAS exhibit typical instrumental noise, e.g. common-mode noise and optical fading (Mateeva et al., 2014; Lindsey, Rademacher, & Ajo-Franklin, 2020; Lindsey & Martin, 2021; Wang et al., 2023). Common-mode noise is generated by vibrations of the DAS interrogator, which introduce synchronous signals along the entire fibre (Lindsey, Rademacher, & Ajo-Franklin, 2020; Lindsey & Martin, 2021). Fading arises from destructive interference at quasi-random locations generating weak amplitudes of the backscattered field that cannot be measured with acceptable SNRs (Zhou et al., 2013; Hartog, 2017; Lindsey, Rademacher, & Ajo-Franklin, 2020).

In this chapter, we provide a concise overview of the main principles of DAS measurements and its fundamental features. We delineate the basic notion about light propagation in optical fibres alongside scattering processes in Section 1.3. In Section 1.4, we then describe the basic principles of phase-based optical time domain reflectometry, i.e. one of the most typical schemes for DAS systems (Muanenda et al., 2019; Lindsey, Rademacher, & Ajo-Franklin, 2020; Jousset et al., 2024). Last, in Sections 1.4.2 and 1.4.3, we delineate the effects arising from the choice of the gauge length and the directional sensitivity of DAS.

1.3 Light propagation in optical fibres

An optical fibre is a thin waveguide designed to transmit light over long distances with minimal attenuation. A standard step-index fibre consists of two materials, i.e. a central core and an outer cladding (Fig. 1.1a). These have distinct refractive indices, denoted as n_1 (for the core) and n_2 (for the cladding), where $n_1 > n_2$. The difference in these

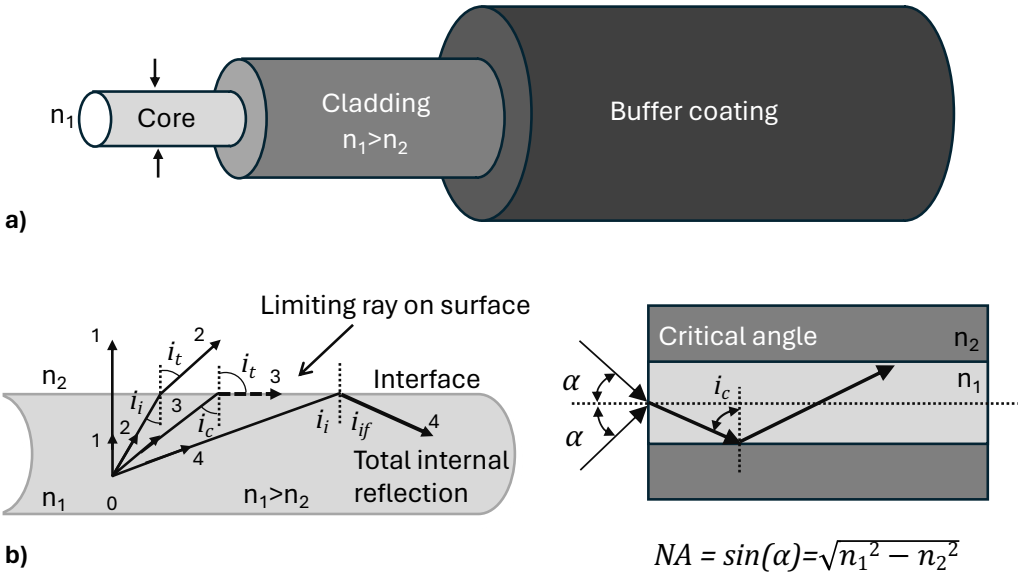

Figure 1.1: (a) Typical internal structure of an optical fibre; (b) scheme of major features regarding light propagation within the core of an optical fibre and the phenomenon of total internal reflection. The angle α in (b) is also known as angle of acceptance and is the angle of a light ray propagating in the air before entering the optical fibre, i.e. an input angle. (a) Is adapted and redrawn from Cabral (2016), while (b) from the following technical note.

refractive indices creates a condition where light entering the fibre within a specific range of angles becomes confined within the guiding core through total internal reflection (Fig. 1.1b). This confinement occurs when the light hits the boundary between the core and cladding at an angle i greater than the critical angle i_c, as determined by Snell's law (Hartog, 2017):

$$i_c = sin^{-1}\left(\frac{n_2}{n_1}\right). \tag{1.1}$$

The range of acceptance of the fibre is also referred to as numerical aperture N_A, following the relationship (Hartog, 2017):

$$N_A = \sqrt{n_1^2 - n_2^2}. \tag{1.2}$$

Nevertheless, optical fibres cannot guide too many light rays but rather a discrete set of transverse modes. Each mode is a particular light ray having distinct electric field distribution, velocity and path (Hartog, 2017). According to the number of modes that can be guided, fibres are classified into multi-mode (capable of guiding several modes) and single-mode (capable of guiding one single light pulse) types. Single-mode fibres usually have smaller cores and lower N_A than multi-mode ones and typically serve for DAS measures (Hartog, 2017).

1.3.1 Scattering processes and losses within a fibre

As light travels within a fibre, it experiences an attenuation of its power field. Typical values of attenuation for a single-mode fibre are within the range of 0.2-0.4 dB/km for a 1310-1550 nm wavelength (Hartog, 2017; Tahira et al., 2019; Kanamori, 2021). Attenuation within a fibre may result from several processes that can be intrinsic and extrinsic

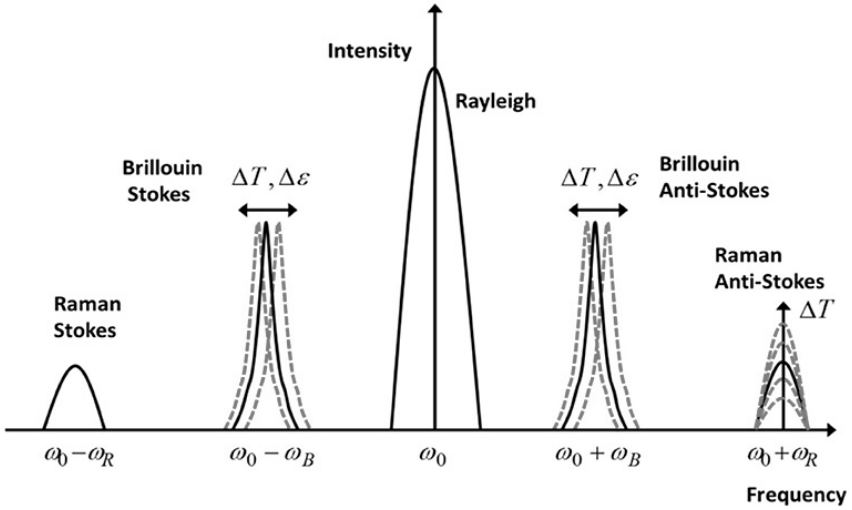

Figure 1.2: Summary of three types of scattering processes, Rayleigh, Brillouin and Raman together with their dependancy on physical parameters such as strain (ε) or temperature (T). Adapted from Muanenda et al. (2019).

(Paschotta, 2010; Hartog, 2017; Al Hasani, 2024). Intrinsic processes mainly comprise absorption and Rayleigh scattering. Conversely, extrinsic ones are due to, e.g., leaky splices and connectors between cables or excessive cable bending, causing light to escape from the waveguide (Hartog, 2017; Al Hasani, 2024).

Scattering in optical fibres is a fundamental process caused by the interaction of light with local variations in the refractive index. These variations arise from glass density and compositional heterogeneities frozen in the fibre structure during fabrication and remain constant over time, randomly distributed throughout the fibre (Lu et al., 2019; Jousset et al., 2024). Due to scattering, a portion of the light is re-directed in multiple directions, including that of origin, i.e. towards the interrogator. Fig. 1.2 shows the several scattering processes, which can be elastic (Rayleigh) or inelastic (Raman, Brillouin).

Elastic scattering means that the energy and frequency of incident and scattered photons do not vary (Hartog, 2017; Muanenda et al., 2019). Rayleigh scattering is the principal attenuation process in optical fibres at the typical wavelength of 1550 nm (Tahira et al., 2019; Al Hasani, 2024). It originates from photons interacting with refractive index variations that are much smaller than the optical wavelength, and its intensity is inversely proportional to the wavelength ($\propto 1/\lambda^4$; Lu et al., 2019). Rayleigh scattering is sensitive to both temperature and strain. It is a permanent feature of one fibre and is the cornerstone of DAS/DVS systems for dynamic strain measurements (Bai & Bai, 2014; Hartog, 2017).

Conversely, in inelastic scattering, the photon's energy varies due to an exchange with the medium (Muanenda et al., 2019; Al Hasani, 2024). Inelastic scattering processes exhibit stokes and anti-stokes components depending on whether the photons gain or lose energy to the medium (Fig. 1.2; Muanenda et al., 2019). The Brillouin scattering process is sensitive to strain and temperature, whereas the anti-stokes components of Raman scattering are sensitive to temperature (Fig. 1.2). The latter process is the basis of distributed temperature sensing (DTS; Hartog, 2017; Lu et al., 2019).

1.4 Basic principles of DAS measurements and response

Having covered the basics of light propagation in optical fibres, we now describe how DAS uses these features for strain measurements. DAS relies on an interrogation unit, an optoelectronic device consisting of a laser source and a photodetector (Fig. 1.3). This unit sends coherent laser pulses into the fibre with a rate limited by the fibre's length to prevent optical interference (Lindsey, Rademacher, & Ajo-Franklin, 2020). As previously mentioned, Rayleigh scattering from fibre irregularities causes light to backscatter towards the interrogator (Fig. 1.3). The backscattered light reaches the interrogator at a time t within a range:

$$\tau_0 < t < \tau_0 + 2\frac{x_{max}}{c_n}, \tag{1.3}$$

being τ_0 the time at which the pulse enters the fibre, x_{max} the fibre's length and c_n the effective speed of light in the glass (typically ~$2{\times}10^8$ m/s for a refractive index of 1.45; Daley et al., 2013; Lindsey, Rademacher, & Ajo-Franklin, 2020). Eq. (1.3) accounts for the round-trip time of light travelling to a scatterer at position x and back. The photodetector then captures backscattered radiation (Fig. 1.3).

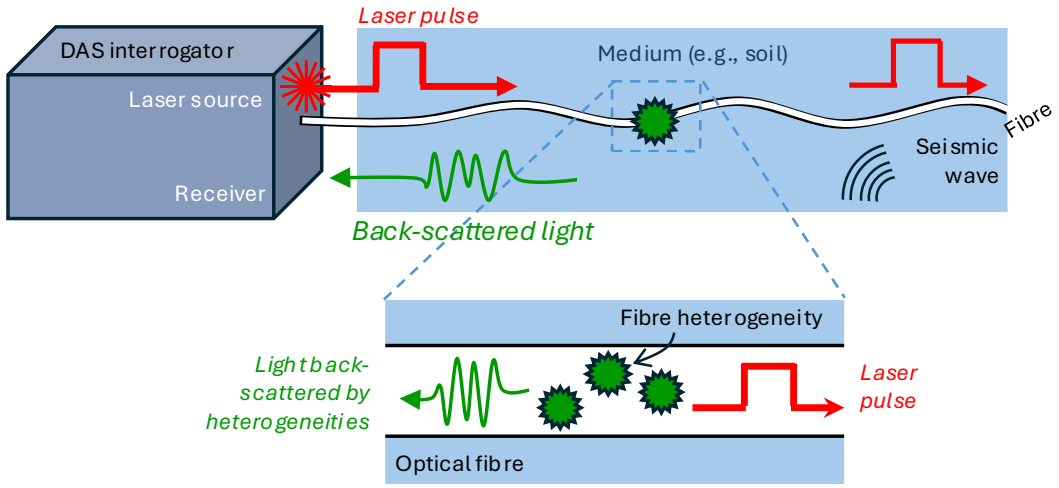

Figure 1.3: Illustration of DAS working principle. A DAS interrogator sends coherent optical pulses (in red) into the fibre and captures the radiation backscattered from random heterogeneites within the fibre glass (in green). Redrawn from Bakku (2015), Lindsey, Rademacher, and Ajo-Franklin (2020), and Al Hasani (2024).

Various techniques enable the extraction of information from the backscattered signal. These techniques may vary based on the pulse length or frequency content, the use of single or dual pulses, or whether they analyze the phase or amplitude of the backscattered radiation in the time or frequency domain (Fernández-Ruiz et al., 2020; Lindsey, Rademacher, & Ajo-Franklin, 2020; Jousset et al., 2024). Common methods include e.g. optical time domain reflectometry (OTDR), measuring the time it takes for light to travel from the interrogator to a scatterer, the phase-sensitive OTDR (ϕ-OTDR), polarization-sensitive OTDR (P-OTDR), and optical frequency domain reflectometry (OFDR; Hartog, 2017; Lu et al., 2019; Muanenda et al., 2019; Jousset et al., 2024).

1.4.1 Retrieving the fibre strain from optical phase changes (ϕ-OTDR

ϕ-OTDR is widely used in DAS systems and measures phase changes in backscattered light between successive coherent and narrow linewidth pulses with stable frequency (Muanenda et al., 2019; Zhang et al., 2019; Fernández-Ruiz et al., 2020; Lindsey, Rademacher, & Ajo-Franklin, 2020; Xie et al., 2021; Diaz-Meza et al., 2023; Jousset et al., 2024). The signal collected by the photodetector arises from the coherent interference of multiple scatterers within a resolution cell defined by the width of the laser pulse (Hartog, 2017; Muanenda et al., 2019; Zhang et al., 2019; Fernández-Ruiz et al., 2020). The random backscattered signal stays consistent across multiple pulses if the fibre is stationary. However, phase shifts occurring at each scatterer influence the backscattered field. These phase changes may be due to factors, such as vibration or heating, that change the refractive index (Δn) or photon path length (Δx) at specific locations (Muanenda et al., 2019; Fernández-Ruiz et al., 2020). ϕ-OTDR uses these variations in the backscattered radiation to measure longitudinal strain in the fibre (Hartog, 2017; Zhang et al., 2019; Fernández-Ruiz et al., 2020).

The axial fibre strain over time is evaluated with respect to a distance L_G known as gauge length (Masoudi et al., 2013; Lindsey, Rademacher, & Ajo-Franklin, 2020; Al Hasani, 2024). This implies that the gauge length L_G is larger than the laser pulse width and that every location x is mapped with an uncertainty of $x \pm L_G/2$ (Masoudi et al., 2013; Lindsey, Rademacher, & Ajo-Franklin, 2020). Gauge lengths typically are from a few metres to tens of metres and define a low-pass filter of the strain field (Dean et al., 2017; Lindsey, Rademacher, & Ajo-Franklin, 2020).

The phase Φ of a light pulse with a wavelength λ that travelled a distance x within a fibre having an effective refractive index n is defined as:

$$\Phi = \frac{4\pi n x}{\lambda}. \tag{1.4}$$

However, a strain perturbation in the surrounding medium that gets transferred to the fibres induces a displacement of the scatterers and, therefore, phase (and amplitude) changes of the backscattered radiation. The incremental phase change $\Delta\Phi$ between two successive laser pulses at a given location x_j is defined as:

$$\Delta\Phi(x_j, t) = \frac{4\pi n L_G}{\lambda}\left[\frac{\Delta x}{x} + \frac{\Delta n}{n} + \frac{\Delta\lambda}{\lambda}\right], \tag{1.5}$$

with $\Delta x/x$, $\Delta n/n$, and $\Delta\lambda/\lambda$ representing variations in fibre length (i.e. the axial strain ε), refractive index, and optical wavelength, respectively. These changes can all affect the phase of the backscattered signal. Assuming no thermo-optic effect ($\Delta n/n = 0$) and no optical dispersion ($\Delta\lambda/\lambda = 0$), only the axial strain effect is considered. Although temperature can cause axial deformation of the fibre and changes in refractive index, seismic-induced effects occur on much shorter timescales (10^{-2} to 10^{2} seconds) than those of temperature fluctuations (10^{4} seconds; Lindsey, Rademacher, & Ajo-Franklin, 2020). Therefore, the dynamic axial fibre strain ε_{xx} can be directly linked with phase changes of the backscattered radiation $\Delta\Phi$ using the relationship:

$$\varepsilon_{xx}(x, t) = \frac{\lambda}{4\pi n L_G \xi}\Delta\Phi, \tag{1.6}$$

being ξ an optoelastic coefficient linking fibre strain to changes in the fibre refractive index (Hartog, 2017; Lindsey, Rademacher, & Ajo-Franklin, 2020).

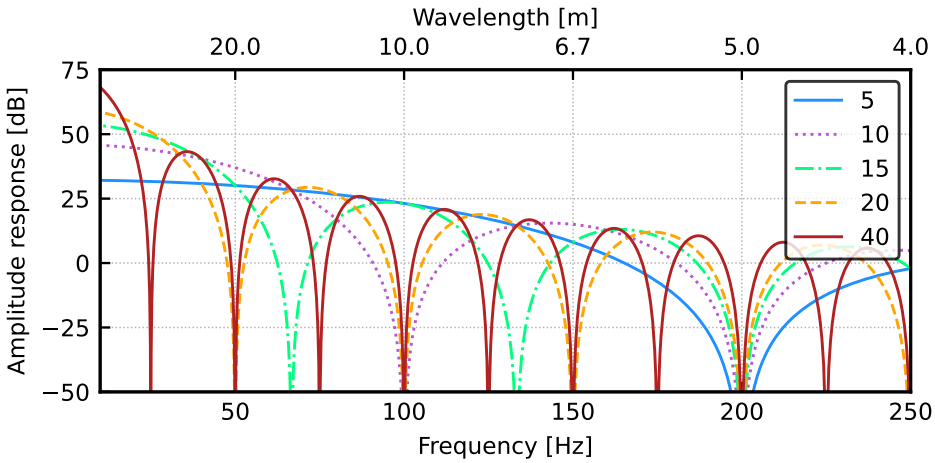

Figure 1.4: Amplitude response for several gauge lengths L_G as a function of both frequency (bottom x-axis) and wavelength (top x-axis) considering a wave velocity of 1000 m/s.

1.4.2 Gauge length effects

In contrast to typical, point-wise seismic measurements, DAS records the strain (rate) induced by the seismic waves at several channels sampled at a spatial rate Δx whose lower bound is defined by the laser pulse width (Mateeva et al., 2014; Dou et al., 2017; Al Hasani, 2024). Nevertheless, DAS/DVS systems average the fibre strain over a gauge length L_G and the effective measured strain ε_f is defined as (Hartog, 2017):

$$\varepsilon_f(x,t) = \frac{1}{L_G} \int_{x-LG/2}^{x+LG/2} \varepsilon_x(x,t). \tag{1.7}$$

Therefore, the gauge length (usually longer than the channel spacing to avoid nonlinear phase-strain relations) controls the spatial resolution of DAS measurements and fixes a maximum frequency (and minimal wavelength) that the DAS can resolve (Näsholm et al., 2022). In particular, it acts as a spatial moving average along the cable and implies a wavenumber response $R_{LG}(k)$ defined as (Dean et al., 2017; Näsholm et al., 2022):

$$R_{LG}(k) = \frac{sin(\pi k L_G)}{\pi k}, \tag{1.8}$$

that creates spectral notches at wavelengths that are integer multiples of the gauge length multiplied by k yielding zero strain average (Fig. 1.4).

In most DAS applications, the gauge length ranges between 5 to 40 m and is typically 10 m (Dean et al., 2017; Näsholm et al., 2022). Tuning the gauge length may be done concerning the seismic frequencies (wavelengths) and velocities of interest (Dean et al., 2017; Näsholm et al., 2022). Increasing the gauge length provides higher SNR and better response at low frequencies (Fig. 1.4), yet it reduces the spatial resolution and introduces additional directivity beside those due to the cable geometry (see later Section 1.4.3)(Bakku, 2015; Dean et al., 2017; Hartog, 2017; Näsholm et al., 2022; Al Hasani, 2024).

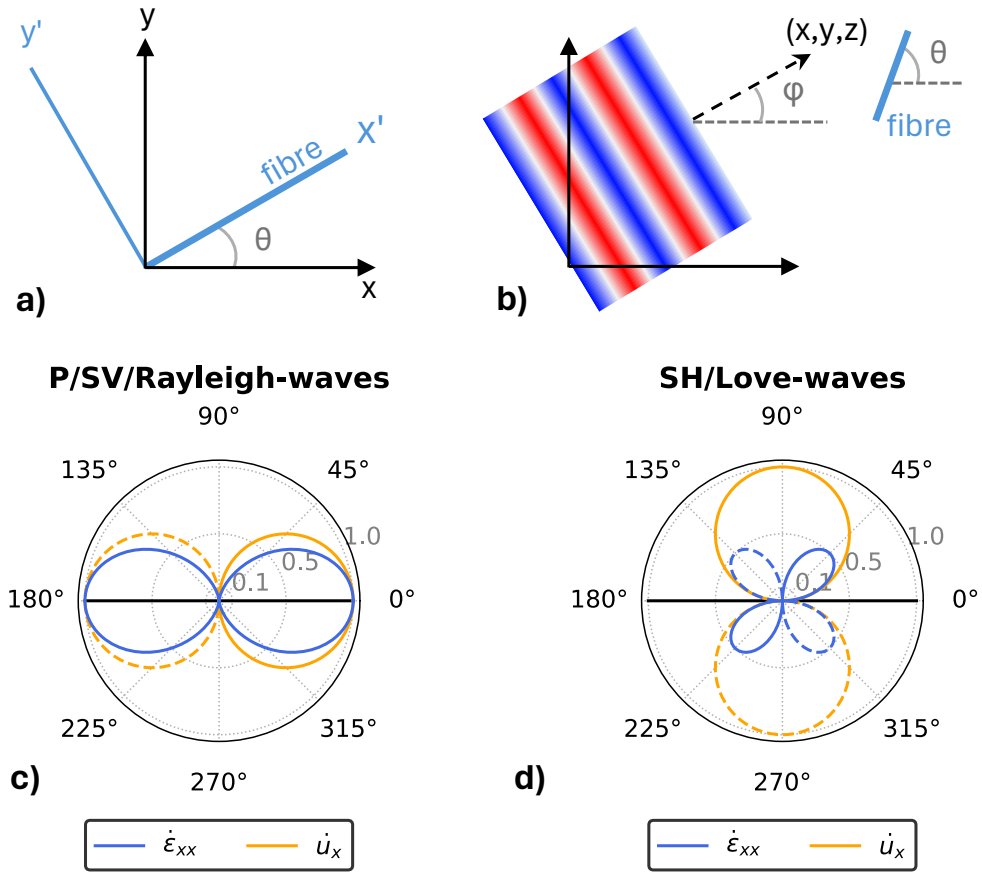

Figure 1.5: (a) Change of the reference system towards fibre direction θ. (b) Seismic wave propagating horizontally along a direction ϕ and reaching an optical fibre having an orientation θ. (c) Sensitivity to P/SV/Rayleigh-waves of particle velocity (orange) and axial fibre strain (blue) under the assumption of a long wavelength with respect to the gauge length. Same as (c) but for SH/Love-waves. (b) Is redrawn from Martin (2018), while (c,d) are redrawn from Trabattoni et al. (2022).

1.4.3 DAS theoretical response

Let us consider a particle velocity vector $\dot{\mathbf{u}}$ recorded by a 3C seismometer and defined as:

$$\dot{\mathbf{u}}(x, y, z, t) = \left[\dot{u}_x(x, y, z, t), \dot{u}_y(x, y, z, t), \dot{u}_z(x, y, z, t)\right]. \tag{1.9}$$

The rotation of the three components of the seismometer along a different direction θ in the horizontal plane can be carried out by applying the rotation matrix R as:

$$\dot{\mathbf{u}}' = \begin{bmatrix} \dot{u}'_x \\ \dot{u}'_y \\ \dot{u}'_z \end{bmatrix} = \begin{bmatrix} cos(\theta) & sin(\theta) & 0 \\ -sin(\theta) & cos(\theta) & 0 \\ 0 & 0 & 1 \end{bmatrix} \begin{bmatrix} \dot{u}_x \\ \dot{u}_y \\ \dot{u}_z \end{bmatrix} = R\dot{\mathbf{u}}, \tag{1.10}$$

being (x', y', z') the new coordinate system.

The strain rate $\dot{\Sigma}$ is a tensor quantity defined as:

$$\dot{\Sigma} = \begin{bmatrix} \dot{\varepsilon}_{xx} & \dot{\varepsilon}_{xy} & \dot{\varepsilon}_{xz} \\ \dot{\varepsilon}_{xy} & \dot{\varepsilon}_{yy} & \dot{\varepsilon}_{yz} \\ \dot{\varepsilon}_{xz} & \dot{\varepsilon}_{yz} & \dot{\varepsilon}_{zz} \end{bmatrix} = \begin{bmatrix} \frac{\partial \dot{u}_x}{\partial x} & \frac{1}{2}\left(\frac{\partial \dot{u}_x}{\partial y} + \frac{\partial \dot{u}_y}{\partial x}\right) & \frac{1}{2}\left(\frac{\partial \dot{u}_x}{\partial z} + \frac{\partial \dot{u}_z}{\partial x}\right) \\ \frac{1}{2}\left(\frac{\partial \dot{u}_x}{\partial y} + \frac{\partial \dot{u}_y}{\partial x}\right) & \frac{\partial \dot{u}_y}{\partial y} & \frac{1}{2}\left(\frac{\partial \dot{u}_y}{\partial z} + \frac{\partial \dot{u}_z}{\partial y}\right) \\ \frac{1}{2}\left(\frac{\partial \dot{u}_x}{\partial z} + \frac{\partial \dot{u}_z}{\partial x}\right) & \frac{1}{2}\left(\frac{\partial \dot{u}_y}{\partial z} + \frac{\partial \dot{u}_z}{\partial y}\right) & \frac{\partial \dot{u}_z}{\partial z} \end{bmatrix}. \tag{1.11}$$

The rotation of the tensor $\dot{\Sigma}$ of an angle θ is:

$$\dot{\Sigma}' = R\dot{\Sigma}R^T = \begin{bmatrix} \dot{\varepsilon}_{x'x'} & \dot{\varepsilon}_{x'y'} & \dot{\varepsilon}_{x'z'} \\ \dot{\varepsilon}_{x'y'} & \dot{\varepsilon}_{y'y'} & \dot{\varepsilon}_{y'z'} \\ \dot{\varepsilon}_{x'z'} & \dot{\varepsilon}_{y'z'} & \dot{\varepsilon}_{z'z'} \end{bmatrix} = \tag{1.12}$$

$$= \begin{bmatrix} cos(\theta) & sin(\theta) & 0 \\ -sin(\theta) & cos(\theta) & 0 \\ 0 & 0 & 1 \end{bmatrix} \begin{bmatrix} \dot{\varepsilon}_{xx} & \dot{\varepsilon}_{xy} & \dot{\varepsilon}_{xz} \\ \dot{\varepsilon}_{xy} & \dot{\varepsilon}_{yy} & \dot{\varepsilon}_{yz} \\ \dot{\varepsilon}_{xz} & \dot{\varepsilon}_{yz} & \dot{\varepsilon}_{zz} \end{bmatrix} \begin{bmatrix} cos(\theta) & -sin(\theta) & 0 \\ sin(\theta) & cos(\theta) & 0 \\ 0 & 0 & 1 \end{bmatrix}. \tag{1.13}$$

Therefore, the point-wise axial strain rate $\dot{\varepsilon}_\theta = \dot{\varepsilon}_{x'x'}$ in the θ direction is:

$$\dot{\varepsilon}_\theta = \dot{\varepsilon}_{x'x'} = cos^2(\theta)\frac{\partial \dot{u}_x}{\partial x} + cos(\theta)sin(\theta)\left(\frac{\partial \dot{u}_x}{\partial y} + \frac{\partial \dot{u}_y}{\partial x}\right) + sin^2(\theta)\frac{\partial \dot{u}_y}{\partial y}. \tag{1.14}$$

Eq. (1.14) implies that DAS measurements exhibit different and more pronounced sensitivity patterns compared to single component measurements made by seismometers. Under the assumption of a gauge length L_G sufficiently shorter than the seismic wavelength (i.e. in the approximation of a point-wise strain measurement), DAS sensitivity to P, SV and Rayleigh waves is similar (Mateeva et al., 2014; Bona et al., 2017; Martin, 2018; Näsholm et al., 2022; Trabattoni et al., 2022). The sensitivity pattern to these waves depends on $cos^2(\vartheta)$, being $\vartheta = \theta - \varphi$ the angle between the fibre axis θ and the wave's direction of propagation φ. The two-lobed pattern implies that DAS is not sensitive to broadside P waves, similarly to single component velocity, yet with increased directivity (Fig. 1.5c). Under the same assumptions, the DAS sensitivity pattern to SH and Love waves (Fig. 1.5d) exhibit a dependence on the $sin2(\vartheta)$, resulting in a four-lobed pattern with maximum amplitudes for waves reaching the fibre with an angle of 45°.

Eq. (1.14) indicates the strain rate measured by DAS for infinitesimally narrow gauge lengths (Martin, 2018). However, DAS measures the strain (rate) averaged over a given gauge length L_G. Implementing the gauge length effect in the sensitivity pattern for different wave types results in several notches indicating blind angles whose number increases with decreasing wavelength (Martin, 2018).

Martin (2018) and Martin et al. (2017) laid down the mathematical equations of strain rate measurements along the fibre direction for different types of seismic waves. Following Pujol (2003), the equation of a plane monochromatic P wave characterised by an angle of incidence γ from the vertical direction, a propagation velocity α, and an angular frequency ω is:

$$\mathbf{u}(x, y, z, t) = (Asin(\gamma)e^{i\omega(t-(xsin(\gamma)-zcos(\gamma))/\alpha)}, 0, -Acos(\gamma)e^{i\omega(t-(xsin(\gamma)-zcos(\gamma))/\alpha)}), \tag{1.15}$$

being A the amplitude constant. Therefore, the point-wise axial strain ε measured along a horizontal fibre is:

$$\varepsilon(x, y, z, t) = -icos^2(\vartheta)\frac{\omega}{\alpha}Asin^2(\gamma)e^{i\omega(t-(xsin(\gamma)-zcos(\gamma))/\alpha)}, \tag{1.16}$$

Depending only on the fibre's orientation relative to the wave's propagation direction ϑ. By including also the effect of the gauge length L_G, the axial strain ε in Eq. (1.16) becomes:

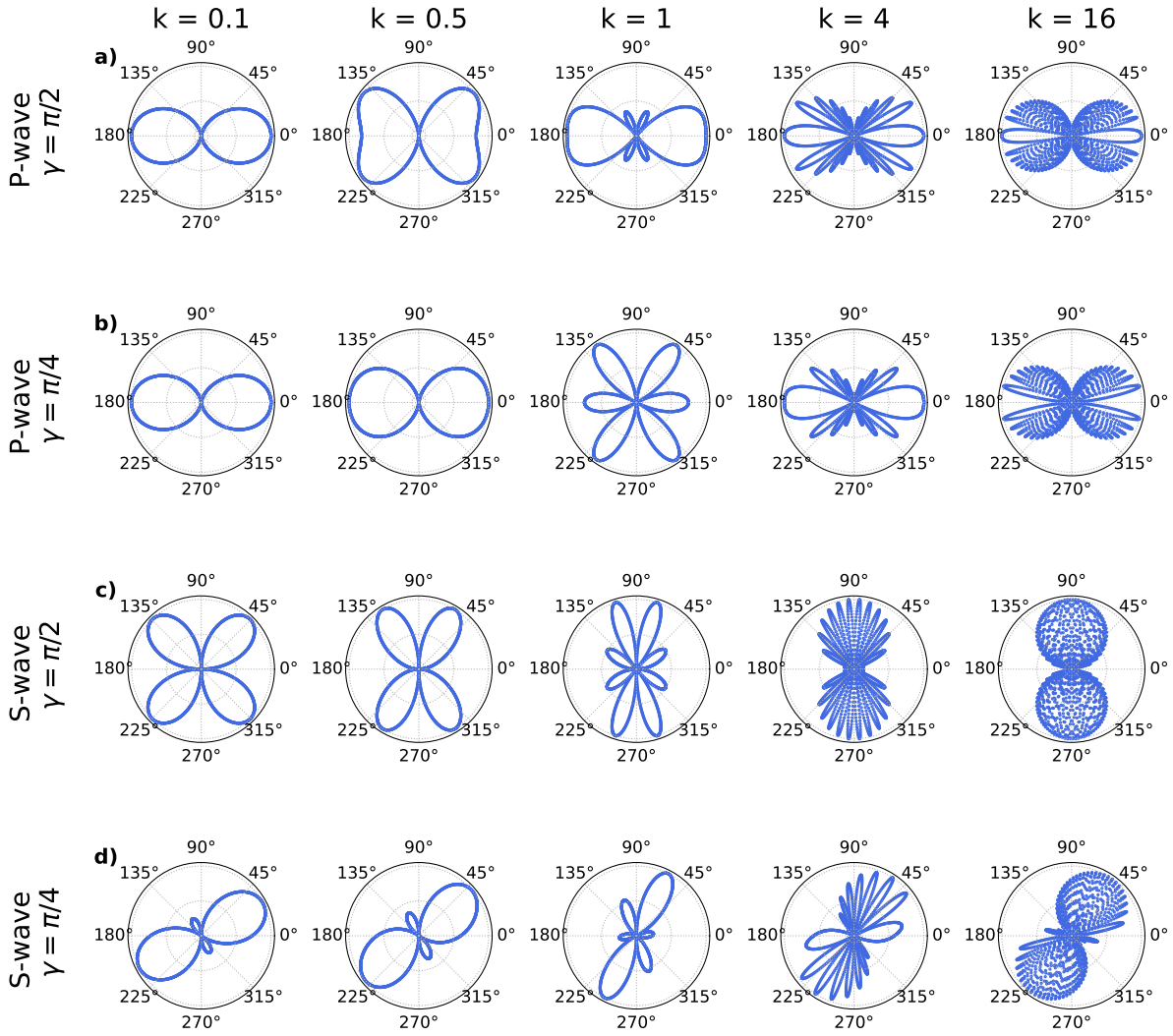

Figure 1.6: Axial strain rate sensitivity along a horizontal fibre oriented at that angle ϑ from the direction of propagation of P (a,b) and S (c,d) waves. We present two cases with waves reaching the surface at an angle γ of 90° and 45° from the vertical. We consider different wavenumbers k (0.1, 0.5, 1, 4 and 16) and a gauge length L_G=10 m. Except for the case of small wavenumbers (i.e. large wavelengths compared to L_G), we observe a significant variation of the strain rate sensitivity with several notches appearing at various angles. Recalculated and redrawn from Martin (2018).

$$\varepsilon(x,y,z,t) = 2iAcos(\vartheta)sin(\gamma)e^{i\omega(t-(xsin(\gamma)-zcos(\gamma))/\alpha)}sin(\frac{\omega L_G cos(\vartheta)sin(\gamma)}{2\alpha}), \quad (1.17)$$

and exhibits a geometry-dependent amplitude factor $(cos(\vartheta)sin(\gamma)sin(\omega L_G cos(\vartheta)sin(\gamma)/2\alpha))$, accounting for both the fibre orientation and the product between the gauge length L_G and the wavenumber $k = \omega/\alpha$. A more detailed development of the Eq. (1.17) can be found in Martin et al. (2017).

Similarly, Martin et al. (2017) derived the strain formulation as measured by the DAS for S waves having an angle γ from the vertical axis z and a propagation velocity β. Following Pujol (2003), the SV and SH motions in the $x-z$ plane are described by Martin et al. (2017) as:

$$\mathbf{u}(x,y,z,t) = e^{i\omega(t-(xsin(\gamma)-zcos(\gamma))/\beta)}(Bcos(\gamma), C, Bsin(\gamma), \quad (1.18)$$

with B and C the amplitude constants for SV and SH waves, respectively. As for Eq. (1.16), the point-wise axial strain along a horizontal fibre deployed at an angle ϑ from the S wave's propagation direction is:

$$\varepsilon(x,y,z,t) = \frac{-i\omega sin(\gamma)}{\beta}e^{i\omega(t-(xsin(\gamma)-zcos(\gamma))/\beta)}cos(\vartheta)(Bcos(\vartheta)cos(\gamma) + Csin(\vartheta)). \quad (1.19)$$

Conversely, the axial fibre strain calculated along a gauge length L_G is:

$$\varepsilon(x,y,z,t) = 2ie^{i\omega(t-(xsin(\gamma)-zcos(\gamma))/\beta)}(Bcos(\vartheta)cos(\gamma) + Csin(\vartheta))sin(\frac{-\omega L_G cos(\vartheta)sin(\gamma)}{2\beta}). \quad (1.20)$$

As for Eq. (1.17), we observe a geometry-dependent amplitude factor proportional to both the angle between the fibre orientation and the seismic wave propagation direction ϑ and the product kL_G.

In Fig. 1.6, we present examples of the angular sensitivities of axial strain generated by P and S waves with different wavenumbers k, propagating either horizontally ($\gamma = 90°$) or reaching the surface at an angle γ =45°. We assume amplitude constants $A = B = C = 1$ and consider a gauge length $L_G = 10$ m. For wavelengths longer than the gauge length, the sensitivity patterns resemble the point strain patterns shown in Fig. 1.5c,d. However, as the wavelength decreases (i.e., with increasing kL_G), different notches emerge at varying angles due to the integration of the strain over the gauge length, reducing the sensitivity of DAS measurements

Chapter 2

Stromboli eruptive activity

2.1 Abstract

Stromboli is one of the most active volcanoes in the world, rising from the sea with its iconic profile. Its volcanic activity mainly consists of mild explosions repeating every ~5-10 minutes. This persistent and partially predictable eruptive style makes Stromboli one of the most studied volcanoes in the world and a perfect test site for novel instruments. However, this ordinary activity is not stationary in time. Changes may occur at scales of days or even hours, leading to sudden morphological variations and increasing system instability. Occasionally, the volcano produces more violent explosions, the so-called "paroxysms". Usually, short-term geophysical signs precede these events. Paroxysms eject ballistic materials at great distances and typically generate pyroclastic density currents that may reach settled areas (as in 1930). Tsunami waves, generated by large and rapid mass movements reaching the sea, pose a significant threat to nearby islands and italian coastlines. In this chapter, we introduce the volcanological context of our DAS experiments. We provide an overview of the several eruptive phenomena at Stromboli and some of their geophysical signatures. This will serve as the basis for a better understanding of the thesis aim and the significance of volcanic monitoring.

2.2 Introduction

Stromboli is a volcanic island belonging to the Aeolian archipelago in the Southern Tyrrhenian Sea, Italy (Fig. 2.1). The volcano rises to 924 m above the sea level (a.s.l.). However, the largest portion (~97%) lies underwater as a large, steep-sided and NE-SW-elongated basaltic stratovolcano whose roots go down to more than ~2000 m depth (Fig. 2.2; Bosman et al., 2009; Francalanci et al., 2013). The size of the entire Stromboli edifice resembles other major European volcanoes such as Etna (Italy; Chiocci et al., 2008).

The subaerial part of Stromboli emerged ~85 ka, with rocks formed during effusive and explosive processes in several growth stages (Francalanci et al., 2013). The cur-

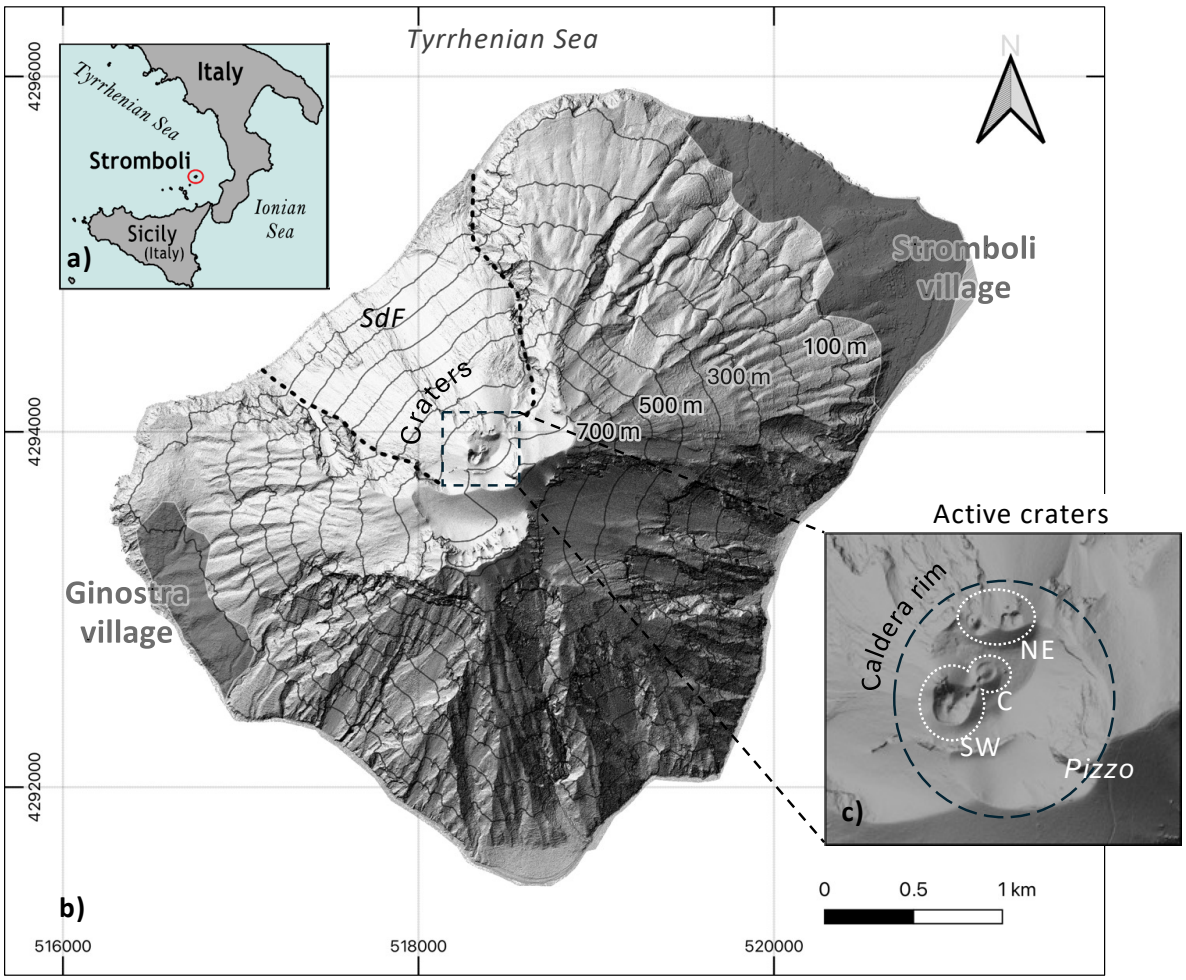

Figure 2.1: (a) Location of Stromboli volcano in the Southern Tyrrhenian Sea. (b) Hillshaded DEM of Stromboli island. The SdF and the active craters are indicated. Stromboli and Ginostra villages are marked as dark grey areas. Isolines in (b) are every 100 m. (c) Close-up view of the crater area with the NE, C and SW sectors. The DEM is computed from images taken in 2014 and courtesy of Italian Civil Protection.

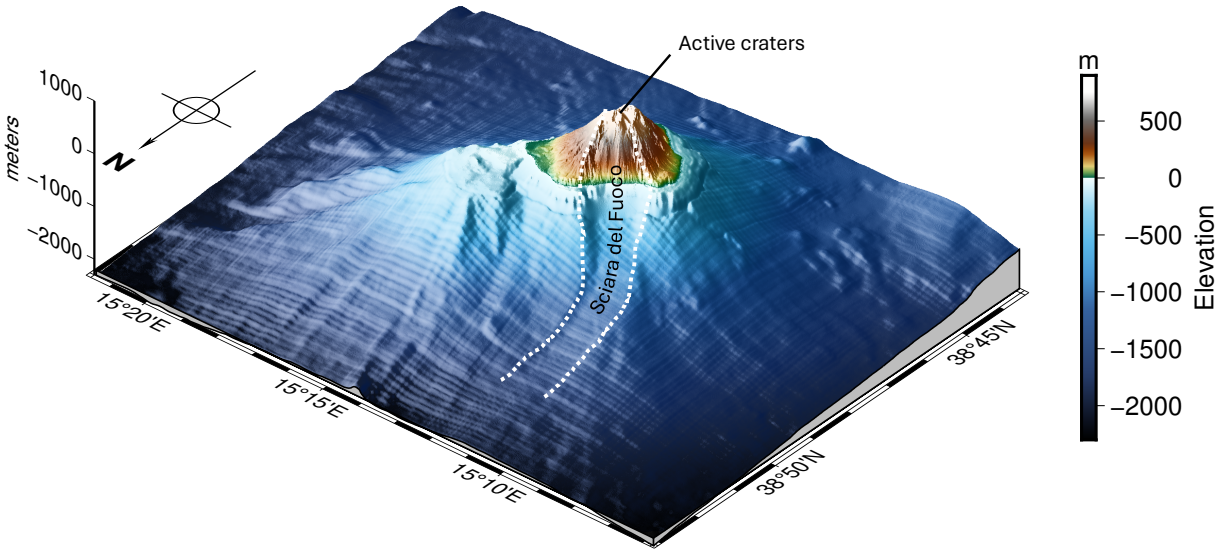

Figure 2.2: 3-D view (from NW) of Stromboli DEM comprising topography and bathymetry (vertical exaggeration 1.5x).

rent volcanic structure is the result of recurrent periods of volcanic edifice formation and degradation, represented by slow erosion processes and volcano-tectonic collapses (Tibaldi, 2001; Apuani et al., 2005; Francalanci et al., 2013). Large-scale caldera and sector failures strongly modify the feeding system, eventually leading to compositional changes of the erupted products (Francalanci et al., 2013). Nowadays, slope instabilities mainly concentrate on the NW and SE-facing flanks. The former features the so-called Sciara del Fuoco (SdF), a steep (~35°), horseshoe-shaped and partially filled collapse scar that continues offshore to a depth of roughly 1700 m below the sea surface (Fig. 2.2; Bosman et al., 2009; Francalanci et al., 2013; Rosi et al., 2013). The SdF results from several gravitational failures over the past 13 ky (Tibaldi, 2001).

The active craters are currently at an altitude of ~750 m a.s.l. Despite frequent morphological variations, the craters usually cluster into three main areas defined as Southwest (SW), Central (C) and Northeast (NE) sectors (Fig. 2.1c; Rosi et al., 2013). The craters connect to a shallow (<1 km) reservoir below the surface that drives the ordinary volcanic activity (Ripepe et al., 2008; Landi et al., 2011; Rosi et al., 2013).

Stromboli usually exhibits a persistent and mild explosive regime which started at least ~1300 years ago (Rosi et al., 2000). The ordinary Strombolian activity, as described by Mercalli (1881), mainly consists of continuous degassing alongside low-intensity and repeating explosions. This feature makes Stromboli a widely studied volcano. Over the years it has been the test bench for many pioneering experiments in several fields such as volcano acoustics (Ripepe et al., 1996; Vergniolle & Brandeis, 1996; Ripepe & Gordeev, 1999) and broadband (Neuberg et al., 1994; Chouet et al., 1999; Wielandt & Forbriger, 1999; Chouet et al., 2003) and rotational (Wassermann et al., 2022) seismology.

However, this activity is nonstationary. The typical eruptive style is occasionally interrupted by different types of events, such as more violent (paroxysmal) explosions and lava flows (Fig. 2.3). Paroxysmal explosions significantly threaten the inhabitants and tourists due to the broader ejecta coverage and the eventual formations of PDCs (Rosi et al., 2013). Rapid changes in the activity style may occur within days to hours (Ripepe et al., 2008), potentially leading to violent explosive phases or large-scale gravitational

Figure 2.3: Examples of different processes occurring at Stromboli, such as (a) ordinary explosions, (b) major explosions, (c) paroxysmal explosions, (d) lava flows or overflows, and (e) PDCs, landslides and rockfalls. Credits are in the bottom left of each picture. (c) Is taken from Bevilacqua et al., 2020.

collapses and suddenly worsening risk scenarios.

The magmatism at Stromboli results from a late Quaternary, subduction-related volcanism in the eastern sector of the Aeolian archipelago started ~800 ka (De Astis et al., 2003) within the complex Africa-Eurasia convergence frame. Several petrological and mineralogical studies of ejected material have enhanced our understanding of the complex plumbing system of Stromboli, comprising different magma ponding zones responsible for distinct explosive phenomena (Voloschina et al., 2023). The normal activity is driven by a shallow (<3 km), crystal-rich (~50 vol%), partially degassed basaltic and highly-porphyritic magma (HPM) reservoir (Fig. 2.4; Bonaccorso et al., 2008; Métrich et al., 2010; Voloschina et al., 2023). Conversely, deeper sources feed the paroxysmal explosions with crystal-poor (<10 vol%), gas-rich, basaltic and low-porphyritic magma (LPM) located at ~6-9 km depth (Fig. 2.4; Bertagnini et al., 2003; Métrich et al., 2005, 2010; Francalanci et al., 2013).

In the following Sections, we provide an overview of the main features of eruptive (e.g., ordinary and paroxysmal explosions) and non-eruptive (e.g., landslides and PDCs) processes at Stromboli (Fig. 2.3) and their geophysical signatures. We will lay the basis for a better understanding of the rest of the thesis.

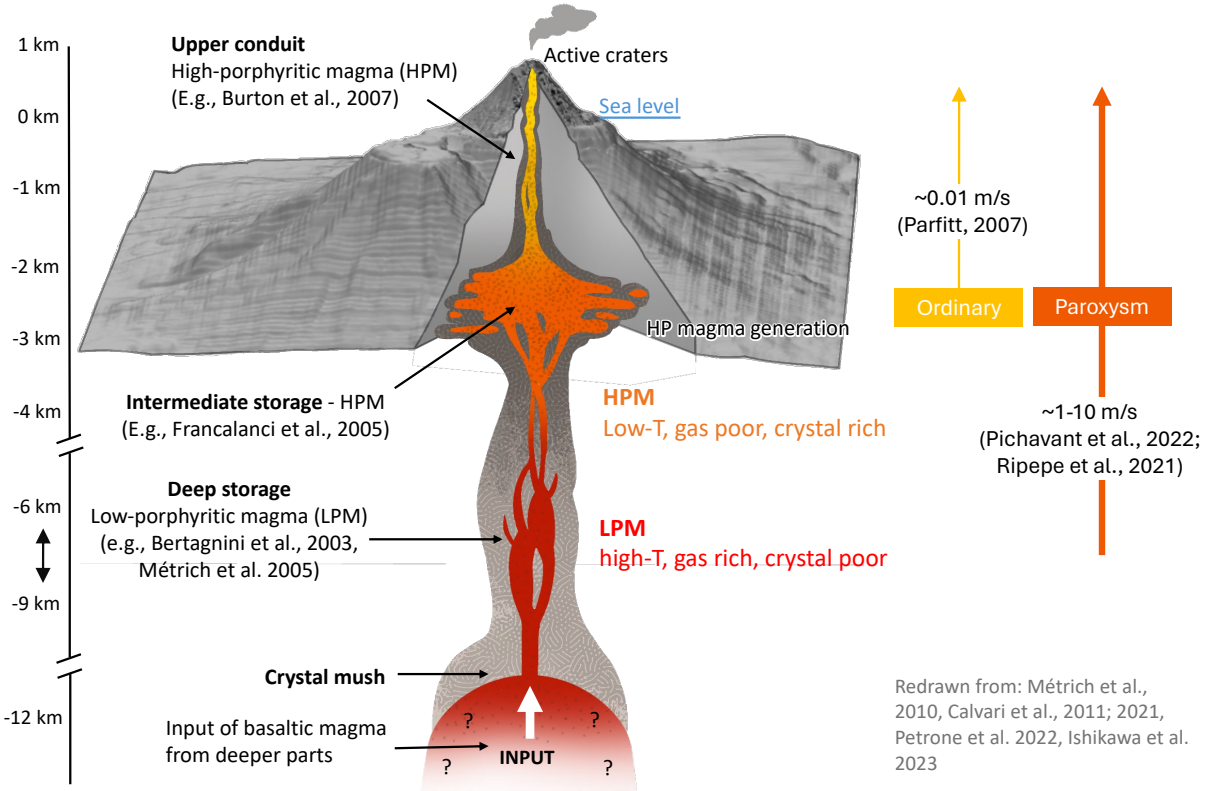

Figure 2.4: Model of the plumbing system of Stromboli based on literature findings (Bertagnini et al., 2003; Parfitt, 2004; Francalanci et al., 2005; Métrich et al., 2005; Burton et al., 2007; Métrich et al., 2010; Calvari et al., 2011; Métrich et al., 2021; Ripepe, Lacanna, et al., 2021; Petrone et al., 2022; Pichavant et al., 2022). Redrawn from Métrich et al. (2010), Calvari et al. (2011), Petrone et al. (2022), and Ishikawa (2023). Vertical exaggeration of the 3D DEM is 2x.

2.3 Ordinary explosions

The ordinary activity at Stromboli consists of passive gas streaming and active degassing (puffing) alongside recurrent (~10 events/hr), short-lived and low-intensity explosions ejecting low volumes (1–10 m^3) at heights of ~50-400 m above the craters (Figs. 2.3a, ; Rosi et al., 2000; Delle Donne et al., 2006; Ripepe et al., 2008; Rosi et al., 2013; Voloschina et al., 2023). General modelling of explosions involves large gas slugs that enucleate, rise, and eventually explode in the conduit, generating seismo-acoustic emissions (Blackburn et al., 1976; Ripepe et al., 1996; Vergniolle & Brandeis, 1996; Chouet et al., 2003).

The seismic record at Stromboli exhibits a continuous volcanic tremor (1-5 Hz; Nappi, 1976; Langer & Falsaperla, 1996; Ripepe et al., 1996; Wassermann, 1997) overlaid by explosion signals ranging between $10^{-2} - 10$ Hz (Neuberg et al., 1994; Chouet et al., 1997, 2003). Tremor signals are due to the active degassing (puffing) of the magma column, resulting from small (<0.5 m) gas bubbles bursting every 1-2 s (Ripepe et al., 1996; Ripepe & Gordeev, 1999). Volcanic explosion quakes (VEQs; 1-10 Hz) are usually generated during each explosion and have emergent onset and durations of ~10-20 s (Chouet et al., 2003). However, Strombolian explosions also generate very-long-period (VLP) transients having frequencies of 0.01-0.3 Hz (Fig. 2.5; Neuberg et al., 1994; Chouet et al., 1999; Kirchdörfer, 1999; Wielandt & Forbriger, 1999; Chouet et al., 2003; Ripepe, Delle Donne, et al., 2021).

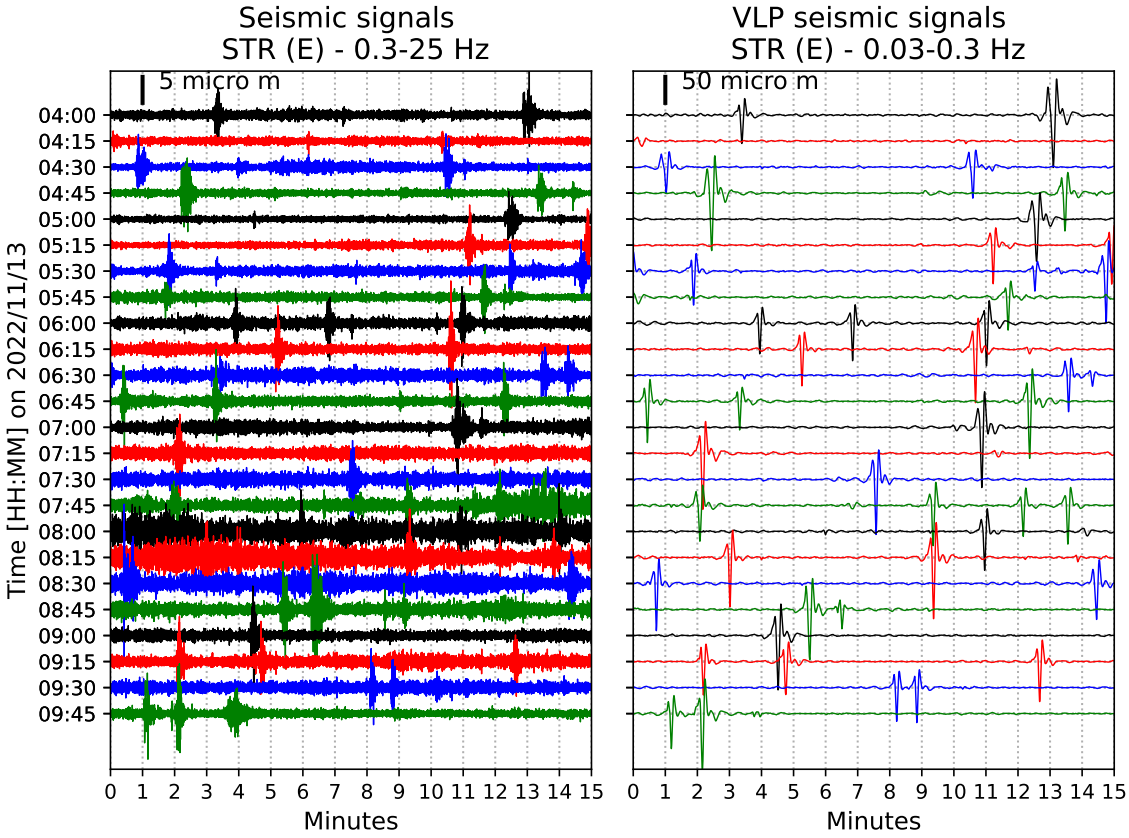

Figure 2.5: Drumplot of six hours of seismic signals recorded at Stromboli (STR station, component E) between 04:00 and 10:00 UTC on 11 November 2022. We observe 45 explosive events, generating both high frequency (left) and VLP (0.03-0.3 Hz, right) signals.

2.3.1 VLP seismicity at Stromboli

VLPs represent a typical feature of the seismic wavefield observed at Stromboli. VLPs exhibit similar waveforms and can be divided into different families, indicating a non-destructive and repetitive source (Chouet et al., 2003; Ripepe, Delle Donne, et al., 2021). VLP waveforms exhibit (i) a first, low-amplitude compressive phase (A1 in Fig. 2.6d) followed by (ii) a higher amplitude decompression (A2 in Fig. 2.6d) and (iii) a coda (A3 in Fig. 2.6d). Several studies relying on short-lasting experiments located the VLP centroid at stable and shallow (~220-260 m below the craters) depths below the upper part of the SdF (Chouet et al., 1999; Chouet, 2003; Marchetti & Ripepe, 2005; Sugimura et al., 2021). Moment tensor inversions explain the VLP source mechanisms as the effect of an inclined (~60°) dyke producing a sudden expansion of the gas slugs rising in the shallow conduits (Chouet et al., 2003).

However, the VLP centroid locations may change vertically over the years (Marchetti & Ripepe, 2005; Giudicepietro et al., 2009; Ripepe et al., 2015). These fluctuations correlate with variations in crater altitude and lateral effusive eruptions, which lower the magma column as lava flows out of the conduit (Giudicepietro et al., 2009; Ripepe et al., 2015; Valade et al., 2016; Ripepe, Delle Donne, et al., 2021). Moreover, multi-parametric studies observed that most of the VLP energy develops after the explosion onset. Joint analysis of VLP seismicity and ground deformation also reveals that VLPs represent the final stage of recurrent ~150-200 s long inflation/deflation cycles generated

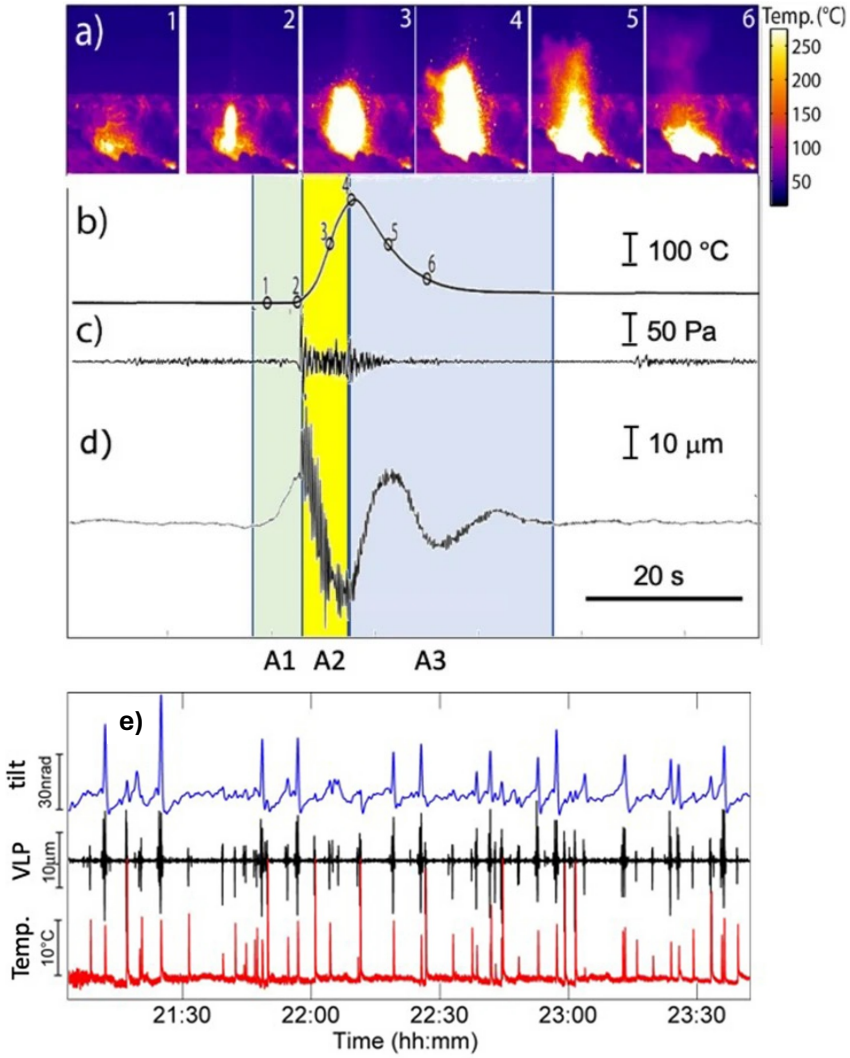

Figure 2.6: (a) Thermal images of one ordinary explosion linked with its (b) thermal, (c) infrasound and (d) seismic signals. The VLP component of the seismic wavefield is visible in (d) with periods of ~10 s. (e) 2.5 hr long traces showing the ground tilt (top), VLP signals (middle) and thermal flux (bottom) associated with each explosion. Adapted from Ripepe, Delle Donne, et al. (2021).

by gas charge/discharge processes in the shallow conduit associated with each explosion (Fig. 2.6e; Genco & Ripepe, 2010; Ripepe, Delle Donne, et al., 2021). According to Ripepe, Delle Donne, et al. (2021) and Legrand and Perton (2022), the inflation phase in the ground tilt is due to the increase of the magma level in the conduit driven by the gas accumulation below a crystal-rich and shallow (<250 m depth) magma mush. The subsequent ascent of the gas slug accelerates the inflation until the explosion. The compressive phase of each VLP (A1 in Fig. 2.6d) represents the peak inflation caused by accelerating gas expansion. Conversely, the dilatation phase (A2 in Fig. 2.6d) arises from the sudden decompression of the magma column and the ground deflation after the release of gas overpressure in the atmosphere (Ripepe, Delle Donne, et al., 2021). However, this mild explosive style is not the only one observed at Stromboli, which instead includes events of far greater magnitude.

2.4 Violent explosions

More violent and long-lasting explosions may occasionally occur at Stromboli, posing significant threats to the inhabitants, visitors, and scientists (Fig. 2.3b,c; Barberi et al., 1993; Rosi et al., 2006, 2013; Voloschina et al., 2023). These events have varying magnitudes and typically group into two main categories based on their intensity and associated hazards, i.e. "major" (intermediate-scale) and "paroxysmal" (high-intensity) explosions (Barberi et al., 1993; Rosi et al., 2013).

Mass discharge rates and fall-out volumes of major explosions (10^4-10^5 kg/s and 10^2-10^3 m^3) and paroxysms (> 10^6 kg/s and 10^4-10^5 m^3) are several order of magnitudes higher than ordinary activity (Fig. 2.7a; Rosi et al., 2013; Voloschina et al., 2023). Paroxysms may eject meter-sized ballistics at velocities higher than 200 m/s and over great distances, possibly including settled areas at sea level (Rosi et al., 2006; Pistolesi et al., 2011; Rosi et al., 2013). The eruptive columns can reach heights from 1 and up to 8 km (Rosi et al., 2006; Pistolesi et al., 2011; Rosi et al., 2013) and occasionally collapse, leading to the formation of PDCs (Rosi et al., 2013). While major explosions typically occur at an annual rate (Barberi et al., 1993), paroxysms exhibit a lower average rate of one event every four years for the last 140 years (Bevilacqua et al., 2020). Five paroxysms occurred since 2003 on 5 April 2003, 15 March 2007, 3 July 2019, 28 August 2019 and 11 July 2024 (Rosi et al., 2006; Pistolesi et al., 2011; Bevilacqua et al., 2020; Andronico et al., 2021)

These events usually have roots in the deeper part of the plumbing system, making them trickier to forecast (Aiuppa et al., 2021). Models of paroxysm formation usually indicate the fast ascent and injection of deep, volatile-rich LPM in the shallow (HPM) reservoir (Métrich et al., 2005; Aiuppa et al., 2010; Allard, 2010; Aiuppa et al., 2021; Voloschina et al., 2023). The triggering process depends on the destabilization of the deep reservoir, which can result from both top-down and bottom-up mechanisms (Ripepe et al., 2015, 2017; Aiuppa et al., 2021). The top-down trigger relies on the rapid decompression of the deep reservoir resulting from the magma depletion in the shallow conduit during effusive activity (Ripepe et al., 2015; Aiuppa et al., 2021). This process may ease the rise of deep LPM as possibly occurred during the April 2003 (Rosi et al., 2006), March 2007 (Pistolesi et al., 2011) and August 2019 (Andronico et al., 2021) paroxysms. Conversely, the bottom-up trigger indicates a dominance of the deep reservoir over the shallow one, as was probably the case for the 1930 (Bertagnini et al., 2011) and July 2019 (Aiuppa et al., 2021; Andronico et al., 2021) paroxysms whose occurrence was not coupled with effusive eruptions. According to this model, the LPM ponding zone becomes progressively unstable, building up pressure due to the addition of gas and volatile-rich melts, eventually leading to rapid ascent and eruption (Métrich et al., 2005; Aiuppa et al., 2010; Allard, 2010; Aiuppa et al., 2021).

Despite the deeper origin, ground deformation allows for a timely warning of these events (Fig. 2.7b; Ripepe, Lacanna, et al., 2021). Both major and paroxysmal explosions occur at the peak of a short-term, exponential inflation visible in ground tilt (Ripepe, Lacanna, et al., 2021) and strain (Di Lieto et al., 2020) measurements (Fig. 2.7b). The durations and amplitudes of the inflation scale with the explosion intensity. Major explosions exhibit inflation trends lasting for ~300 s and reaching amplitudes of ~1 μrad. Conversely, paroxysms produce longer-lasting (~600 s) ground deformation reaching amplitudes of ~10 μrad (Fig. 2.7b). Despite the magnitude of the events, ground deformation

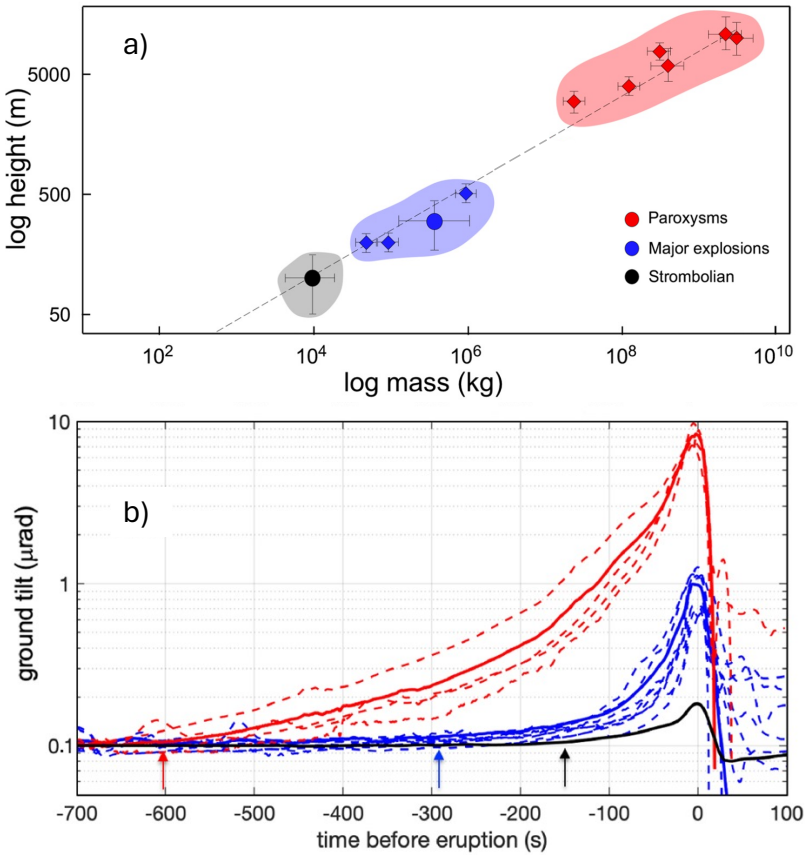

Figure 2.7: (a) Log-log plot linking the typical plume heights with the erupted mass of ordinary (black), major (blue), and paroxysmal (red) explosions. (b) Ground tilt traces exhibit the exponential inflation (on a log scale) preceding ordinary (black), major (blue), and paroxysmal (red) explosions. The bold blue and red lines represent the stacking of several major explosions and paroxysms, respectively. (a) Is adapted from Voloschina et al. (2023), while (b) from (Ripepe, Lacanna, et al., 2021).

associated with ordinary, major and paroxysmal explosions exhibits the same inflation trend (Fig. 2.7b), suggesting a scale-invariant conduit process for explosions at Stromboli (Ripepe, Lacanna, et al., 2021).

2.5 Lava flows

Effusive eruptions may also occur at Stromboli and exhibit varying sizes. They range from small-scale (10^3 m^3) overflows confined within the crater area to long-lasting (up to months), large (>10^6 m^3) lava flows (Barberi et al., 1993; Rosi et al., 2013). Since 1985, six large-scale effusive eruptions occurred: in 1985-1986, 2002-2003, 2007, 2014 and 2024 (Rosi et al., 2006; Barberi et al., 2009; Ripepe et al., 2015; Valade et al., 2016; Ripepe et al., 2017). Recent effusive crises usually occur at the culmination of a months-long phase of intensified volcanic activity. Geophysical evidence of this trend is the rising amplitudes of the volcanic tremor, VLPs and acoustic pressures, and the increasing deformation of the crater area (Martini et al., 2007; Casagli et al., 2009; Ripepe et al., 2009; Di Traglia et al., 2014; Valade et al., 2016). This is due to increasing magma supply, which raises the magmatic column in the conduit. High magma input rates (>0.3 m^3/s; Coppola et al., 2012) increase the pressurization of the shallow system leading to fissures opening along

the SdF from lateral dykes propagating from the conduit (Ripepe et al., 2017). Lava flows typically descend the SdF, eventually reaching the coast and forming deltas (Rosi et al., 2013). In the last 2000 years, eruptive fissures have always formed within the SdF (Rosi et al., 2013), possibly causing slope failures and originating large-scale landslides.

2.6 Rapid mass movements and tsunamis

Stromboli edifice is the result of several large-scale collapses mainly concentrated in the NW and SE flanks (Tibaldi, 2001; Corazzato et al., 2008; Romagnoli et al., 2009; Francalanci et al., 2013; Lucchi et al., 2019). Therefore, slope instability and rapid gravity-driven mass movements are typical phenomena at Stromboli. These events mainly comprise rockfalls, PDCs and major landslides leading to sector or flank collapses.

Small-scale landslides and rockfalls occur daily along the SdF, representing the faintest but most evident marker of its gravitational instability. The formation of PDCs is mainly due to eruptive column collapses or gravitational instabilities of the crater rim during paroxysms (Rosi et al., 2013; Di Roberto et al., 2014; Bevilacqua et al., 2020; Calvari et al., 2020; Calvari et al., 2022; Di Traglia, Borselli, et al., 2023; Giudicepietro et al., 2023; Ripepe & Lacanna, 2024). PDCS typically propagate down the SdF, reaching front velocities from 40 to 70 m/s (e.g., Calvari et al., 2022; Ripepe & Lacanna, 2024, this thesis), possibly generating metre-scale tsunami waves upon impact with the sea (Ripepe & Lacanna, 2024). PDCs may also propagate outside the SdF, affecting the settled areas and claiming victims, as in 1930 (Di Roberto et al., 2014; Bevilacqua et al., 2020). Finally, large-scale collapses may result from violent explosions or effusive eruptions leading to the opening of lateral vents in the SdF (Rosi et al., 2013). Large PDCs and landslides reaching the sea can trigger tsunami waves, endangering the island and neighbouring coastlines (La Rocca, Galluzzo, et al., 2004; Ripepe & Lacanna, 2024).

In pre-historical and historical times, Stromboli has been the source of several tsunamis typically coupled with intense volcanic activity (Rosi et al., 2013; Pistolesi et al., 2020). Historically, tsunamis caused damage on Stromboli island with inland progressions of up to 300 m (Rosi et al., 2013). During the Middle Ages, the destruction of the Naples and Amalfi harbours (~240 km from Stromboli) may be due to tsunami waves generated by large collapses of the SdF (Rosi et al., 2019). Since 1900, tsunamis have occurred at Stromboli every ~15 years (Maramai et al., 2005), mainly sourced by gravitational instabilities of the SdF. The major event among them occurred on 30 December 2002, when an effusive eruption triggered the collapse of ~1-10^6 m^3 along the SdF resulting in a ~10 m high tsunami wave causing severe damage to the island (La Rocca, Galluzzo, et al., 2004; Chiocci et al., 2008; Tinti et al., 2008; Rosi et al., 2013).

Chapter 3

DAS experiments at Stromboli volcano: from cable installation to analysis of seismo-volcanic signals

3.1 Abstract

This chapter outlines the DAS experiments conducted at Stromboli from 2020 to 2023. Starting in September 2020, we deployed 4 km of fibre-optic cable in a 30 cm hand-dug trench on the NE flank of Stromboli, providing good coverage of the summit craters despite natural and topographical constraints. The fibre layout is shaped in several sub-arrays with triangular and grid-like geometries, ensuring strain recordings along different directions. Multiple recording campaigns were conducted each year, with nodal and broadband seismometers deployed alongside providing a comparison for DAS measurements. This chapter lays the foundation for further data analysis, aimed at extracting maximum value from the extensive dataset collected. The dataset includes signals from volcanic processes such as explosions (ordinary and more violent), rockfalls, and pyroclastic density currents. We also find evidence of DAS's capabilities to record very long period (VLP) signals (0.04-0.1 Hz) generated by the explosive activity. The VLP strain waveforms from DAS closely match those recorded by permanent broadband seismometers and are consistent across different events, pointing to a repetitive, non-destructive source. DAS strain measured along different directions also allows us to determine the orientations and values of the principal strains, which show greater amplitude along the radial direction to the craters, consistent with literature observations. These results highlight the effectiveness of DAS in capturing various volcanic phenomena, offering valuable insights into volcanic activity.

3.2 Introduction

Installing and maintaining seismic stations in volcanic environments poses significant challenges, particularly for volcanoes lacking infrastructures and requiring hand carriage of equipment up steep slopes. The DAS technology may offer a valid solution by turning optical fibres into large numbers of strain sensors that are continuously active as long as a power source is available. Deploying an equivalent number of traditional seismometers on a volcano would require considerable labour and maintenance and face limitations due to battery life.

In many applications, using preinstalled telecom fibres ensures a significant reduction in costs and logistical complexities. These infrastructures may be valuable for monitoring volcanoes near urban areas, such as Campi Flegrei (Italy), or in submarine environments, like Vulcano Island (Italy) and Tonga (Currenti et al., 2023; Jousset et al., 2024; Nakano et al., 2024). However, these fibres restrict the DAS array geometry to the existing telecom deployment (Jousset et al., 2024).

During our project, we deployed a dedicated fibre optic cable on the northeast flank of Stromboli volcano (Italy). During three years, from 2020 to 2022, we installed 4 km of cable in segments of either 500 m and 1 km, joined together by splices or connectors. Individual cables consist of eight tight-buffered single-mode fibres loosely packed within a polyethylene jacket. The fibre layout was designed to meet our research objectives while accommodating natural obstacles such as steep slopes and lava outcrops. The highest point of the fibre is about 900 metres from the active craters. Additionally, we implemented four fibre-optic arrays: three with triangular geometries and apertures ranging from 30 to 150 m, and one with a grid-shaped geometry consisting of four 30-meter squares. We designed these geometries to obtain information on the location of seismic sources and wavefield characteristics by applying array techniques (e.g. beamforming) to strain rate data.

Using a Febus A1-R interrogator, we collected nearly five months of DAS data during several experiments carried out between 2020 and 2023. We mainly recorded periods of ordinary eruptive activity, characterised by continuous volcanic tremor and frequent mild explosions (~10 events/hr). However, our dataset also comprises three major explosions, several pyroclastic density currents (PDCs), and three lava overflows. In the various experiments we configured the DAS interrogator with a gauge length of either 5 or 10 m and a sampling rate between 50-1000 Hz. During each experiment, we also deployed co-located arrays of 5 Hz nodal seismometers to validate the DAS measurements and to compare the results of array analysis techniques obtained with the two datasets.

In this chapter we provide a summary of all experiments and an overview of the acquired dataset. First, in Section 3.3, we describe the four years of fieldwork, detailing the optical cable deployment, the DAS interrogator parametrisation during each experiment and the geometries of co-located seismometer arrays. We illustrate our procedure to accurately geolocate the DAS channels in Section 3.5. We then provide an overview of the dynamic strain rate waveforms generated by volcanic tremor, ordinary and major explosions, rockfalls, and PDCs in Section 3.6. We highlight the key features of the DAS records in both time and frequency domains and compare them with data from broadband seismometers and infrasound sensors at the summit. Finally, Section 3.7 deals with the DAS capability to capture the Very Long Period (VLP) component of the explosive seismic wavefield between 0.04-0.1 Hz. We also retrieve the directions and values of the principal

Figure 3.1: Pictures capturing the various stages of optical cable installation at Stromboli. (a-b) trench digging. (c) cable deployment in the trench. (d) Ensuring good contact between the cable and the ground and geolocation of the cable layout with differential GPS. (e) Covering the trench. (f) Performing tap tests. (g-h) Eventual fibre reparation and splicing.

strains of VLPs using DAS strain recordings along three different directions (Section 3.7.1). This chapter sets the stage for more detailed waveform analysis and the application of array techniques to infer the location of stationary (explosions and tremors) and moving (PDCs) sources in subsequent Chapters 5 and 6.

3.3 Experimental setup

3.3.1 Optical cable deployment

In Fig. 3.1, we summarise the several steps of our DAS installation:

- Excavation of the trench for the fibre-optic cable (Fig. 3.1a,b).
- Deployment of the cable in the trench (Fig. 3.1c).
- Partial trench covering, ensuring a good coupling between soil and cable. Simultaneously, geolocation of the track and incremental distance measurement along the cable (Fig. 3.1d).
- Total trench covering to avoid erosive phenomena due to, e.g. water run-off (Fig. 3.1e).
- Connection of the fibre to the interrogator and start the acquisition. Then, perform the tap tests to geolocate later the DAS channels (Fig. 3.1f).

The optical cable we deployed is composed of a polyethylene jacket (5 mm in diameter) which encloses a loose kevlar layer (without gel) surrounding eight tight-buffered single-mode optical fibres having a diameter of 600 μm and an 8 μm sensing core. On the one hand, this flexible structure makes the cable particularly suitable for harsh volcanic environments. On the other hand, its loose nature allows the radial compression of the fibre bundle within the cable. This effect may influence the ground-to-fibre strain coupling, as later pointed out in Section 5.9.

Local workers (see Acknowledgements) and the scientific team dug the trench with a depth of ~20-30 cm (Fig. 3.1a,b). We started from the UniFi Geophysical Observatory (OSV in Fig. 3.2) and continued towards the summit. The first part of the deployment, installed in 2020, develops along the path to the summit from 200 to ~475 m a.s.l. and is oriented radially towards the craters (Fig. 3.2a). At its uppermost end, we implemented a small-aperture triangular array (CT, i.e. central triangle, in Fig. 3.2c) with sides of ~30 m. In 2021, we added two branches extending from the CT array, one heading north and the other south (Fig. 3.2a). At the end of each branch, we deployed the optical fibres shaping two triangular arrays: NT (north triangle; Fig. 3.2b) and ST (south triangle; 3.2d). The NT array has an aperture of ~150 meters, while the ST array is ~70 meters wide. The southern branch also includes a straight segment roughly 170 meters long, aligned radially to the craters. Finally, in 2022, we completed the installation by adding a grid-shaped array (GR) south of ST (Fig. 3.2e). The GR array spans about 130 m and consists of four squares, each with sides of ~30 m, positioned at ~45° to the direction of the craters. Additionally, we added a 130 m segment along the diagonal of three squares oriented towards craters.

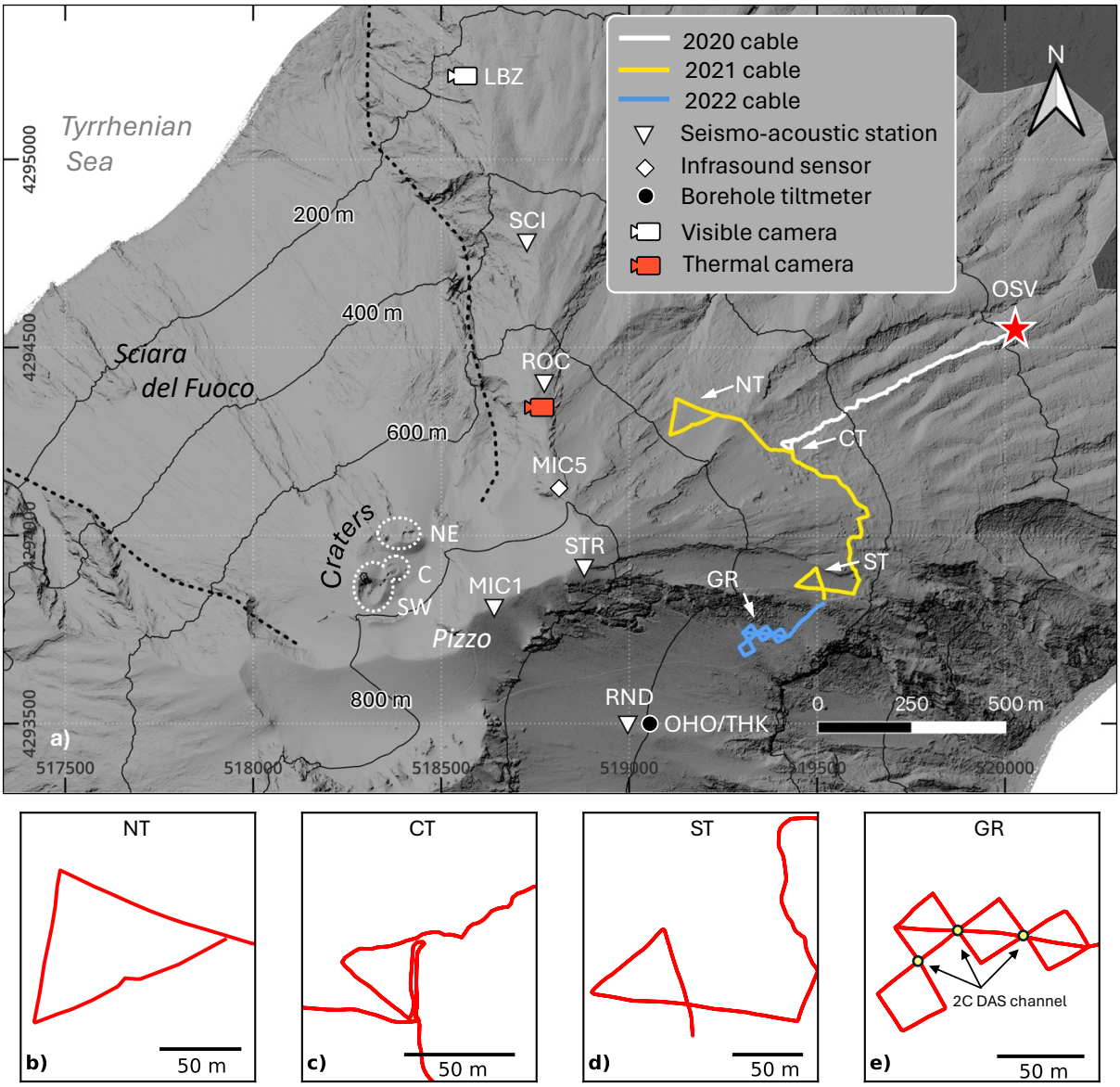

Figure 3.2: (a) Map of Stromboli volcano with the DAS fibre layout (white, yellow and blue lines) and the permanent UniFi monitoring network, comprising broadband seismometers (white triangles), borehole tiltmeters (black circle), infrasound sensors (white diamond) and thermal (ROC) and visible (LBZ) cameras. The UniFi geophysical observatory is marked by a red star. (b-e) Show the various DAS arrays, i.e. NT (b), CT (c), ST (d), and GR (e).

This cable layout allows us to measure strain rate along different directions and test array processing techniques on DAS measurements (see Sections 5 and 6). In particular, the GR array has three intersections where two DAS segments meet at right angles (Fig. 3.2e), enabling the retrieval of two horizontal components of the seismic wavefield, as theorized by van den Ende and Ampuero (2021). Furthermore, the cable geometry provides good coverage of the summit craters (~48°) while constrained by natural and topographical obstacles. We faced several challenges during the installation, such as the steep slope, the high density of the vegetation below 400 m a.s.l., the ashy nature of the soil and the presence of lithic blocks and solid lavas. After the deployment, we could connect the DAS interrogator to measure the dynamic strain rate of the fibre induced by the volcano seismicity.

3.3.2 DAS measurements and parametrisation

We used a Febus A1-R DAS interrogator to measure strain rate signals generated by the volcanic activity. The UniFi Geophysical Observatory (OSV in Fig. 3.2) hosted the DAS interrogator during the experiments. Below, we provide a brief description of several experiments between 2020 and 2023, indicating the total length of the probed fibre, the duration of the experiment and the parameterisation of the DAS interrogator (also summarised in Table 3.1):

2020 We probed 1 km of cable oriented radially towards the craters (Fig. 3.3a). We carried out DAS measurements for one week, from September 15 to 23, 2020, with continuous recording sessions of 7-8 hr/d. We set the optical power and width of the pulse to 27 dB and 2 m, respectively. We recorded dynamic strain rate signals with a sampling frequency of f=2 kHz. We set a channel spacing dx=2.4 m and a gauge length L_G=5 m, corresponding to one-quarter of a 20 m wavelength. This wavelength is characteristic of a low-speed wave (400 m/s) at 20 Hz, which we consider the lower limit of the wavelengths of interest. However, we mainly focus on waves with velocities between 1000-400 m/s in the 1-10 Hz frequency band. These values result in wavelengths ranging between 1000-40 m. Such values minimise the 5 m gauge length effects discussed in Section 1.4.3. We obtained a total of 362 ground-coupled channels. Data presented in this thesis are decimated at 200 Hz. The size of the dataset acquired during this experiment is ~2 TB.

2021 We connected the different fibre instances together at their ends so that the laser pulse would make a complete circle within the cable, passing twice through the same point. This setup provides 6 km of interrogated cable comprising the D-NT, D-CT and D-ST arrays (Fig. 3.3b). The interrogator probed the fibre between September 16 and October 20, 2021. We set the pulse optical power and width to 30 dB and 2 m, respectively. We parametrised the interrogator with a sampling frequency f=2 kHz, decimated to 400 Hz, a channel spacing dx=2.4 m and a gauge length L_G=5 m. We obtained a total of 2443 ground-coupled DAS channels. The size of the dataset acquired during this experiment is ~20 TB.

2022 We interrogated the whole fibre, comprising D-NT, D-CT, D-ST and D-GR sectors (Fig. 3.3c). We connected the various fibre instances so that the laser pulses would pass twice through the ST and GR sectors, providing 6 km of interrogated cable. The interrogator probed the fibre for more than four months, between

September 15, 2022, and January 30, 2023. Due to higher noise levels observed at the end of the fibre, we used a laser optical power of 33 dB. We set the pulse rate frequency to 5 kHz and the pulse width to 5 m. We then reduced the channel spacing to dx=2 m and increased the gauge length to L_G=10 m to enhance the SNRs at lower frequencies. Also, in this case, the difference between wavelength and gauge length minimises the presence of additional sensitivity lobes blinding various directions (Section 1.4.3). We acquired the strain rate data at a sampling frequency of f=50 Hz after decimating the raw measurements sampled at 5 kHz. We then obtained a total of 2770 ground-coupled DAS channels. The size of the dataset acquired during this experiment is ~16 TB.

2023 We used a similar configuration as in 2022. We probed 6 km of fibre (Fig. 3.3d) between September 25 and October 20, 2023. As for the 2022 experiment, we used a laser pulse with a width of 5 m and an optical power of 33 dB. We set the pulse rate frequency to 5 kHz and decimated the data to f=100 Hz. We set the channel spacing dx=2 m and the gauge length L_G=10 m. We obtained 2770 ground-coupled DAS channels. The size of the dataset acquired during this experiment is ~8 TB.

3.3.3 Co-located instruments

During each experiment we also installed inertial seismometers co-located with the fibre optic cable. We used SmartSolo IGU-16HR three-component (3C) nodes. Smartsolo nodes have a Sampling rate of 250 Hz, a corner frequency of 5 Hz and documented frequency response[1]. We deployed the nodes with the aim of comparing DAS data with translational ground motion measurements using different approaches later detailed in Chapter 4. In addition, we wanted to compare the results of the array techniques obtained from the strain rate and ground velocity signals that serve as a reference as shown in Chapters 5 and 6. We designed the inertial sensor distribution along fibre to reach these purposes. In Fig. 3.3 and Table 3.1 we provide a summary of the location and geometry of the node arrays during each experiment.

3.3.4 Permanent monitoring network

We also investigate the data of the permanent UniFi network (Fig. 6.1a), comprising five broadband seismometers, eight infrasonic pressure sensors, two borehole tiltmeters, one thermal camera, three visible cameras and two tsunami gauges at sea. Seismic stations (STR, ROC, SCI, RND, MIC1) consist of Guralp digitizers equipped with Guralp CMG-40T seismometers having sampling rates of 100 Hz and a flat instrumental response up to 30 s. Seismic stations are also provided with differential acoustic pressure transducers with flat frequency responses between 0.01 – 100 Hz, a full-scale range of 250 Pa, and sampling at 100 Hz (Ripepe, Delle Donne, et al., 2021). We also consider one (MIC5) stand-alone acoustic sensor with the same characteristics. Borehole tiltmeters are Pinnacle T5000 (OHO) and Denali (THK) and are installed on the southeast flank of the volcano at depths of ~6 and ~4 m respectively. Both tiltmeters have a sensitivity of 1 nrad and

[1] https://www.passcal.nmt.edu/content/instrumentation/all-one-systems/smart-solo

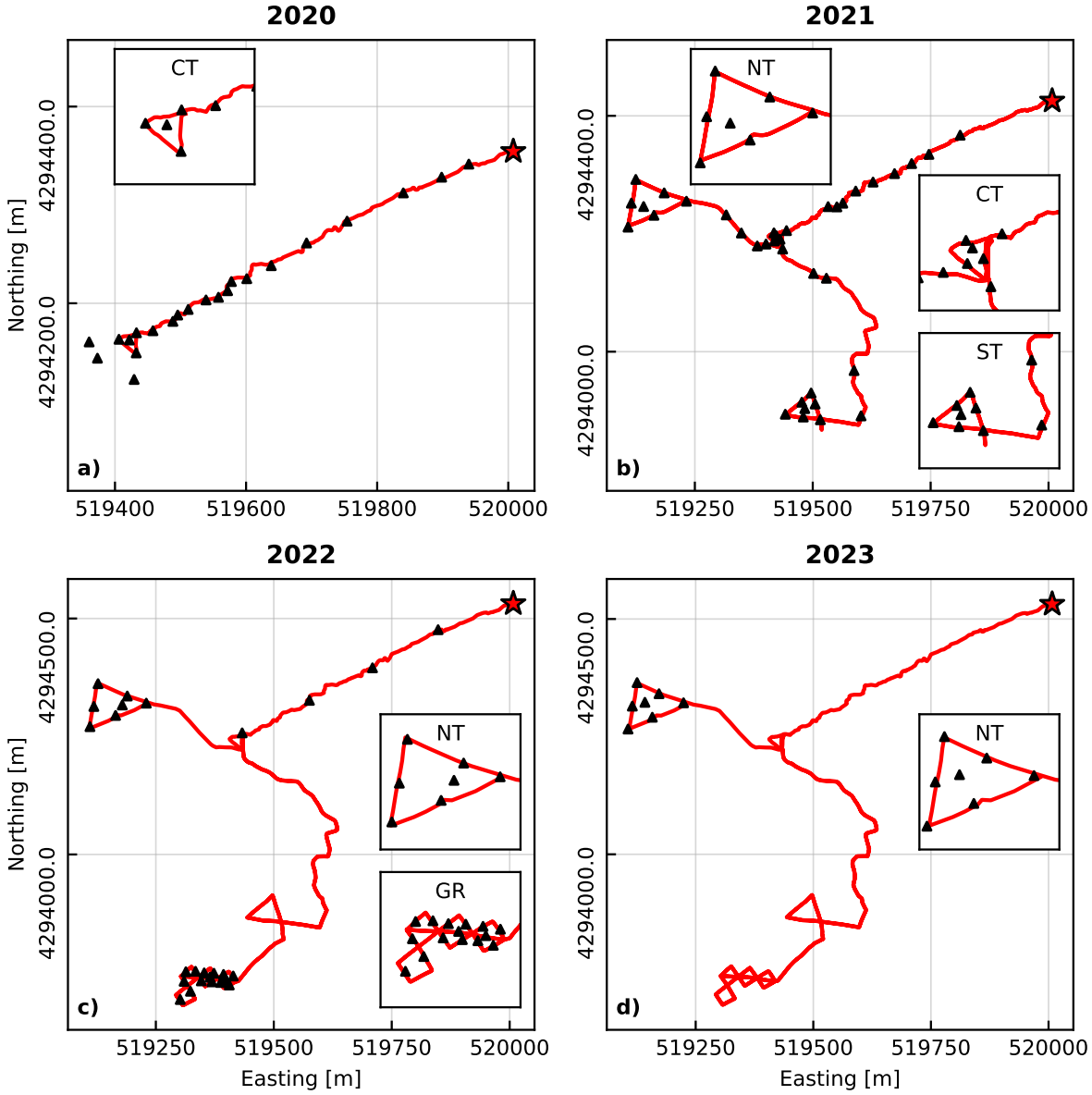

Figure 3.3: Fibre layout and node deployment during each experiment.

Experiment	Start date	End date	Duration [days]	Data size [TB]	Fibre installation	Probed fibre length [km]	Gauge length [m]	Dx [m]	F [Hz]	Events recorded	Co-located instruments
2020	2020/9/15	2020/09/23	2.3	2	Trenched into soil (15-30 cm)	1	5	2.4	2000	Ordinary activity.	22 SmartSolo IGU-16HR 5-Hz 3C nodes (of which 8 at CT). One 30s 3C Guralp CMG-40T (at CT).
2021	2021/9/16	2021/10/20	27.1	20	Trenched into soil (15-30 cm)	6	5	2.4	400	Ordinary activity and one major explosion (2021/10/06).	36 SmartSolo IGU-16HR 5-Hz 3C nodes, divided in several sub-arrays (at CT, NT, and ST). Three 30s 3C Guralp CMG-40T (at CT, NT, and ST).
2022	2022/9/15	2023/1/30	95.7	16	Trenched into soil (15-30 cm)	6	10	2	50	Ordinary activity, two major explosions (2022/09/29, 2023/01/30), two PDCs (2022/10/09, 2022/12/04), and four lava overflows (2022/10/09, 2022/11/16, 2022/12/04, 2022/12/13).	26 SmartSolo IGU-16HR 5-Hz 3C nodes, divided in several sub-arrays (at NT and GR).
2023	2023/9/25	2023/10/20	19.5	8	Trenched into soil (15-30 cm)	6	10	2	100	three lava overflows (2023/09/27, 2023/10/03, 2023/10/06).	7 SmartSolo IGU-16HR nodes at NT. 67 1-Hz 1C Stryde nodes (at NT).

Table 3.1: Overview of all the DAS experiments that have been performed at Stromboli between 2020 and 2023. Dx denotes the DAS channel spacing and f denotes the sampling frequency.

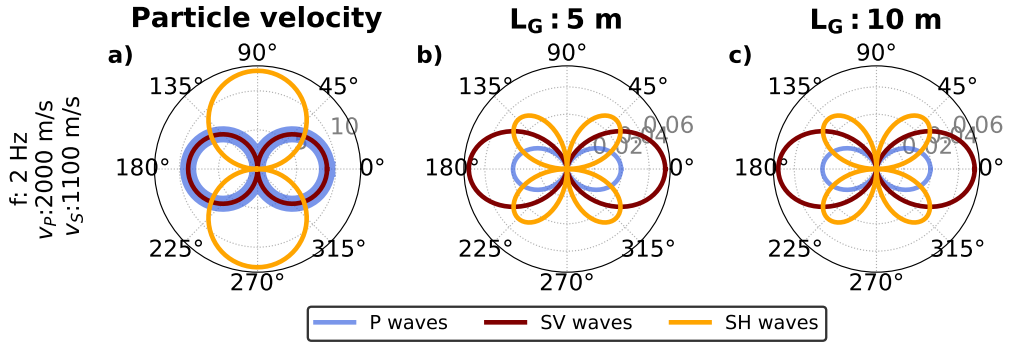

Figure 3.4: Theoretical sensitivity patterns of seismometers (a) and DAS with a gauge length of 5 m (b) and 10 m (c) for P (blue), SV (purple), and SH (yellow) waves with velocities V_P = 2000 m/s and V_S = 1140 m/s and a frequency of 2 Hz. The vertical incidence angle of the waves is 45°.

1 Hz of sampling rate. The visible camera LBZ is a visible FOSCAM camera with 4 mm of focal length, horizontal and diagonal fields of view of 70° and 75°, respectively and a 2 s sampling rate. The thermal camera (ROC) is a FLIR-A20 camera fitted with a $34° \times 25°$ optical lens (9.2 mm), having $0.1°C$ thermal resolution and 2 Hz of sampling rate (Ripepe, Delle Donne, et al., 2021).

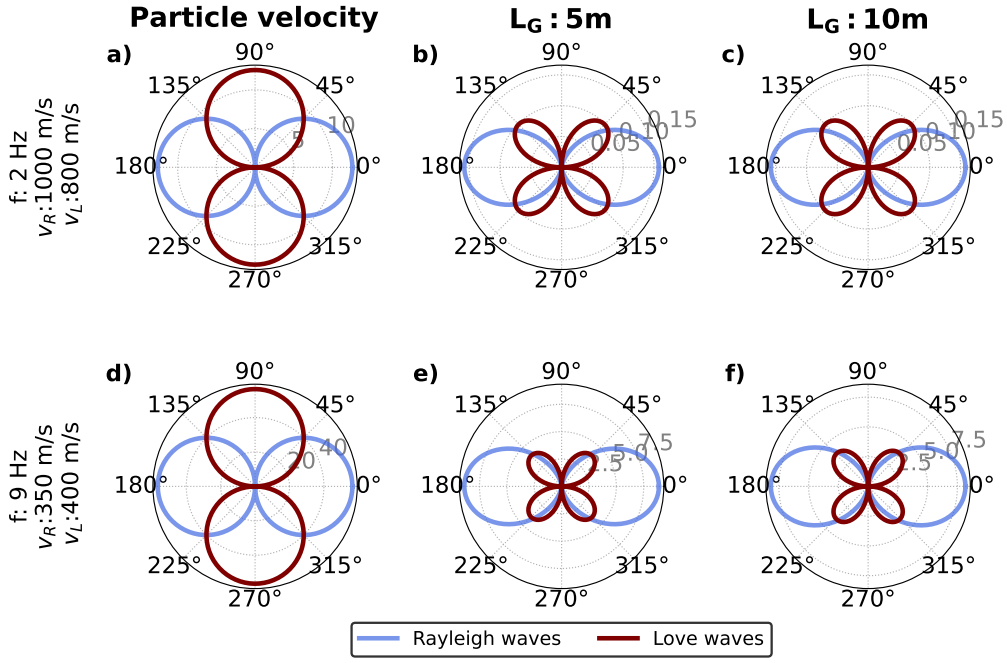

Figure 3.5: Theoretical sensitivity patterns of particle velocity (a,d) and DAS strain rate with a gauge length of 5 m (b,e) and 10 m (c,g) for Rayleigh (blue) and Love (purple) waves. In the first row (a-c), we use velocities of Rayleigh and Love waves of V_R = 1000 m/s and V_L = 800 m/s, respectively, at 2 Hz. In the second row (d-f), we use velocities V_R = 350 m/s and V_L = 400 m/s at 9 Hz.

3.4 Sensitivity patterns for wavelenghts observed at stromboli

We configured our DAS acquisitions with gauge lengths L_G of 5 m (2020 and 2021) and 10 m (2022 and 2023). For wavelengths λ larger than L_G, the gauge length has little impact on DAS recordings, and theoretical response patterns closely resemble those of point-wise strain measurements (shown in Fig. 1.5c,d), depending mainly on cable geometry (Martin, 2018). However, as the wavelength approaches L_G, the gauge length effects become significant, introducing additional notches and lobes in the sensitivity pattern (Martin, 2018; Näsholm et al., 2022). We briefly assess whether our chosen gauge lengths are valid for capturing the wavefield at Stromboli.

Seismic array measurements by Chouet et al. (1997) show that the wavefield of tremor and explosions at Stromboli consists of a complex mix of body and surface waves, with body waves dominant between 0.5-2.5 Hz and surface waves above 2.5 Hz. Chouet et al. (1998) report P and S wave velocities of 2000 m/s and 1140 m/s, respectively, at 90 m depth. Using these values and a frequency of 2 Hz, we applied the equations from Martin (2018) (Table 2.2) to compute sensitivity patterns for P, SV and SH waves, which produced favourable results (Fig. 3.4). Besides differences with particle velocity measurements, DAS sensitivity to P and SV waves shows a two-lobed pattern, while SH waves display a four-lobed pattern for the 5 m and 10 m gauge lengths. Furthermore, we observe identical patterns for both gauge lengths.

Chouet et al. (1998) also reported phase velocities for Rayleigh waves between 1000 and 350 m/s and Love waves between 800 and 400 m/s in the 2-9 Hz frequency range.

These values imply minimum wavelengths of about 40 m, a few times larger than the chosen gauge lengths. We computed the sensitivity patterns based on Martin (2018) and present them in Fig. 3.5. In both cases, we confirm that the selected gauge lengths are suitable for accurately recording signals from Strombolian activity.

3.5 Geolocating the DAS channels

Channel geolocation is an essential step for most DAS applications and is crucial to apply array analysis on strain rate data (Biondi et al., 2022). While DAS provides the distance of each channel from the interrogator, their exact geographical locations are often unknown. Already deployed telecom fibres pose additional challenges for geolocation due to complex geometries, poor mapping, and possible spare cable coiling, whereas fibres installed for specific experiments are usually better mapped (Biondi et al., 2022).

A typical geolocation method is "tap testing" (Klaasen et al., 2021; Biondi et al., 2022; Jousset et al., 2022), which uses localised active sources (e.g., jumps, taps, weight drops, or hammer strikes) along the fibre to identify the nearest DAS channels and interpolate the others. For longer fibre deployments, alternative methods like using seismic signals from tracked vehicles have been proposed (Biondi et al., 2022).

Our DAS geolocation procedure combines precise GPS tracking during the fibre installation with tap testing afterwards. Fig. 3.6 summarises the workflow. During each deployment, we first conducted a kinematic GPS survey using two Leica GR25 receivers. One receiver was placed at the UniFi Geophysical Observatory for continuous recording, while we used the other to track the fibre layout and geolocate tap tests. As we laid the fibre in the trench, we recorded its GPS position and the positions of specific points approximately every 10 m (Fig. 3.6a). At these points, we also measured the incremental distance along the fibre, which is labelled every meter on the cable's outer coating (Fig. 3.6a). These measurements serve as a later validation of the tap test results. Once the fibre was operational, we performed tap tests by jumping at various points along the fibre. We then analyse the strain rate traces to identify the DAS channels closest to each tap, focusing on channels showing the highest amplitudes and earliest arrivals as the closest to each source (Fig. 3.6b,c).

We validate these estimates by comparing the distances between DAS channels from tap tests with the actual cable distances recorded at the same locations during the deployment. We then determine the number of DAS channels between each tap test location. After cleaning and smoothing the GPS track, we perform a 3D linear interpolation of the fibre layout between adjacent tap tests to obtain the 3D geographical location of the DAS channels.

To ensure accuracy, we finally calculate the channel spacing between interpolated channels. For instance, if we consider the first fibre branch from the start (OSV) to the CT array (Fig. 3.7a) and an initial DAS channel spacing of 2 m (as in 2022 and 2023), we obtain an average spacing between interpolated channels of 1.98±0.03 m (Fig. 3.7b). The interpolated spacing is consistently less than 2 meters (Fig. 3.7b), likely due to bends and minor fluctuations in the fibre deployment, which reduce the actual 3D distance between channels. The interpolated channel spacing never exceeds the original channel spacing over the entire fibre and shows almost identical values.

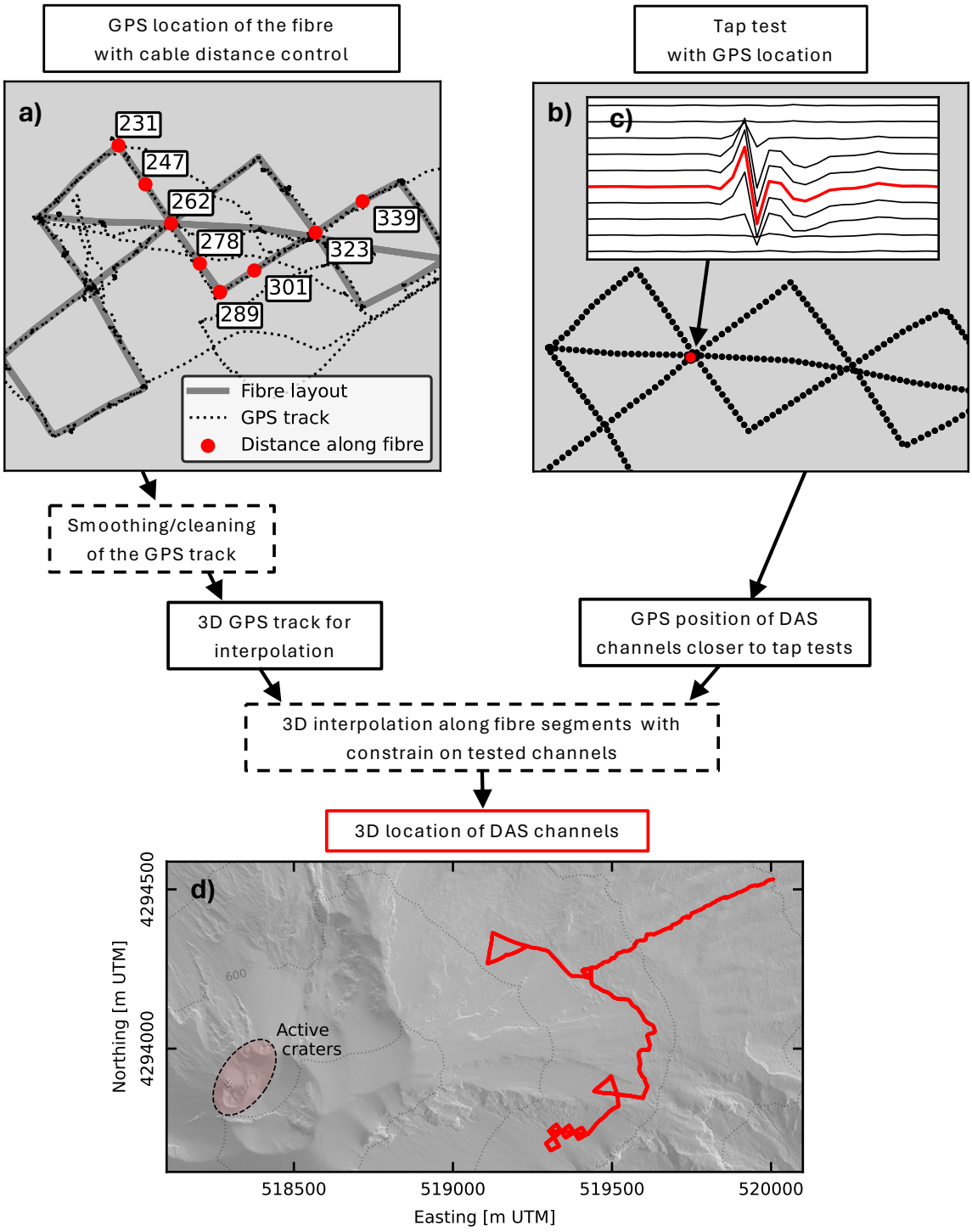

Figure 3.6: Workflow describing the several steps to locate the DAS channels. (a) Geolocation of the fibre layout with a differential GPS. Approximately every 10 m (red dots), we measure the incremental distance along the fibre later used to validate the tap-test locations The solid grey line is the final fibre layout, while the dashed black line is the raw differential GPS track. (b,c) Tap-test location of several DAS channels along the fibre. (c) Shows the strain rate waveforms of one tap recorded at ten DAS channels. The red trace in (c) indicates the channel that we identify as the closest to the tap. (d) Final 3D location of all the DAS channels.

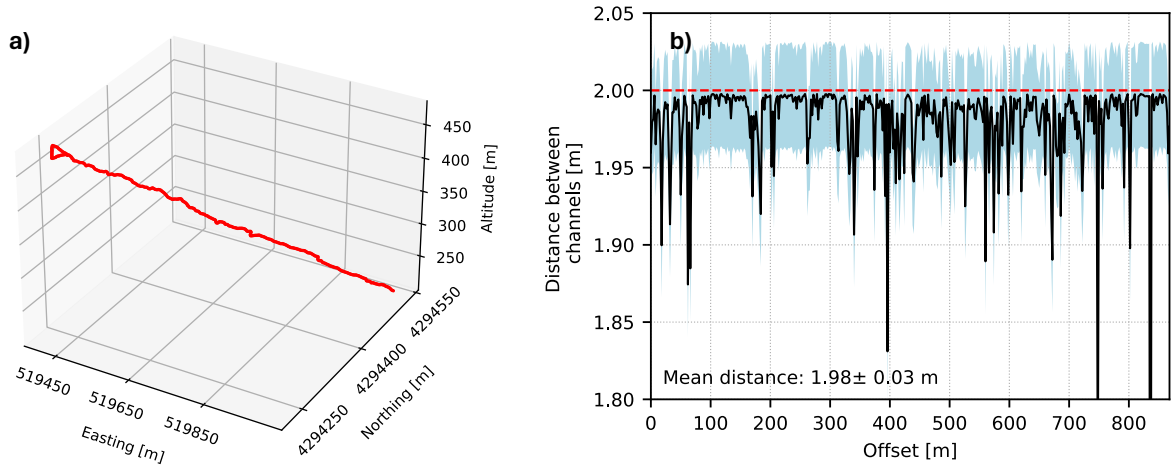

Figure 3.7: (a) 3D location of the lowest branch of our fibre deployment, along the path to the summit. (b) Distance between subsequent DAS channels (in black) and standard deviation (blue interval). With a channel spacing of $\Delta x = 2$ m along the fibre, we measure $\Delta x = 1.98 \pm 0.03$ m. Additionally, the interpolated channel spacing is consistently less than 2 m, likely due to bends and loops reducing the actual 3D distance between channels.

3.6 Data overview

Between 2020 and 2023, we gathered nearly five months of DAS measurements of volcanic activity. Figure Fig. 3.8 shows data availability for each experiment conducted during this period. Most of the time, the volcano displayed an ordinary eruptive regime characterized mainly by volcanic tremor and mild explosions. Occasionally, such activity was interrupted by major explosions (three in total), lava overflows (five in total), and two significant pyroclastic density currents (PDCs), as shown in Fig. 3.8.

We analysed the DAS strain rate data to assess whether our installation successfully captured signals from various volcanic phenomena, i.e. volcanic tremor, ordinary explosions, major explosions, rockfalls and pyroclastic density currents (PDCs). In this section, we provide an overview of different types of phenomena and their recorded signals and briefly explain some of their characteristics. We compare DAS strain rate signals with measurements from broadband seismic sensors and infrasound pressure transducers located at the summit (STR station, Fig. 3.2) and along the Sciara del Fuoco depression (SCI station, Fig. 3.2). For each type of event, we show waveforms in seismic velocity, infrasound pressure and strain rate. We also show the strain rate traces recorded along the entire fibre both in time and frequency domains.

3.6.1 Volcanic tremor

Volcanic tremor is a persistent feature of the seismic wavefield recorded in Stromboli (e.g., Nappi, 1976; Langer & Falsaperla, 1996; Ripepe et al., 1996; Ripepe & Gordeev, 1999). Figure 3.9 shows 15 seconds of tremor (on October 5, 2022) recorded by the STR broadband seismometer (seismic velocity, Z component; Fig. 3.9a) and the DAS (strain rate, channel 912; Fig. 3.9e), along with the infrasound waveform from the STR station during the same period (Fig. 3.9c).

The infrasound trace (Fig. 3.9c) reveals clear infrasonic transients (amplitudes <1

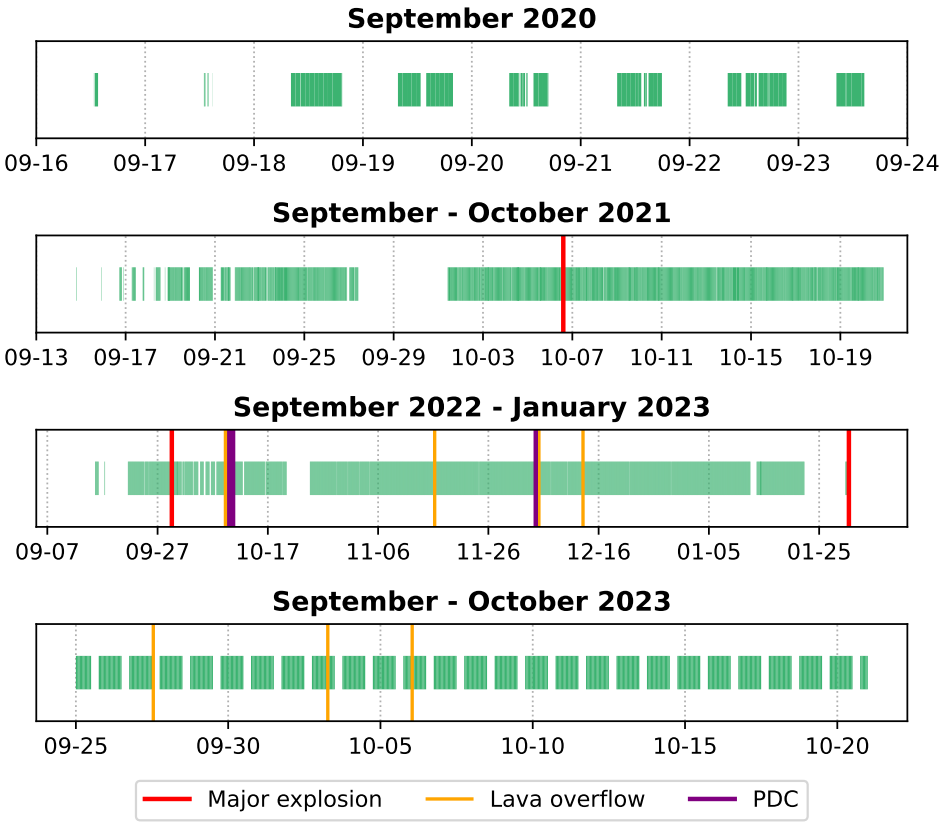

Figure 3.8: Data availability of the DAS measurements (in green) during the (a) 2020, (b) 2021, (c) 2022, and (d) 2023 experiments at Stromboli. The red vertical lines indicate major explosions that occurred on 2021/10/06, 2022/09/29, and 2023/01/30. The orange vertical lines indicate lava overflows on 2022/10/09, 2022/11/16, 2022/12/04, 2022/12/13, 2023/09/27, 2023/10/03, and 2023/10/06. The purple vertical lines indicate PDCs that occurred on 2022/10/09, 2022/10/10 and 2022/12/04.

Pa) repeating approximately every 2 seconds. These are due to active degassing processes (puffing) at the vents caused by the coalescence and bursting of small (~0.5-1 m) gas bubbles (Fig. 3.9j; Ripepe et al., 1996; Ripepe & Gordeev, 1999). In contrast, the seismic velocity (Fig. 3.9a) and strain rate (Fig. 3.9e) tremor traces lack impulsive phases or clear arrivals. The strain rate tremor waveform (recorded at channel 912) shows frequencies between 2.5-10 Hz, peaking at 5 Hz (Fig. 3.9f), while the seismic velocity trace is characterised by lower frequencies (<5 Hz, peaking at 2.5 Hz; Fig. 3.9b). Nevertheless, one must consider the difference in distance from the source, which varies from ~500 m for STR to ~1100 m for the DAS 912 channel and possibly influences the propagating wavefield.

Both time (Fig. 3.9g) and frequency (Fig. 3.9h) domain representations of the DAS strain rate waveforms recorded over the entire fibre highlight distinct zones with varying site responses. Certain sections of the fibre (e.g., offsets <600 m) show lower amplitudes and higher frequencies (5-10 Hz), while others (offsets 600-1400 m or 1600-1800 m) exhibit significantly higher amplitudes (up to an order of magnitude) and frequencies as low as ~2 Hz.

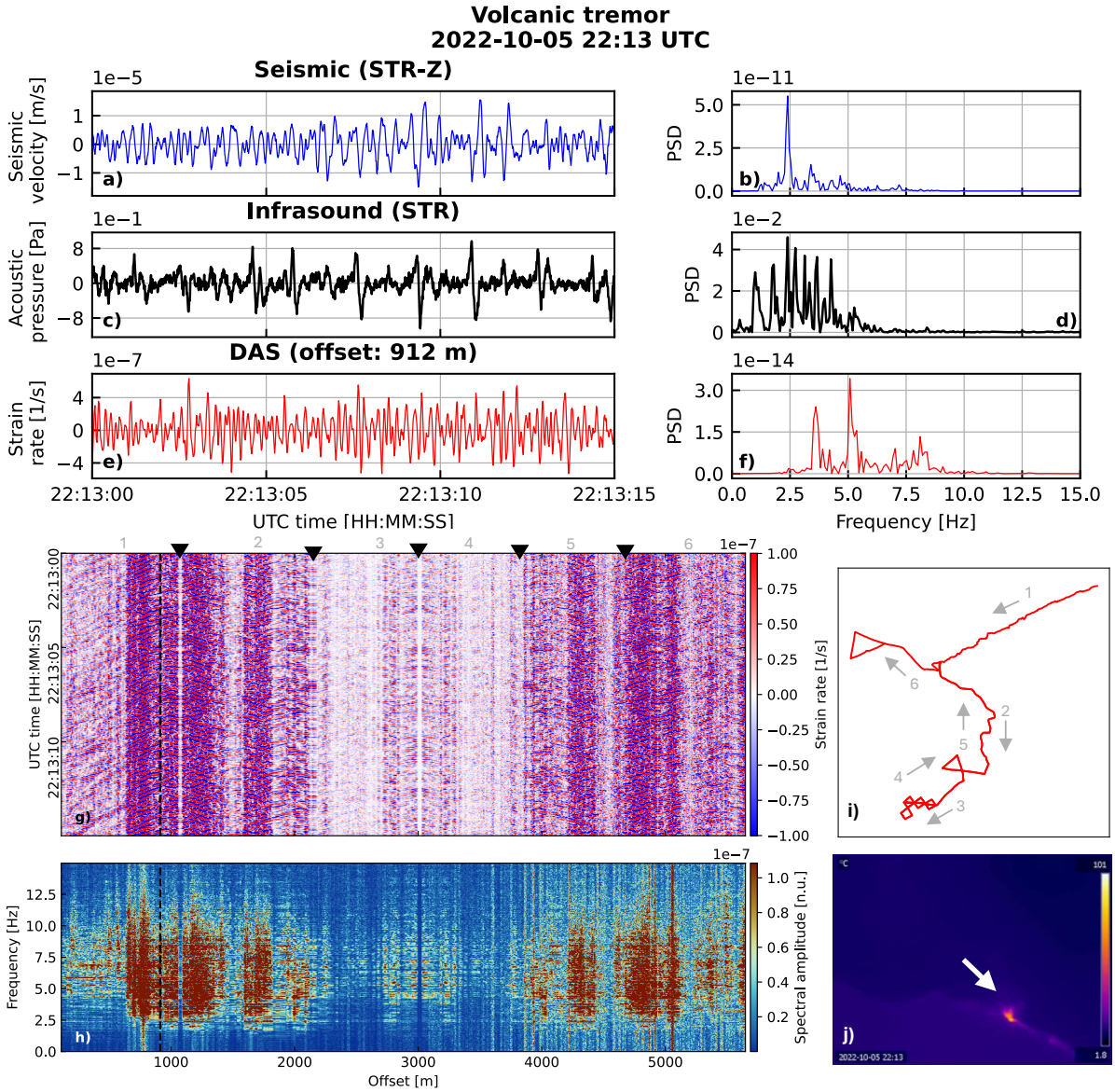

Figure 3.9: (a) Seismic velocity trace (Z component, blue) of 15 seconds of volcanic tremor recorded by the broadband seismometer STR (Fig. 3.2a) on 2022/10/05 at approximately 22:13 UTC. (b) Power spectral density (PSD) of the ground velocity from (a). (c) Infrasonic pressure trace (black) recorded by the STR station. We observe several pressure transients (puffing) repeating every 1-2 s. (d) PSD of the pressure trace in (c). (e) DAS strain rate trace (red) recorded at channel 912. (f) PSD of the strain rate in (e). (g) Strain rate record along the entire 6 km fibre. The vertical dotted line in (g) indicates the position of channel 912 shown in (e). Black triangles above (g) indicate offsets where fibre segments (indicated by grey numbers from 1 to 6) are connected. (h) Frequency domain representation below 15 Hz of the strain rate in (g). (i) Map of the 2022 fibre layout showing the direction of light travel in the cable. (j) Snapshot from the ROC thermal camera during the event, with a white arrow pointing to the active vent in the NE crater area responsible for the puffing activity observed in (c).

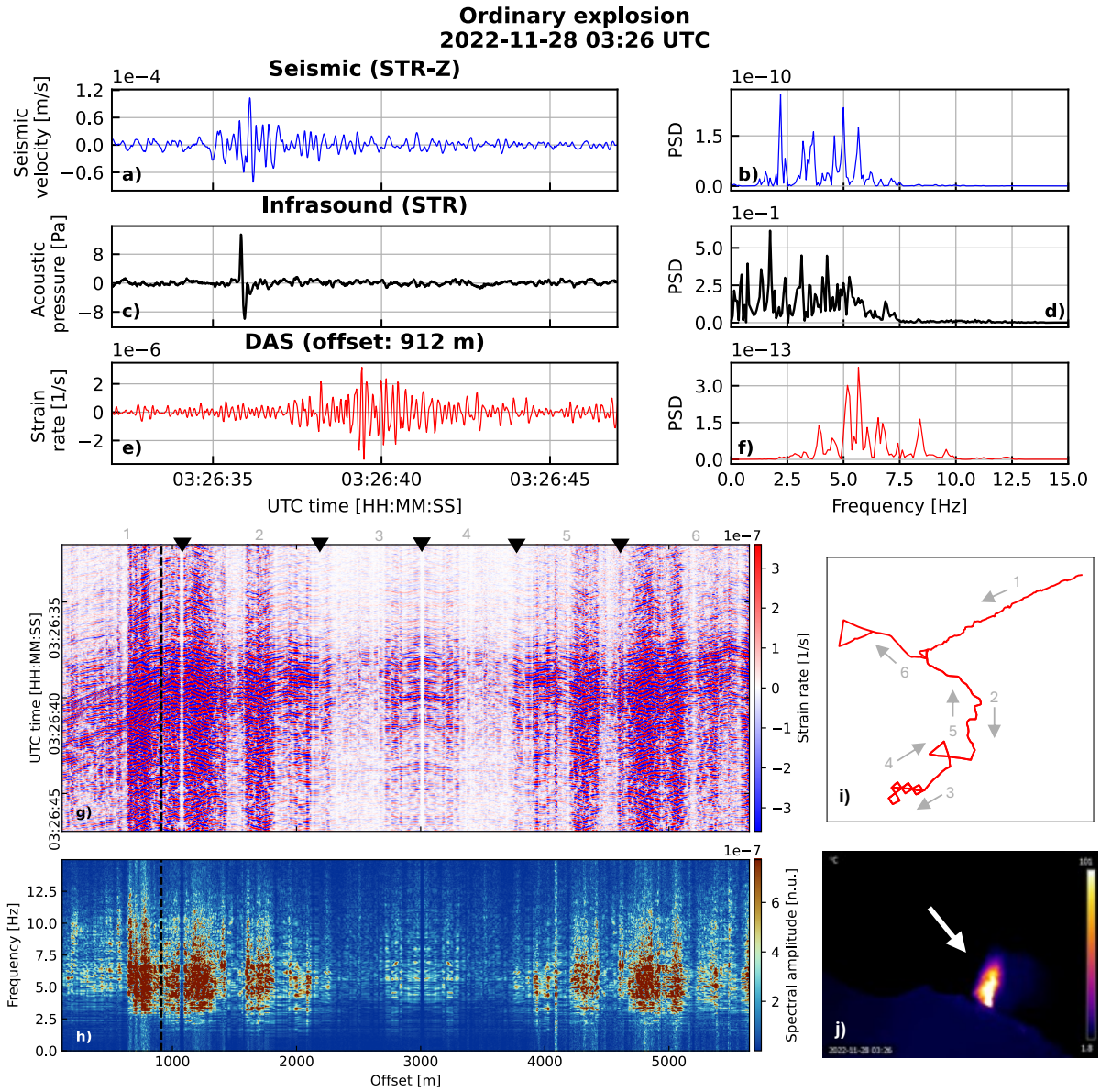

Figure 3.10: (a) 15 s seismic velocity trace (Z component, blue) recorded by the broadband seismometer STR (Fig. 3.2a) during a volcanic explosion on 2022/11/28 at approximately 03:26 UTC. (b) Power spectral density (PSD) of the ground velocity from (a). (c) Infrasonic pressure trace (black) recorded by the STR station. (d) PSD of the pressure trace in (c). (e) DAS strain rate trace (red) recorded at channel 912. (f) PSD of the strain rate in (e). (g) Strain rate record along the entire 6 km fibre. The vertical dotted line in (g) indicates the position of channel 912 shown in (e). Black triangles above (g) indicate offsets where fibre segments (indicated by grey numbers from 1 to 6) are connected. (h) Frequency domain representation below 15 Hz of the strain rate in (g). (i) Map of the 2022 fibre layout showing the direction of light travel in the cable. (j) Snapshot from the ROC thermal camera during the event, with a white arrow pointing to the explosion.

3.6.2 Ordinary explosion

During our experiments, the volcanic activity was mainly ordinary and characterised by frequent and mild explosions. Here, we focus on one explosive event on November 28, 2022, at 03:26:35 UTC. As shown in Fig. 3.10j, the explosion originated from the NE crater and produced a short-lived, ~70 m high jet of hot material. The seismic velocity trace from the STR summit station (Z component) reveals an initial low-frequency signal lasting 2 seconds, followed by a higher-frequency coda, with a maximum amplitude of 1×10^{-4} m/s (Fig. 3.10a). The explosion-generated seismic signal at STR predominantly spans frequencies between 1-7 Hz (Fig. 3.10b). An infrasonic pulse of ~14 Pa (approximately seven times higher than the transients in Fig. 3.9) was also detected at STR at around 03:26:36 UTC (Fig. 3.10c).

The strain rate signal recorded at DAS channel 912 during this explosion exhibits a maximum amplitude of 3×10^{-6} 1/s (Fig. 3.10e) and higher frequencies (2.5-10 Hz) than the seismic velocity at STR, lacking resolution below ~2.5 Hz (Fig. 3.10f). The infrasonic pressure wave is also observed in the signals from DAS channel 912, arriving approximately 2.4 seconds after its detection at STR (indicated by the black arrow in Fig. 3.10e). In Fig. 3.10g, the pressure wave is observed propagating along the entire fibre, especially in sector 1 (offsets below 600 m), with apparent velocities of ~340-370 m/s. This wave overlays others travelling at higher apparent velocities (~600-700 m/s) within the same sector. As previously mentioned, certain sections of the fibre exhibit significantly higher amplitudes (and lower dominant frequencies) compared to others, suggesting that local site effects play a role in influencing the DAS measurements (Fig. 3.10g,f).

3.6.3 Major explosion

Major explosions are intense explosive events occurring approximately twice per year over the past 25 years (Bevilacqua et al., 2020). These explosions pose a considerable hazard to residents, tourists, and scientists on the island. In Fig. 3.11, we present the seismic velocity, acoustic pressure, and strain rate signals produced by the major explosion that occurred on 6 October 2022 at 14:17:45 UTC. This event differs from ordinary explosions, ejecting large quantities of hot material across the crater area, over a width of about 300 m (Fig. 3.11j).

The seismic velocity (STR station, Z component) and strain rate (channel 912) traces generated by the explosion exhibit peak amplitudes of 2×10^{-3} m/s and 5×10^{-5} 1/s, respectively (Fig. 3.11a,e) with dominant frequencies between 2 and 6 Hz (Fig. 3.11b,f). Notably, the seismic velocity signal (Fig. 3.11a) displays a 3-second low-frequency onset prior to the arrival of the infrasonic pressure wave, a feature absent in the strain rate waveforms. The explosion generated an infrasonic pressure wave with an amplitude of approximately 300 Pa, recorded at the STR station (3.11c). This pressure wave propagated along the entire fibre at a speed of 340 m/s (yellow line in Fig. 3.11g) and was recorded by the DAS generating the most energetic phase in the strain rate recordings.

The amplitudes of the strain rate, seismic velocity, and acoustic pressure signals are approximately ten times higher than those from a typical explosion (Fig. 3.10) and a hundred times higher than those linked to volcanic tremors (Fig. 3.9). Moreover, the amplitudes of the strain rate signals generated by the major explosion show marked variability along the fibre (Fig. 3.11g,h), as previously mentioned. However, the dominant frequencies observed along the cable are slightly different from those of the ordinary

explosion (Fig. 3.10). Specifically, the lower part of sector 1 (for offsets <600 m) shows dominant frequencies of 7.5-10 Hz, compared to 5-7.5 Hz for the ordinary explosion.

3.6.4 Rapid gravity-driven mass movements

Landslides of small to medium scale typically occur at Stromboli, primarily along the Sciara del Fuoco depression (SdF). These result from the continuous deposition of volcanic material from explosive or effusive eruptions on steep slopes, usually manifesting as rockfalls and gravel flows (Falsaperla et al., 2006; Di Traglia, Calvari, et al., 2023). However, more severe landslides involving volumes exceeding 10^6 m^3 can occur due to volcanic activity. These events also include PDCs triggered by paroxysmal explosions or the collapse of hot material from the crater rim. Signals from rockfalls and PDCs tend to last longer than those from explosions, with emergent, spindle-shaped waveforms lacking clear onsets and characterised by higher frequencies. Below, we present examples of seismo-acoustic signals from rockfalls and PDCs. In addition to the STR station, we also show seismic velocity signals (Z component) recorded at the SCI station. This station is installed on the edge of the SdF (Fig. 3.2) and serves for monitoring slope instability.

Rockfall

Figure 3.12 shows the signals generated by a small-scale rockfall on 25 October 2022 at 12:20 UTC. The event lasted around 120 s and was characterised by material travelling down the SdF, eventually reaching the sea (3.12j). The seismic velocity (Fig. 3.12a) and strain rate traces (Fig. 3.12e) display longer durations (~100 s) compared to waveforms from explosive events (~15-30 s). The seismic velocity trace from the STR station shows lower amplitudes than those from the SCI station along the SdF (and closer to the source), which peaked at approximately ~3×10^{-5} m/s. The DAS strain rate waveform (channel 912) mirrors the seismic signal (SCI station) in shape and has amplitudes of 5×10^{-7} 1/s. Strain rate signals recorded along the fibre have higher frequencies (up to 12 Hz) than those from explosive events (Figs. 3.10 and 3.11), and their frequency content (Fig. 3.12f,h) is similar to that of the SCI station (Fig. 3.12b), with comparable spectral peaks. Nevertheless, as visible in Fig. 3.12g,h, after around 4 km of fibre (sectors 5 and 6 in Fig. A), the DAS waveforms are heavily affected by noise, making it difficult retrieve the seismic wavefield.

Pyroclastic density current

Fig. 3.13 displays the seismo-acoustic signals from a PDC that occurred at Stromboli on 9 October 2022, around 07:22 UTC. The PDC was triggered by the partial collapse of the NE crater rim (Giudicepietro et al., 2023) and reached the sea in approximately 30 seconds, travelling at an average speed of ~40 m/s. Upon reaching the water, it generated an 8 cm tsunami wave.

Both the seismic velocity (SCI, Fig. 3.13a) and strain rate (channel 912, Fig. 3.13e) signals have spindle-shaped, emergent onsets with durations of around 120 s. The amplitudes of the seismic velocity and strain rate traces (~4×10^{-4} m/s and ~5×10^{-6} 1/s, respectively) are about ten times greater than those of the rockfall event on 25 October 2022 (Fig. 3.12). This difference is also evident in visual observations captured by the

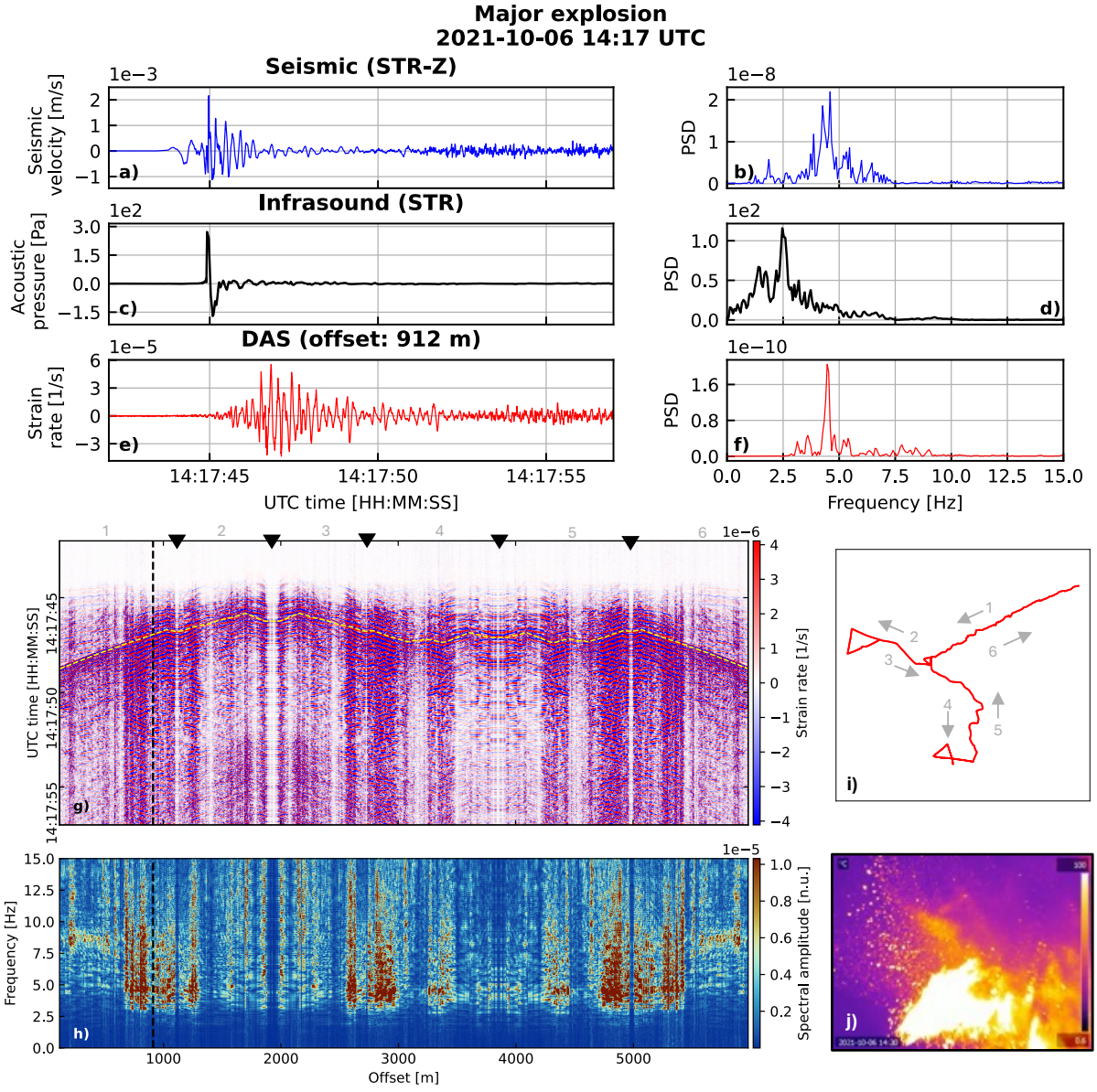

Figure 3.11: (a) 15 s seismic velocity trace (Z component, blue) recorded by the broadband seismometer STR (Fig. 3.2a) during a major explosion on 2021/10/06 at approximately 14:17 UTC. (b) Power spectral density (PSD) of the ground velocity from (a). (c) Infrasonic pressure trace (black) recorded by the STR station. (d) PSD of the pressure trace in (c). (e) DAS strain rate trace (red) recorded at channel 912. (f) PSD of the strain rate in (e). (g) Strain rate record along the entire 6 km fibre. The dashed yellow line in (g) marks the theoretical arrival times at the several channels of an infrasonic pressure wave propagating from the active craters at 340 m/s. The vertical dotted line in (g) indicates the position of channel 912 shown in (e). Black triangles above (g) indicate offsets where fibre segments (indicated by grey numbers from 1 to 6) are connected. (h) Frequency domain representation below 15 Hz of the strain rate in (g). (i) Map of the 2021 fibre layout showing the direction of light travel in the cable. (j) Snapshot from the ROC thermal camera during the event.

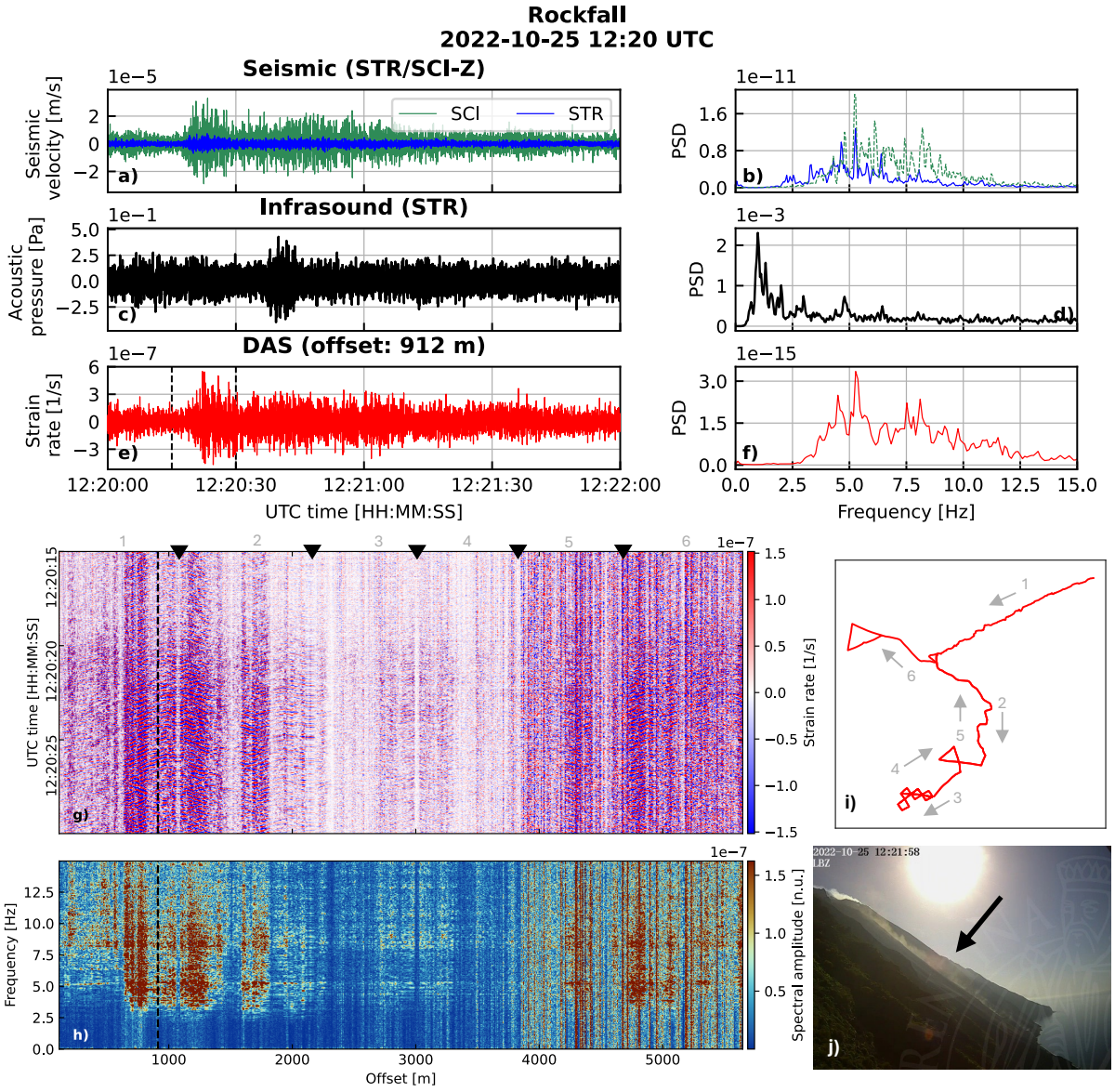

Figure 3.12: (a) 2 minutes of seismic velocity traces (Z component) recorded by the broadband seismometers STR (blue) and SCI (teal) (Fig. 3.2a) during a rockfall that occurred on 2022/10/25 at approximately 12:20 UTC. (b) Power spectral density (PSD) of the ground velocities from (a). (c) Infrasonic pressure trace (black) recorded by the STR station. (d) PSD of the pressure trace in (c). (e) DAS strain rate trace (red) recorded at channel 912. (f) PSD of the strain rate in (e). (g) 15 s strain rate record along the entire 6 km fibre. The vertical dotted line in (g) indicates the position of channel 912 shown in (e). Black triangles above (g) indicate offsets where fibre segments (indicated by grey numbers from 1 to 6) are connected. (h) Frequency domain representation below 15 Hz of the strain rate in (g). (i) Map of the 2022 fibre layout showing the direction of light travel in the cable. (j) Snapshot from the LBZ visible camera during the event, with a black arrow indicating the rockfall along the SdF.

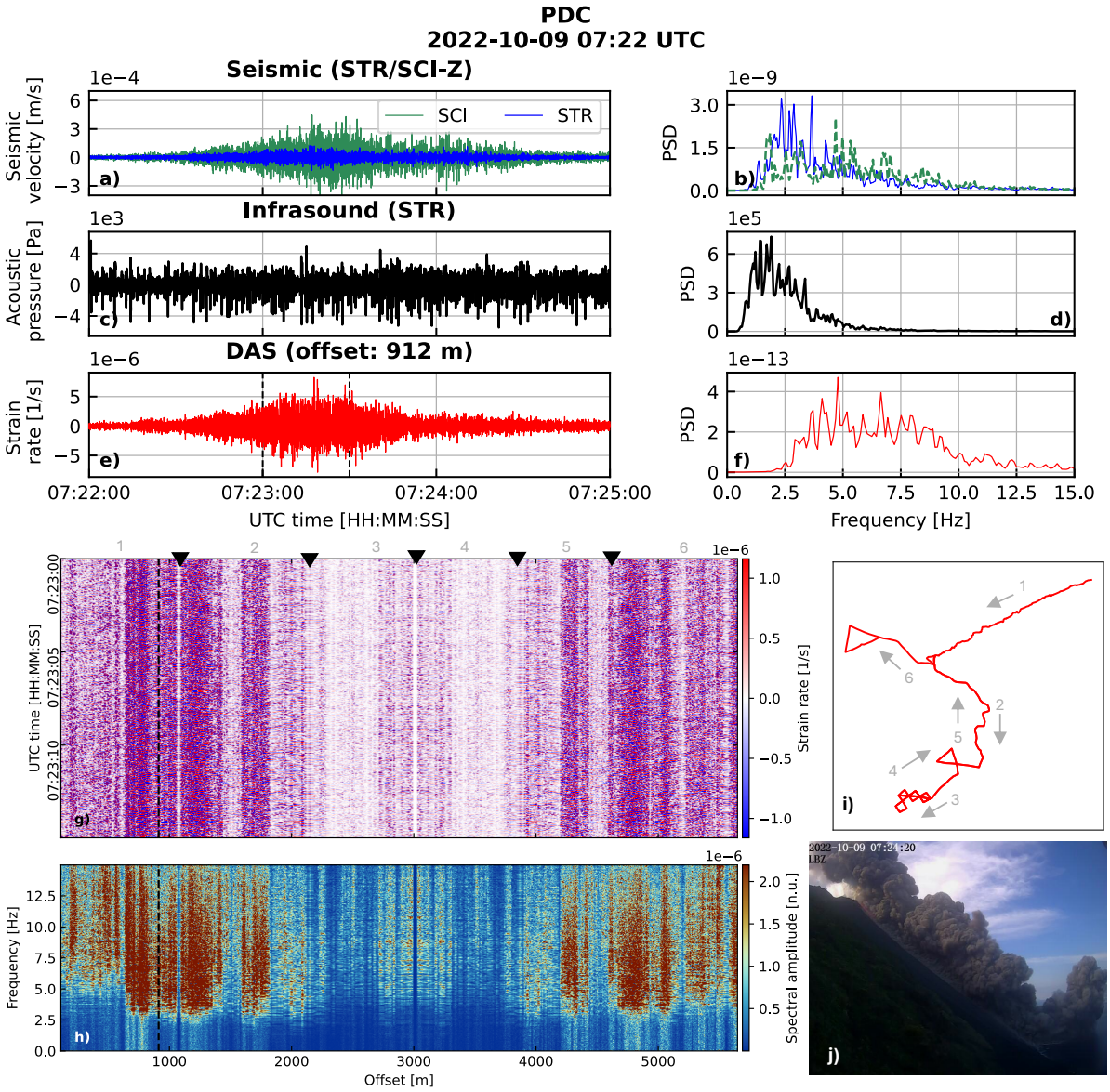

Figure 3.13: (a) 3 minutes of seismic velocity traces (Z component) recorded by the broadband seismometers STR (blue) and SCI (teal) (Fig. 3.2a) during a rockfall that occurred on 2022/10/25 at approximately 12:20 UTC. (b) Power spectral density (PSD) of the ground velocities from (a). (c) Infrasonic pressure trace (black) recorded by the STR station. (d) PSD of the pressure trace in (c). (e) DAS strain rate trace (red) recorded at channel 912. (f) PSD of the strain rate in (e). (g) 15 s strain rate record along the entire 6 km fibre. The vertical dotted line in (g) indicates the position of channel 912 shown in (e). Black triangles above (g) indicate offsets where fibre segments (indicated by grey numbers from 1 to 6) are connected. (h) Frequency domain representation below 15 Hz of the strain rate in (g). (i) Map of the 2022 fibre layout showing the direction of light travel in the cable. (j) Snapshot from the LBZ visible camera during the event showing the PDC propagating along the SdF.

LBZ camera (Figs. 3.13j and 3.12j), highlighting the contrast between the two phenomena. Even for this event, DAS signals exhibit high frequencies, ranging from 3 to 15 Hz (Fig. 3.13f,h), similar to those recorded by the SCI broadband station (Fig. 3.13b). No infrasonic signals were detected from the PDC, though the infrasound record (Fig. 3.13c) is dominated by high-amplitude (5 Pa) pressure transients from intense spattering at the NE craters during the PDC (Giudicepietro et al., 2023).

A more detailed analysis of this PDC and its associated signals is provided in Chapter 6, focusing on DAS strain rate array analysis of PDCs at Stromboli.

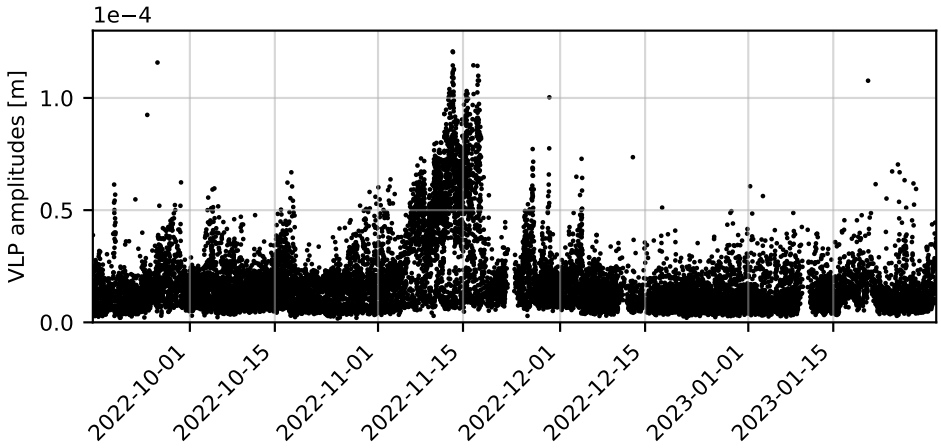

Figure 3.14: From 2022/09/15 to 2023/02/01, VLP amplitudes (in seismic displacement) recorded at the UniFi STR broadband station (Fig. 3.2a) reach maximum values between approximately November 10 and 20, 2022.

3.7 DAS measurements of VLP signals

In the previous section, we briefly introduced the various signals generated by volcanic activity, whether explosive or related to slope instability. In this section, we focus on and discuss DAS strain rate recordings of syn-eruptive VLP signals at Stromboli. VLPs are distinctive seismic features observed at several volcanoes with varying behaviour and magmatism (e.g., Ohminato et al., 1998; Almendros et al., 2002; Hidayat et al., 2002; Chouet et al., 2010; Ripepe, Delle Donne, et al., 2021). They are associated with fluid movement and are crucial for understanding magma and fluid dynamics beneath volcanoes (Ripepe, Delle Donne, et al., 2021). VLP have frequencies down to 0.01 Hz, and their amplitudes drop sharply with distance from the craters, meaning they are primarily observed within a few kilometres from the source (Chouet et al., 2003; Ripepe, Delle Donne, et al., 2021).

At Stromboli volcano, VLPs are frequently recorded and deeply linked with its explosive regime, representing the evidence of an efficient degassing mechanism of the magmatic column (Neuberg et al., 1994; Kirchdörfer, 1999; Wielandt & Forbriger, 1999; Chouet et al., 2003; Ripepe, Delle Donne, et al., 2021). VLPs at Stromboli mainly lie in the 0.01-0.2 Hz frequency range, have simple waveforms and a marked rectilinear polarisation pointing towards the active craters, typical of P-waves (Kirchdörfer, 1999; Chouet et al., 2003; Ripepe, Delle Donne, et al., 2021). Moreover, VLPs have wavelengths of tens of kilometres (Ripepe, Delle Donne, et al., 2021).

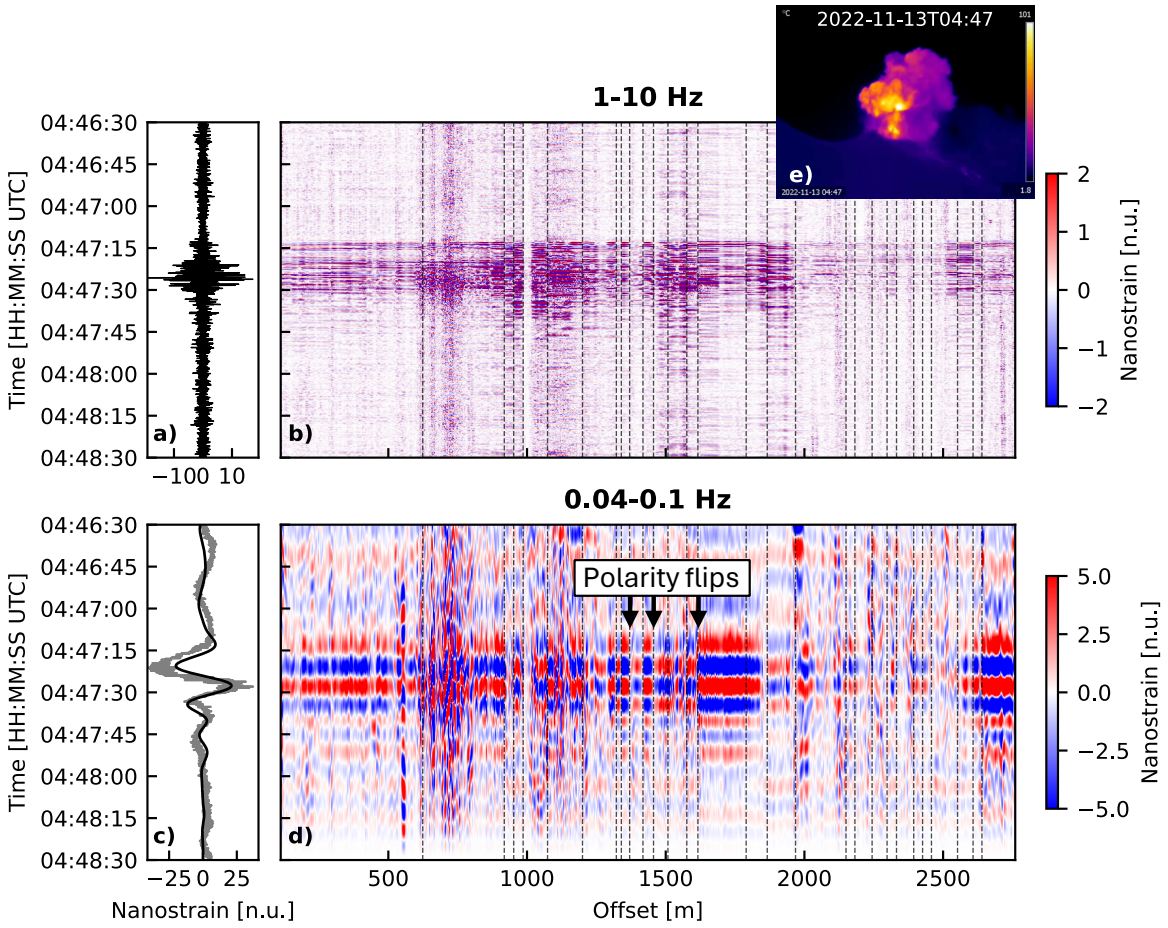

Figure 3.15: (Top row) 2 minutes strain measurements of an explosion occurred on 2022/11/13 at 04:47 UTC filtered between 1-10 Hz recorded by (a) single DAS channel (offset 1730 m) and (b) along the entire fibre. (Bottom row) Same as in (a,b) but filtered between 0.04-0.1 Hz. The grey curve in (c) shows the raw strain waveform at channel 1730. Vertical lines in (b,d) indicate DAS channels corresponding to changes in cable orientation. (e) Frame recorded by the thermal camera during the explosion.

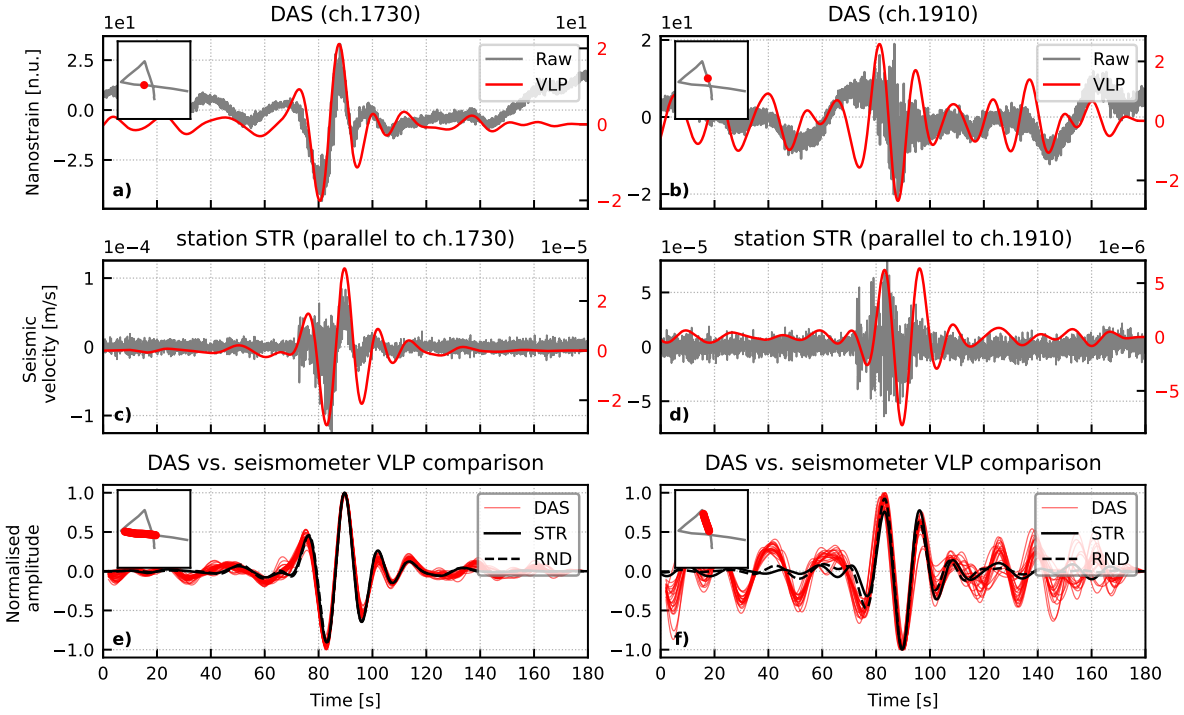

Figure 3.16: (a) 180 s traces of DAS strain recorded at channel 1730 (ST array) during the 13 November 2022 explosion at 04:45:20 UTC. We show both raw (grey) and filtered in the VLP band between 0.04-0.1 Hz (red). (b) Same as (a) but considering the DAS channel 1910. (c) 180 s particle velocity traces recorded at the UniFi STR station (Fig. 3.17) along the direction (~263°) of the DAS channel 1730 (a). The grey and red traces respectively indicate raw and VLP (0.04-0.1 Hz) signals. (d) Same as (c) but considering the seismic signal along the direction of the DAS channel 1910 (~161°). (e) Normalised VLP strain traces recorded at channels 1700-1780 (red), overlaid with normalised seismic velocity records from the STR and RND broadband stations (Fig. 3.17) rotated along the same direction (black). (f) Same as (e) but considering the traces recorded at channels 1876-1920 and the seismic components of the STR and RND stations along the same direction. The maps within (a, b, e, f) show the position of the DAS channels in the ST array (grey line) as red circles.

As discussed in Section 2.3.1, Chouet et al. (2003) modelled VLPs at Stromboli as originating from a fixed dislocating point source using classical seismological methods. They attributed the VLP source to the expansion of a rising gas slug passing through a dyke inclined at ~60°, located at a depth of 220-260 m and roughly 160 m northwest of the active vents beneath the SdF. Conversely, rather than seismic waves from a point-source dislocation, Ripepe, Delle Donne, et al. (2021) and Legrand and Perton (2022) modelled VLPs as quasi-static ground displacement caused by pressure variations in an extended cylindrical conduit within the crater area, partially filled with pressurised magma.

During the DAS experiment in 2022, the volcanic activity was mainly ordinary, with frequent and mild explosions interrupted by episodes of flank instability along the SdF, leading to several PDCs in October and December. Nevertheless, between 5 and 18 November, volcanic tremor and VLP amplitudes surged concurrently with a lava overflow on 16 November. In particular, the amplitude of syn-eruptive VLPs peaked up to almost ten times their average (Fig. 3.14). We then focus on strain records from this period to evaluate DAS's ability to record VLP signals. The linear fibre strain is obtained through integration of the strain rate signals.

Fig. 3.15 shows both the high-frequency (1-10 Hz) and VLP (0.03-0.3 Hz) components

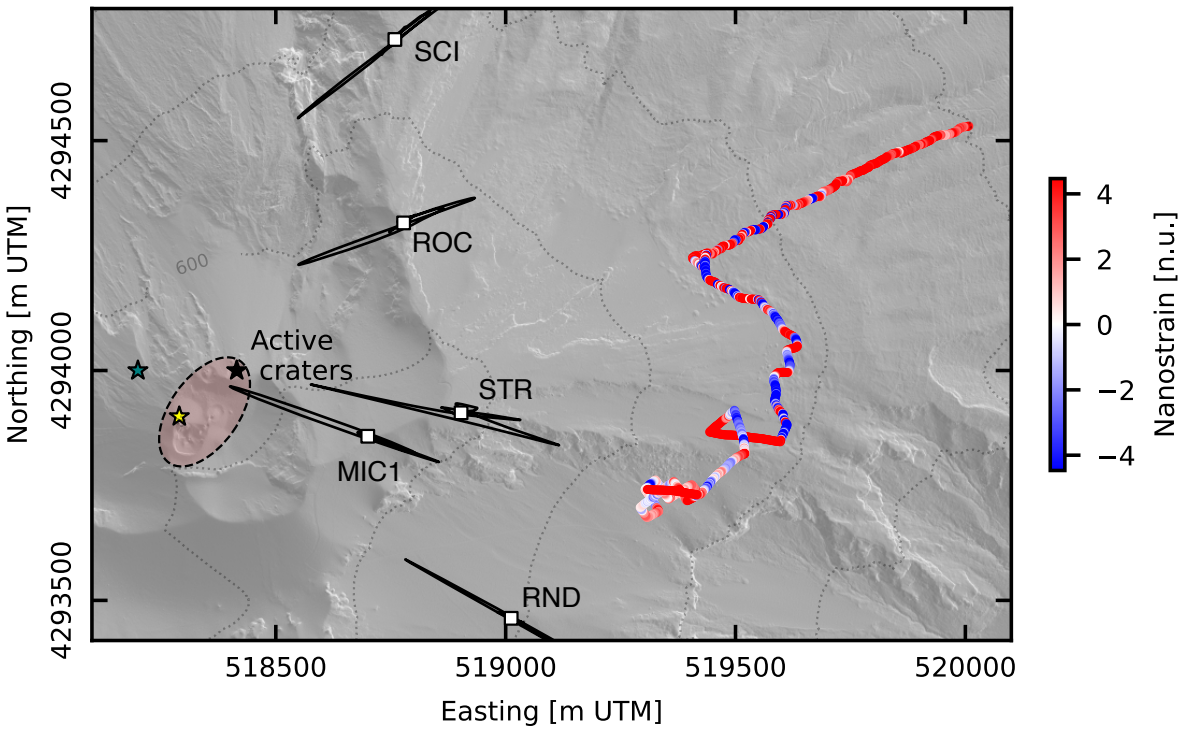

Figure 3.17: Hillshaded view of Stromboli volcano showing the optical fibre layout. Each DAS channel is coloured with respect to the amplitude of the VLP strain signal in Fig. 3.15 at 04:47:25 UTC, i.e. at the midpoint of the waveform. The blue and red colors indicate negative and positive polarities, respectively. White squares represent the permanent UniFi broadband stations. Black lines indicate the horizontal particle displacement of the explosion in Fig. 3.15 in the VLP band. The red area indicate the crater terrace. The yellow and teal stars indicate the position of the VLP source centroid according to Ripepe, Delle Donne, et al. (2021) and Chouet et al. (2003), respectively. The black star indicates the location of the explosion as seen by the thermal camera. The dotted lines are altitude contours every 200 m.

of the seismic wavefield from a mild explosion on 13 November 2022 at 04:47:20 UTC. The explosive event was of mild intensity and generated a short-lived jet of scoria followed by an ash plume (Fig. 3.15e). High-frequency strain waveforms (Fig. 3.15a) exhibit a typical emergent onset and similar features of other VEQs (as the explosion shown in Fig. 3.10). However, raw strain signals (grey trace in Fig. 3.15c) are characterised by a longer period fluctuation superimposed on the higher frequency component. Filtering between 0.04-0.1 Hz reveals clear VLP signals in the DAS record, with simple waveforms and a dominant period of ~10 seconds (black trace in Fig. 3.15c). The strain waveforms in the VLP frequency band in Figs. 3.15 and 3.16 (channel 1730) are characterised by a first low-amplitude positive phase (~5 s) followed by a larger-amplitude negative pulse lasting ~10 s. This second phase is then followed by two additional cycles with decreasing amplitudes. Such VLP strain waveforms are stable at channels across the same linear segment and exhibit an excellent agreement with particle velocity measurements from permanent broadband sensors (e.g., STR and RND) along the same direction (Fig. 3.16).

VLPs are recorded along the entire fibre, showing varying amplitudes. Notably, VLPs recorded at channels corresponding to the areas characterised by higher amplitudes (e.g. those shown in Fig. 3.9g,h) exhibit more distortion and noisier waveforms. Additionally, several polarity inversions in the VLP strain signals align with changes in cable direction

(black vertical lines in Fig. 3.15d). Fig. 3.17 displays different fibre channels coloured according to the strain amplitude at 04:47:25 UTC. The maximum positive amplitudes are recorded at channels radially oriented towards the craters, while the maximum negative ones appear in channels perpendicular to them. Moreover, channels at ~45° to the crater direction show the weakest amplitudes. This pattern is consistent with broadband station data, showing inverted polarity between radial and transverse components to the craters (Fig. 3.16b).

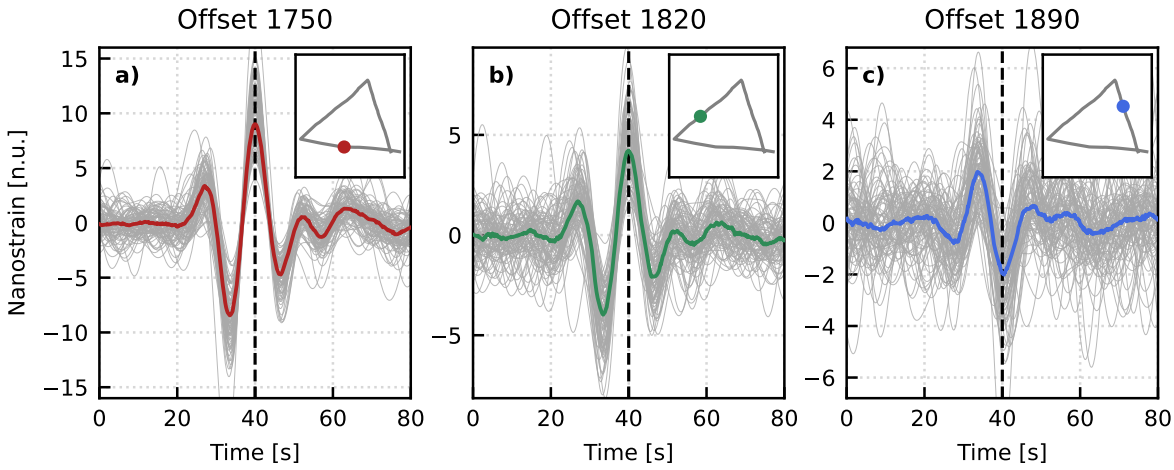

Figure 3.18: Stack (in red, green, and blue) of 95 different VLP strain waveforms (in grey) recorded on 2022/11/13 at three different channels of the ST array: 1750 (a), 1820 (b), and 1890 (c).

Moreover, VLPs show remarkably similar waveforms across multiple events, suggesting a consistent, non-destructive source (Ripepe, Delle Donne, et al., 2021). Fig. 3.18 shows the stacked VLPs from 95 explosions on 13 November 2022, at different fibre offsets in the ST array (1750, 1820, and 1890 m). Channels oriented towards the active craters exhibit higher amplitudes (Fig. 3.18a), while perpendicular channels provide lower amplitudes and reversed polarities (Fig. 3.18c). Furthermore, Fig. 3.19 shows the stack of the 95 VLPs recorded along the entire fibre, exhibiting the same features as Fig. 3.15, but with significantly reduced noise.

Following (Ripepe, Delle Donne, et al., 2021) and (Legrand & Perton, 2022), we suggest that the characteristics of the DAS-recorded VLPs reflect quasi-static strain in the near field, given source-to-receiver distances of ~1 km and wavelengths of tens of kilometres. In the following section, we derive the principal strain axis of one VLP signal using the strain measurements along three fibre segments with different orientations.

3.7.1 Principal strain axis

Measuring linear strain in different directions using DAS enables us to determine the principal axis direction of the strain tensor and the values of the principal strains. Consider the strain tensor Σ near the surface of a homogeneous elastic half-space, as in Fig. 3.20. The principal horizontal direction α and the unknown principal strains ε_{11} and ε_{22} can be derived from three measured linear strains (e_1, e_2, e_3) taken along three different directions (θ_1, θ_2, θ_3; Fig. 3.20). The strain tensor Σ' in a new reference system defined by the rotation matrix R is defined as $\Sigma' = R\Sigma R^T$ (see Section 1.4.3). Thus, the linear

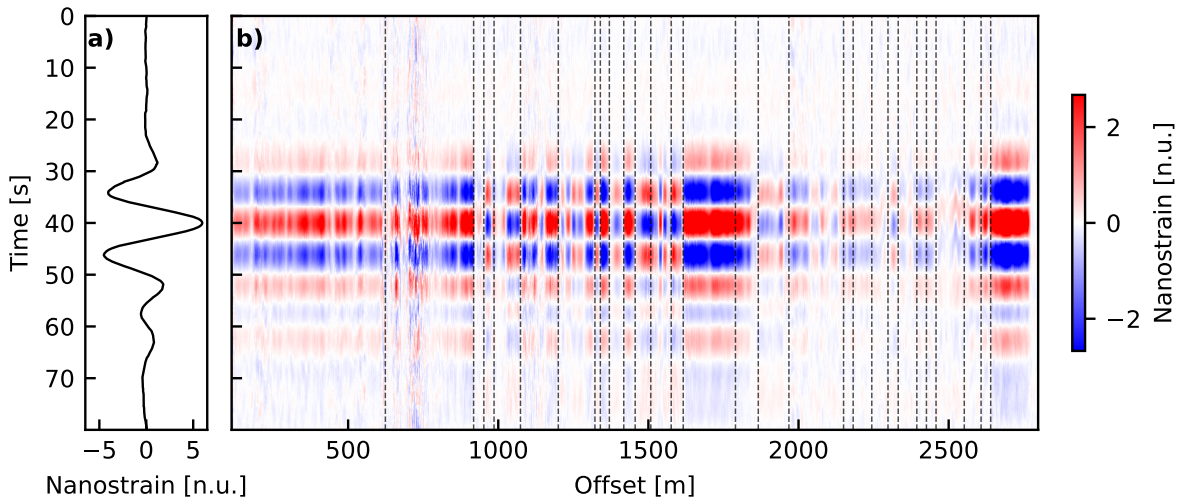

Figure 3.19: (a) Stack of 95 different VLP strain waveforms recorded on 2022/11/13 at the offset 1730 m. (b) VLP strain measurements along 2.8 km of fibre resulting from the stack of 95 VLP signals recorded on 2022/11/13. The vertical dashed lines in (b) indicate changes in fibre direction.

strain e_i in the θ_i direction is expressed as:

$$e_i = C_i\varepsilon_{11} + S_i\varepsilon_{22}, \tag{3.1}$$

being $C_i = cos^2(\theta_i - \alpha)$ and $S_i = sin^2(\theta_i - \alpha)$.

Therefore, following Eq. (3.1), three strain measurements in three different directions (e_1, e_2, and e_3) result in the following system of equations:

$$\begin{cases} e_1 = C_1\varepsilon_{11} + S_1\varepsilon_{22} \\ e_2 = C_2\varepsilon_{11} + S_2\varepsilon_{22} \\ e_3 = C_3\varepsilon_{11} + S_3\varepsilon_{22}. \end{cases} \tag{3.2}$$

Our first goal is to find the principal horizontal direction α. To reduce the number of unknowns and eliminate ε_{11} and ε_{22}, we can divide e_3/e_1 and e_3/e_2. Dividing e_3/e_1 results in:

$$\frac{e_3}{e_1} = \frac{C_3\varepsilon_{11} + S_3\varepsilon_{22}}{C_1\varepsilon_{11} + S_1\varepsilon_{22}}, \tag{3.3}$$

which can be readily converted in the following formulation by bringing all terms to one side:

$$\varepsilon_{11}(e_3C_1 - e_1C_3) + \varepsilon_{22}(e_3S_1 - e_1S_3) = 0. \tag{3.4}$$

Similarly, we can write the ratio e_3/e_2 as:

$$\varepsilon_{11}(e_3C_2 - e_2C_3) + \varepsilon_{22}(e_3S_2 - e_2S_3) = 0. \tag{3.5}$$

Therefore, from Eqs. (3.4) and (3.5), we obtain a system of two equations:

$$\begin{cases} \varepsilon_{11}(e_3C_1 - e_1C_3) + \varepsilon_{22}(e_3S_1 - e_1S_3) = 0 \\ \varepsilon_{11}(e_3C_2 - e_2C_3) + \varepsilon_{22}(e_3S_2 - e_2S_3) = 0 \end{cases} \tag{3.6}$$

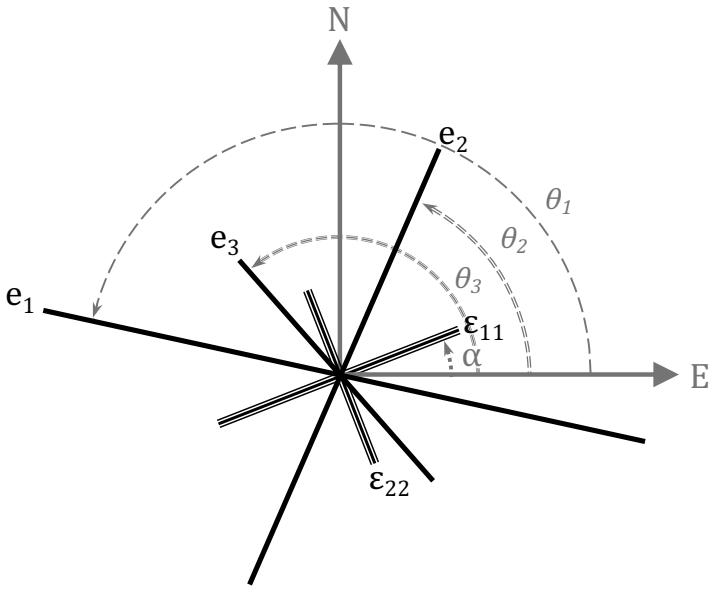

Figure 3.20: Schematic drawing of the two principal unknown strains ε_{11} and ε_{22} (with ε_{11} having an unknown direction α with respect to the East) and the three known linear strains (e_1, e_2, and e_3) along three different directions (θ_1, θ_2, θ_3).

which implies that for non-trivial solutions (both ε_{11} and ε_{22} are not zero), the determinant $D(\alpha)$ of the coeffiecent matrix must be zero, i.e.:

$$D(\alpha) = det \begin{bmatrix} (e_3C_1 - e_1C_3) & (e_3S_1 - e_1S_3) \\ (e_3C_2 - e_2C_3) & (e_3S_2 - e_2S_3) \end{bmatrix} = \tag{3.7}$$

$$= (e_3C_1 - e_1C_3)(e_3S_2 - e_2S_3) - (e_3S_1 - e_1S_3)(e_3C_2 - e_2C_3) = 0. \tag{3.8}$$

The solution can be approximated numerically by varying α from 0° to 359° with a chosen step. Once the angle α has been found, the system of equations (3.2) is over determined and ε_{11} and ε_{22} can be derived via a linear inversion.

To determine the principal strain axis direction and the values of the principal strains, we focus on the VLP generated by the explosion shown in Fig. 3.15 (2022/11/13-04:47:20 UTC). We first integrate the DAS strain rate over time to obtain the fibre strain. The workflow then begins by filtering the DAS waveforms between 0.04-0.1 Hz and selecting three linear segments corresponding to the three sides of the ST array (Fig. 3.2d). These segments (ST1, ST2, and ST3) have orientations of 173° (Fig. 3.21a), 39° (Fig. 3.21b), and -71° (Fig. 3.21c) relative to the East. We stack the signals recorded by the DAS channels within each segment (Fig. 3.21) and extract the strain amplitude at the same time 04:47:27 (grey circle in Fig. 3.21). The fibre strains along the three directions are e_1=e_{ST1}=14.8, e_2=e_{ST2}=7.8, e_3=e_{ST3}=-3.1 nanostrain. Next, we compute the determinant of the coefficient matrix following Eq. (3.8), varying the angle α from 0° to 180° in 0.01° increments. This yields two distinct and perpendicular angles, α_1=1.82° and α_2=91.82°, corresponding to the directions of ε_{11} and ε_{22}, respectively (Fig. 3.22). Finally, we invert the system of equations (3.2) to determine the principal strain values, which are ε_{11}=15.2 and ε_{22}=-4.7 nanostrain. These results are presented in Fig. 3.23, that shows the principal strain direction pointing towards the active craters. This is consistent with the particle motion of broadband seismometers (Fig. 3.17) and aligns with the axisymmetric VLP pressure source modelled by Ripepe, Delle Donne, et al. (2021).

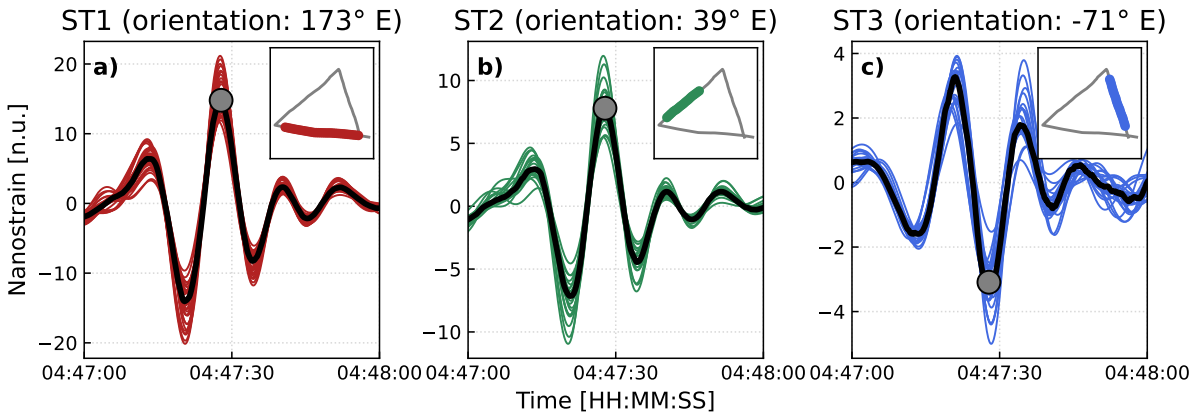

Figure 3.21: Stack (in black) of the VLP strain waveforms generated by the explosion at 04:45:20 UTC on 2022/11/13 and recorded at several channels along three different segments of the ST array (ST1, ST2, ST3) having different orientations (indicated on top of each plot relative to the East).

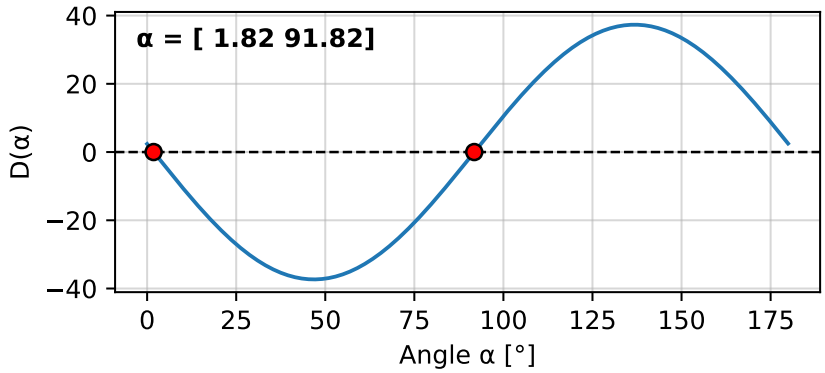

Figure 3.22: Determinant $D(\alpha)$ of the coefficient matrix in Eq. (3.7) considering different angles α from 0° to 180°. The red dots indicate the angles α for which $D(\alpha) = 0$, i.e., 1.82° and 91.82°.

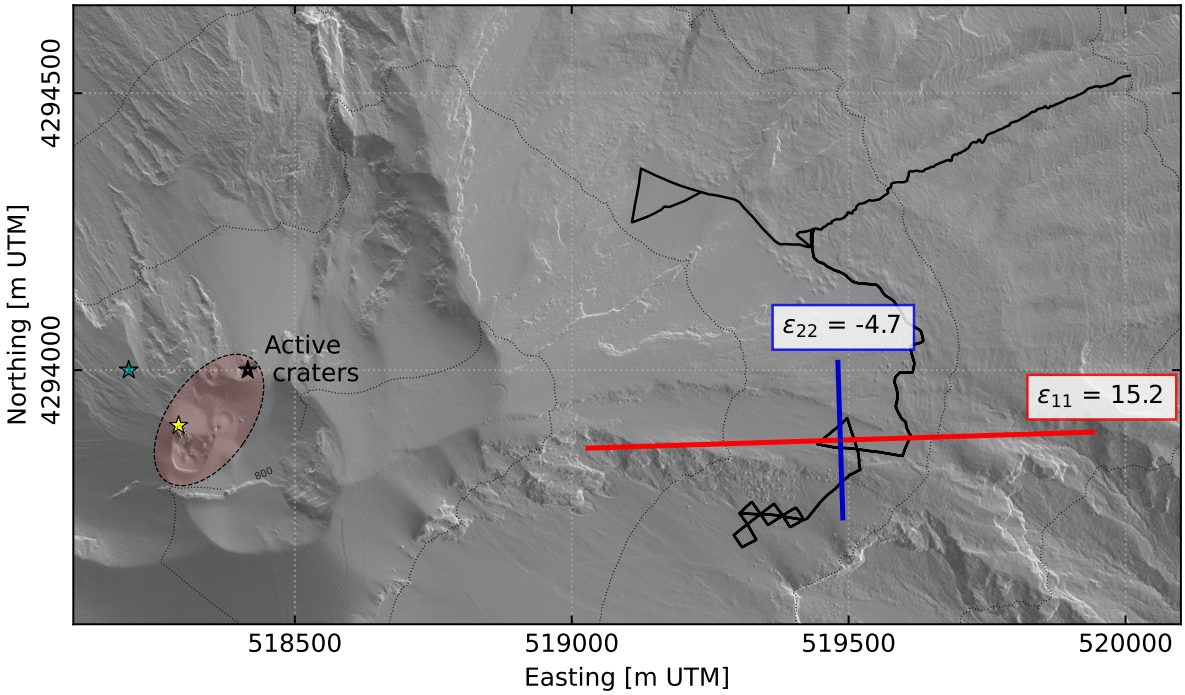

Figure 3.23: Principal strain axes obtained from the explosion at 04:45:20 UTC on 2022/11/13. The red and blue colours respectively indicate positive and negative strains. Values of ε_{11} and ε_{22} are in nanostrain.

3.8 Discussion and conclusions

Between 2020 and 2023, we conducted several experiments at Stromboli, deploying a total of 4 km of fibre-optic cable along the NE flank of the volcano. We interrogated the fibre with DAS technology and recorded a wide range of strain signals generated by volcanic activity. Throughout these experiments, we configured the DAS interrogator with gauge lengths from 5 to 10 m, spatial sampling rates of 2.4 to 2 m, and temporal sampling rates ranging from 50 to 2000 Hz. This parameterisation was tuned to efficiently capture the seismic wavefield generated by volcanic phenomena within the frequency range of interest (i.e. <15 Hz), which encompasses the majority of seismo-volcanic signals at Stromboli.

We employed differential GPS measurements (with centimetre-level resolutions) and tap testing to geolocate the DAS channels for each experiment, ensuring high positional accuracy within ±4 m. Additionally, the locations are in close agreement with estimates of the fibre length during the cable deployment. This is a crucial step for applying array processing techniques to DAS measurements.

During the various experiments, we recorded volcanic activity at Stromboli for a total of almost five months, including ordinary explosions, Major explosions, rockfalls and PDCs. The signals generated by the different events show peculiar features, in agreement with measurements from co-located nodes and permanent seismometers for volcanic monitoring. In particular, we observe that DAS signals lack resolution below ~2.5 Hz and exhibit varying amplitudes (up to an order of magnitude) at different locations. We believe that such amplitude variability is due to local amplification effects induced by the subsurface characteristics to which DAS is particularly susceptible (Trabattoni et al., 2022). We discuss this feature in more detail in Chapter 5.

Finally, we report the first DAS observations of VLP signals at Stromboli, focusing

on explosions between 10 and 20 November 2022. These VLP signals exhibited amplitudes reaching up to ten times their average value. VLP strain signals recorded by DAS have simple waveforms with a dominant period of around 10 seconds. These VLP waveforms display similar shapes across multiple explosions, indicating a non-destructive and repetitive deformation source. Furthermore, different fibre directions reveal varying polarities in the VLP waveforms, contrasting with far-field DAS directivity patterns of P/SV/Rayleigh and SH/Love waves. Building on previous studies (Ripepe, Delle Donne, et al., 2021; Legrand & Perton, 2022), we suggest that these VLP signals reflect quasi-static strain recorded in the near field. The principal strain axis of one VLP signal, obtained from linear DAS strain measurements across three fibre directions, is oriented radially towards the craters, comparable with observations from broadband seismometers and literature findings (Kirchdörfer, 1999; Chouet et al., 2003; Ripepe, Delle Donne, et al., 2021; Legrand & Perton, 2022).

This chapter serves as the starting point for the subsequent analysis of DAS data throughout the thesis. We confirm the capability of DAS to record strain rate seismic signals from various volcanic phenomena, even at low frequencies (0.04 Hz). In the following Chapter 4, we calibrate the DAS measurements to assess their quality by comparing them with independent records from co-located nodal seismometers. In Chapters 5 and 6, we also apply array techniques to DAS waveforms to investigate the location of the seismic sources of these signals and enhance our understanding of their dynamics.

Chapter 4

Empirical calibration of DAS measurements at Stromboli

Preface

To write this chapter, and in particular Section 4.4, we partially adapt the article Trabattoni et al. (2023), published in December 2023 in *Geophysical Journal International*:

A. Trabattoni, F. Biagioli, C. Strumia, M. van den Ende, F. Scotto di Uccio, G. Festa, D. Rivet, A. Sladen, J.P. Ampuero, J.-P. Métaxian, E. Stutzmann, **From strain to displacement: using deformation to enhance distributed acoustic sensing applications**, *Geophysical Journal International*, Volume 235, Issue 3, December 2023, Pages 2372–2384, https://doi.org/10.1093/gji/ggad365.

In this chapter, we evaluate the quality of DAS measurements at Stromboli by comparing them with independent recordings from co-located 5 Hz seismometers. We use two different approaches to convert different measurements into comparable quantities. The first one, which we refer to as the "finite-difference" method, is well-established in the literature (e.g., Bakku, 2015; Wang et al., 2018; Jousset et al., 2022). It allows for retrieval of the strain rate along a linear segment by calculating the finite difference between seismic velocities recorded by seismometers at the segment endpoints. In Section 4.3, we compare DAS signals with those from nodal seismometers converted to strain rate using this method.

We also apply this finite-difference method later in this thesis, specifically in Chapters 5 and 6, each presented as an independent article. Chapter 5 has already been published (Biagioli et al., 2024), while Chapter 6 is currently under preparation. Including the method and results in both articles ensures they stand alone as self-contained works, providing an initial validation of the DAS data before further analysis. However, in both

articles (and chapters) we focus solely on volcanic tremor and ordinary explosion signals. Conversely, this chapter also covers signals from major explosions that occurred in 2021 and 2022. Nevertheless, we acknowledge potential repetition and redundancy between this chapter and the following ones.

The second and more novel approach enables the independent retrieval of velocity waveforms through numerical integration along the spatial direction of strain rate recordings without relying on co-located seismometers. This work was developed through a collaboration between our research group, Université Côte d'Azur (France), and the University of Naples Federico II (Italy). Some of the research presented in this thesis has also been included in Trabattoni et al. (2023). We discuss the method in Section 4.4, first providing a theoretical overview and then demonstrating its application using signals of an ordinary explosion at Stromboli. We adapt the text and figures from the published article. However, the article also validates the method using full-waveform simulations and practical applications, such as magnitude estimation. We encourage interested readers to refer to the full article for further details.

4.1 Abstract

Unlike traditional inertial sensors, the instrumental response of DAS systems remains largely unquantified, accounting for the features of both interrogators and sensing fibres. In this chapter, we assess the quality of our DAS measurements at Stromboli by comparing them to independent recordings from co-located seismic nodes. We use two methods to convert DAS and node recordings into the same units: "finite-difference" and "spatial-integration". The finite-difference method, well-established in the literature, calculates strain rate signals from the finite difference of the seismic velocity recorded by two nodes. Conversely, the spatial-integration method derives seismic velocity from DAS strain rate signals through numerical integration without requiring additional instruments like seismometers. To calibrate DAS data, we focus on signals from ordinary and major explosions in 2021 and 2022. We find that DAS and node waveforms exhibit a strong phase match, with cross-correlation coefficients reaching up to 0.99. However, DAS records lower amplitudes (approximately 1.5-5 times) than nearby nodes, likely due to inefficient ground-to-fibre strain transfer in a loose cable. We also do not observe any significant changes in the amplitude of the signals recorded in the different years. Despite this, our validation confirms that DAS can effectively record signals comparable to traditional inertial seismometers. It also highlights the potential of the spatial-integration method for converting strain rate into seismic velocity.

4.2 introduction

Seismic measurements aim to accurately record the ground motion induced by elastic perturbations (Lindsey, Rademacher, & Ajo-Franklin, 2020). Inertial seismometers typically measure the relative motion between the ground, to which the instrument is coupled, and an internal mass serving as inertial reference (Lay & Wallace, 1995; Wielandt, 2012). These instruments have well-known frequency-dependent response functions (in both phase and amplitude) that translate their recordings into physical units of ground motion (Wielandt, 2012; Lindsey, Rademacher, & Ajo-Franklin, 2020).

Conversely, DAS instrumental response arises from several factors, such as interrogator and cable features, which may hinder accurate characterisation (Lindsey, Rademacher, & Ajo-Franklin, 2020; Celli et al., 2024). The cable mechanical properties and the ground-to-cable coupling significantly influence the strain transfer from the surrounding medium to the fibres within a cable, thus impacting the accuracy of the recordings (Reinsch et al., 2017; Hubbard et al., 2022). These effects are also due to fibre installation conditions, which may vary between different cable sections for the same deployment and from one experiment to another (Celli et al., 2024; Jousset et al., 2024). These characteristics make it challenging to develop standardised methodologies for validating DAS signals. Additionally, DAS measurements exhibit a restricted broadside sensitivity (Martin, 2018) and are strongly susceptible to local heterogeneities (Capdeville & Sladen, 2024) and site effects (Trabattoni et al., 2022). The latter may be particularly relevant since the cable is often coupled with unconsolidated soil used for backfilling trenches (Celli et al., 2024).

Therefore, evaluating the quality of DAS measurements is crucial, especially for seismological applications requiring accurate ground motion measurements. To this aim, several studies compared the data quality of DAS and traditional instrumentation (e.g., broadband seismometers and geophones) in different frequency bands (10^{-3}-10^{1} Hz) and contexts (e.g., Jousset et al., 2018; Martin, 2018; Wang et al., 2018; Lindsey, Rademacher, & Ajo-Franklin, 2020; Paitz et al., 2020; Currenti et al., 2021). The comparisons were made either by deriving strain along the cable direction using seismic records (Bakku, 2015; Wang et al., 2018; Currenti et al., 2021), or by converting strain data into particle displacement (and other time derivatives of this quantity; Daley et al., 2016; Lindsey, Rademacher, & Ajo-Franklin, 2020). These studies provided valid results, demonstrating DAS capabilities in retrieving accurate ground motion measurements. However, the authors also pointed out the necessity of further field and laboratory experiments to better quantify DAS parameters such as, e.g., the instrument response, frequency range, self-noise and dynamic range considering varying interrogators, parametrisations and fibre installations (Lindsey, Rademacher, & Ajo-Franklin, 2020; Paitz et al., 2020).

Moreover, most seismological tools (e.g., those used for magnitude estimation) are designed for translational ground motion measurements and require adaptation when applied to strain recordings (Strumia et al., 2024). van den Ende and Ampuero (2021) also noted that beamforming of strain signals can fail due to the dominance of scattered waves, which reduces wavefield coherence. Given these challenges, which extend beyond the scope of DAS calibration and validation, it is also essential to develop accurate methods for converting strain into displacement.

In this chapter, we validate DAS measurements of Strombolian activity by comparing them with independent recordings from co-located 5 Hz seismometers. We use two different methods to convert the different recordings into the same units of measurement. We refer to them as "finite-difference" and "spatial-integration" methods. The finite-difference method (e.g., Wang et al., 2018) allows us to retrieve strain rate along linear cable segments from seismic velocity recorded by seismometers. Conversely, the spatial-integration method, enables the independent retrieval of the 1D seismic velocity from strain rate signals (Trabattoni et al., 2023).

First, in Section 4.3, we compare the DAS signals with the strain rate derived from the nodes using the finite-difference method. We consider the signals generated by both ordinary and major explosions occurred in 2021 and 2022. We also investigate whether any changes from one year to another in ground-to-cable coupling due to e.g. soil compaction

could affect the quality of the DAS data. Subsequently, in Section 4.4, we retrieve seismic velocity traces of one ordinary explosion from DAS strain rate signals using the spatial-integration method and compare them with co-located seismometer recordings of the same event. The spatial-integration method was developed through a collaboration between our research group, Université Côte d'Azur (France), and the University of Naples Federico II (Italy). Notably, applying this method on the dataset recorded at Stromboli and comparing the outcomes with co-located seismometers serves as a first field calibration for this novel technique. We show that if the geometry of the DAS deployment is made of sufficiently long rectilinear sections, the strain rate can be used to recover the particle velocity without the need of additional instruments.

4.3 Converting node seismic-velocity to strain rate: finite-difference method

In this section, we compare the strain rate signals recorded with DAS along linear cable segments and obtained from the finite difference of the seismic velocity recorded by co-located nodes (Bakku, 2015). This approach is largely documented in the literature. Wang et al. (2018) presented and used this method to compare DAS and node waveforms of an M_L4.3 earthquake recorded at Brady Hot Springs (Nevada), obtaining excellent results in both phase and amplitude. Moreover, Jousset et al. (2022) found similar outcomes for signals generated by volcanic explosions at Mount Etna (Italy). We first provide a short theoretical background for this method (Section 4.3.1), and then show the results obtained with our recordings (Section 4.3.2).

4.3.1 Theoretical background

The strain rate $\dot{\varepsilon}$ is defined as:

$$\dot{\varepsilon} = \frac{\partial \varepsilon}{\partial t} = \frac{\partial}{\partial t}\left(\frac{\partial u}{\partial x}\right), \tag{4.1}$$

being u the particle displacement along the cable direction x (Wang et al., 2018). Following Eq. (4.1), and considering the spatial average of the strain over the gauge length L_G (shorter than the wavelength of interest), we can obtain a finite-difference relationship (Bakku, 2015) between the DAS strain rate at a single channel and the particle velocity measured by two seismometers:

$$\begin{aligned} \dot{\varepsilon}_{DAS}|_x = \frac{1}{L_G}\int_{x-L_G/2}^{x+L_G/2} \dot{\varepsilon}(l)dl = \\ \frac{1}{L_G}\int_{x-L_G/2}^{x+L_G/2} \frac{\partial}{\partial t}\frac{\partial u}{\partial x} = \frac{\dot{u}|_{x+L_G/2} - \dot{u}|_{x-L_G/2}}{L_G}, \end{aligned} \tag{4.2}$$

where $\dot{\varepsilon}$ and $\dot{u}$ are evaluated at different positions x along the cable.

Equation (4.2) indicates that the DAS strain rate at a position x is the difference in seismic velocity measured at distances of half the gauge length L_G before and after that position (Wang et al., 2018). This concept can be extended to a linear segment of length

L_G, where n is the number of gauge lengths within the segment. The average strain rate along the segment is either (i) the sum of the strain rate $\dot{\varepsilon}$ recorded by the DAS channel within the segment or (ii) the finite difference of seismic velocities $\dot{u}$ at the segment's endpoints, divided by the gauge length L_G (Wang et al., 2018), as summarised by the following equation:

$$\dot{\varepsilon}|_{x=-(n-1)L_G/2} + \cdots + \dot{\varepsilon}|_{x=0} + \cdots + \dot{\varepsilon}|_{x=(n-1)L_G/2} = \\ = \frac{\dot{u}|_{x=nL_G/2} - \dot{u}|_{x=-nL_G/2}}{L_G}. \tag{4.3}$$

In the following section, we compare the left hand and right hand sides of Eq. (4.3) along several cable segments and for different events, notably ordinary and major explosions.

4.3.2 Application to DAS measurements: ordinary and major explosions

To compare DAS and node signals following Eq. (4.3), we consider several rectilinear segments belonging to both 2021 and 2022 deployments (Fig. 4.1). Concerning the 2021 deployment, we apply the finite-difference method on six segments of the NT sector (between nodes N1-N2, N2-N3, N3-N4, N4-N5, N5-N6, N6-N1 in Fig. 4.1a) and four segments of the ST sector (S4-S5, S5-S6, S6-S7, S7-S8 in Fig. 4.1b). In 2022, we installed nodes along the NT branch in similar positions. Therefore, we apply Eq. (4.3) on signals recorded in 2022 along the same segments as in 2021 (i.e. between N1 and N6; Fig. 4.1c). We also test Eq. (4.3) on the data of five segments of the GR array (G3-G6, G4-G7, G5-G10, G9-G11, G13-G14 in Fig. 4.1d). The different segments we consider have varying lengths, ranging between ~30-80 m.

To have independent estimates of the strain rate in space, the left-hand side of Eq. (5.2) is the sum of one DAS channel every gauge length L_G along each fibre segment. Please note that the gauge length varies from 5 m in 2021 to 10 m in 2022. Regarding the nodes, first, we remove the instrumental response. We then project the 3D particle velocity along the fibre direction (considering both orientation and slope inclination), subtract the longitudinal components recorded at the segment's endpoint and divide by L_G to obtain the strain rate. We then decimate the strain rate signals retrieved from DAS and nodes using Eq. (4.3) to the same sampling rate (200 Hz) and filter them between 0.5 and 15 Hz (i.e., the frequency band of interest for VEQs).

Fig. 4.2 shows the comparison between the strain rate traces of one ordinary explosion (that occurred on 2021/09/26 at 20:47 UTC) derived from DAS and nodes using Eq. (4.3). We show the results obtained for six segments of the 2021 deployment, three belonging to the NT sector (Fig. 4.2a-f) and three to the ST sector (Fig. 4.2g-l). The segments have different lengths, azimuth and slopes (the latter two are noted in each subplot in Fig. 4.2). We compare the traces both in time (left column of Fig. 4.2) and frequency (right column of Fig. 4.2) domains. We define two metrics to estimate the similarity between the DAS and node traces: the maximum cross-correlation coefficient CC and the ratio R between the root mean square amplitudes of node and DAS strain rate traces.

The strain rate waveforms recorded by DAS and derived from the nodes belonging to the NT sector (Fig. 4.2a-f) have a good phase match and exhibit high CC (around 0.9).

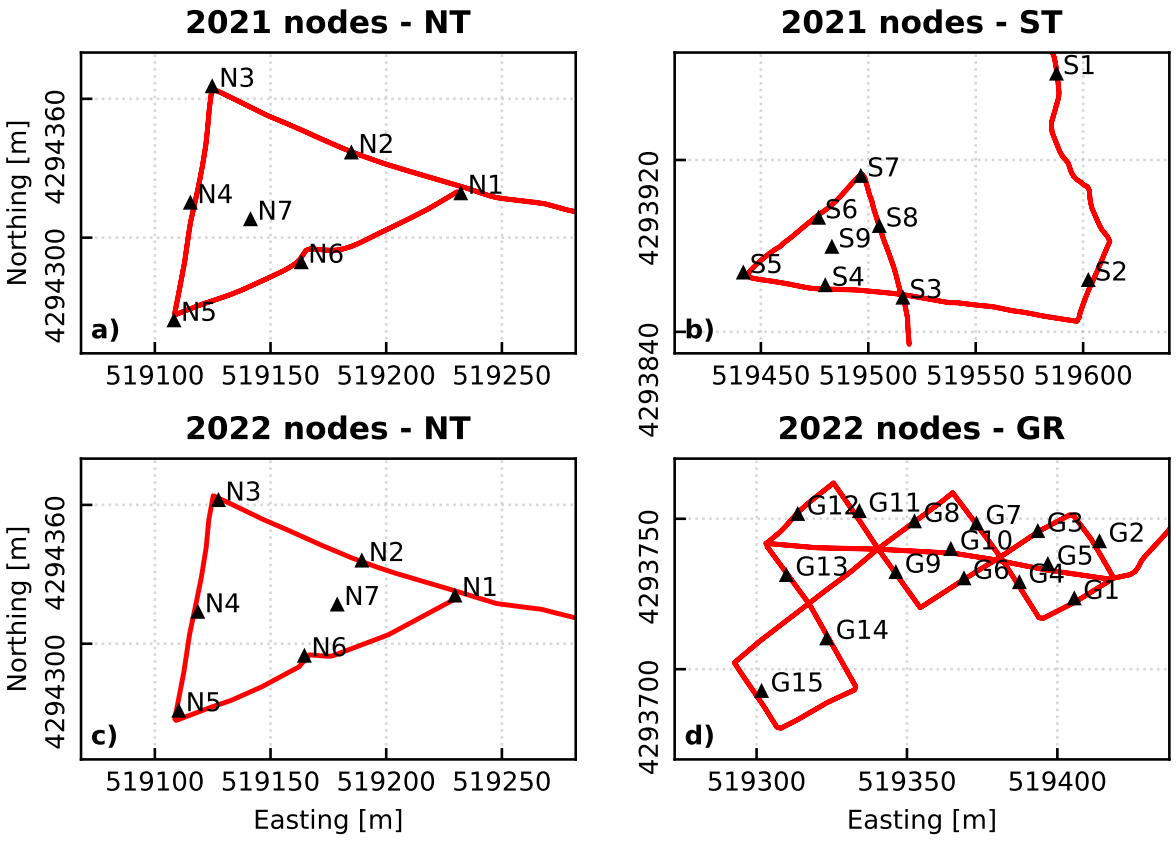

Figure 4.1: Geometries of the NT, ST and GR arrays. The fibre optic segments we use are coloured in red. Black triangles indicate the 3C nodes. The top row shows the deployment of nodes in 2021 at the NT (a) and ST (b) arrays. The bottom row shows the installation in 2022 at the NT (c) and GR (d) arrays.

Conversely, DAS and node traces of the ST sector have lower CC values (between 0.4-0.7). This issue probably arises from lower SNRs of signals generated by ordinary explosions. Moreover, we observe that the strain rate values recorded by DAS are lower than those recorded by the nodes. The R ratios between the root mean square amplitudes of node and DAS traces vary from ~1.8 (S4-S5) to a maximum of 3.8 (N2-N3). This holds for each segment except S7-S8 (which, however, exhibits a low CC of 0.45). Furthermore, R values do not depend on the frequency of the signal in the 0.5-15 Hz frequency range (Fig. 4.2, right column).

Similarly, Fig. 4.3 shows DAS and node strain rate traces of a major explosion that occurred on 2021/10/06 at 14:17 UTC. In this case, DAS and node waveforms (between 0.5-15 Hz) corresponding to each segment exhibit an almost perfect agreement in phase. CC values increase in all segments up to a maximum of 0.99 obtained for S4-S5. This is likely due to a higher SNRs than ordinary explosions. Conversely, R values are stable between 1.6-4.2. These values indicate lower amplitudes recorded by DAS that do not vary significantly depending on the magnitude of the explosion. For both events (i.e. the ordinary and the major explosion), we obtain similar values of CC and R considering the remaining segments of NT and ST arrays, as summarised in Table 4.1.

We examine if lower amplitudes result from inefficient ground-to-fibre coupling and whether this effect diminishes over time at the same location due to soil compaction in the cable trenches. To do so, in Fig. 4.4, we compare DAS and node strain rate waveforms generated by four events: two ordinary and two major explosions, with one of each type occurring in 2021 and 2022. The explosions of 2021 are those shown in Figs. 4.2 and 4.3. Waveforms in Fig. 4.4 are filtered between 0.5-15 Hz. Between one year and another, CCs do not vary significantly and have high values of 0.91-0.97. Similarly, ratios R exhibit similar values. After one year, we only observe a slight decrease in R between 10-15%. Table 4.2 summarizes the metrics obtained by comparing DAS and node signals recorded in the NT and GR sectors during the ordinary and major explosions of 2022 shown in Fig. 4.3.

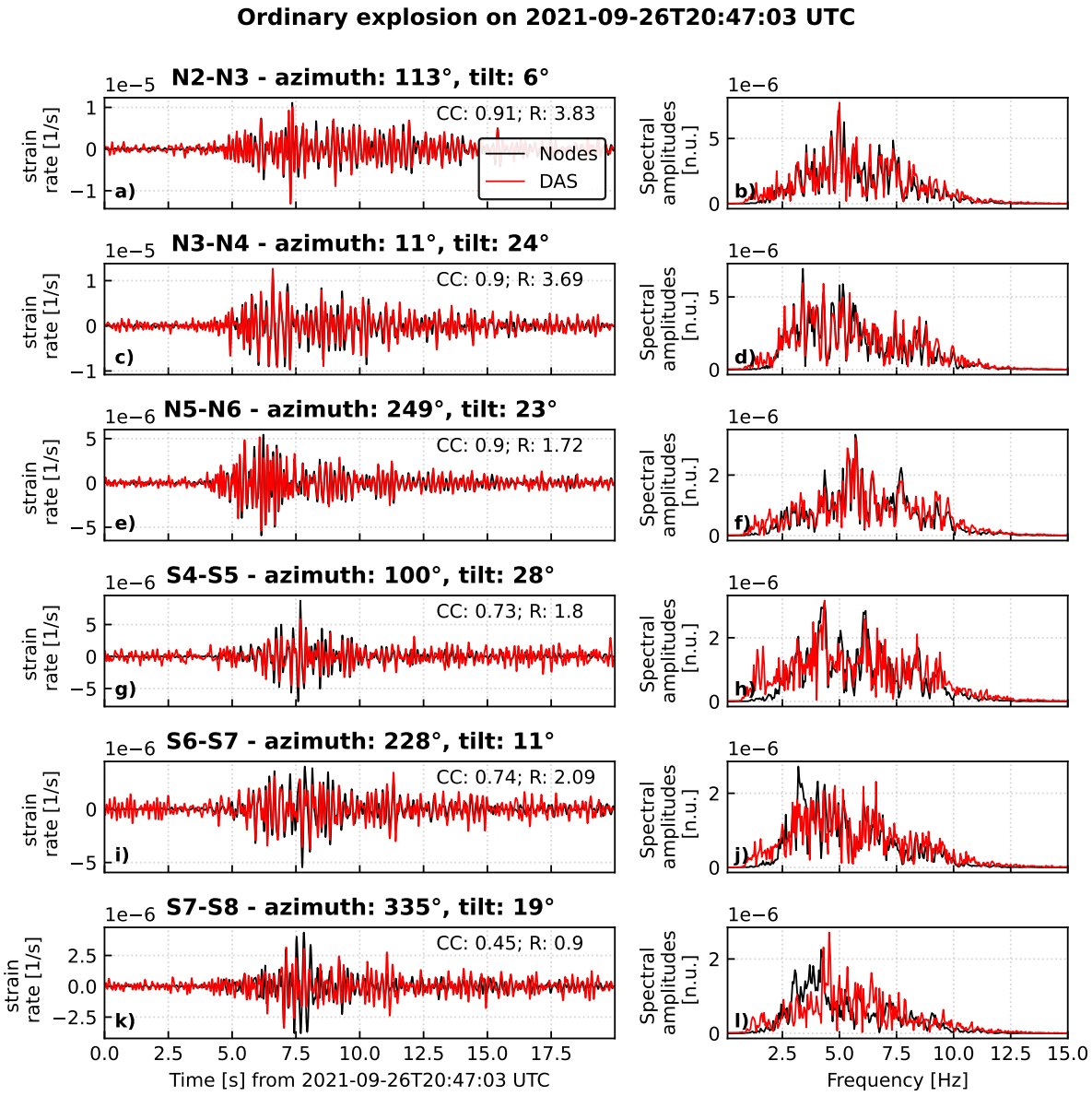

Figure 4.2: Comparison between 20 s strain rate traces of an ordinary explosion occurred on 2021/09/26 recorded by DAS (red) and obtained from nodes (black) using Eq. (4.3). We consider six cable segments, corresponding to the three sides of both NT (N2-N3, N3-N4 and N5-N6) and the ST (S4-S5, S6-S7, S7-S8) arrays (Fig. 4.1). We compare DAS and node measurements both in time (left column) and frequency (right column) domains. The ratios (R) between the RMS amplitudes of node and DAS traces, and the maximum cross-correlation coefficients (CC) between the two waveforms are shown in the top right in the left column. To enhance clarity, we rescale DAS strain rate traces by multiplying them with the ratio R. Waveforms are filtered between 0.5-15 Hz.

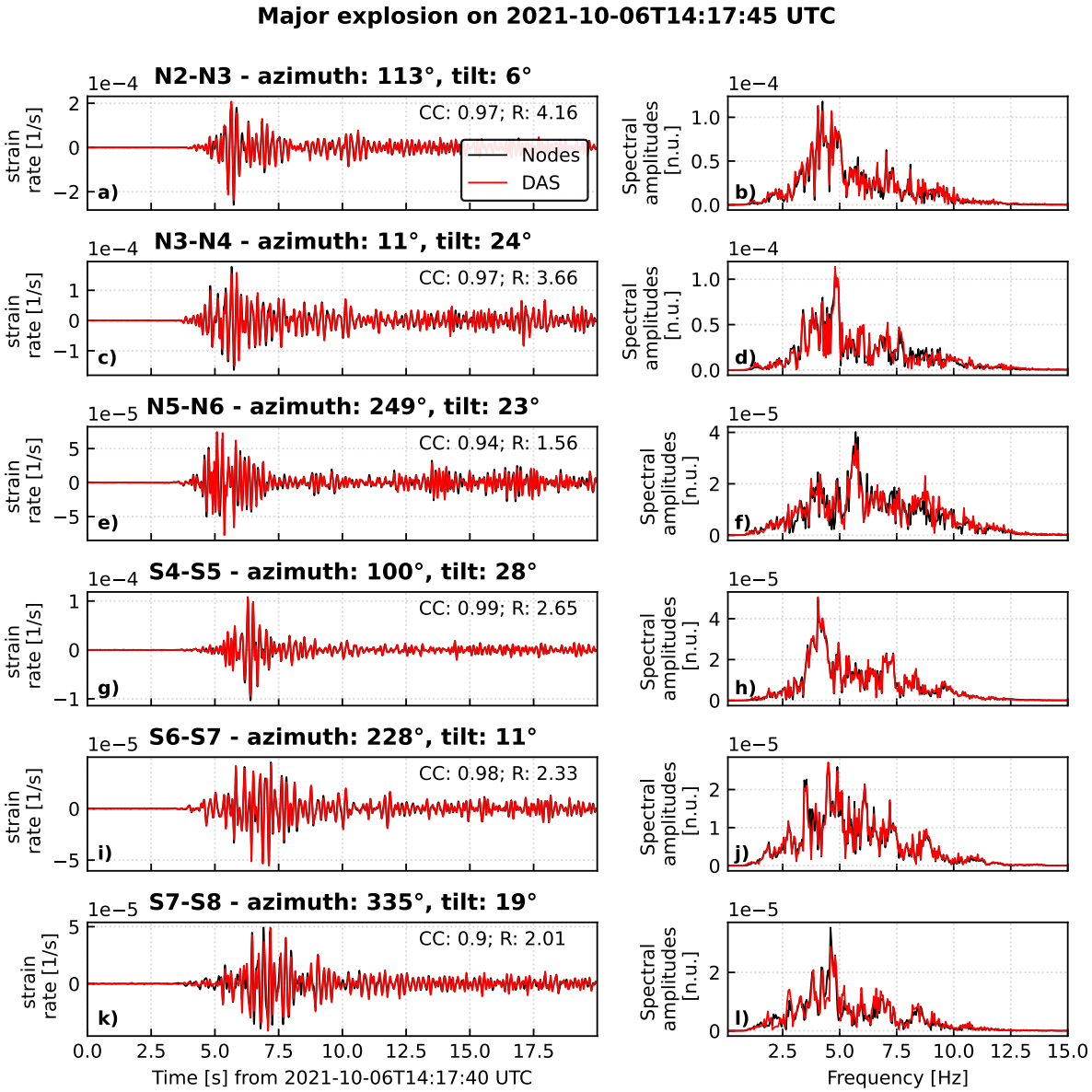

Figure 4.3: Same as Fig. 4.2, but considering a Major explosion occurred on 2021/10/06 (same explosions as in Fig. 3.11).

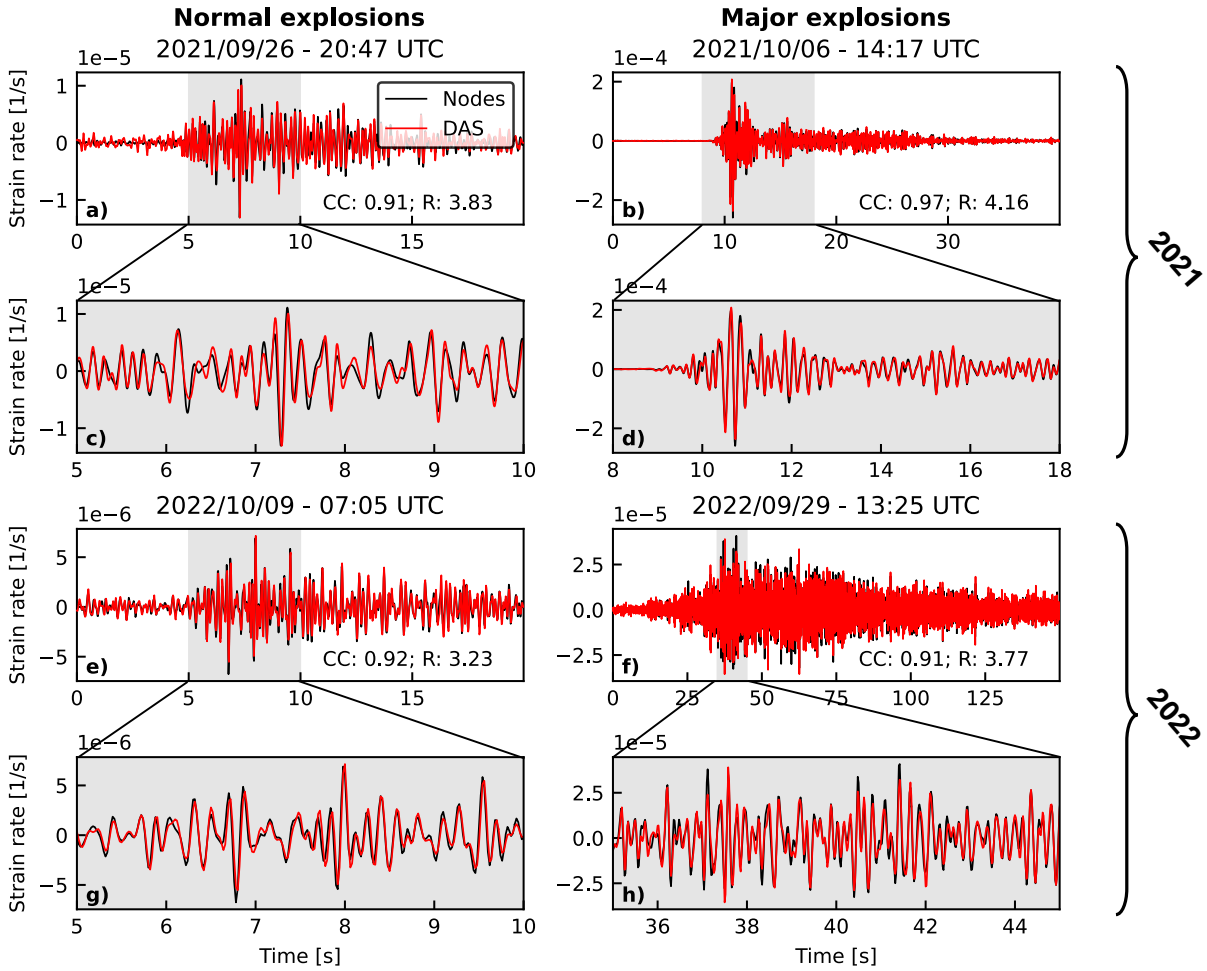

Figure 4.4: Comparison between strain rate traces of ordinary (left column) and major (right column) explosion occurred in 2021 (top row) and 2022 (bottom row) recorded by DAS (red) and obtained from nodes (black) using Eq. (4.3) along the segment N2-N3. Normal explosions occurred on (a,c) 2021/09/26 (same event as in Fig. 4.8) and (e,g) 2022/10/09. Major explosions occurred on (b,d) 2021/10/06 (same event as in Fig. 3.11) and (f,h) 2022/09/29. The ratios (R) between the RMS amplitudes of node and DAS traces, and the maximum cross-correlation coefficients (CC) between the two waveforms are shown in the top right in the left column. To enhance clarity, we rescale DAS strain rate traces by multiplying them with the ratio R. (c,d) Show a 5 s zoom on the signals of ordinary explosions, while (g,h) show a 10 s zoom on the signals of major explosions. Waveforms in Fig. 4.4 are filtered between 0.5-15 Hz.

Table 4.1: Metrics obtained by comparing DAS and node strain rate signals (between 0.5-15 Hz) obtained using Eq. (4.3) along 10 linear fibre segments and considering one ordinary and one major explosion that occurred in 2021. CC is the maximum cross-correlation coefficient between the two waveforms. R is the ratio between the RMS amplitudes of node and DAS traces.

2021	**Ordinary explosion (2021/09/26 20:47 UTC)**		**Major explosion (2021/10/06 14:17 UTC)**	
Segment	**CC**	**R**	**CC**	**R**
N1-N2	0.87	4.29	0.96	5.03
N2-N3	0.91	3.83	0.97	4.16
N3-N4	0.9	3.69	0.97	3.66
N4-N5	0.86	2.37	0.93	2.6
N5-N6	0.9	1.72	0.94	1.56
N6-N1	0.91	1.47	0.95	1.58
S4-S5	0.73	1.8	0.99	2.21
S5-S6	0.76	1.81	0.85	2.65
S6-S7	0.74	2.09	0.98	2.33
S7-S8	0.45	0.9	0.9	2.01

Table 4.2: Metrics obtained by comparing DAS and node strain rate signals (between 0.5-15 Hz) obtained using Eq. (4.3) along 11 linear fibre segments and considering one ordinary and one major explosion that occurred in 2022. CC is the maximum cross-correlation coefficient between the two waveforms. R is the ratio between the RMS amplitudes of node and DAS traces.

2022	**Ordinary explosion (2022/10/09 07:05 UTC)**		**Major explosion (2022/09/29 13:25 UTC)**	
Segment	**CC**	**R**	**CC**	**R**
N1-N2	0.85	3.18	0.93	3.7
N2-N3	0.92	3.17	0.91	3.82
N3-N4	0.96	3.11	0.92	4.0
N4-N5	0.86	2.82	0.92	2.98
N5-N6	0.88	1.44	0.82	2.05
N6-N1	0.94	1.55	0.91	1.87
G3-G6	0.94	3.84	0.98	3.91
G9-G11	0.9	3.32	0.88	3.65
G13-G14	0.87	4.13	0.75	5.27
G4-G7	0.98	1.35	0.97	1.39
G5-G10	0.98	1.41	0.98	1.39

4.4 Converting DAS strain rate to velocity: spatial-integration approach

In this section, we instead compare DAS and node data using the opposite approach of the previous Section 4.3, i.e. converting strain rate signals into seismic velocity. As we

mentioned previously, several studies have compared seismometer-based ground motion measurements with the seismic displacement (or velocity) derived from DAS strain (or strain rate) signals (Daley et al., 2016; Wang et al., 2018; Lindsey, Rademacher, & Ajo-Franklin, 2020). These studies have proposed various methods for converting strain to particle displacement (or its time derivatives).

One straightforward method uses the dominant apparent velocity of observed phases along the cable direction (Daley et al., 2016). While simple, this approach has limitations, particularly in accurately converting only dominant phases. This can be problematic when dealing with phases of interest that have faint amplitudes, such as body waves whose much higher apparent velocity compared to shallow scattered phases results in lower strain amplitudes (van den Ende & Ampuero, 2021; Trabattoni et al., 2022).

Another method for converting DAS signals to particle velocity is FK rescaling (Daley et al., 2016; Wang et al., 2018; Lindsey, Rademacher, & Ajo-Franklin, 2020; Yang et al., 2022), which involves spatial integration and time differentiation of the strain rate in the FK domain. In this approach, amplitudes are weighted by the quantity $-\omega/k$, where ω is the frequency, and k is the apparent wavenumber along the cable. However, since the apparent wavenumber k can approach zero, all studies that used the FK rescaling suggested to dampen small wavenumbers to avoid instabilities and the emergence of spurious low-wavenumber signals. This is done by introducing a waterlevel at low wavenumbers to ensure numerical stability (Lindsey, Rademacher, & Ajo-Franklin, 2020; Paitz, 2021). However, the waterlevel may significantly influence the wavefield, adding further and unphysical information (Paitz, 2021). Additionally, FK rescaling is limited to finite 2D time-space windows.

However, the main issue regarding the spatial integration (as done in FK rescaling) is that the initial time-varying value (i.e., the integration constant) is unknown. van den Ende and Ampuero (2021) estimated particle velocity along rectilinear segments by integrating the strain rate spatially, using co-located seismometers as a reference. However, this method is limited to setups comprising such sensors. Alternatively, Yang et al. (2022) utilised a new generation of DAS systems that natively record integrated strain rate, referred to as "deformation rate". They found that integrated measurements often include spurious low-wavenumber signals. Spatial or FK filtering may empirically remove these effects.

Fichtner, Bogris, et al. (2022) explored the origin of these spurious signals in strain-integrated recordings along curvilinear paths, focusing on transmission measurements, where a pulse emitted at one end of the cable is recorded at the other end by a single sensor. These measurements are not distributed (sensitive to strain at each point) but integrated (sensitive to the total strain along the cable). The study revealed that strain-integrated measurements are generally insensitive to the displacement wavefield except at specific locations: the cable's endpoints (where the relative displacement between the two is measured) and at curves or kinks. By accurately estimating these spurious signals at such points, we can remove them from the integrated strain (or strain rate) to estimate particle displacement (or velocity) with enhanced accuracy.

We present an alternative way to convert strain to ground motion based on numerical integration along the space dimension. We first present the theoretical background of the method (Section 4.4.1) and then its application on strain rate signals of one ordinary explosion recorded at Stromboli in September 2021 (Section 4.4.4.

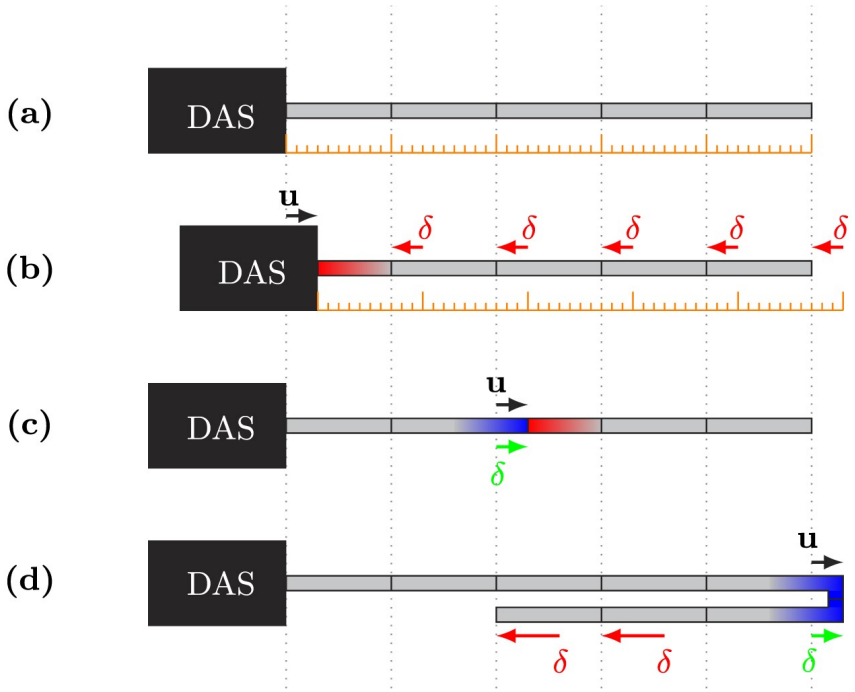

Figure 4.5: (a) A rectilinear fibre-optic cable (grey line) at rest with reference markers (black ticks) placed at regular intervals from the DAS interrogator (orange ruler). Three snapshots (b-d) show a zero-average localized impulsive wavelet moving through the cable from left to right. (b) As the wavelet reaches the start of the cable, ground displacement occurs, with blue indicating elongation and red indicating contraction. The displacement of the DAS interrogator causes a contraction at the beginning of the cable. This contraction reduces the distance to all subsequent points, adding a constant deformation $\delta(s,t) = -u(0,t)$ along the entire cable. (c) The deformation becomes confined within the linear section. Since shortening on one side balances elongation on the other, the integrated strain cancels out, leaving subsequent points unaffected. With a stationary reference point (the DAS interrogator) stationary, the measurement is local: $\delta(s,t) = u(s,t)$. (d) When the impulse reaches the end of the rectilinear section, and if the cable bends (e.g., with a 180° kink), the elongation is no longer balanced by an equal contraction, which occurs outside the cable. In this case, the backward part of the kink elongates by the same amount, increasing the arc length to points beyond the kink by twice the displacement: $\delta(s,t) = 2u(s,t)$. This illustrates that integration cannot be applied directly across a kink due to geometric effects.

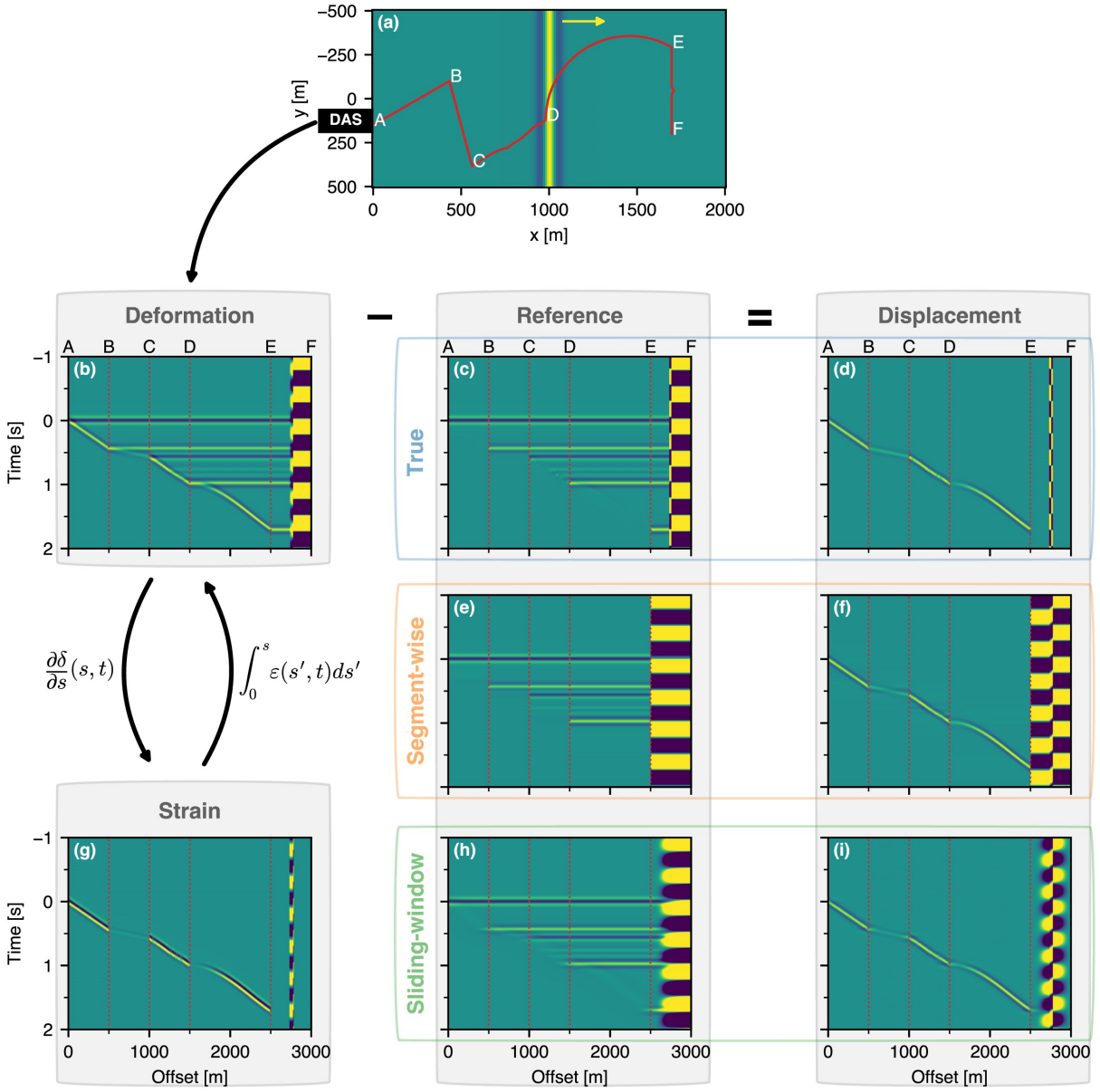

Figure 4.6: Illustrative simulation. (a) An impulsive plane P wave propagating along the x-axis produces a horizontal displacement wavefield (blue–green–yellow background raster). A fibre-optic cable (red line) records the deformation along a given geometry. Deformation (b) is the sum of (d) the true displacement and (c) a reference term (also referred to as 'non-local effects') that must be estimated and removed. We observe non-local effects as horizontal features. They are space invariant signals starting at a given offset. The origin is either the beginning of the cable (marker A), a kink (markers B, C, D and E), a perturbation of the rectilinear segment (section CD), the curvature of the cable (section DE), or a nonlinear effect, here produced by a 50-m hanging section at the middle of the segment EF. (f) Segment-wise method in which we remove the averaged deformation (e) on each segment. Sliding-window method: an alternative solution is to remove (h) a sliding average (we use a 500 m long window with a Hann tapering) to get (i). Spatial differentiation of the deformation gives (g) strain, which is a local measurement. The red vertical dotted lines in (b-i) indicate linear cable segments.

4.4.1 Theoretical background

First, we lay down the theory behind the method to recover displacement (or velocity) from DAS data. The displacement of a body is the result of rigid-body displacement (translation/rotation) and deformation (shape/size changes) components (Fossen, 2016). DAS is sensitive to deformation along the cable direction. From here onwards, we refer to this curvilinear deformation along the cable as "deformation" (as in Yang et al., 2022). We then relate this quantity to usual DAS (e.g. strain/strain rate) and seismological ground motion (e.g. displacement/velocity) quantities.

Each point of an optical fibre can be identified by a curvilinear coordinate s, indicating the distance at rest $L_0(s)$ from the interrogator $L_0(s) = s$. An elastic perturbation affecting the ground and transferred to the cable induces a variation of the distance $L(s,t)$ over time. The deformation $\delta(s,t)$ refers to the change in distance relative to the undeformed distance at rest:

$$\delta(s,t) \equiv L(s,t) - L_0(s). \tag{4.4}$$

When the ground motion is small, the deformation equals the curvilinear integration of the strain component $\varepsilon(s,t)$ along the fibre (Fichtner, Klaasen, et al., 2022), i.e. the projection along the cable direction ($\mathbf{e}(s)$) of the curvilinear derivative of the displacement $\mathbf{u}(s,t)$:

$$\delta(s,t) = \int_0^s \varepsilon(s',t)ds' = \int_0^s \mathbf{e}(s') \cdot \frac{\partial \mathbf{u}}{\partial s'}(s',t)ds'. \tag{4.5}$$

Regular typed characters in Eq. (4.5) and below indicate the projection along the fibre of the quantities expressed with bold characters.

DAS measures the displacement of the scatterers within a fibre using the phase of the backscattered radiation. At rest, the phase $\phi_0(s)$ of the backscattered light from a position s along the cable is randomly defined due to heterogeneities in the fibreglass. Changes in fibre length due to elastic perturbations induce changes in the light optical path. These generate phase shifts $\phi(s,t)$ of the backscattered light as defined by the equation:

$$\phi(s,t) = \frac{4\pi n\xi}{\lambda}\delta(s,t) + \phi_0(s), \tag{4.6}$$

where n is the effective index of the optical fibre, ξ is a photo-elastic coefficient representing changes in the refractive index due to fibre strain, and λ is the laser's central wavelength in the vacuum (Hartog, 2017). The coefficient 4π equals $2{\times}2\pi$ and accounts for the round-trip of the light pulse within the fibre, from the interrogator to the scatterer and back. Since $\phi_0(s)$ is unknown, static deformation cannot be recovered. However, by deriving the phase in both time and space, this unknown is eliminated, allowing for the calculation of the strain rate $\dot{\varepsilon}(s,t)$ as:

$$\frac{\partial \dot{\phi}}{\partial s}(s,t) = \frac{4\pi n\xi}{\lambda}\dot{\varepsilon}(s,t). \tag{4.7}$$

In our approach, we use the deformation (proportional to phase following Eq. (4.4)) to retrieve the displacement by spatial integration. Let us consider a linear cable geometry (Fig. 4.5). Integrating Eq. (4.5) along a constant direction $\mathbf{e}(s)$ implies that the deformation equals the difference of the displacement $u(s)$ between the integration limits:

$$\delta(s,t) = u(s,t) - u(0,t), \tag{4.8}$$

being $u(0,t)$ the displacement at the fibre start, serving as reference. If $u(0,t)$ is null, the deformation equals the displacement. Conversely, if $u(0,t) \neq 0$, the motion of the reference position generates a space-invariant (and time-varying) signal affecting the whole cable. These spurious features, referred to as non-local effects, originate at the cable's start, at kinks and curvatures, at perturbations of linear segments or uncoupled sections (e.g., hanging sections) that provide non-linear effects. Integrating the deformation along a linear segment cancels the effects of the displacement of one point. The displacement of a point along a linear segment induces a positive strain on one side and a negative one on the opposite side (Fig. 4.5c), and these contributions cancel out in the integration. For not rectilinear geometries, the displacement at a cable kink results in an unbalanced strain (Fig. 4.5d). These spurious signals have to be estimated and removed from the recovered displacement.

For a cable geometry composed of linear segments, the total deformation is the sum of the deformation of each segment up to the point s of interest. Dividing Eq. (4.5) into segments and applying Eq. (4.8) for each of them gives:

$$\delta(s,t) = u(s,t) - \sum_{k=1}^{n} \left[u\left(s_k^+, t\right) - u\left(s_k^-, t\right) \right] - u(0,t), \tag{4.9}$$

where s_k are the location of the n cable kinks before the location s. Superscript $-$ and $+$ in Eq. (4.9) indicate the displacement along the cable before and after each kink. New additive terms appear at each change in cable direction, influencing all the following channels. In the measurements, these constant terms appear as horizontal, space-invariant signals starting at each change in the fibre direction. In Fig. 4.6, we provide an example of such effects considering a synthetic cable deployment comprising linear and curved sections alongside fibre kinks. Furthermore, the cable includes a free-hanging and oscillating section. We simulate an impulsive P wave using a 7.5 Hz Ricker wavelet. The medium hosting the fibre is homogeneous and has a P wave velocity of 1 km/s. We observe that the deformation (Fig. 4.6b) induced by the P wave and obtained using Eq. (4.9) arises from the contribution of both the actual displacement (Fig. 4.6d) and spurious signals appearing at each cable kink and curve (markers A-F in Fig. 4.6c). Furthermore, the radius of the cable curvature influences the amplitude of these spurious geometric effects. Because of this, the signals originating at smooth curvature (e.g. in section DE in Fig. 4.6c) are not as pronounced as for fibre kinks (Fig. 4.6c).

4.4.2 Removing non-local signals

These "non-local" effects disappear after the spatial derivation (Eq. (4.7)), with the strain having the advantage of being a local measurement being every measurement compared to its neighbours. The spurious signals appear after integrating the strain into deformation and are space-invariant over each linear segment (Fig. 4.6b). Conversely, seismic signals have a finite wavelength variation (Fig. 4.6d) exhibiting a zero spatial mean when averaged over sufficiently large length scales. We can apply two conceptually similar but practically different approaches to remove these non-local signals and better approximate the displacement, as shown in Fig. 4.6.

Segment-wise method

The first approach (Fig. 4.6e, f) relies on computing the spatial mean over each linear segment to approximate the spurious signals and remove them from the deformation, obtaining a better displacement estimate. We refer to this approach as the "segment-wise" method. By applying this method to Eq. (4.9), we obtain an estimate of the displacement $\hat{u}(s,t)$ as the difference between the displacement $u(s,t)$ minus its spatial average $\overline{u}_n(t)$ over the nth segment at the location s, i.e.:

$$\hat{u}(s,t) = \delta(s,t) - \overline{\delta}_n(t) = u(s,t) - \overline{u}_n(t). \tag{4.10}$$

The spatial mean can be computed using a weighting (or tapering) window $w_n(s)$ integrating to one and with zero values outside the nth segment:

$$\overline{\delta}_n(t) = \int w_n(s')\delta(s',t)ds'. \tag{4.11}$$

Sliding-window method

Unfortunately, deploying linear fibre segment may be complex. Moreover, the precise knowledge of the fibre geometry is not always possible (e.g. for submarine cables). For these reasons, we also implemented another (and more flexible) method relying on the spatial mean removal over a sliding window with a characteristic length:

$$\hat{u}(s,t) = \delta(s,t) - (w * \delta)(s,t) = u(s,t) - (w * u)(s,t), \tag{4.12}$$

being w the weighting window and $*$ the convolution operator along space. We refer to this approach as the "sliding-window" method (Fig. 4.6h, i). Padding is necessary to get the values at the cable end. Padding can be done by filling with zeros, with the edge value, or with reflecting values (i.e. using mirrored values on the edge). We use the latter in this study.

Both the segment-wise and sliding-window methods reduce measurement non-locality. The segment-wise approach confines it to each segment's size. Conversely, the sliding-window method, similar to a finite impulse response (FIR) filter, restricts non-locality to the window's width, thereby reducing the impact of corrupted channels within a limited range. Both methods yield similar results (Fig. 4.6).

4.4.3 Additional note on DAS sensitivity to displacement

Using these methods, we can only recover an approximation of the true displacement. One of the reasons is that the removal of the spatial mean affects the response at low wavenumbers. Below, we describe the DAS sensitivity of the recovered displacement, focusing on the sliding-window approach. The convolution theorem allows to express Eq. (4.12) as,

$$\hat{U}(k,t) = (1 - W(k))U(k,t), \tag{4.13}$$

with uppercase characters indicating the spatial Fourier transform of the quantities indicated by the lowercase ones (i.e., $\hat{u}$, w and u).

The length and shape of the weighting window $w(s)$ both affect the accuracy of the recovered displacement. The sensitivity also varies based on the nature of the signals and the objectives of the analysis. The length of rectilinear fibre sections determines the maximum retrievable displacement wavelengths (Fig. 4.7a). However, long rectilinear sections may average out much shorter wavelengths. Additionally, a rectangular window produces a sinc weighting function in the wavenumber domain, offering higher sensitivity at low wavenumbers but introducing significant sidelobes (Fig. 4.7a). In contrast, a Hann window reduces sidelobes but decreases sensitivity at low wavenumbers (Fig. 4.7a). Thus, choosing the window shape involves balancing a flat response (without sidelobes) against a strict low cut-off wavelength.

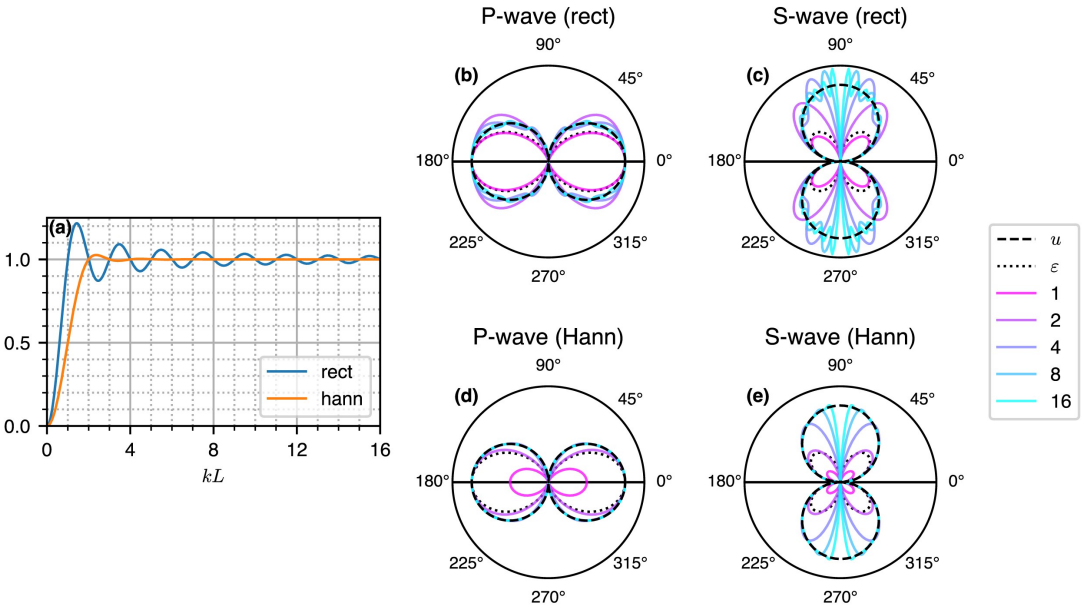

Figure 4.7: Sensitivity characteristics of deformation-recovered displacement. (a) The sensitivity is a function of the product between the apparent wavenumber and the length of the rectilinear section (kL); and the shape of the window (here rectangular and Hann windows are shown). (b–e) Directivity patterns for P (b,d) and S (c,e) waves using the rectangular and the Hann windows for different kL values ranging from 1 to 16 (see legend on the right). The horizontal black lines in (b-e) indicate the cable direction. From Trabattoni et al. (2023).

The apparent wavenumber varies with the wave's angle of incidence on the cable, implying a directional sensitivity of the deformation-recovered displacement (Fig. 4.7b-e). The infinite apparent wavelengths of waves striking the cable perpendicularly prevent their recovery. Concerning P waves, this results in no sensitivity at broadside angles, similar to single-component displacement (Fig. 4.7b, d). In this case, the DAS sensitivity converges to the desired displacement response as kL increases, i.e. with increasing ratio of rectilinear length to wavelength (from 1 to 16 in Fig. 4.7b, d). In Fig. 4.6, the strain (Fig. 4.6g) appears similar to the displacement (Fig. 4.6d) but exhibits lower amplitudes at almost normal incidence (therefore longer apparent wavelengths).

Additionally, S waves display a notch in the orthogonal direction of the directivity pattern, making them impossible to retrieve (Fig. 4.7c, e). The width of this notch depends on the kL value and the window type. As kL increases, the notch narrows (from 1 to 16 in Fig. 4.7c, e). The rectangular window converges twice as fast and has a notch half as wide as the Hann window, but it also produces more ripples (Fig. 4.7c, e). We

then validate this method to recover the by comparing data acquired on the Stromboli volcano by both DAS and co-located seismometers.

4.4.4 Application to DAS measurements: ordinary explosion

We compare DAS-recovered velocities with traces from co-located nodes using data from September 2021. We focus on a 600 m portion of the cable composed of three relatively rectilinear segments in the NT fibre sector. We analyse the recordings of a mild explosion on September 26, 2021, at 20:47:03 UTC.

To compare DAS and nodal seismometer data, we decimate the recordings to the same sampling rate (50 Hz) and filter them between 2.5 and 15 Hz (limited by the noise floor of the DAS instrument). We remove the instrumental response of the nodes and project the 3D particle velocities along the cable direction. We spatially integrate the strain rate recorded by DAS to obtain the deformation rate (Fig. 4.8c). However, this process is affected by noise accumulation at each change in cable direction. We then recover the velocity using both the segment-wise (Fig. 4.8d) and sliding-window (Fig. 4.8e) approaches. We manually define the segment boundaries (A-E) to apply the segment-wise approach. Due to a decline in recovery performance metrics, we treat a gradual change in orientation between B and C as a single straight segment, suggesting a need for balance between segment length and rectilinearity.

For the sliding-window approach, we determine an optimal Hann window length of 250 meters by varying the window length and calculating the correlation coefficient (CC) between DAS-recovered velocity and the particle velocity at each node (Fig. 4.9). The window length should ideally exceed the apparent wavelength of the waves and be shorter than the characteristic rectilinear length of the cable. Our results indicate that the extent of the longest rectilinear segment centred on the channel of interest limits the value of the optimal window length. Finally, we extract the DAS channels nearest to each node (#1-6 in Fig. 4.8e, g).

Using both methods, the DAS velocity waveforms align well in phase with the node recordings. For most stations, the correlation coefficients (CC) range from 0.7 to 0.8, reaching up to 0.9 at station #1 with the segment-wise method. Two stations showed poorer performance: station #6, affected by a sharp cable bend to avoid a rock outcrop, and station #5, limited by being on the shortest segment (DC). Both the sliding-window and segment-wise methods provide similar results in terms of CC. However, DAS velocity waveforms have amplitudes 2 to 7 times smaller than nodes, possibly due to imperfect cable coupling implying possible instrument miscalibration. We adjust the DAS waveforms to match the RMS values of the co-located nodes.

Examining the DAS data in space-time plots (Fig. 4.8), the segment-wise approach reveals space-invariant artefacts (e.g., before the event, near the BC segment borders in Fig. 4.8d) and wavefield discontinuities at segment boundaries (e.g., for the strongest arrival at marker B in Fig. 4.8d). These issues arise because the average is removed across all channels simultaneously, and each segment is processed independently. While both methods perform similarly, the sliding-window approach is more adaptable and generates fewer space-invariant artefacts.

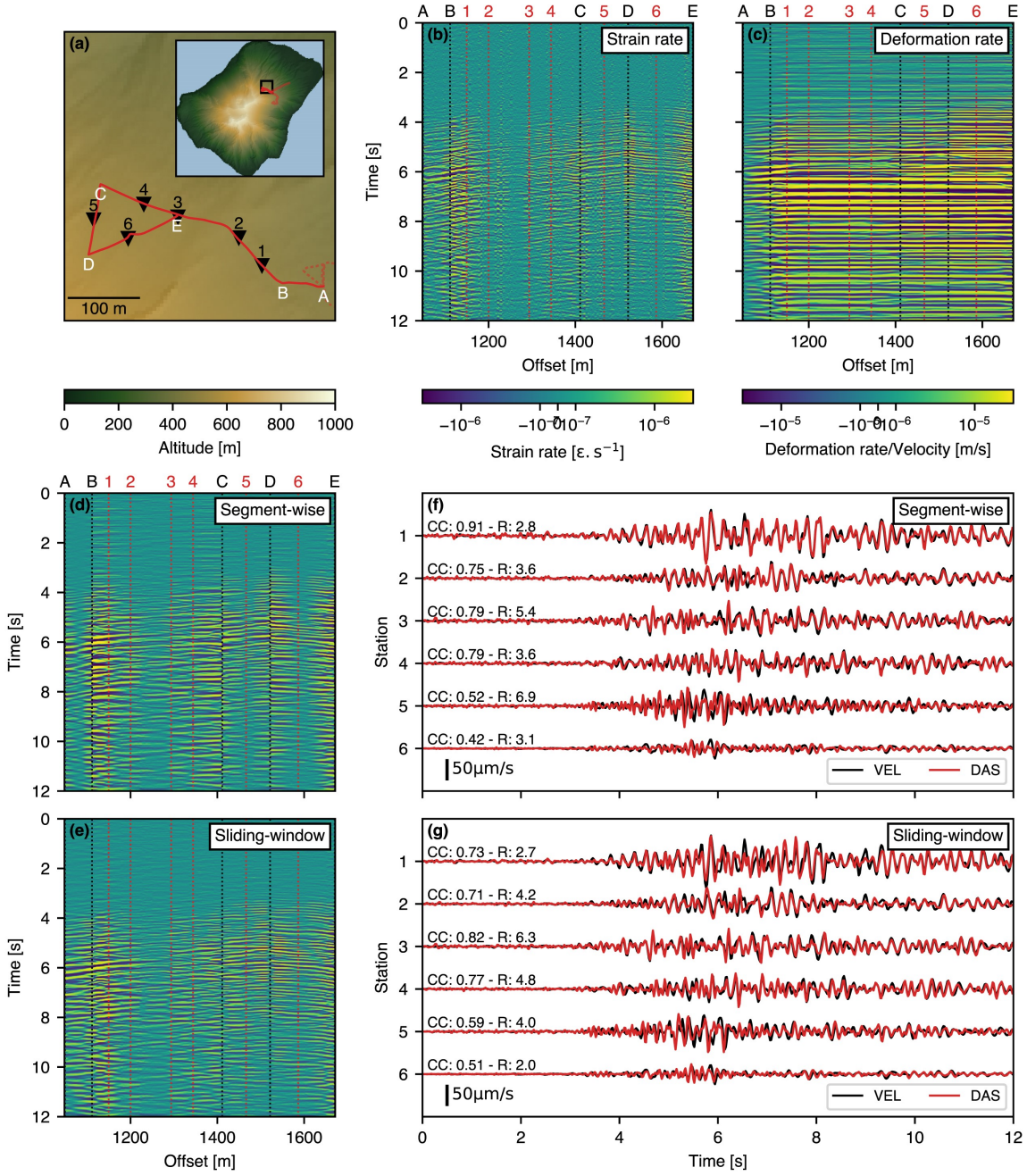

Figure 4.8: Comparison between velocities recovered from DAS and co-located seismometers. (a) Deployment of the fibre-optic cable on the Stromboli's NE flank, with a detail of the fibre section (NT) considered in this comparison (solid red line). Six nodes were deployed (#1-6) at the midpoints of the straight segments (black inverted triangles). Letters from A (i.e., the beginning of the cable section) to E (its end) mark the sharp changes in orientation. (b) Strain rate recorded along the NT cable segment. Dashed black lines indicate the changes in cable direction marked in (a). Red dotted lines represent the offsets of the DAS channel closest to each node. (c) Deformation rate without any processing. (d) Velocity recovered with the segment-wise approach using the A-E markers as segment limits. (e) Velocity recovered with the sliding-window approach with a 250 m Hann window. (f-g) Comparison between the velocity waveforms from the seismometers (in black) and recovered from DAS (in red), described using correlation coefficient (CC) and RMS ratio (R), for the segment-wise and sliding-window approaches respectively.

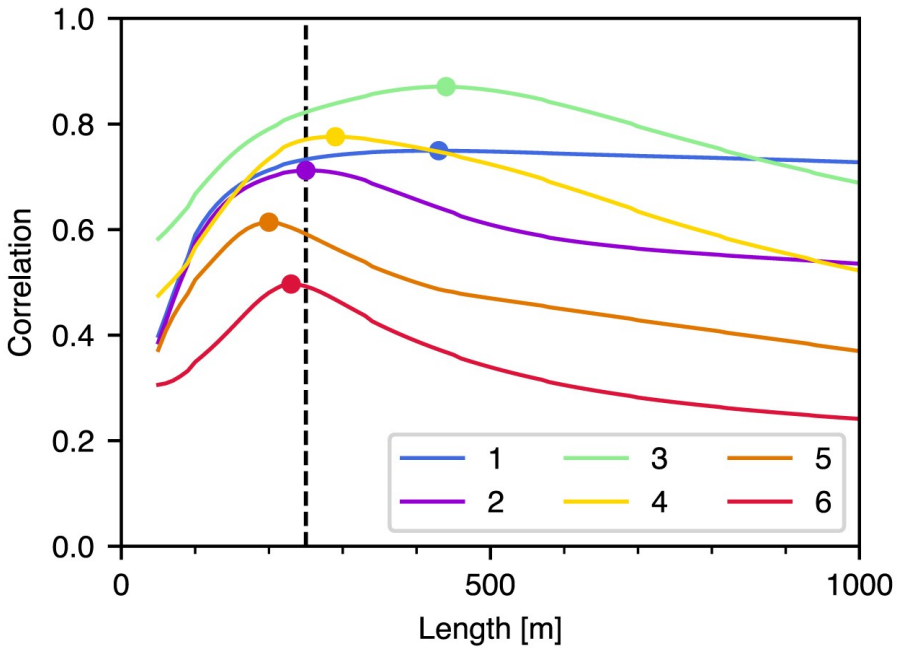

Figure 4.9: Search of the optimal window length L*. We compare DAS-recovered velocity computed with different window lengths using the sliding-window approach with the ground velocity recorded at the six co-located seismometers (nos 1–6). We use the CCs metric. Circles mark the optimal values for each channel. We find a correlation between the segment lengths and the value of L*. Channel no. 5 is located on the smaller segment (DE) and has the smallest L*. Its L* is twice its segment length because the effective length of the Hann window is half its size. Channel no. 3 is in the middle of the longest section (BC) and exhibits the longer L* of 450 m. The distance to the closest edge seems to be the main factor dictating L*. We chose a fixed value of 250 m (vertical dashed line) as the global L* (Figs 4.8e and g).

4.5 Discussion and conclusions

We investigate the phase and amplitude response of our DAS records at Stromboli by comparing DAS signals with independent measurements from co-located inertial seismometers. We use DAS and node data recorded in 2021 and 2022 and filtered between 0.5-15 Hz. Using the finite-difference method, we observe an almost perfect match in phase between DAS and node waveforms for most segments, as demonstrated by CC values up to 0.99 (Figs. 4.2 and 4.3; Tables 4.1 and 4.2). This is valid for ordinary and major explosions, with the latter exhibiting higher CCs probably due to higher SNRs (Table 4.1).

However, the amplitudes of DAS signals are lower than node ones by a factor $\boldsymbol{R}$ ranging between ~1.5 and 5 (Tables 4.1 and 4.2). We do not observe significant variations in this phenomenon depending on the intensity of the event and the year of measurement. Events of similar intensity recorded in different years show comparable results in terms of CC and R (Fig. 4.4; Tables 4.1 and 4.2). We speculate that although soil compaction changes over a year, it does not do so to an extent significantly enhancing ground-to-fibre coupling or increasing the amplitudes recorded by DAS. Moreover, the amplitude difference between DAS and node signals remains stable at different frequencies (Figs. 4.2 and 4.3).

Other studies reported slight differences between DAS and seismometer amplitudes, but never to such an extent (Wang et al., 2018; Currenti et al., 2021; Jousset et al., 2022). This amplitude underestimation may result from poor ground-to-fibre or cable-to-fibre coupling. As shown by several studies, the internal structure of the cable can

significantly affect how efficiently strain is transferred from the ground to the individual fibres, thereby impacting the amplitude of the recorded signals (Her & Huang, 2011; Reinsch et al., 2017; Diaz-Meza et al., 2023; Biagioli et al., 2024). In our experiments, we deployed a cable composed of a polyethylene jacket surrounding a loose kevlar layer and eight tight-buffered single-mode fibres. This structure is possibly at the origin of the low amplitudes of our measurements. Later in the thesis, in Section 5.9.1, we develop this concept further, showing how loose fibres in a cable (as in our case) may lead to underestimating the strain rate recorded by the DAS.

The spatial-integration method provides comparable results. Seismic velocity waveforms obtained from DAS data have a good similarity to those recorded by the nodes, as demonstrated by high CC of ~0.7-0.9 for most of the stations (Fig. 4.8). We also observe similar differences in amplitudes between DAS and co-located node measurements, up to a factor of 7. Moreover, the performance of the two solutions to remove the spatial mean from the integrated strain rate (i.e. segment-wise and sliding-window) is comparable (Fig. 4.8), although situationally dependent. Owing to its flexibility and lesser artefacts, we recommend the sliding-widow scheme as the standard conversion procedure.

These results demonstrate that DAS can effectively record signals comparable to traditional inertial seismometers. They also highlight the potential of the spatial-integration method for deriving seismic velocity waveforms from DAS strain rate signals without needing additional seismometers. Converting strain rate to seismic velocity or displacement enhances instrumental sensitivity, offering several advantages: (i) compatibility with standard seismological tools, (ii) increased sensitivity to long-wavelength signals and a wider directivity pattern, and (iii) proportionality to the phase of the backscattered light, which is the primary measurement from most modern DAS interrogators using coherent detection techniques. However, deformation-based methods are limited by the straightness of the deployed fibre optic cable, as the maximum recoverable wavelength for a straight section directly relates to its length. This suggests using geometries with long rectilinear segments. With these data conversion methods, we make DAS data more comparable to traditional seismological data, allowing the reuse of existing seismological tools.

These findings suggests the data acquired by the DAS is a valid representation of the near surface ground deformation due to seismic waves generated by the volcanic activity. Therefore, we can use DAS signals to obtain information about the location and dynamics of the volcanic phenomena generating such signals in the following chapters.

Chapter 5

Array Analysis of Seismo-Volcanic Activity with Distributed Acoustic Sensing

Preface

In this chapter we attach the paper Biagioli et al. (2024) as it was published in January 2024 in *Geophysical Journal International*:

F. Biagioli, J.-P. Métaxian, E. Stutzmann, M. Ripepe, P. Bernard, A. Trabattoni, R. Longo, M.-P. Bouin, **Array analysis of seismo-volcanic activity with distributed acoustic sensing**, *Geophysical Journal International*, Volume 236, Issue 1, January 2024, Pages 607–620, https://doi.org/10.1093/gji/ggad427.

Nothing has been changed exception made for numbers of figures, tables and equations that are made consistent with the rest of the thesis. Supplementary information of the article are provided in Section 5.9. The numbering of the supplementary figures starts again from 1 with an S in front of the figure number (e.g., Fig. S5.1). References for both main text and supplementary information are at the end of the thesis. The author apologises for any repetition and redundancy necessary to make the article a work in itself.

In the previous chapters we presented our dataset and calibrated our strain rate recordings. In this chapter we continue with the analysis of strain rate data. We use DAS and co-located nodal arrays to derive information about the characteristics and the direction of propagation of seismic waves recorded at Stromboli. The use of seismic array in volcano seismology is crucial, enabling location of events lacking clear onsets such as volcanic tremor and VEQs. Furthermore, the distributed nature of DAS carries a growing interest in possible applications of array processing methods. Several practical and theoretical

approaches have been proposed by e.g. van den Ende and Ampuero (2021), Klaasen et al. (2021), Nayak et al. (2021), Näsholm et al. (2022).

In this study we apply a method relying on the estimation of delay times between sensor pairs with a linear interpolation of the cross-spectrum phase. The method is particularly suited for small-aperture arrays with respect to the wavelengths of interest. Métaxian et al. (2002) successfully applied this method to source-locate VEQs and volcanic tremor at Arenal Volcano (Costa Rica) with several seismic arrays. Furthermore, Métaxian et al. (2020) observed a seismicity migration during a phreatic eruption at Merapi volcano (Indonesia).

First, we exhibit the data collected during our initial DAS survey in September 2020. We expand the visualisation and interpretation of DAS data started in Section 3. We use strain rate traces derived from nodes to calibrate the DAS measurements (as done in Section 4). We then present the results of the array processing technique laid by Métaxian et al. (2002) using small-aperture (~40 – 100 m) DAS and nodal arrays. We perform the analysis in different frequency bands (e.g., between 1 – 3 and 3 – 5 Hz) and compare the results obtained with the two dataset.

5.1 Abstract

Continuous seismic monitoring of volcanoes is challenging due to harsh environments and associated hazards. However, the investigation of volcanic phenomena is essential for eruption forecasting. In seismo-volcanic applications, Distributed Acoustic Sensing (DAS) offers new possibilities for long-duration surveys. We analyse DAS strain rate signals generated by volcanic explosions and tremor at Stromboli volcano (Italy) recorded along 1 km of dedicated fibre-optic cable. We validate DAS recordings with co-located nodal seismometers. Converting node measurements to strain rate, we observe a perfect match in phase between DAS and node waveforms. However, DAS amplitudes appear to be around 2.7 times smaller than those of node records, which we explain as due to the inefficient ground-to-fibre strain transfer in the loose cable. We invert time delays between strain rate waveforms and confirm that the DAS enables us to retrieve a dominant and persistent seismic source in the proximity of active craters. This stable source location is confirmed by node array analyses. Despite an observed high noise level of strain rate signals outside a range of 2 – 15 Hz, our results demonstrate the potential of this new technology in monitoring volcanic areas.

5.2 Introduction

Volcano seismology is essential to investigate the various and complex signals generated by volcanic phenomena, as well as for eruption forecasting and monitoring (Chouet & Matoza, 2013; McNutt & Roman, 2015). Seismic arrays have been proven effective in detecting and locating even faint seismo-volcanic signals (e.g., La Rocca, Saccorotti, et al., 2004; Inza et al., 2011; Hansen & Schmandt, 2015; Glasgow et al., 2018). Dense arrays also improve observations of spatial and temporal changes within the subsurface (e.g., Bruno et al., 2017; Takano et al., 2020). However, volcanic areas are remote and

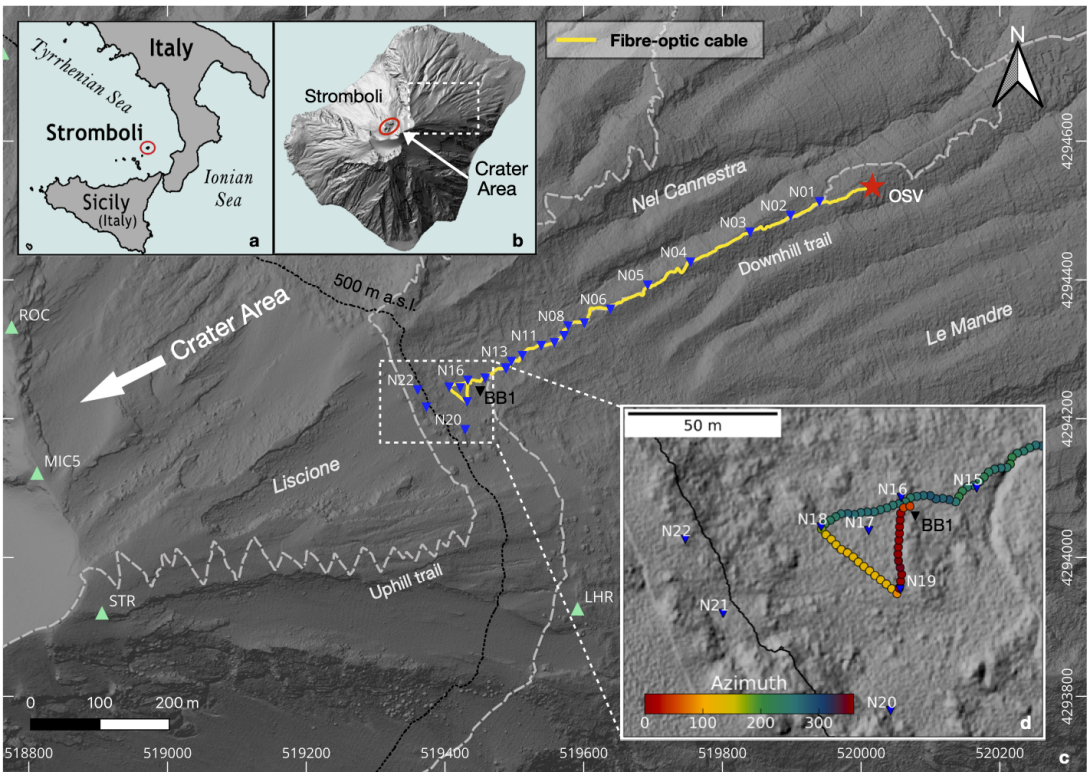

Figure 5.1: High-resolution digital elevation model (DEM) of Stromboli Northeast flank. The fibre-optic cable (yellow line), the 22 SmartSolo nodes numbered from N1 to N22 (blue triangles), the broadband station BB1 (black triangle) are displayed. Some node names are omitted for visual reasons, however they are named from N1 to N22 in a progressive manner starting from the Geophysical Observatory (OSV, red star). Green triangles mark the location of the seismic (ROC, STR), infrasonic (MIC5), and tiltmeter (LHR) stations of the Laboratory of Experimental Geophysics (LGS, University of Florence). (Bottom right) Magnified view of the triangle-shaped DAS and seismic arrays, with DAS channels colored according to their azimuth with respect to the North. The DAS interrogator was hosted inside the OSV. The DEM is computed from images taken in 2014 and courtesy of Italian Civil Protection.

harsh environments presenting high hazard levels. Installing and maintaining seismic arrays in these contexts poses significant challenges. After an initial use in the oil and gas industry (Hartog, 2017), Distributed Acoustic Sensing (DAS) is nowadays widespread in other fields of geophysical application, such as earthquake seismology (Jousset et al., 2018; Wang et al., 2018; Sladen et al., 2019; Williams et al., 2019) and near-surface seismic characterisation and monitoring (Daley et al., 2013; Dou et al., 2017; Ajo-Franklin et al., 2019; Fang et al., 2020; Spica et al., 2020).

In seismo-volcanic contexts, DAS offers new possibilities for long-duration surveys at high temporal (up to kHz) and spatial (to the metre scale) resolutions with reduced risks and costs. DAS measures dynamic longitudinal strain via optical interferometry of the Rayleigh backscattered light of emitted coherent laser pulses, whose signature changes when the cable is lengthwise deformed by propagating seismic waves (Hartog, 2017; Lu et al., 2019; Lindsey, Rademacher, & Ajo-Franklin, 2020). Via the DAS technique, a single interrogation unit can simultaneously probe tens of kilometers of a fibre-optic cable, mimicking a large, meter-scale array of synchronized single-component sensors (Hartog, 2017; Lindsey et al., 2017). DAS measurements can be performed remotely at a fibre end, hosting the interrogation unit in a safe location (Nishimura et al., 2021; Jousset et al., 2022). The optical cable can be buried at a sufficient depth to mitigate the risk associated

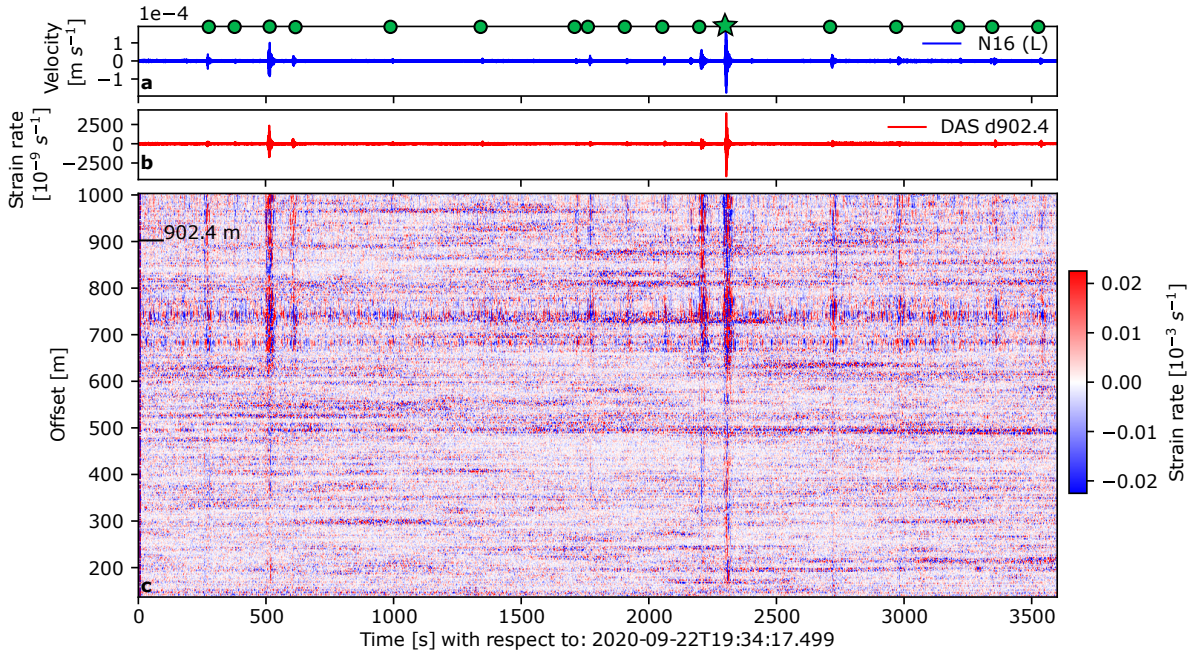

Figure 5.2: (a) Velocity recorded by the L component of node N16 on 09/22/2020 from 19:34 to 20:34. (blue). (b) strain rate at co-located DAS channel d902.4 for the same time interval (red). Green circles in (a) mark the explosive events detected with a recursive STA/LTA algorithm (Beyreuther et al., 2010). The green star marks the largest event. (c) strain rate record at each of the 362 DAS channels ordered according to their offset from the DAS interrogator. The black horizontal segment marks the DAS channel d902.4. Data are filtered between $1 - 10$ Hz in this figure.

with eruptive events.

Previous DAS experiments on volcanoes exhibited promising results. Nishimura et al. (2021) located the hypocenters of shallow volcanic earthquakes and estimated site effects at Azuma volcano, Japan. Klaasen et al. (2021) revealed the presence of a high and low-magnitude seismicity at Mount Meager, British Columbia. At mount Etna, Italy, Currenti et al. (2021) efficiently compared DAS strain measurements with broadband inertial-seismometers, while Jousset et al. (2022) recorded the seismo-acoustic waves associated with small-scale volcanic events linked to fluid migration. This latter study also imaged shallow structural heterogeneities. Currenti et al. (2023) detected and analysed Very Long Period ($0.01 - 0.2$ Hz) seismic signals at Volcano island, Italy, during a volcanic unrest phase.

Stromboli volcano exhibits a persistent ordinary activity (Rosi et al., 2000) accompanied by a high explosion rate (~13 events/hour; Ripepe et al., 2008), and emits signals in a wide range of frequencies ($10^{-2} - 10$ Hz; Neuberg et al., 1994; Chouet et al., 1997, 2003). These characteristics make it one ideal test bench for DAS applications at volcanoes. The origin of the explosions is generally attributed to the nucleation, rise and final burst of gas slugs in the conduit (Blackburn et al., 1976). A continuous and less energetic volcanic tremor is also observed in the seismic records, with frequencies mainly between $1 - 5$ Hz (Nappi, 1976; Langer & Falsaperla, 1996; Ripepe et al., 1996; Wassermann, 1997). Tremor signals at Stromboli are inferred to be linked with the coalescence of small (<0.5 m) gas bubbles in the conduit bursting every $\sim 1 - 2$ s (Ripepe & Gordeev, 1999).

However, this ordinary activity can be occasionally interrupted (or accompanied) by lava flows and violent explosions, the so-called Strombolian paroxysms (Métrich et al.,

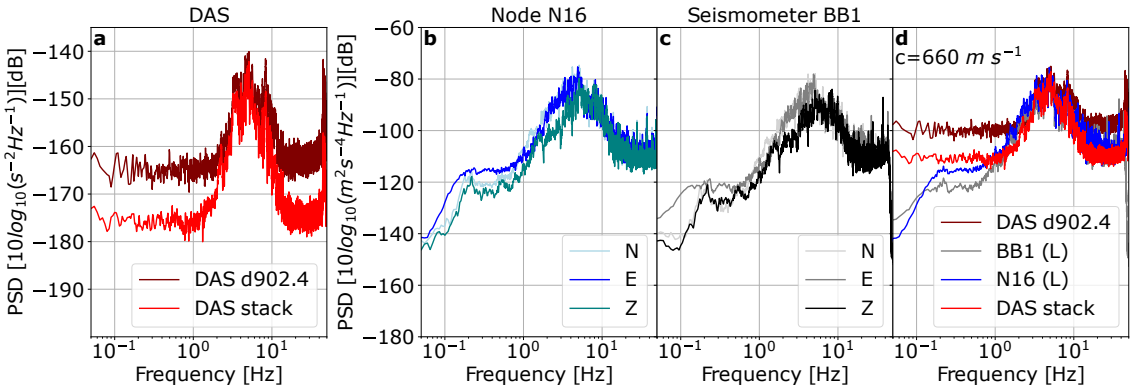

Figure 5.3: PSDs computed during the hour-long time series (09/22/2020 19:34 – 20:34 UTC) for different unfiltered records: (a) PSD of DAS channel d902.4 (brown) and stack of the PSDs calculated for the channels d892.8-912.0 (red), in strain rate. (b) and (c) PSDs of the 3 components of co-located node N16 and broadband seismometer BB1, in acceleration. (d) PSDs of the DAS channel d902.4 and the DAS d892.8-912.0 channel stack converted to acceleration using Eq. (5.1), and the L components of N16 and BB1, in acceleration.

2021; Ripepe, Lacanna, et al., 2021). Those events represents a major threat for both inhabitants and tourists due to the wide areal coverage of the volcanic ballistic projectiles and the potential formation of pyroclastic flows (Rosi et al., 2013).

To address these challenges, we aim to demonstrate that the strain rate recorded by DAS at Stromboli can be used to monitor volcanic explosions and tremor. Seismo-volcanic signals as those observed at Stromboli are spindle-shaped and characterised by emergent onsets without marked S-wave arrivals (Métaxian et al., 2002; La Rocca, Saccorotti, et al., 2004; Wassermann, 2012). Furthermore, volcanic tremor is a continuous signal lacking clear body-wave phases (Chouet, 1996a). It is difficult to locate these signals with classical methods of hypocenter determination (Métaxian et al., 2002; Wassermann, 2012; Inza et al., 2014).

To circumvent this difficulty, we can use array processing methods, such as delay-and-sum beamforming (Capon et al., 1967; Schweitzer et al., 2012) or Multiple Signal Classification (MUSIC; Schmidt, 1986), commonly used in volcanic areas (Chouet, 1996a; Wassermann, 1997; Inza et al., 2011, 2014; Leva et al., 2022). These methods provide insights into seismic wave propagation direction and apparent velocity. Several studies exhibit results of these methodologies applied to DAS arrays with linear to more complex geometries (Lindsey et al., 2017, 2019; Fang et al., 2020; Klaasen et al., 2021; Nayak et al., 2021; van den Ende & Ampuero, 2021; Jousset et al., 2022). In these studies, either single events or events selected by signal detection methods are analysed. In volcanic environments, Klaasen et al., 2021 applied beamforming analysis to high frequency earthquakes most likely related to geothermal fluid movements, while Jousset et al., 2022 located the source of volcanic explosions. Yet, to our knowledge, there has been no reports of employing these or other array techniques to analyse continuous strain rate signals consisting of volcanic tremor together with explosions.

This manuscript is organized as follows. First, we provide a comprehensive account of the fieldwork and the experimental setup (Section 5.3). We then present and compare data recorded with the DAS and with a co-located seismic array (Sections 5.4 and 5.5). Afterwards, we estimate the slowness vector with seismic velocity and strain rate records using array processing techniques (Section 5.6). Finally, we discuss the results and their

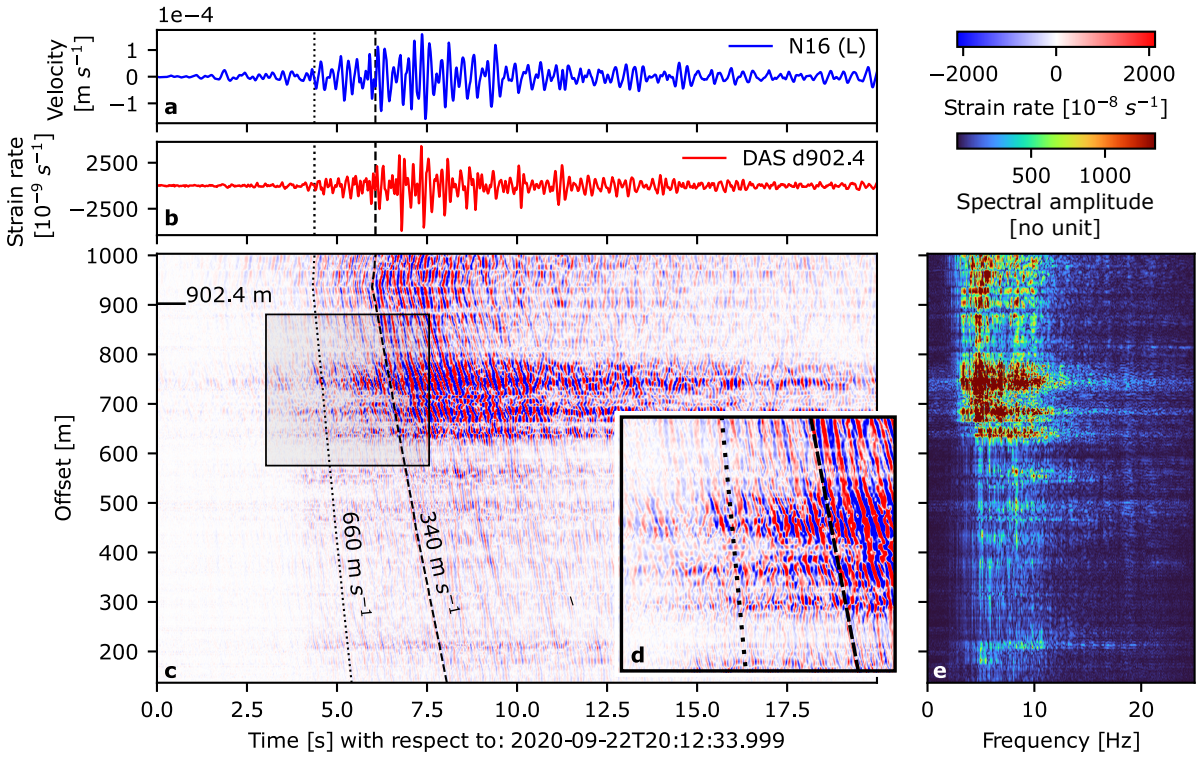

Figure 5.4: (a) velocity measurement of the L component of node N16 (blue) during an explosive event occurred at 20:14:30 UTC on 2020/09/22 (green star in Fig. 5.2). (b) strain rate of the same event at co-located DAS channel d902.4 (red). (c) strain rate record at each of the 362 DAS channels ordered according to their offset from the DAS interrogator. Black horizontal line in (c) marks the location of DAS channel d902.4 along the cable. (d) Zoom-in of the frame in (c). Dashed lines in (a–d) mark the theoretical arrival times at the several sensors of waves with velocities of 660 and 340 m/s starting from the onset of the acoustic wave at the source as recorded by the MIC5 infrasonic station (Fig. 5.1). (e) Frequency domain representation of the strain rate record below 25 Hz along the fibre for the 20 s of the explosion.

significance regarding the use of DAS for volcanic monitoring (Sections 5.7 and 5.8).

5.3 Field experiment and data

5.3.1 Description of the field-work

In September 2020, we deployed 1 km of dedicated fibre-optic cable at Stromboli volcano (Fig. 5.1). The cable is composed of a polyethylene jacket which encloses a loose kevlar layer surrounding 8 tight-buffered optical fibres (see Supplementary Note A in the Supplementary Information). We started from the Geophysical Observatory of the University of Florence, located at an altitude of 200 m a.s.l., and we continued along the path towards the summit. We faced several challenges including the steep slope, the high density of the vegetation below 400 m a.s.l., and the ashy nature of the soil. The trench was dug by hand by local workers, while the scientific team buried the cable trying to ensure the best possible coupling with the ground. This was sometimes complicated in areas of steep drop or in curves because of the nature of the soil. The cable was buried about 30 cm deep over a length of 870 m. First, we followed a path oriented towards the craters. Then, we implemented a triangular array with sides measuring 30 meters at the path's endpoint

(Fig. 5.1d). This specific design allowed us to measure strain rate in directions other than the main cable path and test array processing techniques using DAS data. In this higher area, the fibre was installed under a steep (~ 25°) but relatively flat slope characterised by poor vegetation at an altitude of ~450 m a.s.l.

The DAS interrogator (Febus A1-R) was hosted inside the Geophysical Observatory. We carried out DAS measurements for 1 week, from September 15 to 23, 2020, with continuous recording sessions of $7-8\ hrd^{-1}$. We recorded strain rate data with a sampling frequency of 2 kHz, a spatial interval of 2.4 m and a gauge length of 5 m leading to a number of 362 useful channels.

22 nodes SmartSolo IGU-16HR 3-component (3C) nodes (named from N1 to N22 progressively from the Geophysical Observatory) with a corner frequency of 5 Hz and a sampling rate of 250 Hz were installed along the fibre path (Fig. 5.1, blue triangles) during the second half of the experiment. A Guralp digitizer equipped with a CMG-40T 30 sec seismometer and an infrasound sensor (station BB1) was placed in the upper part of the path, close to the lower corner of the triangle (Fig. 5.1, black triangle). The inertial sensor distribution along the path of the fibre optic cable was designed such that we could compare records made with the different technologies. DAS, nodes, and the broadband seismometer recorded simultaneously between 20 and 23 September 2020.

5.3.2 Pre-processing

To geolocalise each DAS channel we carried out a series of 56 taps along the fibre. By searching for the earliest arrival times, we obtained the relative positions along the cable of a subset of channels as well as their GPS positions. The latter were measured by a kinematic GPS survey. For this purpose, we used 2 Leica GR25 receivers. One of these was installed in a fixed position and in continuous recording at the Geophysical Observatory while we made a pathway with the second. The channels are linearly interpolated along the fibre GPS layout in between the positions of the 56 taps. strain rate data are decimated to 200 Hz. Seismometers are corrected for their instrumental response.

5.4 Data

During the experiment, the volcano showed a typical Strombolian regime, characterised by a number of ordinary explosive events around 14 events/hour emitting acoustic pressures lower than 0.5 bar. A persistent volcanic tremor of amplitude between $1-3$ μm/s was also present. We analyse the entire dataset acquired during the experiment. In this work, we show the results for one hour of raw measurements between 19:34 – 20:34 UTC on 09/22/2020. Due to the level of volcanic activity, this period of time includes 17 explosive events of varying intensity. A persistent volcanic tremor is also present as a background signal throughout the entire hour.

Fig. 5.2 exhibits an example of both strain rate and seismic velocity recorded during 1 hr and filtered between $1-10$ Hz, that is in the spectral band of explosion-quakes ($1-10$ Hz) and volcanic tremor ($1-5$ Hz) at Stromboli (Langer & Falsaperla, 1996; Ripepe et al., 1996; Chouet et al., 1997). Fig. 5.2a shows the seismic velocity of the so-called L component of node N16 along the direction of the co-located fibre-optic cable obtained by rotation (azimuth:250°and tilt:22°). Fig. 5.2b shows the strain rate of co-located DAS channel d902.4. We observe the same events in both strain rate and velocity time series.

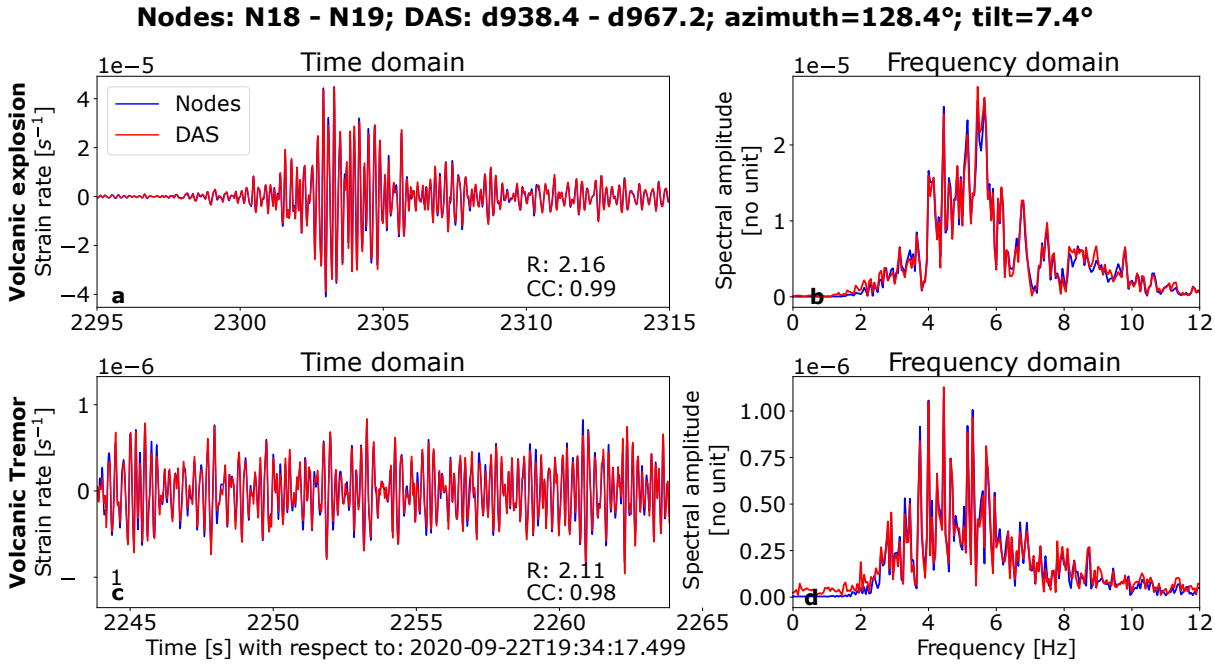

Figure 5.5: Comparison between the strain rate traces recorded by DAS (red) and obtained from nodes (blue) using Eq. (5.2) across the segment N18–19 (DAS channels d938.4-d967.2) for one explosive event (top row) and 20 s of volcanic tremor (bottom row), in both time (left column) and frequency (right column) domains. The ratios (R) between the RMS amplitudes of node and DAS traces, and the maximum cross-correlation coefficients (CC) between the two waveforms are shown in the bottom right of (a) and (c). To enhance clarity, we rescale DAS strain rate traces by multiplying them with the ratio R.

We then compare power spectral densities (PSDs) for 1 hr (09/22/2020 19:34–20:34 UTC) of unfiltered signals recorded by DAS, nodes and the broadband seismometer. Fig. 5.3a shows the strain rate PSD of DAS channel d902.4. For comparison, we also plot the PSD stacked for channels d892.8–912.0 (i.e., in a 20 m window centred on channel d902.4). Fig. 5.3b,c show the seismic acceleration PSDs of the Z, N, and E components of co-located N16 node and BB1 broadband seismometer, respectively. In Fig. 5.3d we compare the seismic acceleration PSDs of the L component of N16 and BB1 with the seismic acceleration obtained from the strain rate used in Fig. 5.3a using the following relation (e.g., Aki & Richards, 2002; Jousset et al., 2018; Wang et al., 2018):

$$\dot{\varepsilon} = \pm \ddot{u}/c, \tag{5.1}$$

where $\dot{\varepsilon}$ is the DAS strain rate, $\ddot{u}$ is the seismic acceleration and c is the apparent phase velocity along the cable direction. We re-scale the strain rate PSDs by considering an apparent velocity of 660 m/s and an amplitude correction factor of 2.7. This apparent phase velocity corresponds to the dominant signals and is determined in Section 5.6.4. The amplitude correction factor is obtained after a proper calibration of DAS strain rate measurements in Section 5.5.

After correcting the amplitudes by the factor 2.7 we observe a good match between the acceleration PSDs derived from DAS and recorded by the L components of N16 and BB1 in the frequency range 2–10 Hz (Fig. 5.3d). Outside this frequency band, the DAS acceleration PSD corresponding to the single channel d902.4 exhibits higher (~15 dB) values of noise levels (Fig. 5.3a,d). As pointed out by e.g. Hudson et al., 2021, stacking the PSDs computed for multiple DAS channels results in improved signal-to-noise ratios.

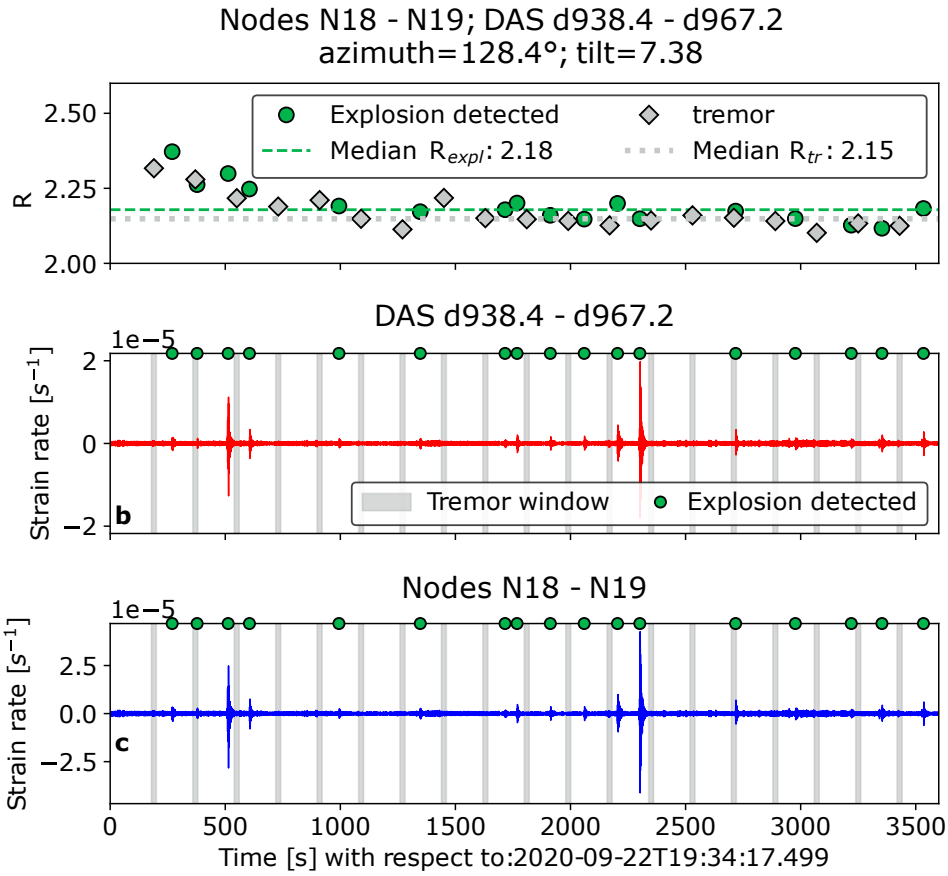

Figure 5.6: (a) Ratios (R) between the RMS amplitudes of strain rate obtained from nodes and DAS along segment N18-19 are calculated for various time windows throughout the entire hour shown in Fig. 5.2. This includes 17 volcanic explosions detected using an STA/LTA algorithm (green circles) and 20 windows containing volcanic tremor signals each with a length of 20 seconds (gray diamonds). The green dashed line in (a) represents the median value of the ratios R_{expl} calculated from explosion signals. The gray dotted line in (a) represents the median value of the ratios R_{tr} calculated from tremor signals. (b) DAS cumulative strain rate trace along the segment. (c) Node-derived strain rate trace along the segment. In (a) and (b), green circles indicate the detected explosions and gray vertical bars represent the 20-second long tremor windows used to compute R in (a).

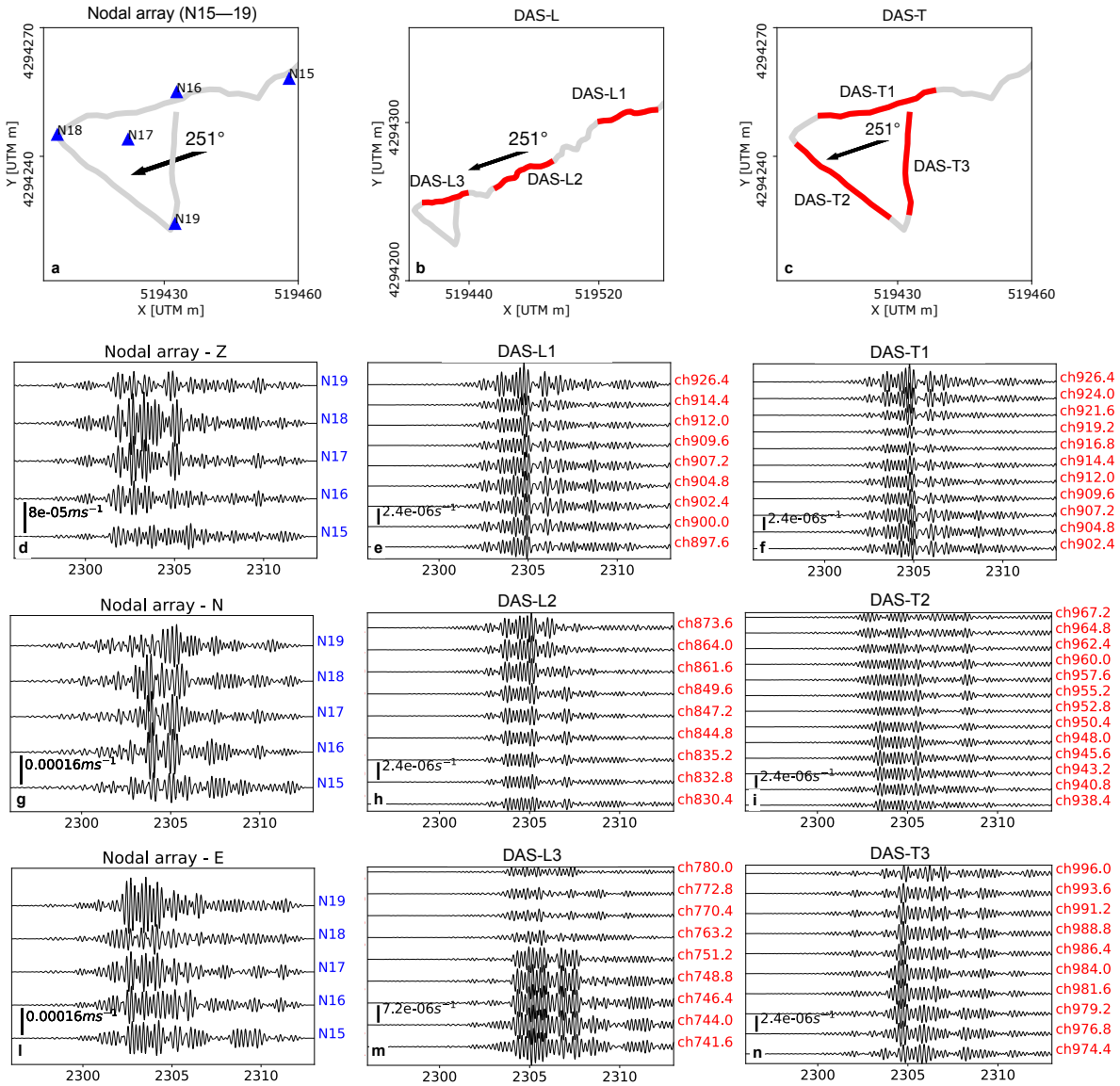

Figure 5.7: Geometry of the nodal array N15–19 (a) and of the DAS-L (b) and DAS-T (c) arrays. The black arrow in (a-c) indicates the back-azimuth (251°) of the central part of the active craters with respect to the centroid of each array. (d-n) show the traces for an explosive event (same as in Fig. 5.4). (d, g, l) show the 3 components of the 5 nodes. (e, h, m) show the 10 DAS channels along the 3 segments of the DAS-L array. (f, i, n) show the 10 DAS channels along the 3 segments of the DAS-T array. Traces are band-pass filtered in the 3–5 Hz frequency range.

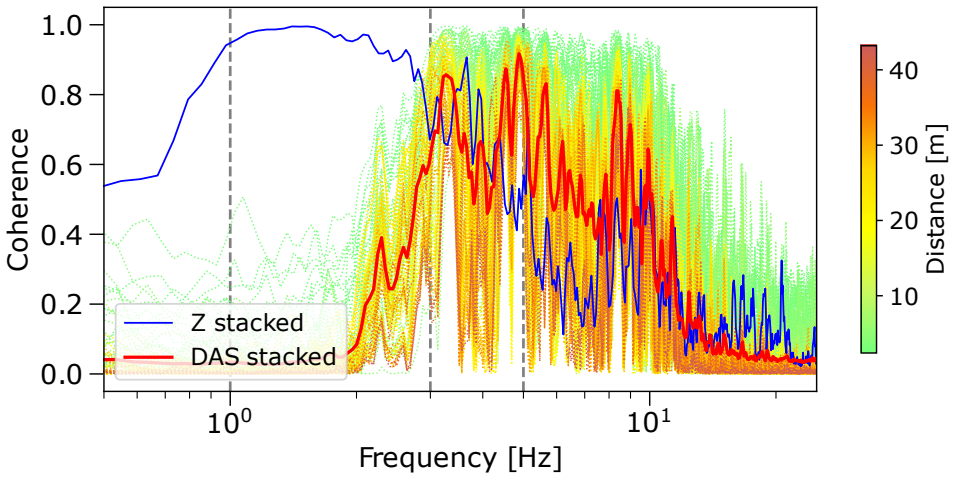

Figure 5.8: In red, average coherence computed during the unfiltered 1 hr long strain rate time series (09/22/2020 19:34–20:34) between all of the 135 channel pairs in the 3 segments of the DAS-L array. Coherence traces of each pair are also shown as dotted lines (with colors relative to the distance between the two channels). In blue, average coherence between the N component of each node pair in the array N15–19 during the same period of time. Grey vertical dashed lines mark the values of 1, 3 and 5 Hz, that are the limits of the two frequency bands (i.e. 1–3 and 3–5 Hz) for which we compare array analysis results with strain rate and seismic velocity data.

In our case (Fig. 5.3a,d), we obtain lower noise levels below 3 Hz and above 10 Hz than in the case of an individual DAS channel. However, the DAS noise level is still too high to observe the 0.1–0.14 Hz spectral peak corresponding to secondary microseisms (e.g., Stutzmann et al. 2009). It is instead visible on acceleration PSDs of the N and Z components of the seismometers (Fig. 5.3b,c). We note that this spectral peak is also scarcely visible in the PSDs of the L components for BB1 and N16 (Fig. 5.3d).

The time-domain signal from DAS channel d902.4 converted into acceleration using Eq. (5.1) bears good resemblance to those recorded by the L components of N16 and BB1 (Fig. 5.3d). The maximum cross-correlation coefficients between the DAS-derived acceleration and N16/BB1 are 0.6 for the entire hour in Fig. 5.2 and 0.7 when specifically analysing the explosion at 20:14:37 UTC on 09/22/2020 (marked by a green star in Fig. 5.2).

Fig. 5.4a,b show the signals generated by this explosion recorded by one node and the co-located DAS channel. The dominant frequencies are mainly between 2–15 Hz (Fig. 5.4e). Fig. 5.4c displays the strain rate recorded by the entire DAS array. The slope of the wavefronts gives the apparent velocity along the fibre. For comparison, we compute the theoretical arrival times for waves traveling from the craters to each sensor starting from the onset of the infrasonic pressure wave (20:14:37 UTC) as recorded by the MIC5 acoustic station (Fig. 5.1). We do not take into account the topography and choose velocities of 660 m/s (corresponding to the dominant signals obtained from the array analysis in Section 5.6.4) and 340 m/s (i.e., the acoustic wave velocity). We observe that the ground-coupled (Braun & Ripepe, 1993) infrasonic pressure wave (340 m/s) is visible on both DAS and seismic data at the time marked by the dashed line in Fig. 5.4a-d. Although it is not the most energetic phase observed, the infrasonic wave propagates all along the cable (Fig. 5.4c,d).

Furthermore, we observe in Fig. 5.4c an area between DAS channels d662.4–d751.2 (zoomed in Fig. 5.4d) where the wavefronts exhibit smaller slopes comparable with ap-

parent velocities lower than the sound speed. The area also displays larger strain rate signals, reaching up to ten times the amplitudes found in other fibre sections. Moreover, this portion of the cable deployment correlates quite precisely with a change in topography along the slope. This change can be observed in Fig. 5.1 close to node N06 (at approximately 360 m a.s.l.). Northeast (and at lower altitudes) of node N06, lava flows are visible. To the southwest (and at higher altitudes) the lava flows disappear where the topography becomes smoother due to ash coverage (see Fig. S5.1 in Supplementary Information). This is discussed in more detail in Section 5.7.

5.5 DAS data calibration

Prior to any further analysis, we calibrate and evaluate the quality of DAS recordings by comparing it with the strain rate retrieved from co-located nodes. The average strain rate along a linear segment of length nL_G (where n is the number of gauge lengths L_G contained in the segment) can both be estimated by stacking the strain rate $\dot{\varepsilon}$ recorded by DAS or by differentiating the seismic velocities $\dot{u}$ in the cable direction at the two endpoints of the segment (van den Ende & Ampuero, 2021). This translates in the following finite-difference relationship (Wang et al., 2018):

$$\begin{aligned} &\dot{\varepsilon}|_{x=-(n-1)L_G/2} + \cdots + \dot{\varepsilon}|_{x=0} + \cdots + \dot{\varepsilon}|_{x=(n-1)L_G/2} = \\ &= \frac{\dot{u}|_{x=nL_G/2} - \dot{u}|_{x=-nL_G/2}}{L_G}, \end{aligned} \tag{5.2}$$

where $\dot{\varepsilon}$ and $\dot{u}$ are evaluated at different positions x along the segment. We consider six cable segments and the corresponding nodes: N19–16, N18–19, N16–18, N10–11, N9–10, N3–4. Given our experimental setup (2.4 m of channel spacing and 5 m of gauge length), the left-hand side of Eq. (5.2) is equivalent to the summation of one DAS channel every two along each fibre segment, in order to mitigate the spatial-averaging effect of the gauge length. We obtain the components of the seismic velocity along the fibre direction by rotating the 3 components of each node according to the azimuth and slope of the corresponding cable segment. In the right-hand side of Eq. (5.2) we differentiate these longitudinal components to ensure an accurate comparison with DAS data.

Fig. 5.5 exhibits the comparison between the strain rate derived from DAS and nodes using Eq. (5.2) for the explosion shown in Fig. 5.4 and for 20 s of volcanic tremor, in both time and frequency domains. In the 2–15 Hz frequency band, DAS and node strain rate waveforms show an excellent agreement in phase. The maximum cross-correlation coefficients between DAS and node traces reach a value of 0.99 for the explosive event (Fig. 5.5a) and 0.98 for the volcanic tremor-only phase (Fig. 5.5c). Therefore, we obtain a better correlation between DAS and node data than using Eq. (5.1) in Section 5.4.

However, DAS strain rate exhibits lower amplitudes with respect to the strain rate derived from the nodes. To systematically estimate these amplitude differences in the time domain, we use the following workflow. Firstly, we apply a recursive STA/LTA algorithm (Beyreuther et al., 2010) over the strain rate time series. This enables us to detect 17 explosive events of varying intensity, as displayed in Fig. 5.6. Next, for each segment we compute the ratio R between Root Mean Square (RMS) amplitudes of nodes and DAS strain rate traces for 4-second time windows centered on each explosive

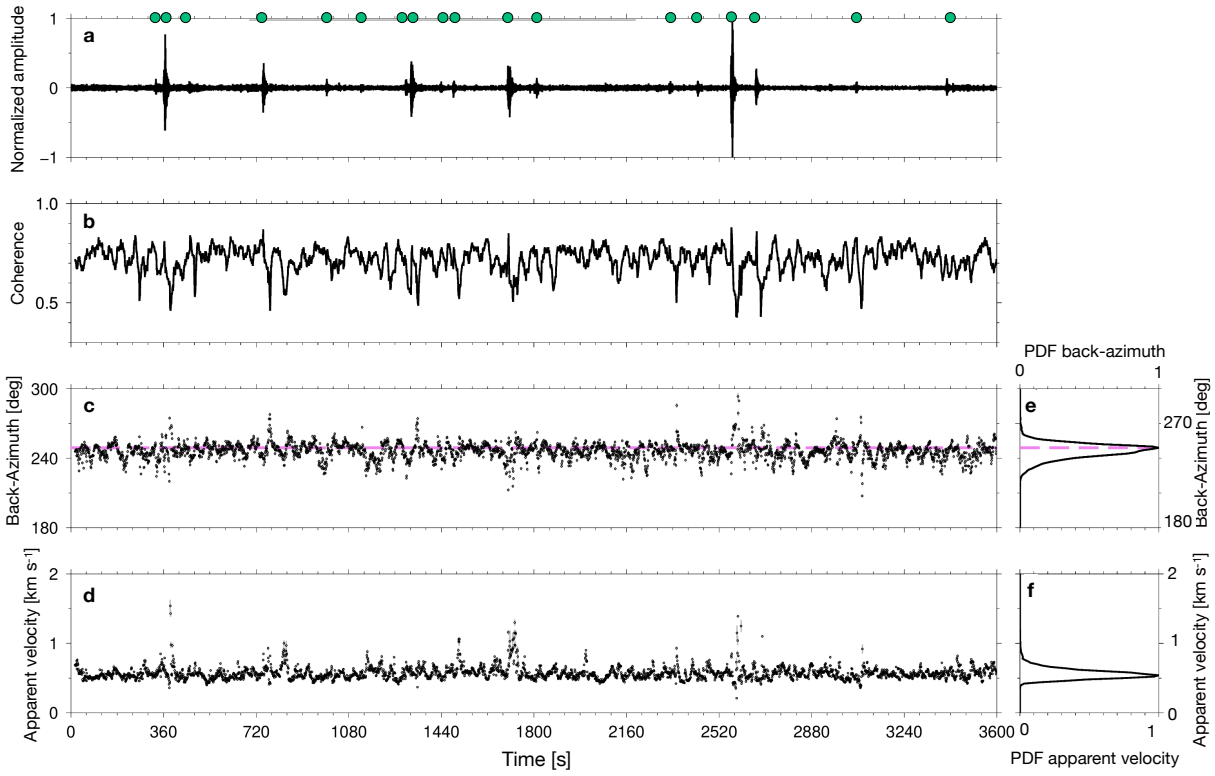

Figure 5.9: (a) 1-hr seismic velocity trace of the N component of node N16 band-pass filtered between 3–5 Hz. Green circles in (a) mark the detected explosive events. Array processing results obtained with the nodal N15–19 array are in b-f considering one hour of signals. (b) mean coherence between traces in each time window. (c) back-azimuths and (d) apparent velocities obtained with the method described in Section 5.6. Corresponding PDFs are shown in (e) and (f). Pink dashed lines in (c) and (e) indicate the back-azimuth of the central point of the active craters with respect to the array centroid.

event. Additionally, we perform the same calculations during volcanic tremor phases. This process is repeated for 20 separate time intervals of tremor, each lasting 20 seconds.

5.6 Slowness vector estimation

5.6.1 Methodology

After validating the DAS strain rate, we investigate whether it could provide meaningful information about the location of the volcanic sources. To do so, we estimate the slowness vector using strain rate records and compare the outcomes with those obtained using co-located nodes. Slowness vector estimation provides information about the apparent velocity and the back-azimuth of incoming waves. Therefore, it is a valuable tool for locating signals generated by the Strombolian activity and for wavefield characterisation (Chouet, 1996a). The characteristics of seismo-volcanic signals such as explosion and tremor (e.g., the emergent onset and the absence of body wave phases) make it necessary to use array processing techniques for locating them (Chouet, 1996a; Métaxian et al., 2002; Wassermann, 2012; Inza et al., 2014).

In this study, we apply the array analysis technique of Métaxian et al., 2002, which is particularly suited for volcanic tremor sources and small-aperture arrays with respect

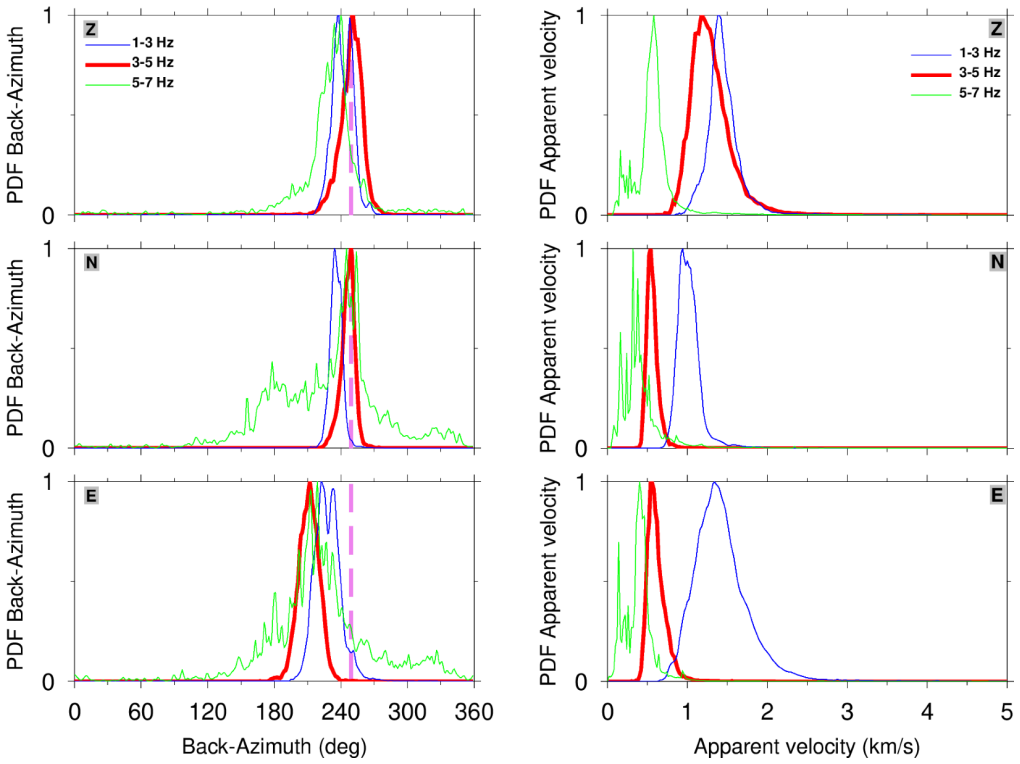

Figure 5.10: PDF results of back-azimuth (left column) and apparent velocity (right column) in the frequency bands of 1–3 (blue), 3–5 (red), 5–7 (green) Hz for the Z, N, and E components of the nodal array N15-19 during the analysed 1-hr time series (09/22/2020 19:34–20:34 UTC). The dashed lines in the left column represent the direction of the central part of the active craters (251°).

to the wavelength. Métaxian et al., 2002 demonstrated the accuracy of this method for recovering the slowness vector of volcanic sources using arrays with apertures lower than 70 m for frequencies between 0.5–5 Hz and wavelengths approximately between 160–800 m. The method consists of slowness vector estimation by inversion of the time delays between each pair of sensors i and j in a network. Time delays are estimated with the cross-spectral method (e.g., Poupinet et al. 1984) on subsequent sliding time windows. The computed time delays have a precision below half the sampling rate (Métaxian et al., 2002). Moreover, the method is independent of the amplitude of the signals, which is favourable in our case as strain rate data show significant amplitude variations along the cable. Furthermore, the amplitudes of the strain rate signals recorded by DAS are lower than those obtained with nodes.

As seen in Fig. 5.6a, node to DAS amplitude ratios (R) averaged across all segments are almost identical for tremor (2.72±0.82) and explosions (2.76±0.70). Only segment N9–10 (not shown) has higher R (4.76). With this exception, the other segments tested all show values of R around between 2 and 3. Furthermore, R values do not exhibit any correlation with the distance from the active craters and neither with the magnitude of the explosions (Fig. 5.6a) or with the frequency (Fig. 5.5b,d).

Under the hypothesis of a unique dominant incoming plane wave the expected theoretical delays τ are given by the equation:

$$\tau_{ij} = \mathbf{s} \cdot \mathbf{r}_{ij}, \tag{5.3}$$

where the dot denotes the usual scalar product, $\mathbf{s} = (-||s|| \sin\theta, -||s|| \cos\theta)$ is the slowness

Table 5.1: Maximum values and confidence intervals of the PDFs of both back-azimuth and apparent velocity computed during 1 hr of data for Z, N, and E components of the nodal array (N15–19). The craters' back-azimuth with respect to the centroid of the nodal array ranges between 246-256°.

Component	Parameter	Frequency band		
		1–3 Hz	**3–5 Hz**	**5–7 Hz**
Z	Back-azimuth [°]	238 ± 10	251 ± 10	240 ± 11
	Apparent velocity [km/s]	1.40 ± 0.14	1.18 ± 0.26	0.58 ± 0.10
N	Back-azimuth [°]	234 ± 8	248 ± 8	245 ± 6
	Apparent velocity [km/s]	0.94 ± 0.18	0.54 ± 0.06	0.32 ± 0.04
E	Back-azimuth [°]	222 ± 14	212 ± 10	219 ± 5
	Apparent velocity [km/s]	1.34 ± 0.32	0.54 ± 0.10	0.40 ± 0.10

vector, θ is the back-azimuth, measured clockwise from the north and $\mathbf{r}_{ij}$ is the relative position vector between stations pairs. Given a set of measured time delays τ_{ij}, with respective errors $\sigma_{\tau_{ij}}$, estimated for each time window, the two components of the slowness vector $\mathbf{s}$ are calculated by linear inversion of the N(N-1)/2 equations (5.3), where N is the number of sensors in the array. The problem is over determined for N≥3 and can be solved by standard least squares method.

5.6.2 Data selection

We select seismic velocity and strain rate records during the 1-hr long time series between 19:34–20:34 on 09/22/2020. Hereafter we describe the selected array geometries and data, first for the nodal and then for the DAS arrays.

The nodal array we consider is composed of nodes N15–19 (Fig. 5.7a) forming a triangle in the upper part of the network (Fig. 5.1d). The seismic antenna has an aperture of 53 m and a minimum inter-receiver distance of 15 m. These dimensions allow us to observe time delays for waves with wavelengths of a few hundred metres. The array response function (ARF) of the N15–19 array (between 3–5 Hz) is displayed in Fig. S5.2c. The 5 nodes in the N15–19 array provide 10 pairs of time delay measurements computed along subsequent 16-second time windows with a 1-second shift. The window size must be long enough to obtain precise calculations of the slowness values through linear interpolation of the cross-spectrum phase (Métaxian et al., 2002). Too long windows, however, decrease the resolution of the results. We select these sliding window parameters after several tests, aiming to find a balance between the dispersion of the results and the shortest possible length. We perform the analysis in 3 frequency bands (1–3, 3–5, and 5–7 Hz) and for the 3 components of the nodes. Fig. 5.7d,g,l show the 16-second waveforms corresponding to an explosion (same as in Fig. 5.4) recorded by the 3 components of the nodal N15–19 array.

To analyse the strain rate records we select three different array geometries:

(1) the first configuration (named DAS-L) consists of 3 linear segments (Fig. 5.7b), each composed of 10 channels (~ 40 m) with similar orientation (250±10°). The array has an aperture of 170 m and a minimum inter-receiver distance of 2.4 m (as all DAS arrays). The 3 segments of the DAS-L array are located at different distances from the craters, which is supposed to yield favorable results with our method.

(2) The second array (named DAS-T) has a triangular geometry, which is expected to be more adequate than the linear layout for the slowness vector estimation (Hudson et al., 2021; Näsholm et al., 2022). It is composed of the three sides (Fig. 5.7c) of the triangle-shaped deployment at the end of the fibre (Fig. 5.1d), and has an aperture of 43 m.

(3) The third array (named DAS-TL) is a combination of the previous two (Fig. S5.3c). The DAS-TL array is composed of the three segment of the DAS-T array and one segment (DAS-L2 in Fig. 5.7b) of the DAS-L array. It has an aperture of 100 m.

To evaluate the resolution and sensitivity of the three DAS arrays, we compute the relative ARFs by taking into account the strain rate polarization patterns for P/SV/Rayleigh and SH/Love waves (Martin, 2018; Zhan, 2019; Trabattoni et al., 2022). The radiation patterns for seismic velocity and strain rate are similar for P/SV/Rayleigh waves (Fig. S5.3g), whereas they are different for SH/Love waves (Fig. S5.3m). We consider synthetic plane waves with a frequency of 5 Hz and a velocity of 500 m/s coming from the direction of the active craters (250°) in Fig. S5.3 and from an orthogonal back-azimuth (160°) in Fig. S5.4. For both P/SV/Rayleigh and SH/Love waves, all three array configurations exhibit correct slowness estimates for the given wave source and all wave types (Figs. S5.3 and S5.4). The DAS-L array provides lower resolution in the slowness direction perpendicular to the cable (Figs. S5.3h, S5.4h) and, as expected, triangle-shaped geometries exhibit more isotropic ARFs (Näsholm et al., 2022). Additionally, the DAS-TL array shows sharper main peak due to its larger aperture. Taking into account the wave polarization does not change much the ARFs for P/SV/Rayleigh waves but it increases the ARF resolution for SH/Love waves. These results show that the selected array configurations are well suited for recovering the slowness vector. Furthermore, our inversion method provides more accurate results than conventional beamforming (Métaxian et al., 2002).

The first step in our method (Section 5.6.1) is to measure differential travel times. Because the cross-spectral method for the time delay estimation strongly relies on the coherence between traces recorded across the array, we investigate the variation with distance and frequency of the similarity between strain rate waveforms. To this aim, we calculate the average coherence between all pairs of DAS channels in the DAS-L array during the 1-hr time series. For comparison, we do the same for the sensors composing the nodal array (N component). Fig. 5.8 compares the coherence between DAS channels with coherence between nodes. We observe that the coherence is maximum below 3 Hz for the nodes, while it is maximum between 3 and 5 Hz for the DAS. The lack of high resolution below 3 Hz for the DAS can be explained by its high noise levels (Fig. 5.3). Additionally, Fig. 5.8 shows that the coherence between DAS channels rapidly decreases with increasing channel distance, even within a range below 40 m. Therefore, we estimate the time differences separately for each segment of the DAS arrays. Having 10 channels for each segment, we obtain 45 time delays. This gives 135 equations like Eq. (5.3) for the DAS-L and DAS-T arrays and 180 for the DAS-TL array. For each array configuration, we retrieve the slowness vector by inverting the corresponding time delays.

For the slowness vector calculation with strain rate data, we use 16-second windows with 1-second shifts and focus on two frequency bands, i.e. 1–3 and 3–5 Hz. Data filtered between 3–5 Hz are shown in Fig. 5.7 for one explosion. We observe a high similarity between strain rate waveforms of each cable segment, which is required for high resolution

differential travel time measurements.

5.6.3 Slowness vector estimation with the nodal array

We apply the method described in Section 5.6.1 to determine back-azimuth and apparent velocity with seismic velocity data. Fig. 5.9c,d show that these parameters, estimated for each window between 3–5 Hz for the N component of the nodal array, are stable during the entire hour for the background volcanic tremor. On the other hand, in the explosion coda, the decrease in coherence (Fig. 5.9b) gives less accurate time delays and consequently higher variability of the inverted back-azimuth and apparent velocity (Fig. 5.9c,d). Probability density functions (PDFs) are shown in Fig. 5.9e,f. The back-azimuth PDF is maximum at 251°, i.e. pointing towards the central part of the crater area that ranges between 246–256°. The corresponding apparent velocity PDF is maximum at 0.54 km/s. Considering a wider array with an aperture of 105 m (Fig. S5.2) gives similar slowness vector (Fig. S5.5).

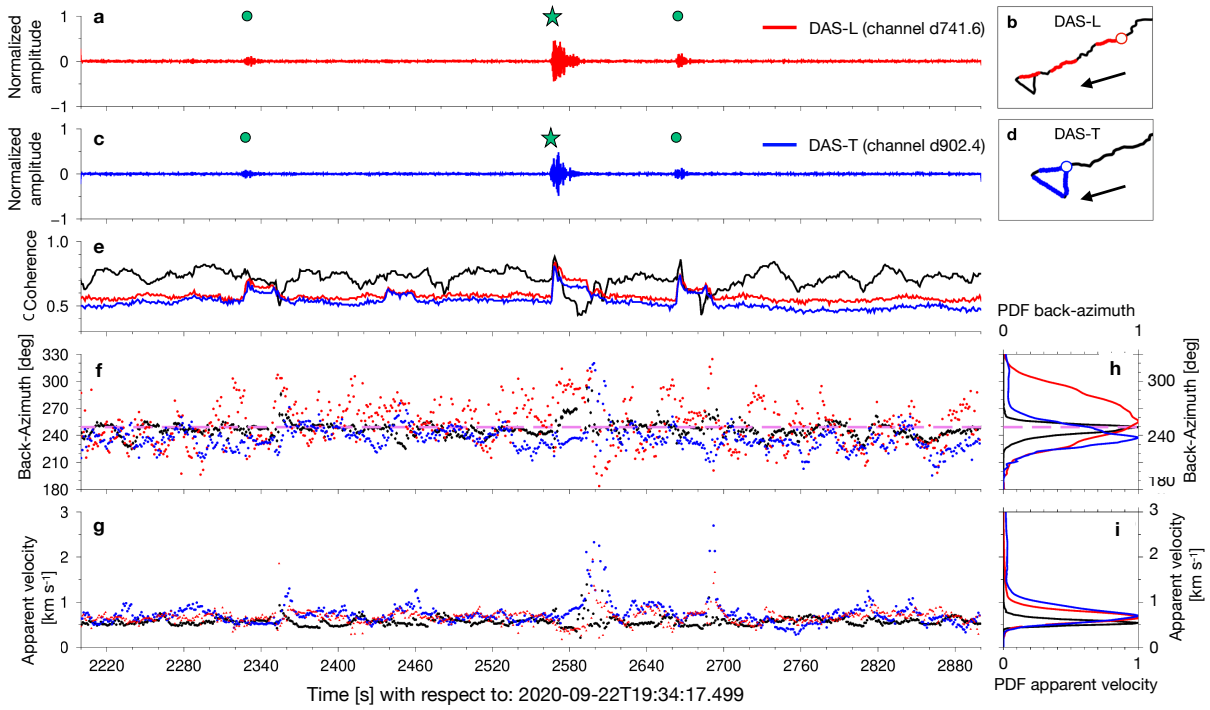

Figure 5.11: strain rate traces corresponding to channels (a) d741.6 (in red) and (c) d902.4 (in blue) arrays, normalized and band-pass filtered between 3–5 Hz. Green circles in (a) and (c) mark the detected explosive events, while the green star marks the most intense event during the time period considered. (b) and (d) show the geometries of the DAS-L and DAS-T arrays. White circles in (b) and (d) mark the location of channels d741.6 and d902.4 along the cable. Black arrows in (b) and (d) represent the back-azimuth of the central part of the crater area (251°) with respect to the array centroids. Array processing results are in e-i for the DAS-L (red) and DAS-T (blue) arrays and for the N component of the nodal N15–19 array (black). (e) mean coherence between traces in each time window. (c) back-azimuths and (d) apparent velocities obtained with the method described in Section 5.6.1. Corresponding PDFs are shown in (h) and (i). Dashed lines in (f) and (h) indicate the direction of the active craters.

Fig. 5.10 summarizes the back-azimuth and apparent velocity PDFs obtained for each component and frequency band during the considered time frame. Table 5.1 exhibits the

maximum PDF values and their confidence intervals. Back-azimuth PDFs between 3-5 Hz have narrower peaks than in the other frequencies and appear better resolved: the obtained values point towards active craters (246–256°) when considering the Z (251°) and N (248°) components, while the E component exhibits a southward shift of ~20-30°. These results show that the apparent velocities are frequency-dependent, especially for the horizontal components. It may be due to dispersive waves or to the fact that at different frequencies, different phases dominate.

5.6.4 Slowness vector estimation with DAS arrays

We now estimate the slowness vector from the DAS strain rate data of the three arrays selected in Section 5.6.2. We then compare the results with those obtained from the nodal N15–19 array in Section 5.6.3. Fig. 5.11 shows higher variability with time of the results obtained with DAS-L and DAS-T arrays compared to the nodal array (N component), but similar PDF maxima.

Back-azimuth PDF (Fig. 5.11h) for the DAS-L array is centred at 256°, i.e., towards the crater direction (246-256°). Back azimuth PDF for the DAS-T array (Fig. 5.11h) exhibit instead a ~10° southward shift. These results are consistent with waves propagating from the volcano summit area, ~200 m away from the active crater area. Apparent velocities obtained from the strain rate and seismic velocity (N component) measurements are similar, i.e. ~0.67 and ~0.54 km/s, respectively (Fig. 5.11i). Fig. 5.12 shows that the slowness vector estimates obtained with the N component of the nodal array and with the three DAS arrays between 3–5 Hz are in agreement.

Table 5.2 summarizes both back-azimuth and apparent velocity PDF maxima and confidence intervals between 1–3 and 3–5 Hz for the three DAS configurations. In both frequency bands, The back-azimuth results of the DAS-L array exhibit a wider distribution than the other two, as marked by higher standard deviations (Table 5.2). This is probably due to the lower broadside resolution of the linear geometry (Figs. S5.3 and S5.4). We observe almost identical back-azimuths obtained with the DAS-T and DAS-TL arrays in the two frequency bands. For all DAS geometries, apparent velocities are comparable in the two frequency bands and range between 0.58–0.68 km/s.

5.7 Discussion

We recorded strain rate signals generated by ordinary Strombolian activity. We observe a persistent background volcanic tremor and several explosive events of varying intensity in the data. Nevertheless, the instrumental noise floor prevents the recovery of most signals outside the 2–15 Hz range. Within this range, the strain rate sensed by DAS shows a perfect agreement in phase with the strain rate estimated from the nodes along 6 cable segments.

However, DAS strain rate amplitudes are more than two times lower than nodes. Despite retrieving small differences in amplitude between DAS and node strain rate, Wang et al., 2018 and Jousset et al., 2022 do not obtain this significant gap after applying the same finite-difference relationship. Additionally, the strain changes derived from a seismic array at Etna volcano by Currenti et al., 2021 closely match the DAS measurements, even in amplitude. We suppose that the lower amplitudes of the DAS strain rate record can be due to ground-to-fibre coupling effects or, more likely, to the response to a deformation

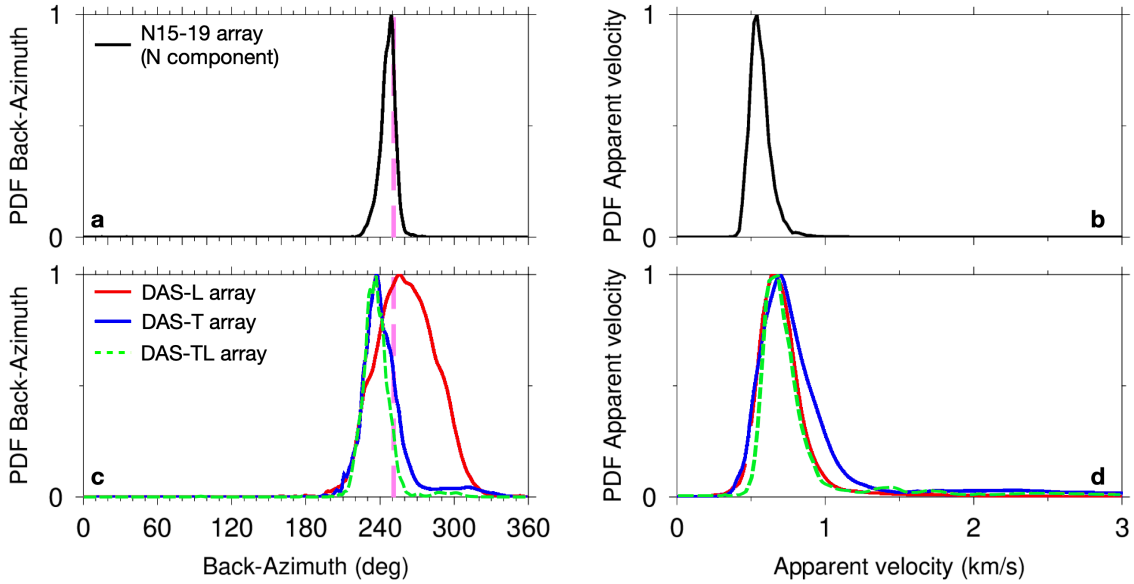

Figure 5.12: PDFs of back-azimuth (left column) and apparent velocity (right column) in the 3–5 Hz frequency band for the N component of the nodal N15-19 array (top row, in black) and for the DAS-L (red), the DAS-T (blue), and the DAS-TL (green) arrays (bottom row). The dashed lines in the left column represent the direction of the central part of the active craters (251°).

of the loose fibre bundle inside the cable (see Supplementary Note A in Supplementary Information). Her and Huang, 2011, Reinsch et al., 2017, and Diaz-Meza et al., 2023 point out that the cable structure can significantly influence the ground-to-fibre strain transfer and, therefore, the amplitude of the recorded dynamic strain rate signals.

The amplitudes of the strain rate signals show marked variability along the fibre path. In particular, DAS measurements reveal an area between channels d662.4–d751.2 characterised by strain rate signal amplitudes up to 10 times greater than those found in other fibre sectors (Fig. 5.4d). This amplitude contrast correlates quite precisely with a change in topography along the slope observed in Figs. 5.1 and S5.1. Fig 5.4c,d show slower wave velocities where higher strain rate amplitudes are present. We suggest that this variation in topography along the slope underlies a change in the waves velocity. The velocity contrast would lead to different site effects that strain rate measurements are notably responsive to (Trabattoni et al., 2022). As inferred from Eq. (5.1) and pointed out by Lior et al., 2021 and Trabattoni et al., 2022, slower waves result in higher strain rate values recorded by the DAS. Furthermore, Trabattoni et al., 2022 point out that the wavelength decrease of a wave entering a low-velocity layer influences DAS recordings twice as much as in the case of seismic velocity measurements.

The slowness vector provides information on the eruptive source location. However, with our method, we can only conclude on trends of the dominant components of the wavefield which is a mixture of body and surface waves on volcanoes (Chouet et al., 1997; Métaxian et al., 1997; Saccorotti et al., 2001; Konstantinou & Schlindwein, 2003). The application of this methodology to strain rate data requires some adaptations compared to its typical use with inertial sensors. First, DAS data exhibit a direction-dependent sensitivity, described by, e.g., van den Ende and Ampuero, 2021, Klaasen et al., 2021, Näsholm et al., 2022. Furthermore, the strain rate is measured parallel to the topography. As implied by Eq. (5.1), and stated by van den Ende and Ampuero, 2021, sub-horizontal

Table 5.2: Maximum values and confidence intervals of the PDFs of both back-azimuth and apparent velocity computed during one hour of data for the DAS-L, DAS-T, and DAS-TL configurations. The craters' back-azimuth with respect to the centroid of the three arrays ranges between 246-256°.

Component	Parameter	Frequency band	
		1–3 Hz	**3–5 Hz**
DAS-L	Back-azimuth [°]	267 ± 32	256 ± 18
	Apparent velocity [km/s]	0.68 ± 0.15	0.66 ± 0.08
DAS-T	Back-azimuth [°]	222 ± 12	237 ± 11
	Apparent velocity [km/s]	0.58 ± 0.14	0.68 ± 0.14
DAS-TL	Back-azimuth [°]	220 ± 9	238 ± 12
	Apparent velocity [km/s]	0.68 ± 0.2	0.68 ± 0.14

waves are favoured by DAS measurements over waves with fast apparent velocities (e.g., reaching the array with steep inclination).

At Stromboli, the 1–10 Hz tremor and explosive sources are located at the same altitude as the fibre network (Chouet et al., 1997; Ripepe, Delle Donne, et al., 2021). Therefore, we mainly record surface or body waves propagating sub-parallel to the optical fibre, which is a favourable condition for DAS measurements. This feature allows us to obtain accurate slowness vectors with strain rate data.

We validate the results obtained with strain rate measurements using the array of co-located nodes between 1–3 and 3–5 Hz. Between 1–3 Hz, back-azimuths derived from the nodes are 10 to 30° south of the active craters, whereas, for the DAS strain rate, back-azimuths are 10° north (DAS-L array) and 20 to 30° south (DAS-T and -TL arrays) of the active craters. A possible explanation for the observed shift in back-azimuth values obtained with both seismic velocity and strain rate data could be the fact that at these frequencies (and wavelengths) the effect of the near-field term may blur the propagative phase of the far-field term. Furthermore, the lower resolution of the selected arrays at these frequencies may adversely affect the results obtained.

In the same frequency band, apparent velocities obtained with the nodal array range between 0.94–1.40 km/s. Conversely, strain rate records also provide lower apparent velocities (0.58–0.68 km/s) than the nodes. Literature results help us interpret the apparent velocities in more detail. Chouet et al., 1997 and Wassermann et al., 2022 respectively applied polarisation analyses on 3C and six-degree-of-freedom (i.e., translational and rotational) measurements at Stromboli. They exhibited the prevalence of S-type motions between 1–3 Hz. The apparent velocities retrieved with the nodal array suggest a domination of body waves in this frequency band. Lior et al., 2021 and Trabattoni et al., 2022 instead pointed out the higher sensitivity of DAS to slower waves, which may explain the velocity discrepancy between node and DAS. Additionally, the low coherence of the strain rate record below ~2 Hz (Fig. 5.8) may hinder a proper slowness vector estimation in this frequency band.

Between 3–5 Hz, the results of the slowness vector estimation from strain rate and seismic velocity data are in agreement, as shown in Fig. 5.12. Back-azimuths derived from the N and Z components of the nodal array and from the DAS-L array point towards the craters, whereas DAS-T and DAS-TL arrays point 10° further south of the crater area (Fig. 5.12a,c). This is however still consistent with a propagation of waves from the summit zone of the volcano and close (~200 m) to the active crater area.

We interpret the low apparent velocities obtained with the horizontal nodes and DAS arrays (around 0.60 km/s; Fig. 5.12b,d) as due to a prevalence of surface waves in this frequencies band. This interpretation is in agreement with Chouet et al., 1997 and Chouet et al., 1998, who suggested that the volcanic tremor at Stromboli is composed of 70% Love waves and 30% Rayleigh waves above 2.5 Hz. The authors also showed that phase velocities of Rayleigh and Love waves between 3–5 Hz at Stromboli range between 0.65–0.40 km/s and 0.65–0.55 km/s, respectively, which is in agreement with our values around 0.60 km/s. The higher velocity observed from the vertical node components (1.18 km/s) may mostly correspond to body waves.

5.8 Conclusion

In September 2020, we installed and interrogated a 1-km-long fibre-optic cable at Stromboli volcano to test DAS capabilities for active volcano monitoring. We aim to confirm two issues: (i) whether DAS accurately records seismic signals generated by Strombolian activity and (ii) whether it can reliably provide its source location. We analyse the entire dataset and show the results for an hour-long time series between 19:34–20:34 on 09/22/2020.

Firstly, we conduct a quality and calibration assessment of DAS measurements. The comparison between strain rate data sensed by DAS along 6 cable segments and derived from co-located nodes shows an excellent phase resemblance of the waveforms (average cross-correlation coefficients above 0.9). However, amplitudes recorded with DAS are, on average, ~2.7 times smaller than those associated with nodes. We demonstrate that this difference can be explained by an ineffective cable-to-fibre strain transfer due to a loose cable structure (e.g., Currenti et al., 2023; Diaz-Meza et al., 2023), which we quantified.

We apply the array processing technique of Métaxian et al., 2002 to estimate the slowness vector. Results obtained from strain rate records between 3–5 Hz indicate seismic waves propagating from the volcano summit area, i.e., corresponding to or in the proximity (maximum distance of ~200 m) of the active craters. We also obtain apparent velocities of ~0.60 km/s, mainly corresponding to surface waves (Chouet et al., 1997; Chouet et al., 1998). The results are stable during the analysed hour, indicating a persistent source location for the explosions and the volcanic tremor. As a confirmation, back-azimuth and apparent velocity results obtained with strain rate and seismic velocity data closely match.

We demonstrated that DAS strain rate signals enable to analyse explosive events of varying intensity and volcanic tremor during ordinary Strombolian activity. Our findings confirm the capability of DAS to measure the strain rate generated by volcanic activity with high accuracy and its potential for volcanic monitoring purposes.

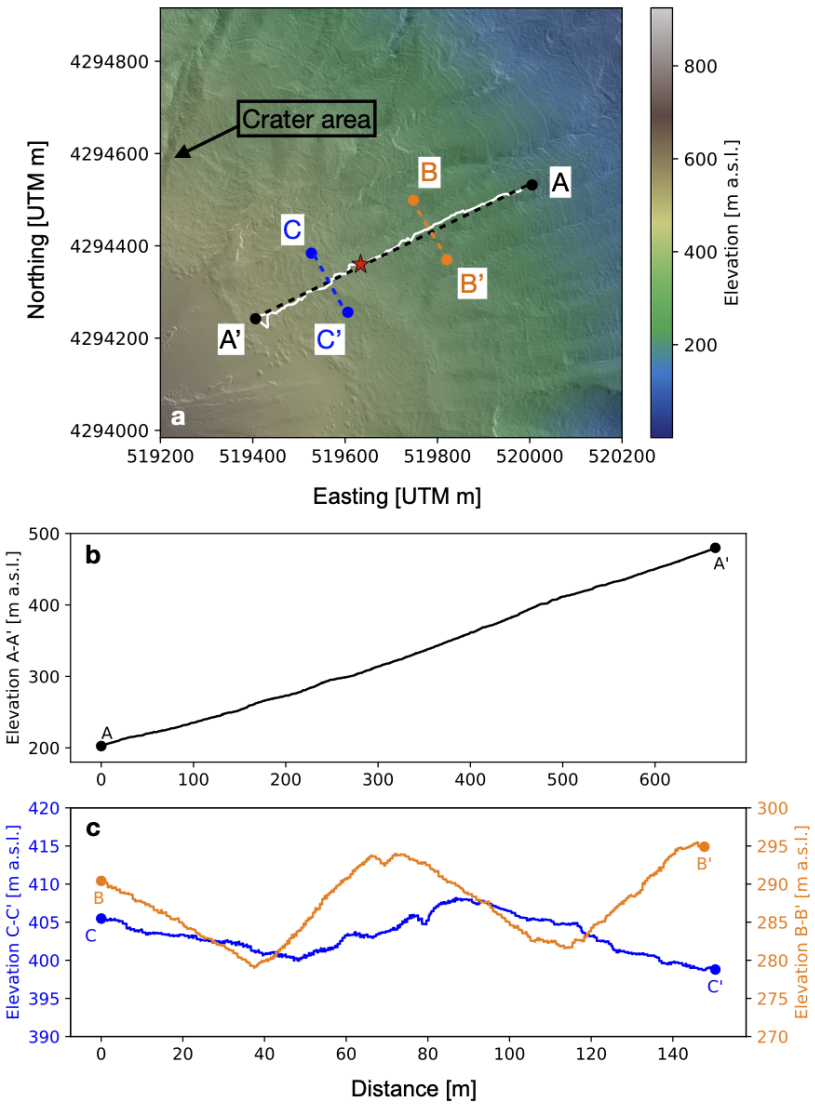

Figure S5.1: (a) DEM of the North-east flank of Stromboli volcano showing the fibre-optic cable (white line). (b) Topographic profile along the A–A' line, approximately corresponding to the cable path. (c) Topographic profiles along the 150 m long B–B' and C–C' sections respectively below and above the position of node N06 (red star). From N06 to A', higher strain rate amplitudes (up to an order of magnitude) are recorded.

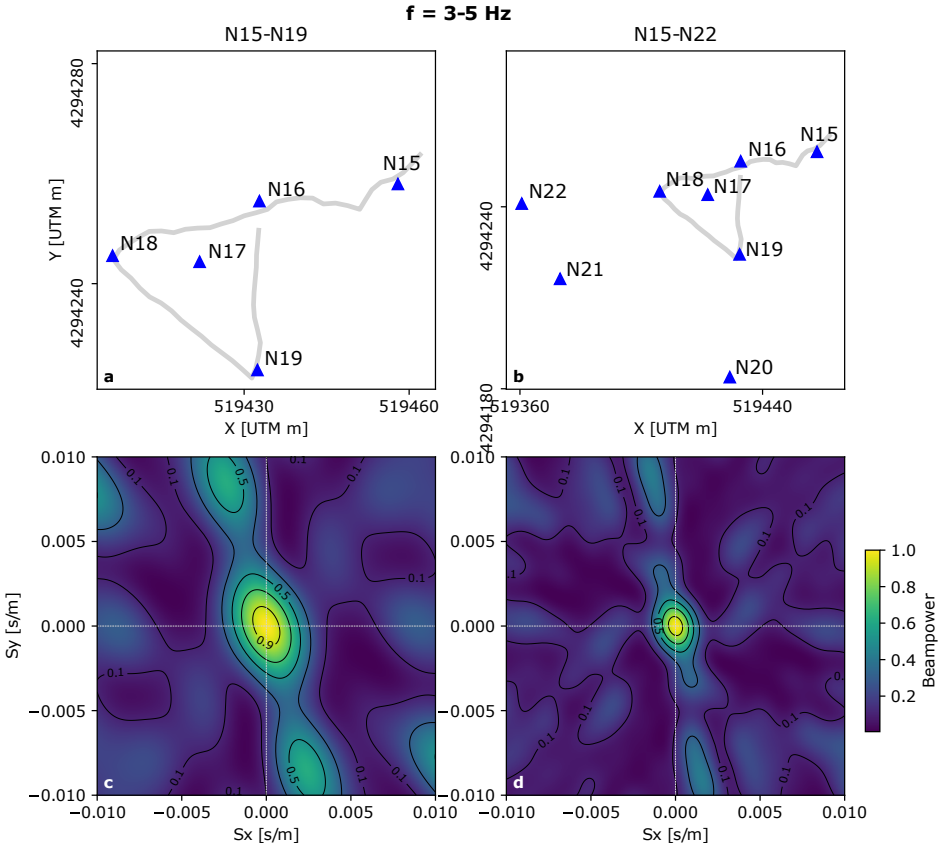

Figure S5.2: (top row) Geometries of the (a) N15–19 and (b) N15–22 nodal arrays. (bottom row) Array response patterns for the (c) N15–19 and (d) N15–22 nodal arrays.

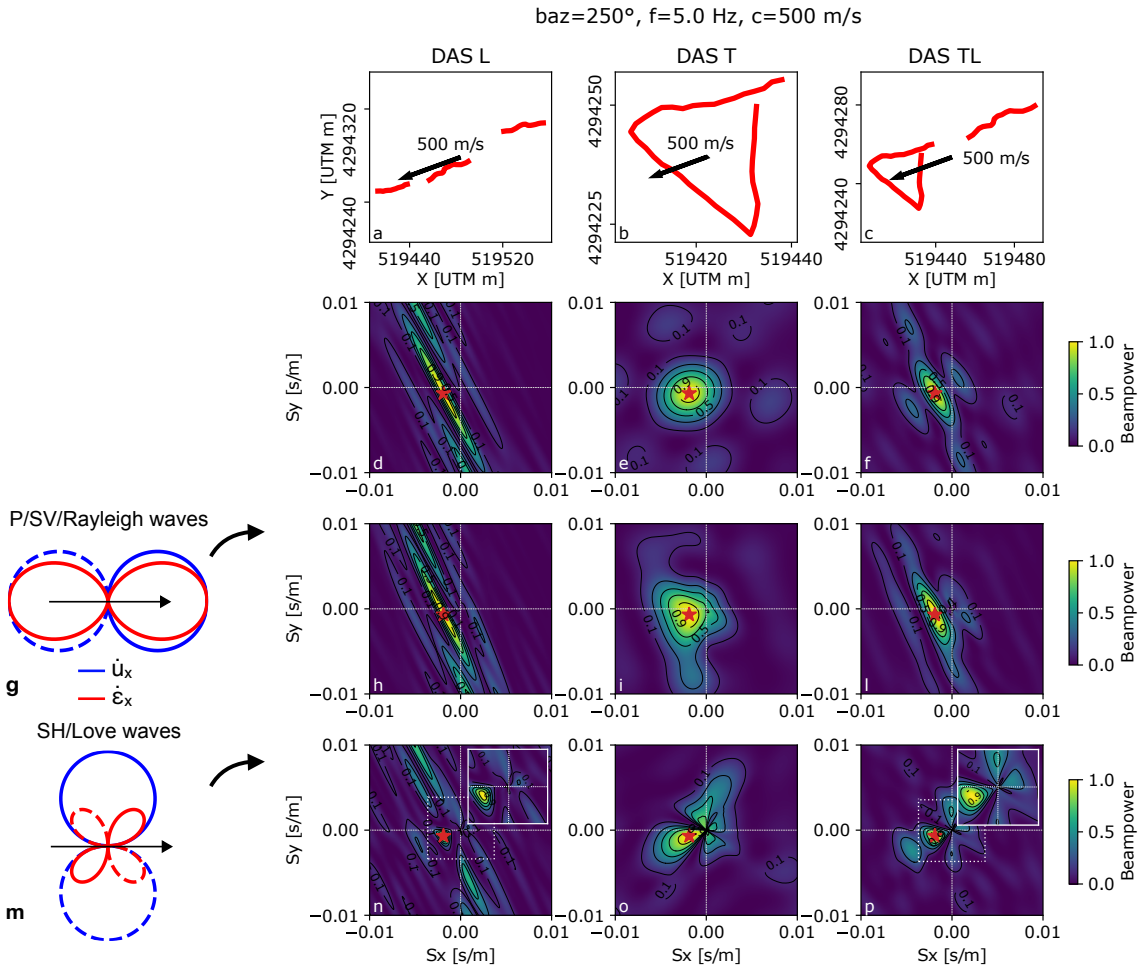

Figure S5.3: DAS array response functions. First row: geometries of the (a) DAS-L, (b) DAS-T and (c) DAS-TL fibre-optic arrays. The black arrow represents the back-azimuth (250°) of a plane wave impinging on the array with a frequency of 5 Hz and an apparent velocity of 500 m/s. Second row: (d-f) are the array responses for the three different geometries calculated without taking into account the DAS polarization pattern. The red star indicates the true location of the considered wave. Third row: (g) polarization pattern of the strain rate (red) and seismic velocity (blue) for P/SV/Rayleigh waves propagating along the black arrow. Solid and dashed lines indicate positive and negative amplitudes, respectively. Modified after Trabattoni et al., 2022. (h-l) are the array responses for the three different geometries shown in a-c calculated by taking into account the strain rate polarization for P/SV/Rayleigh waves. Fourth row: (m-p) same as third row for SH/Love waves. Magnified views between -0.003 and 0.003 s/m are exhibited in (n) and (p), for clarity. This figure shows that an incident wave coming from the active craters at Stromboli can be recovered with our DAS array geometries.

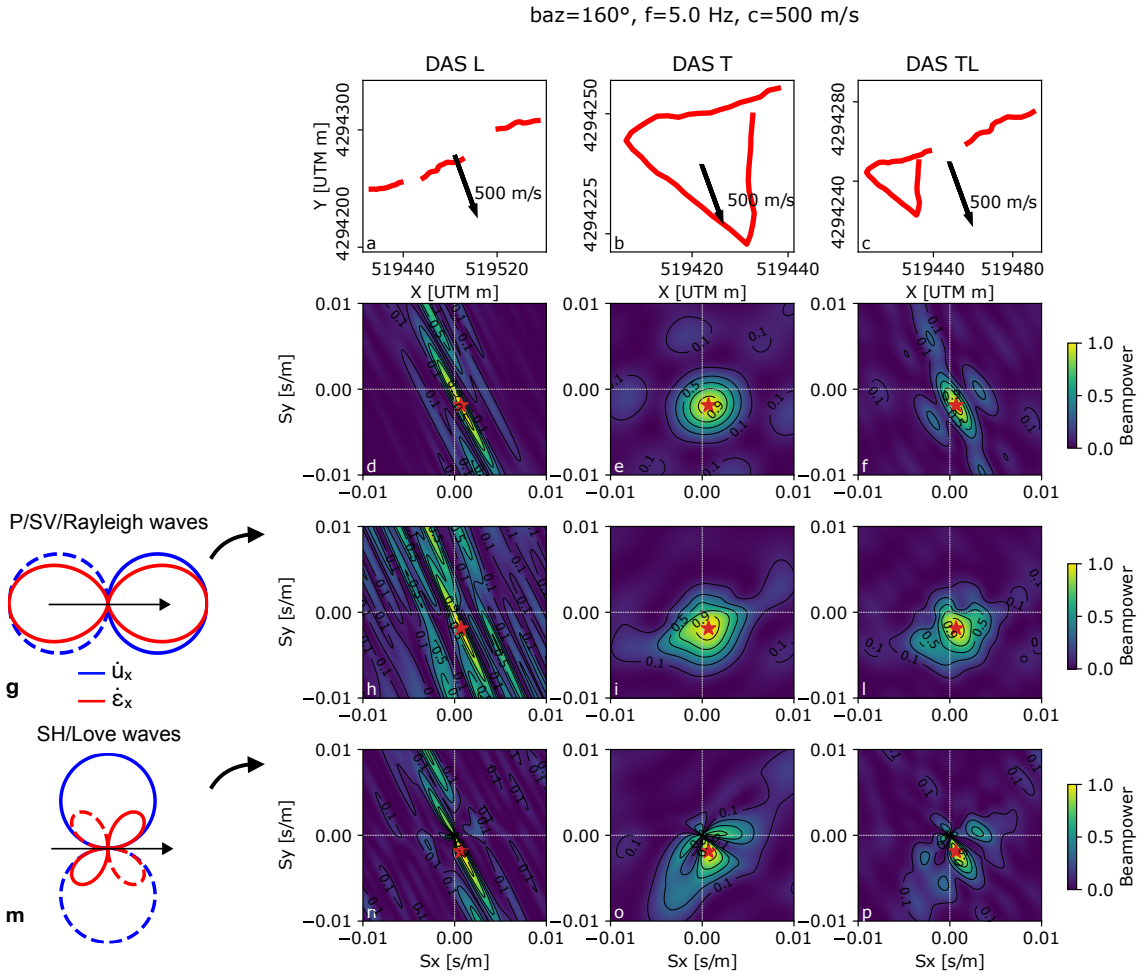

Figure S5.4: Same as Fig. S5.3 for a plane wave impinging on the DAS arrays with a back-azimuth of 160°, a frequency of 5 Hz and an apparent velocity of 500 m/s.

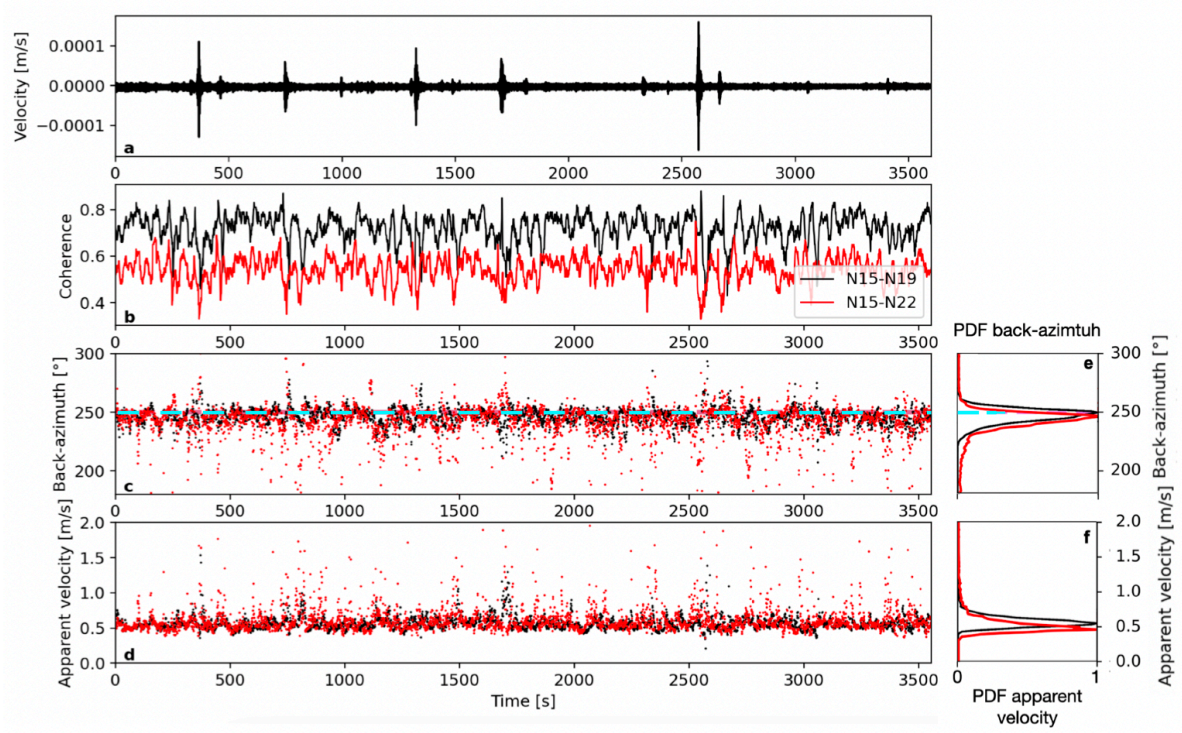

Figure S5.5: (a) 1-hr seismic velocity trace of the N component of node N16 band-pass filtered between 3–5 Hz. Array processing results are in b-f for the array N15-N19 (black) and N15-N22 (red) considering 1 hr of signals. (b) mean coherence between traces in each time window. (c) back-azimuths and (d) apparent velocities obtained with the method described in Section 5.1. Corresponding PDFs are shown in (e) and (f). Dashed lines in (c) and (e) indicate the back-azimuth of the central point of the active craters with respect to the array centroids.

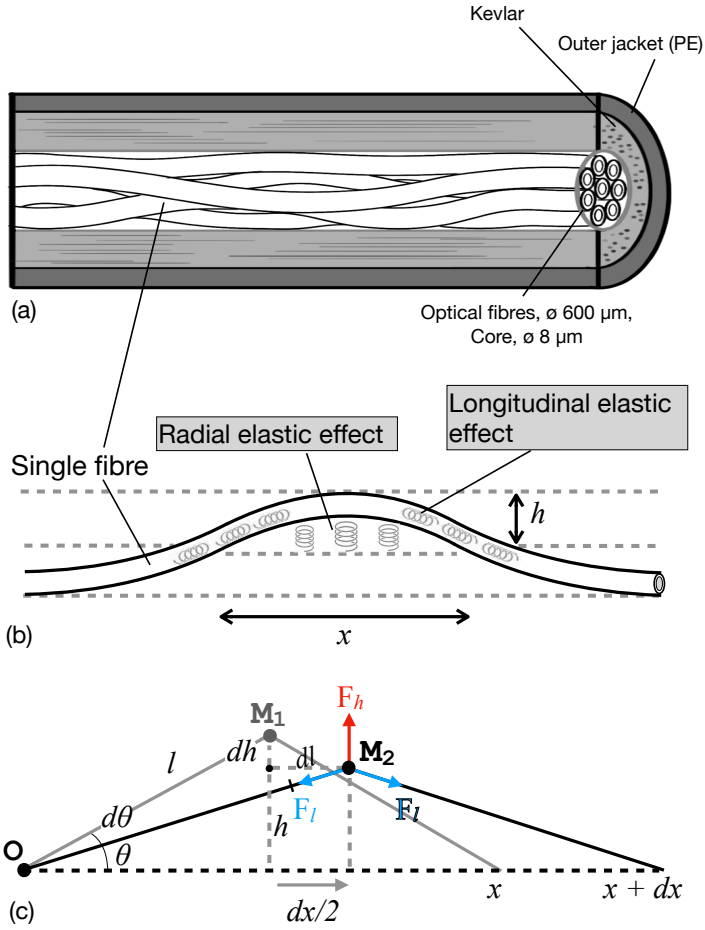

Figure S5.6: (a) Representation of the fibre-optic cable deployed at Stromboli. (b) detail of one single fibre within the fibre bundle. (c) Scheme of the fibre in (b).

5.9 Supplementary Information for: Array Analysis of Seismo-Volcanic Activity with Distributed Acoustic Sensing

5.9.1 Supplementary Note A: Loss of strain sensitivity for a loose fibre bundle in a cable

We provide here a possible explanation for the lower strain rate amplitudes sensed by DAS at Stromboli. The fibre-optic cable deployed at Stromboli depicted in Fig. S5.6a is composed of a polyethylene jacket (5 mm in diameter) which encloses a loose kevlar layer (without gel) surrounding 8 tight-buffered optical fibres (with a diameter of 600 μm and a 8 μm sensing core). This flexible structure makes the cable on the one hand particularly suitable in a harsh volcanic environment, while on the other hand it allows a certain radial compression and adjustment of the fibres within the bundle. We hypothesize that these phenomena may hinder an optimal measurement of the amplitude of the strain (rate) to which the fibre is subjected.

We consider a single fibre within the fibre bundle, characterised by a curvature (Fig.S5.6b).

Upon visual inspection, we detect fibre curvatures ranging from 0.1-1 m in wavelength and millimeter-scale amplitudes. When subjected to a vibrational stimulus, elastic effects will account for both longitudinal lengthening/shortening and radial compression of the fibre bundle (Fig.S5.6b). Fig.S5.6c depicts a schematic version of the fibre – with the curvature represented by a small angle θ – which undergoes longitudinal elongation and radial compression. F_l and F_h are the longitudinal and radial elastic forces, respectively. These are defined as $F_l = k_l dl$ and $F_h = -k_h dh$, where k_l and k_h are the intrinsic stiffnesses of the fibre (longitudinal) and the fibre bundle (radial).

According to the schematic geometry represented in Fig.S5.6c, we can observe the segments $\overline{\mathrm{OM}_1} = (lcos\theta,\ lsin\theta)$ and $\overline{\mathrm{OM}_2} = (lcos\theta + dx/2,\ lsin\theta + dh)$ which represent the undeformed and the deformed fibre, respectively. The segment $\overline{\mathrm{OM}_2}$ can be written as:

$$\overline{\mathrm{OM}_2} = (l^2 cos^2\theta + lcos\theta dx + l^2 sin^2\theta + 2lsin\theta dh)^{\frac{1}{2}} \tag{5.4}$$

$$= l\left(1 + \frac{cos\theta dx}{l} + 2\frac{sin\theta dh}{l}\right)^{\frac{1}{2}} \tag{5.5}$$

$$= l\left(1 + \frac{cos\theta dx}{2l} + \frac{sin\theta dh}{l}\right), \tag{5.6}$$

by assuming a first order approximation. Therefore, longitudinal strain dl/l of the fibre can be written as:

$$\frac{dl}{l} = \frac{\overline{\mathrm{OM}_2} - \overline{\mathrm{OM}_1}}{\overline{\mathrm{OM}_1}} = \frac{\cos\theta}{2}\frac{dx}{l} + \sin\theta\frac{dh}{l}, \tag{5.7}$$

For negligible $d\theta$ (in the order of $10^{-6} - 10^{-5}$ as the ones we are dealing with, due to elastic deformation of the fibre within the bundle) the balance of vertical forces requires that

$$F_h = 2F_l \sin\theta, \tag{5.8}$$

which can be also expressed as

$$k_h dh = -2k_l dl \sin\theta, \tag{5.9}$$

By substituting Eq.(5.9) into Eq.(5.7), and grouping the dl/l terms together, we obtain the following equation

$$\frac{dl}{l}\left(1 + 2\frac{k_l}{k_h}\sin^2\theta\right) = \frac{\cos\theta}{2}\frac{dx}{l}. \tag{5.10}$$

The geometry in Fig.S5.6c implies that $l = x/(2\cos\theta)$, so that we can write Eq.(5.10) as

$$\frac{dl}{l}\left(1 + 2\frac{k_l}{k_h}\sin^2\theta\right) = \cos^2\theta\frac{dx}{x}, \tag{5.11}$$

where dl/l is equivalent to ε_{ll} and dx/x to ε_{xx}, i.e. the elastic deformation experienced by the fibre and the cable, respectively. Eq.(5.11) then simplifies to:

$$\varepsilon_{ll} = \frac{\cos^2\theta}{1 + 2\frac{k_l}{k_h}sin^2\theta}\varepsilon_{xx}. \tag{5.12}$$

We can therefore observe that for small angles θ, if $k_h \rightarrow$ inf – indicating a solid bundle of fibres not susceptible to radial compression – $\varepsilon_{ll} = cos^2\theta\varepsilon_{xx} \simeq \varepsilon_{xx}$, so that the deformation of the fibre is equal to the deformation of the cable. Conversely, for $k_h \rightarrow 0$, $\varepsilon_{ll} \simeq 0$, resulting in no longitudinal fibre strain.

The effective stiffnesses k_l and k_h can be generalized as

$$k_l = \frac{K_l}{l} S, \tag{5.13}$$

and

$$k_h = \frac{x}{2} K_h, \tag{5.14}$$

respectively, where K_l is the effective elastic modulus of the single fibre in the longitudinal direction, K_h is the effective elastic modulus of the fibre bundle in the radial direction, x and l are the lengths of the cable and the fibre segments and S is the section of the individual fibre (in our specific case, 0.6 mm). Eqs.(5.14) and (5.13) are derived for a set of helical springs respectively in parallel and in series (Fig.S5.6b). The factor 2 in Eq.(5.14) accounts for the fibre curvature (Fig.S5.6b). These considerations are valid for a single triangle as depicted in Fig.S5.6c. However, we have to consider that the gauge length (at Stromboli was set to 5 m) averages the strain rate over lengths that may be longer than the observed wavelength of the fibre curvature (0.1-1 m in our case). In this case, we will have a mean value of effective compressibility averaged over the given gauge length.

By considering Eqs. (5.13) and (5.14), Eq.(5.12) can be written as

$$\frac{\varepsilon_{xx}}{\varepsilon_{ll}} = 1 + 16S\frac{K_l}{K_h}\frac{h^2}{x^4}, \tag{5.15}$$

by supposing small fibre curvatures within the cable, i.e., $l \approx x$ and $\theta \approx 2h/x$.

At Stromboli we observed an amplitude ratio R between the strain rate recorded by the DAS and the strain rate derived from the nodes of $\sim 2.7 \pm 0.8$. Assuming this ratio to be equal to $\varepsilon_{xx}/\varepsilon_{ll}$, we find the following relation between K_h and K_l:

$$K_h \approx 9S\frac{h^2}{x^4} K_l. \tag{5.16}$$

By considering a fibre diameter as 8 μm, a wavelength of the fibre curvature (x) ranging between 0.1–1 m with an amplitude (h) of 10^{-3} m, we obtain a relation between the effective elastic moduli of $K_h \approx 10^{-11} - 10^{-15} K_l$. This implies that for a non-tight fibre bundle within a cable, as the one we installed at Stromboli, the recorded elastic deformation of the individual fibres is partially under-estimated due to the effect of the loose fibre deformation in the cable.

We performed a first laboratory experiment to better assess this phenomenon. We used the same cable deployed on the field at Stromboli to which we spliced and secured a single fibre cable without jacketing. We collected data with a Febus A1 DAS interrogator parametrized with 5 m of gauge length, 0.8 m of inter-channel distance and 1 kHz of sampling rate. We energized using three different methods: (i) by hitting the medium in contact with the cables, (ii) by directly tapping the jacketed cable, and (iii) by hitting and letting the cables oscillate freely with one end attached to a wall.

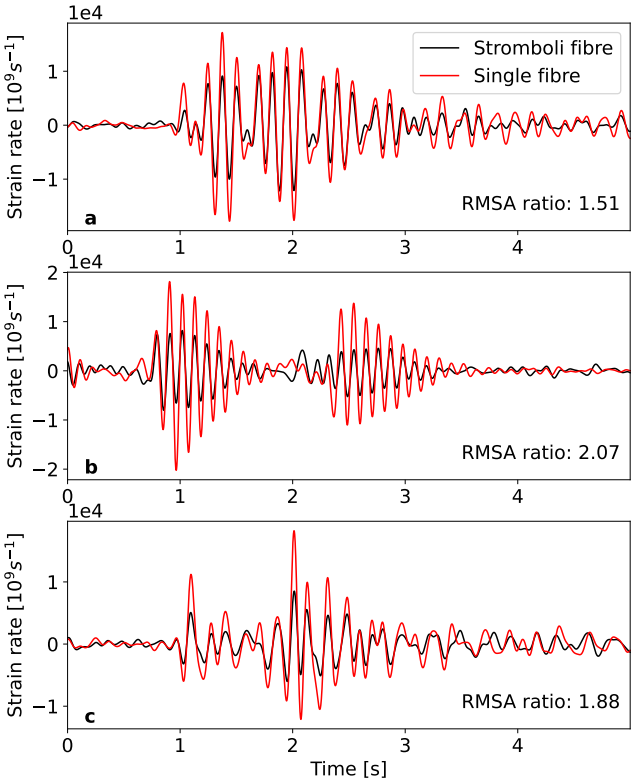

Figure S5.7: strain rate waveforms generated in the laboratory by three different types of energisation and recorded at co-located channels d38.4 (in black) and d125.6 (in red), respectively situated in the optical cable installed at Stromboli, and in the single cable without jacket secured to the previous one. (a) hit close to the cables; (b) tap on the jacketed cable; (c) hit on hanging cable. RMSA between each couple of waveforms are reported in the figure. Waveforms are bandpass-filtered between 1-10 Hz.

The results of this experiment bandpass-filtered between 1-10 Hz are displayed in Fig.S5.7. We can observe that for the three methods, the amplitudes recorded by the single-fibre cable are slightly higher than those of the multi-fibre cable, with a mean ratio between the RMSA of each waveform couple around ~1.8. As a first approximation, these results corroborate our simple model. However, a more detailed study – out of the scope of this manuscript – is necessary to better comprehend the phenomenon and the response of the fibre-optic cables.

Acknowledgments

This study would not have been possible without the work of S. Oliva and his team in digging the trench for the fibre-optic cable. Furthermore, we would like to acknowledge the valuable help offered in the field by G. Diana, M. Masini and C. Caudron for both fibre and nodes deployment. We thank C. Jestin, G. Calbris and V. Lanticq of FEBUS Optics for their support and the two reviewers, T. Hudson and P. Jousset, for their constructive comments that helped us improving this manuscript. DAS data were processed using the Xdas Python library (https://github.com/xdas-dev/xdas, DOI: 10.5281/zenodo.7573824). Seismometers data were processed using the Obspy python library (e.g., Beyreuther et al. 2010). Processing of Differential GPS data was performed with RTKLIB software (https://rtklib.com). Linear interpolation of DAS channels was performed with the help of the Interparc Matlab library (https://www.mathworks.com/matlabcentral/fileexchange/34874-interparc, John D'Errico, 2012, MATLAB Central File Exchange). This work was financially supported by the ANR-19-CE04-0011-01 MONIDAS (Natural Hazard Monitoring using Distributed Acoustic Sensing) Project.

Data availability

Data used for this manuscript are available through IPGP Research Collection at the following DOI: https://doi.org/10.18715/IPGP.2023.lgl6bxby.

Chapter 6

Tracking and characterising pyroclastic density currents with DAS and seismo-acoustic observations

Preface

This chapter is organised in article format and is based on a manuscript currently in preparation with the following authors and title:

F. Biagioli, J.-P. Métaxian, M. Ripepe, E. Stutzmann, P. Bernard, G. Lacanna, A. Mangeney, G. Ulivieri, G. Risica, A. Trabattoni, M. Peruzzetto, and L. Innocenti, **Tracking the dynamics of pyroclastic density currents with DAS and seismo-acousitc observations**, *in prep.*.

This chapter is divided into two parts: the main body (starting from Section 6.1) and the supplementary information (Section 6.6). These two are kept separate to improve readability. Supplementary figures are numbered from S1 (e.g., Fig. S6.1), and references for the main text and supplementary information are listed at the end of the thesis. The author apologises for any repetition necessary to make the chapter self-contained.

Let us briefly outline the motivations behind this study. Between October and December 2022, Stromboli volcano exhibited intense explosive and surface activity. In particular, several pyroclastic density currents (PDCs) occurred, notably on 9-11 October and 4 December, during which the DAS interrogator was active and recording. Additionally, the network of nodal seismometers, consisting of two small-aperture arrays at ST and GR (Fig.3.3c), operated until mid-October, allowing us to analyse the signals generated by such events.

We focus on two PDCs from 9 October and 4 December 2022, which we refer to as PDC1 and PDC2, respectively. This chapter employs array processing techniques to

analyse strain rate, seismic velocity and pressure signals from these PDCs. Specifically, we investigate whether DAS measurements enable the tracking of the seismic source as the flow moves from the craters towards the sea. Strain rate signals between 1-5 Hz, recorded at four fibre-optic arrays (i.e., NT, CT, ST, and GR in Fig/ 3.2), were analysed using the array processing technique described in Chapter 5 (Métaxian et al., 2002).

We applied the same technique to signals from two nodal arrays (NT and GR) to validate DAS results. However, due to battery life limitations, we restricted this analysis only to the first event on 9 October 2022 (PDC1). We also used the infrasonic array at the summit (stations STR, MC1, and MC5) to track the flows using the multi-channel correlation analysis (MCCA) (Cansi, 1995; Ulivieri et al., 2011; Marchetti et al., 2019). Finally, the array processing results were compared with images captured every two seconds by the visible LBZ camera (Fig. 3.2a) overlooking the SdF. We then use the combined seismo-acoustic data and tracking results to simulate the flows and infer key physical parameters, such as the basal friction angle, that govern PDC behaviour.

6.1 Abstract

Pyroclastic density currents (PDCs) are hot, fast, and deadly mixtures of gas and volcanic materials that can travel up to tens of kilometres away from eruptive centres. They are dangerous phenomena accounting for roughly half of the casualties claimed by volcanic activity. Detecting, locating, and tracking these events is fundamental for risk mitigation around volcanoes. Between October and December 2022, several PDCs occurred at Stromboli Volcano (Italy), travelling along the flanks down to the sea and generating centimetre to metre-scale tsunami waves. These events occurred during an experiment involving distributed acoustic sensing (DAS) measurements of the seismo-volcanic activity. 27 geophones and the multi-parameter monitoring network operated by the University of Florence were also active simultaneously. We apply array analysis techniques to DAS, seismic, and infrasonic signals generated by two PDCs of different sizes. The back-azimuths estimated with the three datasets are consistent and enabled us to track PDCs moving from the craters to the sea with velocities between $\sim 30 - 70$ m/s, increasing with flow volumes. We then validate the accuracy of these measurements with georeferenced images acquired by monitoring cameras. These results demonstrate the effectiveness of the three datasets in monitoring PDCs. We deduce information about the flow dynamics and the underlying physical parameters that govern it by analysing the characteristics of seismo-acoustic signals and simulating front velocities using granular flow models. Simulations indicate different Coulomb friction angles for the two PDCs ranging from 21° to 25°, decreasing with increasing volume. Such a pattern is also observed in other gravitational processes on Earth and in extra-terrestrial environments.

6.2 Introduction

Pyroclastic density currents (PDCs) are fast ($10^1 - 10^2$ m/s; Brosch et al., 2021), hot (up to 700°C; Dufek et al., 2015) and high-mobility gravity-driven flows of volcanic gases and particles that can travel up to $10^1 - 10^2$ km from eruptive centres (Lube et al., 2019; Risica et al., 2022). These features make them dangerous volcanic phenomena and the principal cause of death near volcanoes (Tanguy et al., 1998; Brown et al., 2017; Lube et

al., 2019). PDCs may exert dynamic pressures up to 10^2 kPa posing a significant threat to infrastructures (Brosch et al., 2021). Furthermore, other highly hazardous, rapid gravity-driven mass movements (RGMMs), such as rockfalls, debris avalanches and lahars, can occur in volcanic areas. The flow dynamics of these events depend on different physical processes such as the role of gas, water, particle size distribution, leading to different effective friction, controlling their runout extend and dynamic pressure (Roche et al., 2011; Iverson & George, 2014; Delannay et al., 2017). Detecting, locating and estimating the propagation velocity and size of RGMMs is fundamental for risk management around volcanoes. Such information is also crucial for understanding the tsunamigenic potential of RGMMs ending up in water bodies. Furthermore, analysing seismo-acoustic signals generated by PDCs and understanding the physical parameters that control them, such as the basal friction, serve as a more solid base for modelling the spatio-temporal extension and the velocity of the flows.

Similarly to other RGMMs, PDCs are capable of generating seismic and infrasonic ($<$ 20 Hz) signals in the Earth and the atmosphere, respectively (Yamasato, 1997; De Angelis et al., 2007; Allstadt et al., 2018). These signals ensure detection and provide information about PDCs and RGMMs dynamics, whose internal processes are hardly observable at close distances (Dufek, 2016; Watson et al., 2023). Low frequency (10^{-1} – 10^{-3} Hz) seismic waves can help constraining the mass, trajectory, dynamics, timing and rheological parameters of landslides, and serve as a reference for numerical models (Kanamori & Given, 1982; Brodsky et al., 2003; La Rocca, Galluzzo, et al., 2004; Moretti et al., 2012, 2015; Allstadt et al., 2018; Schöpa et al., 2018). Waveforms with frequencies $>$ 1 Hz are usually emergent and spindle-shaped, lacking clear body wave phases. These signals are complex and more challenging to analyse due to the higher attenuation and sensitivity to small-scale heterogeneities (Allstadt et al., 2018). Nevertheless, seismic signals at $f > 1$ Hz exhibit correlation with quantitative RGMMs features, e.g., volume, momentum, frictional processes, and forces applied to the ground by the flow (Norris, 1994; Schneider et al., 2010; Hibert et al., 2011, 2014; Levy et al., 2015). On volcanoes, high-frequency seismic signals can serve as a basis to detect, locate and estimate volumes of rockfalls (e.g at the Piton de la Fournaise, la Réunion; Hibert et al., 2011, 2014; Kuehnert et al., 2021). Methods relying on amplitudes and polarisation allowed the tracking of PDCs using seismic records at Unzen (Japan; Yamasato, 1997), Soufrière Hills (Montserrat; Jolly et al., 2002), Etna (Italy; Watson et al., 2023) and Augustine (Alaska, USA; DeRoin et al., 2012) volcanoes. Additionally, array techniques are commonly applied to infrasonic data to characterise, track and estimate velocities of volcanic RGMMs, such as PDCs (Yamasato, 1997; Ripepe et al., 2010; Delle Donne et al., 2014) and lahars (Johnson & Ronan, 2015).

However, volcanic areas are harsh environments, challenging the installation and maintenance of a dense network of sensors. In seismo-volcanic applications, Distributed Acoustic Sensing (DAS) offers valid opportunities for long-duration surveys with temporal resolutions up to kHz and spatial resolutions down to metres. DAS can turn fibre-optic cables into arrays of thousands of single-component strain sensors through optical interferometry of Rayleigh back-scattered radiation from laser pulses transmitted along the fibres. DAS also guarantees telemetry, with data transmitted at the speed of light. The complementary use of DAS and traditional seismo-acoustic observations can significantly support volcano monitoring, especially in submarine and currently unmonitored areas(Jousset et al., 2022; Nakano et al., 2024). Previous DAS experiments in volcanic contexts exhibited

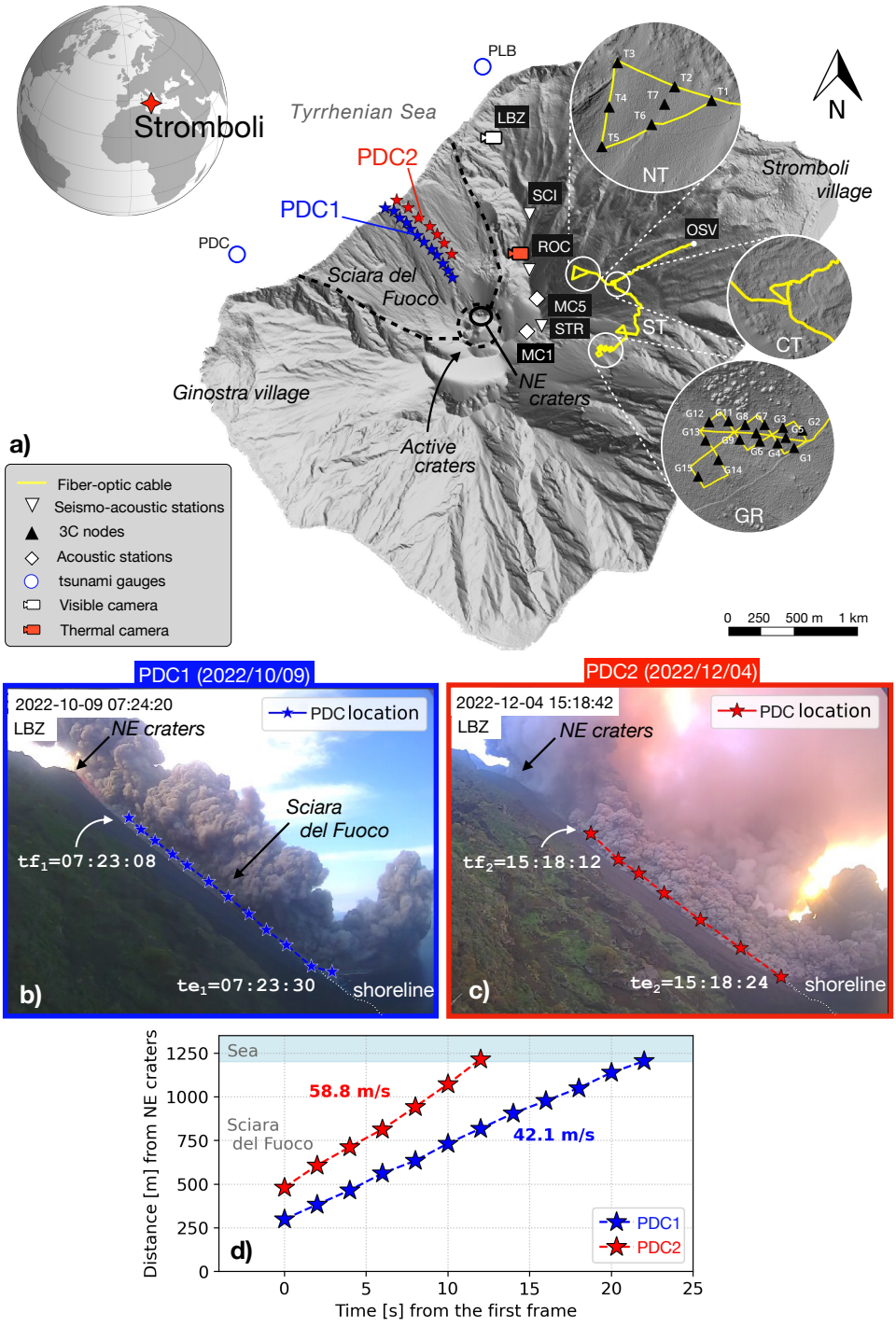

Figure 6.1: (a) Map of Stromboli Volcano showing the monitoring network of the University of Florence, Italy (UniFi) consisting of e.g. broadband seismo-acoustic stations (white triangles), infrasonic pressure sensors (white diamonds), tsunami gauges (blue circles), and the LBZ (visible) and ROC (thermal) cameras. Continues in the next page.

Figure 6.1: Continued from previous page. The yellow line represents the 4 km long DAS cable exhibiting four sub-arrays (i.e., D-NT, D-CT, D-ST and D-GR). The DAS interrogator is hosted in the UniFi Geophysical Observatory (OSV). Black triangles are three-component nodes deployed in two arrays (N-NT and N-GR). Blue and red stars in (a) respectively mark the location of PDC1 and PDC2 flow fronts obtained by LBZ georeferenced frames every 2s (Supplementary Note 1). (b) and (c) show two snapshots recorded by the LBZ camera during PDC1 and PDC2, respectively. Blue and red stars mark the position of the pyroclastic front in the visible images every 2s. tf_1 (07:23:08 UTC) and tf_2 (15:18:12 UTC) in (b) and (c) are the frame times from which PDC1 and PDC2 can be well located. te_1 (07:23:30 UTC) and te_2 (15:18:24 UTC) indicate the arrival times at sea of the two PDCs. (d) Exhibit time vs. distance plot for PDC1 (blue) and PDC2 (red) with the corresponding average front velocities. The DEM is computed from images taken in 2014 and courtesy of Italian Civil Protection.

promising results, such as the identification of unknown seismic signatures related to fluid migration (Klaasen et al., 2021; Jousset et al., 2022), the location of tremor, explosions and volcano-tectonic events (Nishimura et al., 2021; Jousset et al., 2022; Biagioli et al., 2024) or the identification of shallow structural features (Jousset et al., 2018; Currenti et al., 2021; Jousset et al., 2022). Furthermore, different geophysical observations can ensure better characterisation of various and simultaneous volcanic phenomena, improving monitoring systems(Jousset et al., 2022).

To this aim, we report the application of DAS in a joint fashion with conventional seismic and infrasound observations to detect and track PDCs at Stromboli volcano, Italy (Fig. 6.1), and to investigate changes in volcanic behaviour concurrently with these events. Stromboli activity is mainly characterised by a persistent and frequent explosive activity (~13 exp/hr(Rosi et al., 2013)), alongside continuous degassing (Supplementary Note 1). At Stromboli, PDCs are due to eruptive column collapses or gravitational instabilities and are generally confined in the Sciara del Fuoco (SdF) depression (Di Roberto et al., 2014; Bevilacqua et al., 2020; Calvari et al., 2020; Calvari et al., 2022; Di Traglia, Borselli, et al., 2023; Giudicepietro et al., 2023; Ripepe & Lacanna, 2024). SdF is an unstable, ~1 km wide and partially filled sector-collapse scar having a mean slope of ~35° (Fig. 6.1a) that extends down to ~2 km below the sea level. Large PDCs (and landslides) reaching the sea can trigger tsunami waves, endangering the island and neighbouring coastlines (La Rocca, Galluzzo, et al., 2004; Ripepe & Lacanna, 2024). When not channelled in the SdF, PDCs can affect the inhabited centres, claiming victims (Di Roberto et al., 2014; Bevilacqua et al., 2020).

In this study, we analyse two PDCs that occurred at Stromboli in October (PDC1) and December (PDC2) of 2022. The PDCs have different sizes and originated from the collapse of hot material forming the north-east crater (NEC) rim (Fig. 6.1, Supplementary Fig. S6.1). Reaching the sea, PDCs generated tsunami waves up to ~1.4 m. We recorded the DAS strain rate signals generated by the PDCs along 4 km of optical fibre installed on the northeastern volcanic flank (Fig. 6.1a). We analyse data from co-located small-aperture arrays of DAS and nodal seismometers and from the permanent monitoring network of the University of Florence (UniFi; Fig. 6.1a). The latter consists of broadband seismometers, infrasonic pressure sensors, and thermal and visible cameras (Fig. 6.1a; Section 6.3.1, Supplementary Note 2). We calibrate DAS strain rate signals with co-located seismometers, finding a good correlation between the two datasets (Supplementary Fig. S6.2, Supplementary Note 3). We compare the multi-parametric recordings of the two PDCs and apply array processing techniques to DAS, seismic and infrasound traces to track the position of PDCs along the SdF. Changes in the resulting back-azimuths indicate

moving seismo-acoustic sources during the PDCs, consistent with visible observations. These multi-parametric observations allow us to deduce the velocities of both PDCs, ranging from ~30–70 m/s. We then perform numerical simulations that account for the 3-D topography to replicate the velocities and thus deduce flow parameters such as the basal friction. To estimate the flow volumes required for the simulations, we consider both thermal images and the energies of the seismic signals generated by the two PDCs. Finally, we point out that these datasets provide information about sudden changes in volcanic activity and phases of intense slope instability and discuss their significance for volcanic monitoring.

6.3 Methods

6.3.1 Stromboli monitoring network and DAS deployment

University of Florence (Ripepe, Delle Donne, et al., 2021) (UniFi, Italy), Italian National Institute of Geophysics and Volcanology (Giudicepietro et al., 2023) (INGV) and University of Palermo (Aiuppa et al., 2021) (UniPa, Italy) intensively monitor Stromboli volcano with a network of geophysical and geochemical sensors comprising e.g. broadband seismometers, infrasonic pressure sensors, tilt-meters and dilatometers, tsunami gauges, SO_2 cameras, MultiGAS, thermal and visible cameras.

We also use data from the permanent UniFi network (Fig. 6.1a). Seismic stations (STR, ROC, SCI) consist of Guralp digitizers equipped with Guralp CMG-40T 30 s seismometers having sampling rates of 100 Hz. Seismic stations also comprise differential acoustic pressure transducers with flat frequency responses between $0.01 - 100$ Hz, a full-scale range of 250 Pa, and sampling at 100 Hz (Ripepe, Delle Donne, et al., 2021). We also consider two (MC1, MC5) stand-alone acoustic sensors that compose the EAR infrasonic array together with STR station (Fig. 6.2i) LBZ is a visible FOSCAM camera with 4 mm of focal length, horizontal and diagonal fields of view of 70° and 75°, respectively and a 2 s sampling rate. The thermal camera (ROC) is a FLIR-A20 camera fitted with a $34° \times 25°$ optical lens (9.2 mm), having $0.1°C$ thermal resolution and 2 Hz of sampling rate (Ripepe, Delle Donne, et al., 2021).

Additionally, between 2020 and 2024, we deployed 4 km of fibre-optic cable on the northeastern flank of the volcano for DAS measurements. The optical cable consists of a polyethylene jacket which encloses a loose kevlar layer surrounding eight tight-buffered single-mode optical fibres and is buried in a hand-dug trench at $\sim 20 - 30$ cm-depth. We probed the cable with a FEBUS A1-R DAS interrogator hosted in the UniFi Geophysical Observatory (OSV in Fig. 6.1a) and parametrized with a gauge length of $L_G = 10$ m, 2 m of channel spacing and 5 kHz of sampling rate later downsampled at 50 Hz. DAS channels are named according to the offset from OSV (e.g., channel 900 in Fig. 6.2a corresponds to 900 m from OSV). The cable covers a broad area on the volcanic flank and comprises several sub-arrays. Three of them have triangular geometries, i.e. D-NT (north triangle), D-CT (central triangle) and D-ST (south triangle), while one D-GR (grid) has a grid-shaped geometry consisting of 4 squares with ~30 m-long sides (Fig. 6.1a and insets). We interrogated the fibre between 2022/09/19 – 2023/01/20.

22 SmartSolo IGU-16HR three-component (3C) nodal seismometers have been co-located with the optical cable in 2 arrays at NT (N-NT: nodes T1-7) and GR (N-GR: nodes G1-15) locations. N-NT and N-GR have triangular and grid geometries, respectively

(Fig. 6.1a). We conceived such deployment to record the volcanic activity and to calibrate DAS observations (Supplementary Note 6.6.3). The nodes have a sampling rate of 250 Hz and a 5 Hz corner frequency. We corrected node data for the instrumental response. Nodes were active between 2022/09/19 – 2022/10/20. We processed seismometer data processed using the Obspy python library (Beyreuther et al., 2010).

6.3.2 Array techniques

DAS and nodal arrays

Seismic signals generated by volcanic tremor, explosions, and PDCs have no marked P and S wave arrivals, challenging the analysis with traditional source-location methods. Conversely, array techniques allow to identify both back-azimuth and apparent velocity of seismic waves generated by these sources (Capon, 1969; Schmidt, 1986; Goldstein & Archuleta, 1987; Allstadt et al., 2018). We use array techniques to analyse seismic (DAS and nodes) and infrasound data that rely on the inversion of delay times between sensors, assuming a unique and dominant plane wave in each time window.

The array technique we use for DAS and nodes data (Métaxian et al., 2002) consists of estimating time delays between all possible $N(N-1)/2$ pairs of N sensors composing an array with a coherence-weighted linear fit of the cross-spectrum phase (Poupinet et al., 1984) on subsequent sliding time windows. Estimated time delays have an accuracy below half the sampling rate, making this technique suitable for small-aperture arrays with respect to the wavelengths of interest (Métaxian et al., 2002). For a unique plane wave, time delays τ_{ij} between sensors i and j are:

$$\tau_{ij} = \mathbf{s} \cdot \mathbf{r}_{ij}, \tag{6.1}$$

with $\mathbf{s}$ the slowness vector ($\mathbf{s} = (-||s||sin\theta, -||s||cos\theta)$, θ the back-azimuth and $\mathbf{r}_{ij}$ the relative position vector between the sensors. Back-azimuth and apparent slowness for each time window are calculated via inversion of $N(N-1)/2$ Eqs. (6.1) in a least-squares approach.

We apply the technique to DAS and node signals between $1-5$ Hz. In this frequency band, traces exhibit high energy and coherence (Fig. 6.2, Supplementary Fig. S6.3). We use time windows with lengths of 20 and 16 s, respectively, for DAS and nodes and sliding every 1 s. After several tests, we select these windows as a balance between the stability of the results and the shortest possible length. Shorter time windows provide higher resolution, while longer ones allow more precise interpolation of the cross-spectrum phase (Métaxian et al., 2002; Biagioli et al., 2024). We apply the technique on the vertical (Z) seismic signals recorded at N-NT and N-GR arrays (Fig. 6.1) having apertures of ~120 m.

Array analysis of DAS strain rate signals is not as straightforward as in the case of seismometers. DAS data exhibit a direction-dependent sensitivity and an averaging effect of the gauge length (Näsholm et al., 2022). Furthermore, DAS is more sensitive to slower, sub-horizontal waves (van den Ende & Ampuero, 2021; Trabattoni et al., 2022). The technique we propose here has already been applied to DAS records of volcanic tremor and explosions at Stromboli (Biagioli et al., 2024).

For strain rate signals, we use four arrays, i.e., D-NT, D-CT, D-ST and D-GR, each consisting of 4, 30 m-long linear (±10°) segments with different orientations (Fig. 6.1,

Fig. 6.2g, Supplementary Fig. S6.4d-f). DAS channels composing the four DAS arrays are summarised in Supplementary Table S6.1. The DAS arrays have apertures ranging from ~100 (D-CT) to ~220 (D-NT) m. D-NT and D-CT have more favourable locations, showing a craters-to-sea azimuth shift of 50 and 40°, respectively. Nevertheless, D-NT shows higher noise levels due to a significant loss in optical power at the end of the interrogated cable (Supplementary Fig. S6.5). D-ST and D-GR have narrower craters-to-sea azimuth shifts of $25 - 28°$.

The estimation of time delays requires high waveform coherence. We observe a sharp coherence drop between DAS channels at distances > 30 m and having different orientations (Biagioli et al., 2024). Therefore, we estimate the delay times separately for each segment of each DAS array. Under the assumption of a dominant wave type, we obtain back-azimuth and apparent velocity for every array by inverting all delay times together. The array analysis provides peak frequencies between $3.5 - 4$ Hz for strain rate signals and apparent velocities of ~1 km/s. Wavelengths are $\sim 250 - 280$ m, comparable with array apertures. Furthermore, this method has shown valuable results for small arrays with respect to wavelengths (Métaxian et al., 2002, 2020; Biagioli et al., 2024).

Infrasound array

We handle infrasound data with a multi-channel correlation analysis (MCCA) (Cansi, 1995; Ulivieri et al., 2011; Marchetti et al., 2019). For a three-element array and a given time window, delay times τ_{ij} between sensor pairs (i,j) are derived from the maximum of the cross-correlation function. Back-azimuth θ and apparent velocity c_a of a plane acoustic wave crossing the array are obtained by solving the equations:

$$\frac{L_{ij} cos(\beta_{ij} - \theta)}{\tau_{ij}} = c_{ij}, \tag{6.2}$$

$$\frac{L_{ik} cos(\beta_{ik} - \theta)}{\tau_{ik}} = c_{ik}, \tag{6.3}$$

being L and β the distance and azimuth of lines between sensors. For correlated signals across the array, the time residuals τ_n in a triplet,

$$\tau_n = |\tau_{ij} + \tau_{jk} + \tau_{ki}|, \tag{6.4}$$

tend to 0 ($\tau_n \rightarrow 0$), while are positive for uncorrelated records. We define infrasound detections when signals are consistent, i.e. for mean residuals τ_n below an empirical threshold (0.1 s in our case). For each detection, we provide back-azimuth θ and apparent velocity c_a. We perform MCCA on infrasound signals between $1 - 10$ Hz using 3 s-long windows sliding every 1 s. We consider the EAR array (Fig. 6.2i), with an aperture of ~290 m.

6.3.3 Estimating seismic energies

Below, in Section 6.4.3, we perform numerical simulations of the two PDCs. To carry out these simulations, we need an estimate of the volumes, which we derive from visual information (obtained from the thermal camera) and the energies of the seismic signals

generated by the two events. We compute the seismic energies of the PDCs from UniFi broadband seismometers using the equation (Vilajosana et al., 2008),

$$E_s = \int_{t_1}^{t_2} 2\pi r \rho c h u_{env}(t)^2 e^{\alpha r} dt, \tag{6.5}$$

being t_1 and t_2 the starting and ending times of the seismic signal generated by the event, r the source-receiver distance, ρ the ground density, h the thickness of the propagation level of surface waves with speed c, $u_{env}(t) = \sqrt{u(t)^2 + Ht(u(t))^2}$ the envelope of the ground velocity derived from the Hilbert transform Ht, and $\alpha = f\pi/Qc$ a frequency-dependent damping factor with Q the quality factor (Vilajosana et al., 2008; Hibert et al., 2011). We take the signal onset from visible cameras, corresponding to ts_1 and ts_2 provided in Fig. 6.2 for PDC1 and PDC2, respectively (Section 6.4.1). Since PDC2 seismo-acoustic signals are followed by a high-intensity phase probably unrelated to the flow dynamics, to have a consistent estimate of the seismic energies for both events we consider the final time t_2 as 4 s after te_1 and te_2, i.e. when the flows reached the coastline (Fig. 6.2, Supplementary Fig. S6.1). This should provide an underestimation of seismic energies but a correct estimation of energy ratios. Being $f = 5$ Hz the centre of the frequency range with the highest energies (Supplementary Fig. S6.6), we consider $h = 50$ m as one third of the wavelength of Rayleigh waves with a speed of ~700 m/s (as retrieved in Chapter 5). The distance r is calculated between each station and a point halfway down the SdF, $\rho = 2000$ kg/m^3, and $Q = 40$ (Petrosino et al., 2002; O'Brien & Bean, 2009; Hibert et al., 2011). For the sake of for simplicity we only consider here the vertical Z-component of the seismic signal to calculate the energy. Analysis of this simplification is discussed in Levy et al. (2015).

6.3.4 Numerical simulations

We perform granular flows simulation with the SHALTOP numerical model (Bouchut et al., 2003; Bouchut & Westdickenberg, 2004; Mangeney-Castelnau et al., 2005; Mangeney et al., 2007). The model is based on a thin layer approximation (i.e., small thickness compared to longitudinal extension) for depth-averaged equations of mass and momentum conservation and describes dry granular flows over 2D topography $b = z(x, y)$ (Lucas et al., 2014; Levy et al., 2015). SHALTOP calculates changes with time in the flow thickness $h(x, y, t)$ perpendicular to the topography and depth-averaged velocity of the flow $u(x, y, t)$ along the topography, being (x, y, z) the Cartesian reference coordinates. The model successfully reproduced both natural landslides and experimental flows using Coulomb-type friction laws with a constant friction coefficient μ or a friction coefficient $\mu(I)$ depending on the inertial number I (Mangeney-Castelnau et al., 2005; Mangeney et al., 2007; Favreau et al., 2010; Hibert et al., 2011; Moretti et al., 2012; Lucas et al., 2014; Levy et al., 2015; Moretti et al., 2015). In this case, we consider the Coulomb friction law with only one empirical parameter, i.e. the friction coefficient $\mu = tan(\delta)$, being δ the friction angle. This friction coefficient can be considered as a proxy of the effective dissipation during the flow (Favreau et al., 2010; Mangeney et al., 2010; Lucas et al., 2014).

6.4 Results

6.4.1 Observed PDCs and seismo-acoustic signals

We focus on two PDCs of varying sizes that occurred in October and December 2022, referred to as PDC1 and PDC2, respectively (Fig. 6.1b,c). The two PDCs originated from the partial collapse of the NECs (Fig. 6.1a). Georeferenced images recorded by visible (LBZ) and thermal (ROC) cameras (Fig. 6.1a, Supplementary Note 2), together with seismo-acoustic signals (Fig. 6.2), allow a temporal depiction of the PDCs.

First pyroclastic density current (PDC1)

PDC1 occurred on 2022/10/09 after a phase of intense explosive activity at the NECs started at ~06 : 24 UTC(Giudicepietro et al., 2023). Part of the NEC rim collapsed at $ts_1 \simeq$ 07:22:40 UTC, generating PDC1 and a subsequent lava overflow along the SdF(Giudicepietro et al., 2023) (Supplementary Fig. S6.1, Supplementary Movie 1). PDC1 exhibited a granular, concentrated basal layer overlaid with a diluted suspension (Supplementary Fig. S6.1c). PDC1 travelled downslope for about 1250 m, reaching the coastline at $te_1 \simeq$ 07:23:30 UTC (Fig. 6.1b, Supplementary Fig. S6.1d, Supplementary Movie 1). We locate the flow front using georeferenced images starting from the first frame with time tf_1 = 07:23:08 UTC (Fig. 6.1b, Supplementary Fig. S6.1). Until the arrival at sea, PDC1 covered a distance of 920 m in ~22 s, consistent with a front velocity $u_f \simeq$ 42.1 m/s (Fig. 6.1d). When impacting the water, the flow generated a peak-to-peak ~8 cm-high tsunami wave as recorded by PDC and PLB gauges about 1.5 km away (Fig. 6.1).

A preliminary comparison (Supplementary Note 3) between DAS signals and the strain rate obtained from co-localised geophones exhibits a good accuracy of DAS data (Supplementary Fig. S6.2). Fig. 6.2a,b shows an example of strain rate (channel 900) and seismic velocity (node T3, Z component) traces generated by PDC1. The signals are ~2 minutes long, spindle-shaped and emerging from the volcanic tremor (Supplementary Note 1). Corresponding spectrograms exhibit higher energies between $2-10$ Hz, in agreement with the literature(Zobin et al., 2009; Allstadt et al., 2018; Watson et al., 2023). Conversely, PDC1 does not appear in the infrasonic record (Fig. 6.2c), that is instead dominated by pressure transients produced by the intense activity at NECs(Giudicepietro et al., 2023) (Supplementary Fig. S6.1, Supplementary Movie 1).

Second pyroclastic density current (PDC2)

PDC2 (Fig. 6.1) occurred on 2022/12/04 during a phase of lava overflowing and intense flank instability along the SdF that began around 14:25 UTC. Thermal images (Supplementary Fig. S6.1, Supplementary Movie 1) show the source of PDC2 as a ~35 m-high portion of the NECs which began to slide downwards at around ts_2 = 15:17:46 UTC. PDC2 appears clearly in the LBZ frames at tf_2 = 15:18:12 UTC (Fig. 6.1c), about halfway down the SdF (Fig. 6.1c, Supplementary Fig. S6.1f, Supplementary Movie 2). From this point onwards, PDC2 covers 719 m in ~12 s, with an average front velocity $u_f \simeq$ 58.8 m/s (Fig. 6.1d). PDC2 reached the sea at a time $te_2 \simeq$ 15:18:24 UTC, and it produced a $\sim 1.2-1.4$ m tsunami wave at PLB and PDC gauges. The interaction of hot materials with the sea water also generated steam explosions (Supplementary Movie 2).

Seismo-acoustic signals generated by PDC2 are visible in the DAS, seismic and infrasonic data (Fig. 6.2d-f). PDC2 strain rate and seismic velocity waveforms are similar to those generated by PDC1, but exhibit higher amplitudes (Fig. 6.2, Supplementary Fig. S6.7). Furthermore, the signal of PDC2 is followed by a higher-energy phase with onset after the end of PDC2 at te_2 (Fig. 6.2). Strain rate and seismic velocity signals of PDC2 have energies mainly between $2-10$ Hz (Fig. 6.2, Supplementary Figs. S6.7, S6.6). Subsequent signals have higher energies in all frequency bands, in particular below ~2 Hz as visible in ROC seismic traces (Fig. 6.2e). As observed for PDC1, strain rate data (Fig. 6.2a,d) have lower resolutions below ~2.5 Hz than nodes and broadband seismometers (Fig. 6.2b,e). Infrasonic signals generated by PDC2 have amplitudes up to ~5 Pa (at MC5 sensor) and frequencies < 8 Hz (Fig. 6.2f). In the terminal phase of PDC2, and in the subsequent phase characterised by higher acoustic pressures (~10 Pa), signals have higher energies peaking between $0.2-1$ Hz.

6.4.2 Tracking PDCs

PDC1

To track the PDCs, we apply array techniques on DAS, nodes and infrasonic records (Section 6.3.2). We use four DAS arrays (D-CT, D-NT, D-ST and D-GR), two seismic arrays (N-NT, N-GR) and one infrasonic (EAR) array (Fig. 6.1, Supplementary Table S6.1). Fig. 6.2 shows the back-azimuths obtained using the D-CT, N-NT and EAR arrays. D-CT (DAS) and N-NT (nodes) are arrays characterized by low noise levels and an optimal location with respect to the SdF. Furthermore, the sensors composing the two arrays exhibit high waveform coherence between $1-5$ Hz (Supplementary Fig. S6.3). An accuracy test shown in Supplementary Fig. S6.4 for an explosive event that occurred at 07:05 UTC on 09.10.2022 exhibits precise back-azimuths obtained with EAR array and good results using D-CT and N-NT arrays. The latter two identify seismic sources ~$150-250$ m from the exploding crater (Fig. S6.3f). This location shift can be explained by (i) a mismatch of the seismic source between $1-5$ Hz with the crater or (ii) distortions due to topographical/site effects or related to the assumption of a plane wavefront. However, the locations are within the crater terrace and coincide with the zone having the highest temperatures in the area (Revil et al., 2023).

Before PDC1, when seismic traces consist only of volcanic tremor, we estimate back-azimuths pointing towards the active craters for D-CT (~$245-258°$) and N-NT (~$236-250°$) arrays (Fig. 6.2a,b). During the most energetic phase of PDC1, we observe a ~40° shift towards back-azimuths of ~$290-295$ (i.e., the shoreline direction) occurred in ~26–29 s for D-CT and ~33–38 s for N-NT. Considering an SdF length of 1250 m, these timescales imply velocities of $43-48$ and $33-38$ m/s, respectively (Table 6.1). These results match the front velocity of ~42 m/s estimated with georeferenced visible images (Fig. 6.1d).

Time differences (~$10-20$ s) between the arrival of the PDCs at sea (te_1 and te_2) and the time when the back-azimuths obtained with D-CT and N-NT arrays have values corresponding with the coastline can be due to several effects. First, we have a resolution of the results given by the length of the moving time windows, i.e. 20 s for DAS and 16 s for nodal arrays. Furthermore, we are considering extended seismic sources (Arran et al., 2021), and materials continue to fall along the SdF even 20 s after the PDCs reach the sea (Supplementary Movie 1).

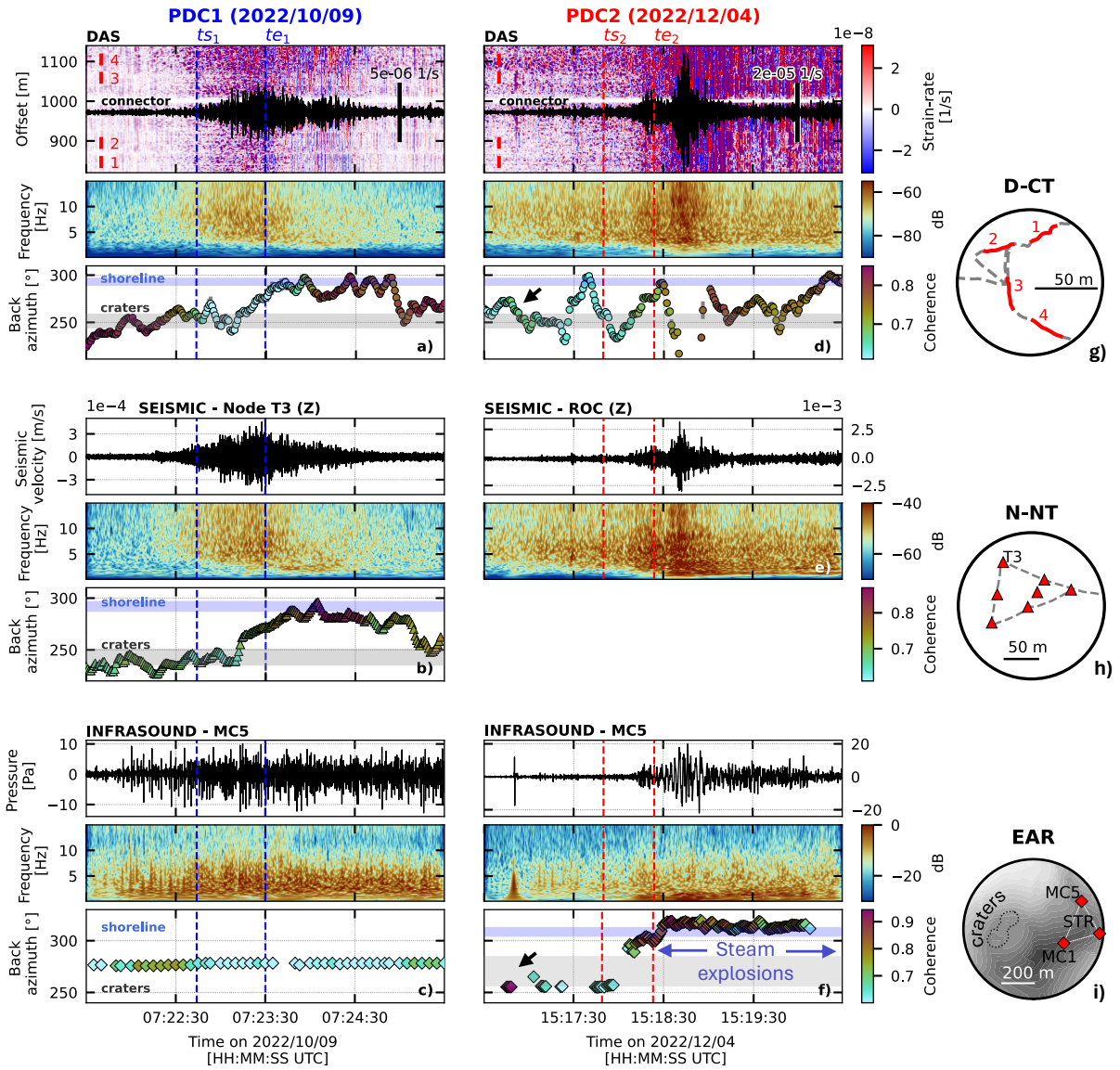

Figure 6.2: 4-minutes-long traces, spectrograms and corresponding back-azimuths of PDC1 (left column) and PDC2 (right column). (a,d) Show the DAS strain rate at the D-CT array. (b,e) Show the seismic velocity (vertical component) recorded by the T3 node (b) and the ROC seismometer (e). (c,f) Show the acoustic pressure recorded by the MIC5 infrasonic sensor. Back-azimuths are calculated using the D-CT, N-NT and EAR arrays. Supplementary Fig. S6.4 shows the results obtained with the remaining DAS and nodal arrays. The blue and red vertical lines indicate the onsets (ts_1 = 07:22:40 and ts_2 = 15:17:46 UTC) and arrival at sea (te_1 = 07:23:30 and te_2 = 15:18:24 UTC) of PDC1 and PDC2, respectively, as observed by the thermal and visible cameras (Supplementary Fig. S6.1, Supplementary Movies 1,2). Back-azimuths obtained with D-CT and N-NT arrays in (a,b,d) are filtered for coherencies> 0.4 and errors$< 10°$ while being smoothed with a 3 s-long window. Back-azimuths obtained with EAR array are filtered for time residuals $< 0.1\ s$ (Section 6.3.2). Black arrows in (d,f) indicate the back-azimuths obtained for an explosion that occurred at the NECs at 15:16:45 UTC. (g-i) Show the geometries of D-CT, N-NT and EAR arrays.

We obtain similar results using the D-NT array (Supplementary Fig. S6.8), although less reliable due to high noise levels (Supplementary Fig. S6.5). Back-azimuths obtained with the N-GR, D-GR and D-ST arrays point instead in the direction of the craters with slight seaward deviations (Supplementary Fig. S6.8), probably due to less favourable locations with respect to the SdF. Similarly, back-azimuths obtained with the EAR infrasound array (Fig. 6.2c) during PDC1 always point towards the active craters, probably due to signals produced by the intense spattering activity at NECs dominating the wavefield (Supplementary Movie 1).

PDC2

We observe crater-to-sea back-azimuth shifts during PDC2 considering the D-CT and EAR arrays (Fig. 6.2d,f). These changes occur in less time than PDC1 and are consistent with flow velocities of ~63-73 and ~52-63 m/s, respectively. Other shifts in back-azimuth, visible in D-CT results before and after PDC2 (Fig. 6.2d), are probably related to landslides along the SdF due to the high instability of the slope (Supplementary Movies 2, 4). After PDC2, the EAR array indicates a stable acoustic source at sea (Fig 6.2f), probably due to steam explosions caused by hot material interacting with seawater (Supplementary Movie 4). The D-CT array instead shows a back-azimuth returning to the craters after PDC2. At this stage, back-azimuth values are around ~190° but with errors up to 30° (Supplementary Fig. S6.9). The apparent velocities rise from stable values of ~1 km/s up to 6 km/s, with errors up to ~3 km/s (Supplementary Fig. S6.9). These results possibly indicate a deeper seismic source within the volcano, representing a limit for our array method. Array analyses using D-GR and D-ST arrays provide similar outcomes (Supplementary Fig. S6.8).

	Average velocity [m/s]	
Method	PDC1	PDC2
D-CT (strain rate)	43-48	63-73
N-NT (seismic Z)	33-38	N.A.
EAR (infrasound)	N.D.	52-63
LBZ (visible camera)	42	59

Table 6.1: Average velocities (m/s) of PDC1 and PDC2 estimated with the back-azimuth results from D-CT and N-NT (seismic) and EAR (infrasonic) arrays and from frames of the LBZ visible camera. PDC1 was not deteced (N.D.) with EAR infrasound array. Node data were not available (N.A.) during PDC2

6.4.3 PDCs Simulations

To understand the different velocities of the two PDCs, we simulate granular flows with SHALTOP numerical model (Bouchut et al., 2003; Bouchut & Westdickenberg, 2004; Mangeney-Castelnau et al., 2005; Mangeney et al., 2007) (Section 6.3.4). SHALTOP simulates dry granular flows over 3-D topography in a Coulomb-type friction law with a friction coefficient $\mu = tan(\delta)$, being δ the friction angle. We used both visual and seismic observation to constrain the volumes of the PDCs needed for the simulations.

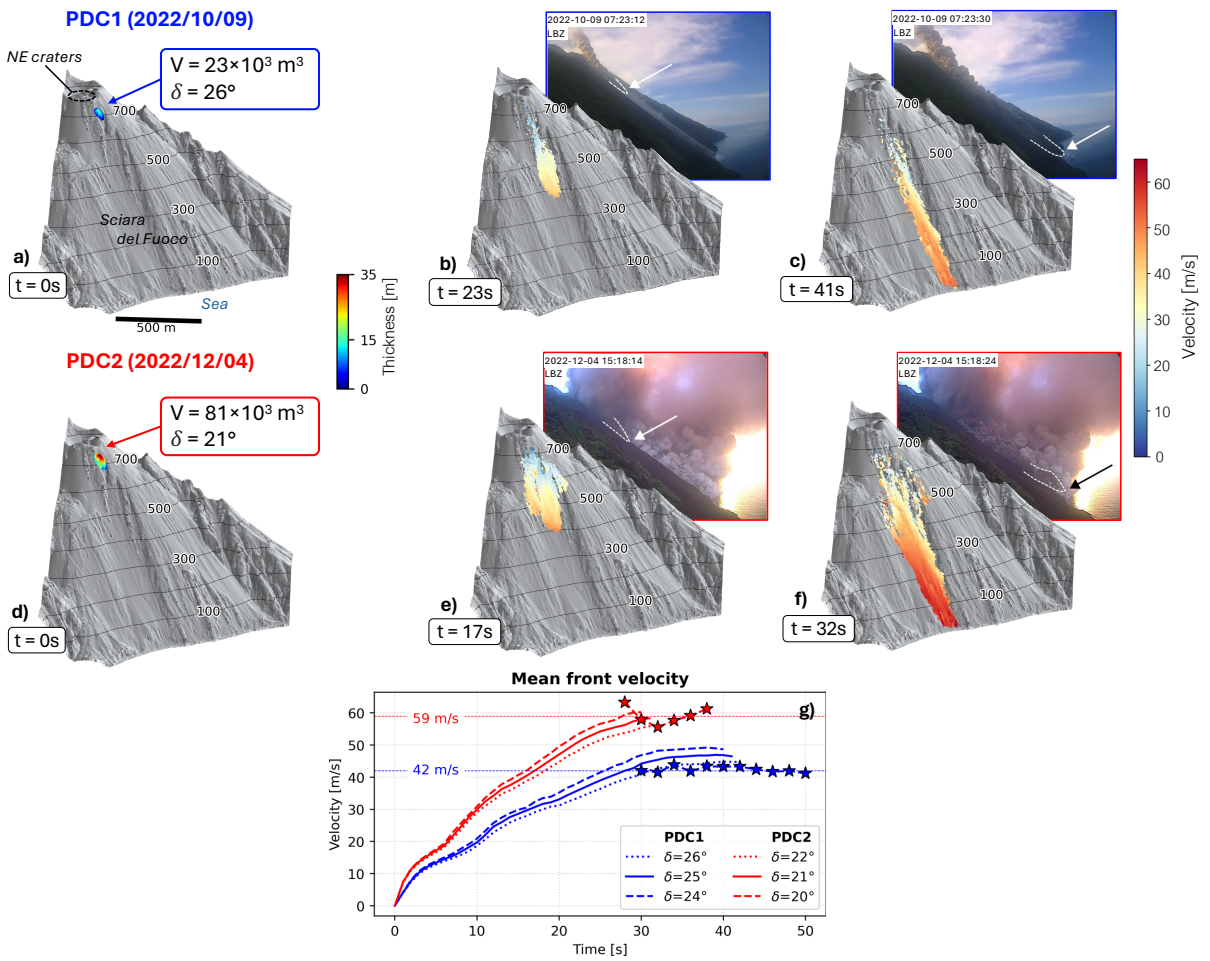

Figure 6.3: Snapshots of the simulations that best fit the observed front velocities of PDC1 (left column, a-c) and PDC2 (right column, d-f). (a) and (d) show the thickness of the initial mass. (b, c) and (e, f) show the velocity of PDC1 and PDC2 at different times, i.e. when the flows are halfway down and reach the shoreline, respectively. Volumes V and friction coefficients δ of PDC1 ($V_1 = 23 \times 10^3\ m^3$, $\delta_1 = 25°$) and PDC2 ($V_2 = 81 \times 10^3\ m^3$, $\delta_2 = 21°$) are shown in (a) and (d) respectively. (g) shows the average front velocity of PDC1 (blue) and PDC2 (red) calculated at every time step for flow thickness > 0.5 m and different friction angles δ. The average front velocity is calculated in a radius of 100 m from the flow front. Blue and red stars in (g) are the front velocities calculated from each georeferenced frame (Fig. 6.1d).

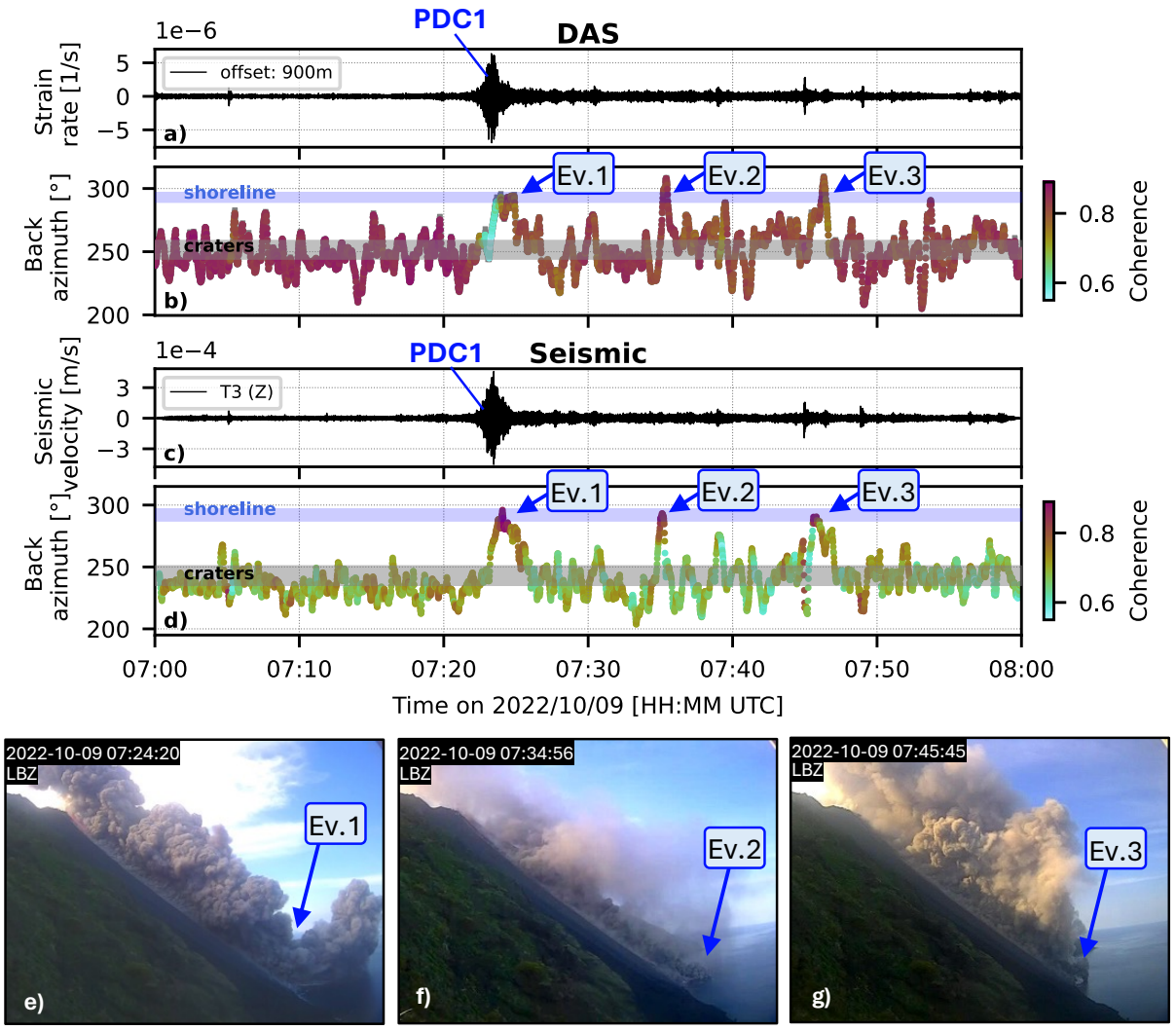

Figure 6.4: (a) DAS strain rate traces (offset 900m) between 08:00–07:00 UTC on 2022/10/09. (b) back-azimuth results obtained with the D-CT array smoothed with a 5 s window. (c) Seismic velocity trace (node T3, Z component) during the same period. (d) back-azimuth results obtained from N-NT array smoothed with a 5 s window. (e-g) Three snapshots of the LBZ visible camera during the three events (Evs. 1-3). Event 1 corresponds to PDC1, while Events 2 and 3 are landslides along the SdF.

Thermal images (Supplementary Fig. S6.1, Supplementary Movie 1) allow us to observe the source of PDC2 as a ~47 m-long and ~35 m-high portion of the volcanic edifice. These dimensions give an estimated volume of PDC2 as $V_2 \simeq 81 \times 10^3$ m^3 considering a paraboloid geometry having an extension of ~90 m (i.e., the diameter of the NEC area; Supplementary Fig. S6.10). We can not estimate the volume V_1 of PDC1 from monitoring images. However, we derive it assuming a linear relation between the volume of PDCs and related seismic energies considering the same area and similar trajectories (Norris, 1994; Hibert et al., 2011). We calculate seismic energies using Eq. (6) (Vilajosana et al., 2008) and the Z components of permanent broadband seismometers (Section 6.3.3). Calculated energies are $0.06 \leq Es_1 \leq 0.40$ MJ and $0.34 \leq Es_2 \leq 1.80$ MJ for PDC1 and PDC2, respectively, while being higher for the E and N components (Supplementary Table S6.2).

The energy ratio $R_{Es} = Es_2/Es_1$ can be thus used to infer the volume $V_1 = V_2 R_{Es}^{-1}$. For the same trajectories and stations, R_E is equal to the ratio between the envelopes of

the seismic traces $u_{env}(t)$. Signals between 1 – 15 Hz of PDC1 and PDC2 recorded by broadband seismometers yield a mean ratio R_{Es} = 4.6 considering all the three seismic components (Supplementary Table S6.3). DAS strain rate traces in the same frequency band exhibit a lower mean ratio R_{Es} = 2.7 (Supplementary Fig. S6.11). These values translate into volumes between $17-30\times10^3$ m^3, from which we derive an average volume $V_1 = 23\times10^3$ m^3.

For the PDC modelling, we use a 5 m resolution DEM of the SdF (Fig. 6.3). We place the released mass of both PDCs below the NECs at an altitude of ~700 m. We derive the friction angle δ from PDC volumes using the empirical relation,

$$\mu \simeq tan(\delta) \simeq V^{-0.0774}, \tag{6.6}$$

obtained by fitting runout distances of landslides having varying sizes and occurring in several terrestrial and extraterrestrial contexts (Lucas et al., 2014). The best fit between measured and simulated PDC1 velocities is for friction angles δ~26° (Fig. 6.3a). We obtain terminal front velocities of ~44 m/s at the end of the SdF (Fig. 6.3g). The friction angle that best fits the velocity and timing of PDC2 is instead δ~21° (Fig. 6.3d). Simulated PDC2 reaches the shoreline in 31 s, exhibiting final front velocities of ~59 m/s (Fig. 6.3g). These values are respectively higher and lower than those obtained directly from Eq. (6.6) using PDCs volumes V_1 and V_2 (i.e., δ = 24.6° and δ = 22.6°) but are within the uncertainty range of $\mu \pm 0.1$ of estimated friction coefficients (Lucas et al., 2014).

6.5 Discussion

We recorded seismo-acoustic signals generated by two PDCs at Stromboli Volcano using DAS, seismometers, and infrasonic pressure sensors from close distances (~1 – 2 km). Back-azimuth shifts of seismo-acoustic sources during the PDCs observed in array analysis results for these three datasets indicate flows propagating from NECs to the sea. We then estimate lower flow velocities for PDC1 (~33 – 48 m/s) than PDC2 (~50 – 73 m/s). These velocities match independent estimates obtained with georeferenced monitoring images (Table 6.1). Major differences between the velocities obtained from DAS and node results and those estimated from monitoring images may be due to (i) effects of the time windows or (ii) the assumption of a single dominant wave in each window. The persistent volcanic tremor may indeed add further complexity to the analysis. These values of velocities are however in agreement with those of other PDCs at Stromboli (Calvari et al., 2020; Calvari et al., 2022; Ripepe & Lacanna, 2024) and different volcanoes (Yamasato, 1997; Jolly et al., 2002; Ripepe et al., 2010; Delle Donne et al., 2014; Watson et al., 2023).

We reproduce reasonably well these velocities with numerical simulations considering volume-dependent (Eq. (6.6)) friction coefficients μ (and angles δ). These outcomes are in agreement with previous studies of PDCs and landslides worldwide, where larger volumes exhibit higher velocities and require lower effective friction angles than laboratory estimates (Mangeney et al., 2000; Heinrich et al., 2001; Bayarri et al., 2009; Lucas et al., 2014; Levy et al., 2015). This effect has been explained by a common mechanism resulting in frictional weakening with increasing flow velocity (Lucas et al., 2014). Furthermore, other complex factors may play a significant role in fluidising PDCs, involving the influence of fine particles, volcanic gases and high temperatures (Delannay et al., 2017).

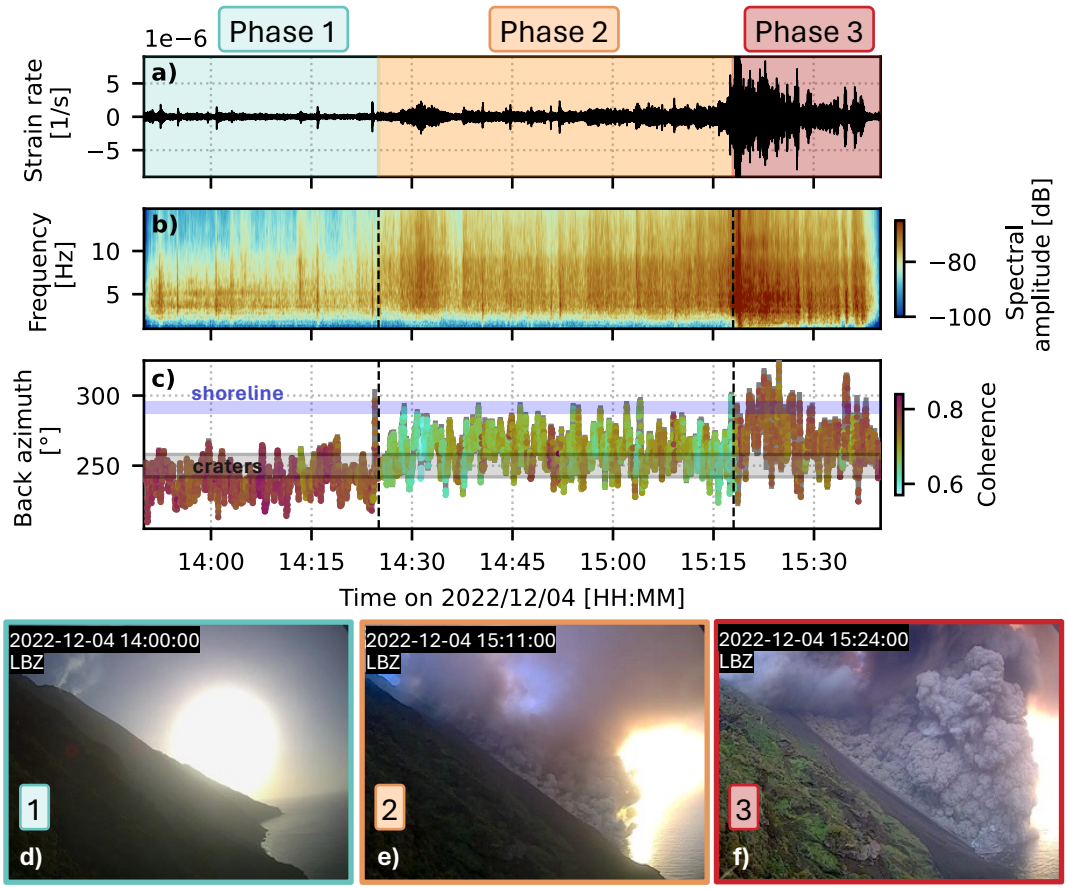

Figure 6.5: (a) Cumulative strain rate time series along offsets 890-910 between 13:50–15:40 UTC on 2022/12/04. The three colours represent three distinct phases of increasing volcanic activity observed from video, spectrogram and back-azimuth results. (b) Spectrogram of (a). (c) Back-azimuth results obtained with the D-CT array. The grey and blue horizontal bands in (c) represent the back-azimuths of the craters and the shoreline, respectively. The black vertical lines in (b) and (c) represent the two times when a change in activity is observed (i.e., ~14:25 and ~15:18 UTC). (d-f) Three snapshots of the LBZ camera during the 3 phases of activity.

DAS signals recorded in our experiment typically exhibit higher noise levels at frequencies < 2.5 Hz and lower amplitudes than nodes (Supplementary Note 6.6.3, Supplementary Fig. S6.2), consistently with previous observations at Stromboli (Biagioli et al., 2024). Implementing array techniques to DAS signals is not straightforward, given cable directivity and gauge-length effects (Näsholm et al., 2022). However, beamforming of DAS signals allowed to retrieve the back-azimuths of earthquakes (Nayak et al., 2021; van den Ende & Ampuero, 2021), rockfalls (Walter et al., 2020), and volcanic explosions (Jousset et al., 2022). Furthermore, DAS is used in several contexts to monitor RGMMs such as avalanches (Fichtner et al., 2021; Paitz et al., 2023) and rockfalls (Walter et al., 2020; Xie et al., 2023). In this study, we apply array analysis methods to individual fibre segments, as previously done in the literature (van den Ende & Ampuero, 2021; Biagioli et al., 2024). Our results also show that, in addition to the dynamics of individual events, DAS data can provide information about sudden changes in volcanic activity and slope instability, in good agreement with inertial seismometers.

Fig. 6.4 shows the back-azimuths obtained with D-CT and N-NT arrays between 07:00–08:00 UTC on 2022/10/09. These results identify a stable source in the crater direction during most of the time. However, we observe 3 phases during which back-azimuths are consistent with seismic sources reaching the coastline. These moments coincide with PDC1 (event 1 in Fig. 6.4) and two minor landslides (events 2 and 3) that occurred at ~ 07:38 and ~ 07:45 UTC and that were visible in monitoring images (Fig. 6.4e-g, Supplementary Movie 3).

Additionally, Fig. 6.5 shows ~2 hr of strain rate traces, spectrogram and back-azimuths estimated with D-CT array on 2022/12/04, before and after PDC2. We observe a first phase (phase 1 in Fig. 6.5) characterised by moderate amplitudes, frequencies mainly between $1 - 5$ Hz and back-azimuths indicating a source in the direction of the craters. Around ~14:25 UTC, a phase of slope instability begins (Fig. 6.5e, Supplementary Movie 4). Strain rate traces exhibit higher amplitudes and frequencies (up to ~15 Hz). At the same time, the coherence of the detections decreases from ~0.8 to ~0.6, while back-azimuths indicate seismic sources oscillating along the SdF due to recurrent landslides. At ~15:18 UTC (when PDC2 occurred), signal amplitudes increase in all frequency bands, along with the intensification of the slope instability as visible from monitoring images (Fig. 6.5f, Supplementary Movie 4). Estimated back-azimuths indicate seismic sources moving several times from the craters down to the sea in conjunction with landslides.

While further research is still needed, in particular, to expand the technique to the entire fibre optic cable to benefit from distributed measurements, our results show that DAS offers a complementary tool for volcano monitoring. Multi-parameter observations also allow us to identify various and simultaneous phenomena, e.g. landslides and steam explosions generated by hot materials reaching the seawater. Besides detecting and tracking RGMMs at volcanoes (and in other environments), the joint use of DAS, seismometers and infrasonic sensors can provide relevant information about sudden changes in volcanic activity that lead to sharp morphological changes and possibly worsening risk scenarios.

6.6 Supplementary Information for: Tracking and characterising pyroclastic density currents with DAS and seismo-acoustic observations

6.6.1 Supplementary Note 1: Stromboli activity

Stromboli is an active volcano within the Aeolian Arc in the Southern Tyrrhenian Sea. Stromboli ordinary activity consists of a persistent explosive regime with frequent ($\sim$ 13 exp/hr; Ripepe et al., 2008), moderate (VEI=1) explosions alongside continuous degassing (Rosi et al., 2013; Ripepe, Delle Donne, et al., 2021). Several models indicate the source of the explosions as gas slugs nucleating, rising and eventually bursting in the conduit (Blackburn et al., 1976). These explosions generate seismic signals in a broad frequency range (10^{-2} – 10 Hz; Neuberg et al., 1994; Chouet et al., 1997, 2003). Gas over-pressure released in the atmosphere produces acoustic waves, in particular in the infrasonic ($<$ 20 Hz) frequency band (Ripepe et al., 2008; Rosi et al., 2013). The seismic records also present a continuous tremor with frequencies typically between $\sim 1-5$ Hz (Nappi, 1976; Langer & Falsaperla, 1996; Ripepe et al., 1996; Wassermann, 1997). Tremor signals at Stromboli are inferred to be linked with the coalescence of small ($<$ 0.5 m) gas bubbles in the magma column bursting every $\sim$ 1–2 s (Ripepe & Gordeev, 1999). These observations are evidence of intense degassing mechanisms of the magma column, similar to other open-conduit basaltic volcanoes (Ripepe, Delle Donne, et al., 2021). However, this normal activity may be interrupted by other eruptive or explosive phenomena, such as lava flows or more explosions, i.e., the so-called Strombolian paroxysms (Métrich et al., 2021). These latter events represent a significant hazard for the island due to the broad dispersal of the volcanic ballistic projectiles and the potential formation of pyroclastic density currents and, contextually, of tsunamis (Rosi et al., 2013; Ripepe & Lacanna, 2024).

6.6.2 Supplementary Note 2: Camera Analysis

Visible images are recorded every 2 s (0.5 Hz of sampling rate) by LBZ camera (Fig. 1a) with a resolution of 640×480 pixels. LBZ is a FOSCAM camera with 4 mm of focal length and horizontal and diagonal fields of view of 70° and 75°, respectively. LBZ is located at an altitude of $\sim$ 190 m a.s.l. (Fig. 1a) and has a view direction of 215°. We use these parameters to georeference each frame with the IMGRAFT software (Messerli & Grinsted, 2015) via a high-resolution (0.5 m) DEM resampled at 5 m. When visible, the pyroclastic front is then selected in each frame (Fig. S6.1) and the pixels are then converted into 3-D UTM coordinates (Fig. S6.1i).

6.6.3 Supplementary Note 3: DAS data calibration

We retrieve strain rate signals from seismic velocities recorded by co-located nodes to calibrate DAS measurements. The strain rate at the midpoint of a line segment of length nG_L (i.e., a multiple of the gauge length G_L) can be obtained by differentiating the seismic velocities $\dot{u}$ (in the fibre direction) recorded at the two endpoints extremes, i.e., -$L/2$ and $L/2$. This estimate can be then compared with the stack of the DAS strain rate $\dot{\varepsilon}$ via the

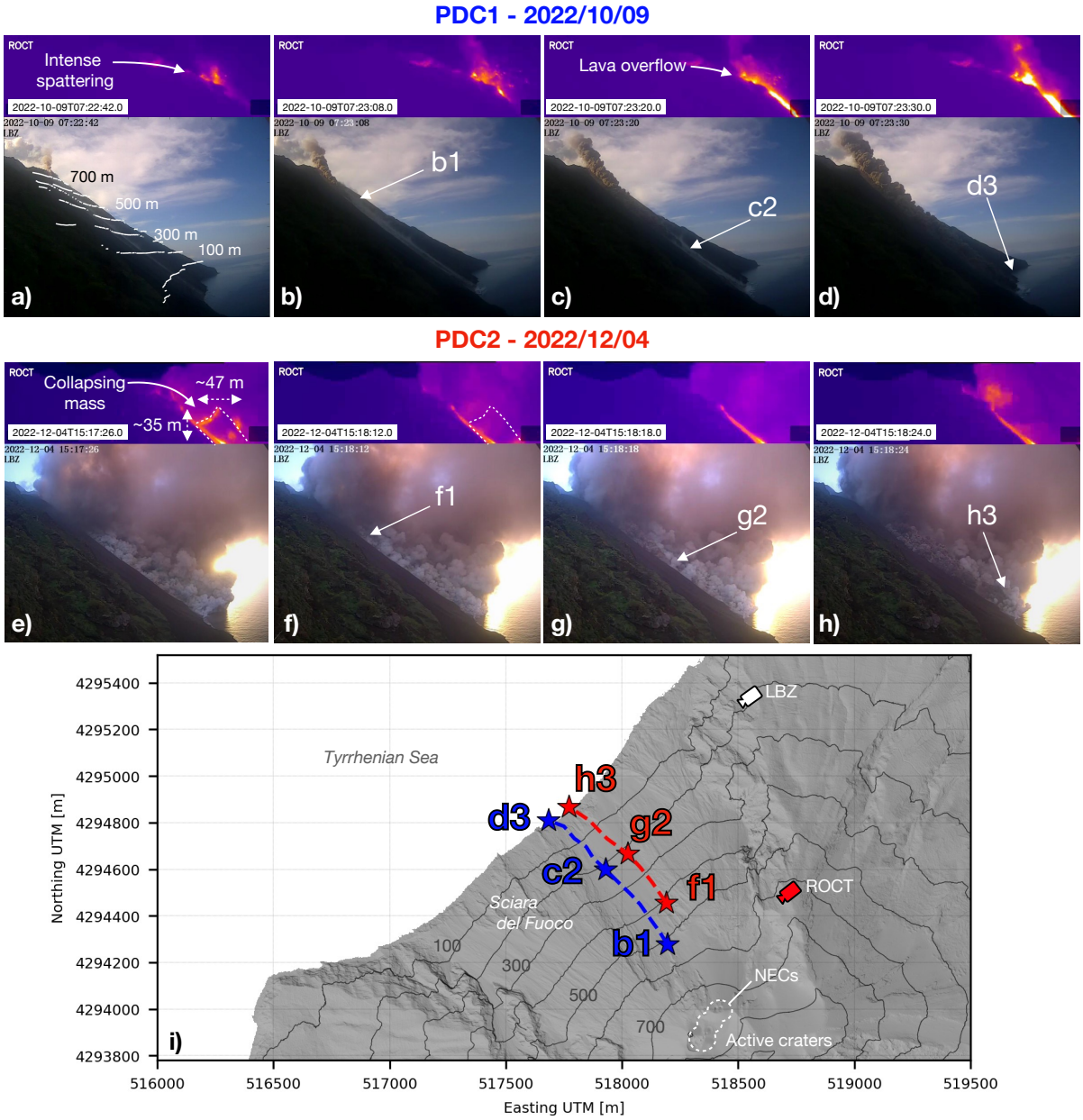

Figure S6.1: (a-d) Thermal images recorded by the ROC camera (top), and georeferenced visible images recorded by the LBZ camera (bottom) during PDC1. In (a), white lines represent the contour lines of the DEM projected onto the image (Supplementary Note 2). (e-h) Same as the top line, but for PDC2. In (e), we can observe the dimensions of the mass that generated PDC2, having a height of $\sim$ 35 m and a width of $\sim$ 47 m. White arrows in (b-d) and (f-h) point towards the location of PDC1 and PDC2 along the SdF. (i) Coordinates of the front position of PDC1 (blue) and PDC2 (red) obtained from visible images at three different times.

finite-difference relationship (Wang et al., 2018),

$$\dot{\varepsilon}|_{x=-(n-1)L_G/2} + \cdots + \dot{\varepsilon}|_{x=0} + \cdots + \dot{\varepsilon}|_{x=(n-1)L_G/2} = \\ = \frac{\dot{u}|_{x=nL_G/2} - \dot{u}|_{x=-nL_G/2}}{L_G}, \tag{6.7}$$

where $\dot{\varepsilon}$ and $\dot{u}$ are evaluated at different positions x along the segment. We consider 11 linear segments (and corresponding nodes) with lengths of 20 to 60 m and belonging

to D-NT and D-GR arrays (Fig. S6.2). We sample DAS channels every 2 m and use a 10 m gauge length. Therefore, the left-hand side of Eq. (6.7) is the sum of one DAS channel every three along each fibre segment to have independent estimates of the strain rate in space. We obtain the seismic velocity components along the fibre direction by rotating the three components of each node according to the azimuth and slope of the corresponding cable segment. The longitudinal components are then differentiated in the right-hand side of Eq. (6.7).

Fig. S6.2 shows the comparison between the left and right-hand sides of Eq. (6.7) for the 11 selected segments considering one explosive eruption occurred on 2022/10/09 at ~07:05 UTC (the same as in Figs. S6.3, S6.4). Between $1 - 15$ Hz, we observe an almost perfect agreement in phase between DAS and node strain rate traces, with maximum cross-correlation coefficients (MCCs) generally above 0.9. These values are rather stable for every segment. Segments T1-T2, G9-G11 and G13-G14 are an exception, exhibiting MCCs of 0.85, 0.86 and 0.69, respectively. DAS strain rate traces exhibit lower amplitudes than those obtained from the nodes. Ratios R between Root Mean Square amplitudes (RMSA) of nodes and DAS strain rate traces for 4-second time windows centred on each explosive event have values ranging between $\sim 1.4-5$ and are typically > 2.5. These values reasonably agree with other estimates at Stromboli volcano (Biagioli et al., 2024). Other studies observed small differences between the amplitudes of the signals recorded by DAS and seismometers but never showed consistent variations of this level (Wang et al., 2018; Currenti et al., 2021; Jousset et al., 2022). We suppose that these amplitude differences may be due to insufficient ground-to-fibre or cable-to-fibre coupling. The internal cable structure may have a significant impact on the efficiency of strain transfer from the ground to the individual fibres, therefore influencing the amplitude of the recorded signals (Her & Huang, 2011; Reinsch et al., 2017; Diaz-Meza et al., 2023; Biagioli et al., 2024).

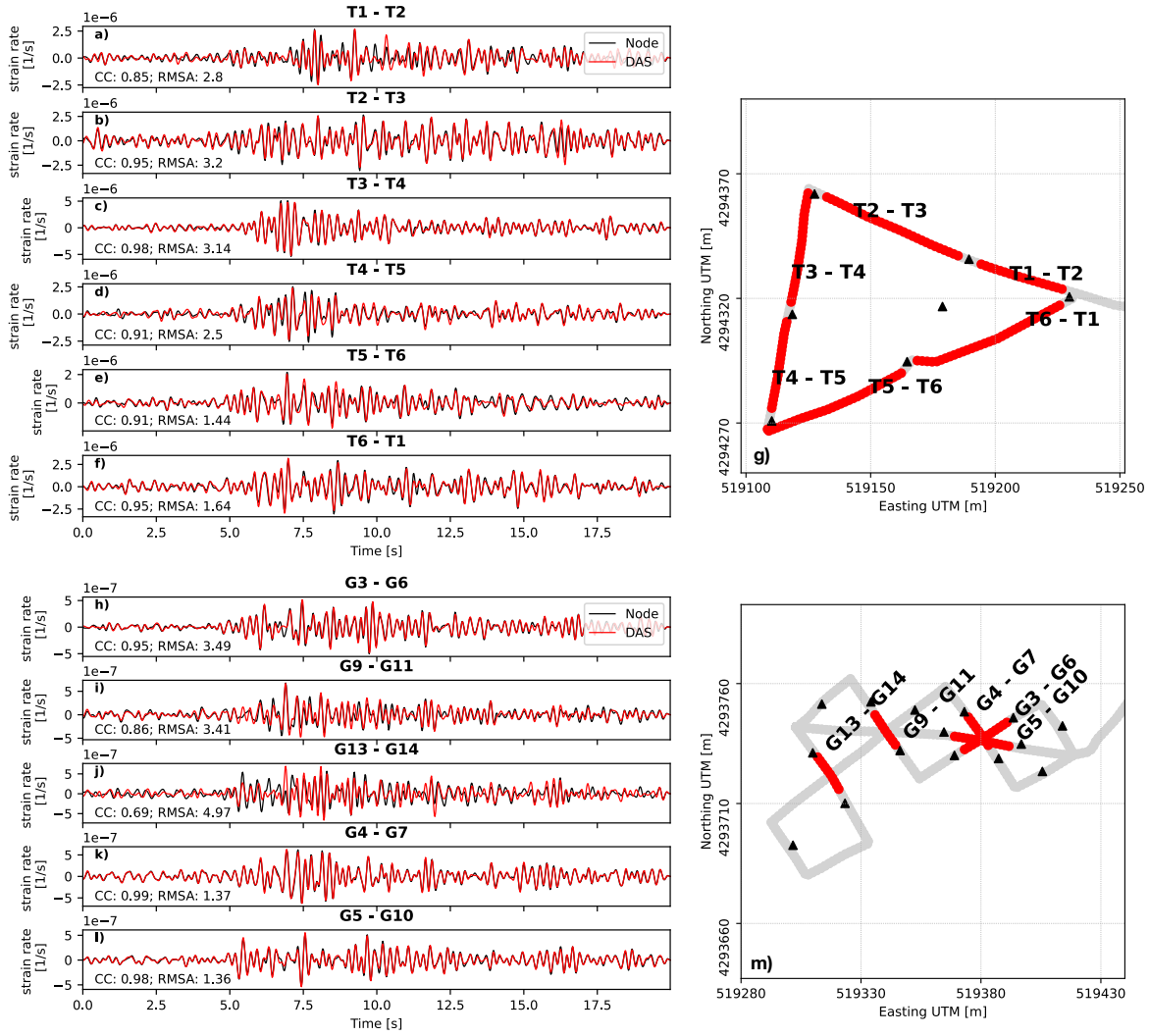

Figure S6.2: Comparison between the strain rate traces recorded by DAS (red) and obtained from nodes (black) using Eq.(5.2) with six segments of the NT array (a-g) and five segments of the GR array (h-l). Traces are filtered between $1 - 15$ Hz. The ratios between the RMSA of node and DAS traces and the maximum cross-correlation coefficients (CC) between the two waveforms appear in the bottom left of each plot. (g) and (m) show the geometry of the NT and GR arrays. The fibre optic segments we use are coloured in red. Black triangles indicate the 3C nodes.

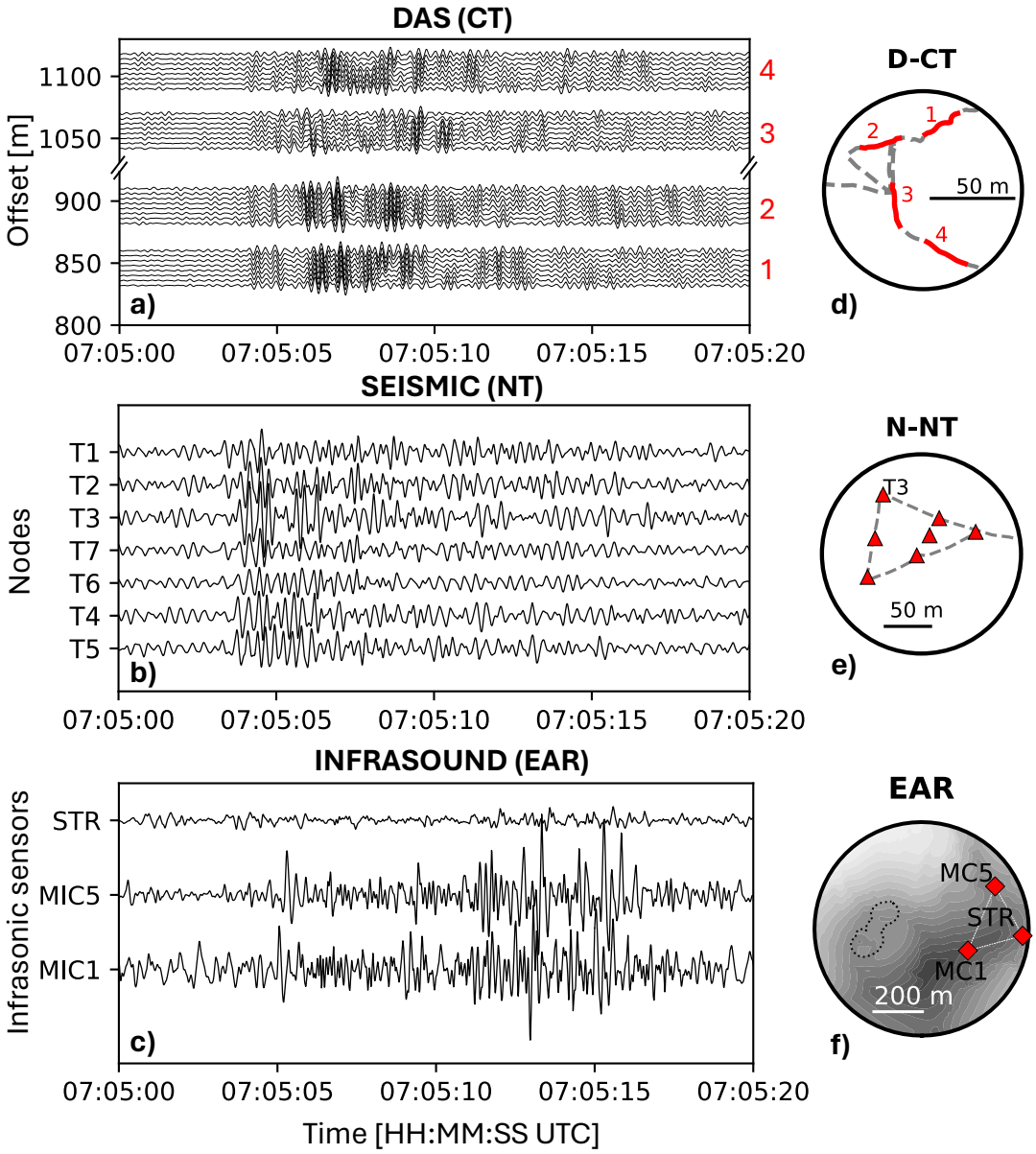

Figure S6.3: (a) Strain rate, (b) seismic velocity, and (c) infrasonic pressure traces generated by one volcanic explosion (occurred on 2022/10/09 at ~07:05 UTC) recorded by D-CT (d), N-NT (e) and EAR arrays (f). DAS and node traces are filtered between $1-5$ Hz, while infrasound traces are filtered between $1-10$ Hz.

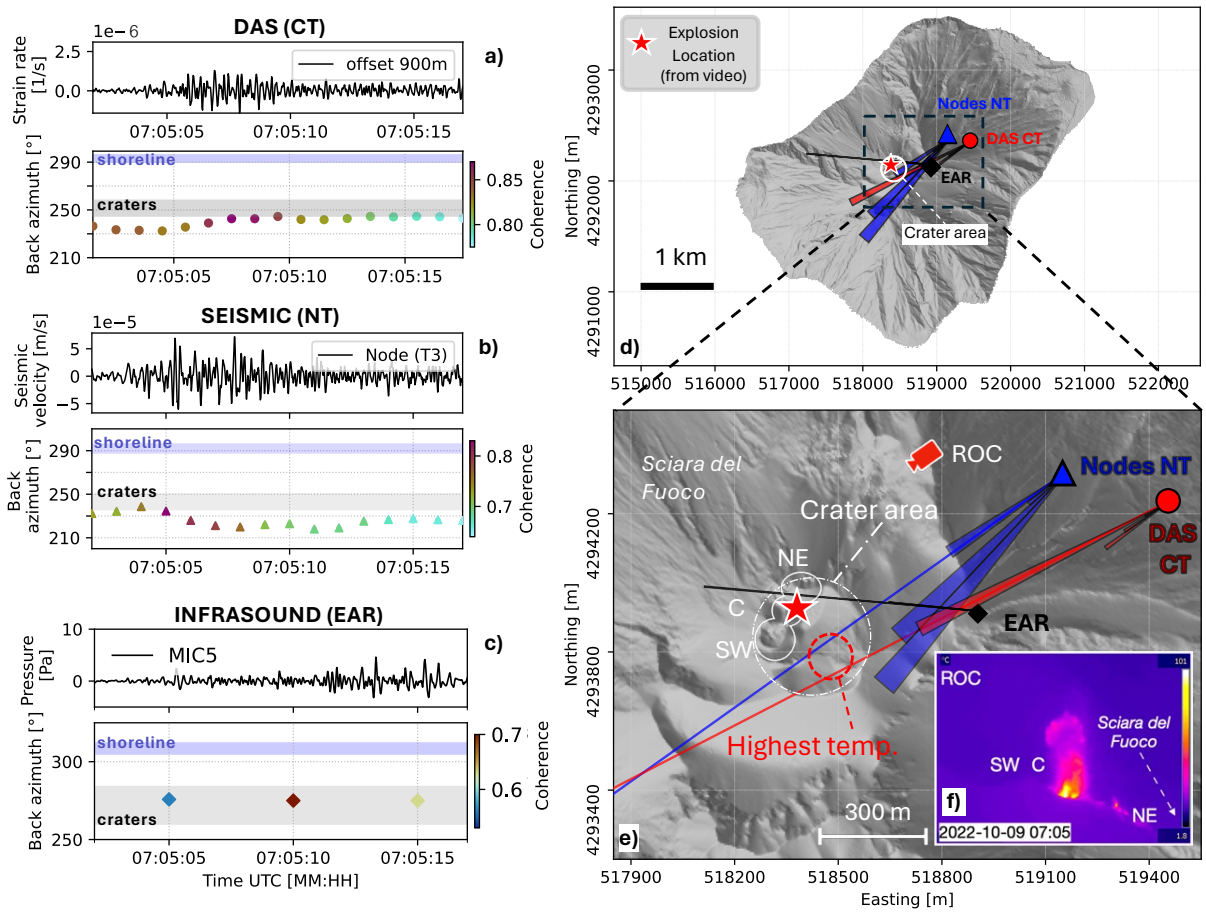

Figure S6.4: (left column) 20 s-long traces and back-azimuth results obtained with D-CT (a), N-NT (b) and infrasound EAR (c) arrays during an explosive event (2022/10/09 at 07 : 05 UTC). (d) Map of Stromboli volcano with rose diagrams of the back-azimuth results obtained with D-CT (red), N-NT (blue) and EAR (black) arrays. (e) Zoom on the crater area. The red circle, blue triangle, and black diamond in (d,e) represent the D-CT, N-NT and EAR array centroids. The red and blue lines in (e) are the back-azimuths obtained using D-CT and N-NT that exhibit the highest coherence. The white dashed circle in (e) represent the total extent of the crater area, while the red one corresponds to the area of highest temperature at the summit(Revil et al., 2023). The red star in (d,e) is the location of the explosive event as seen from ROC thermal camera (f).

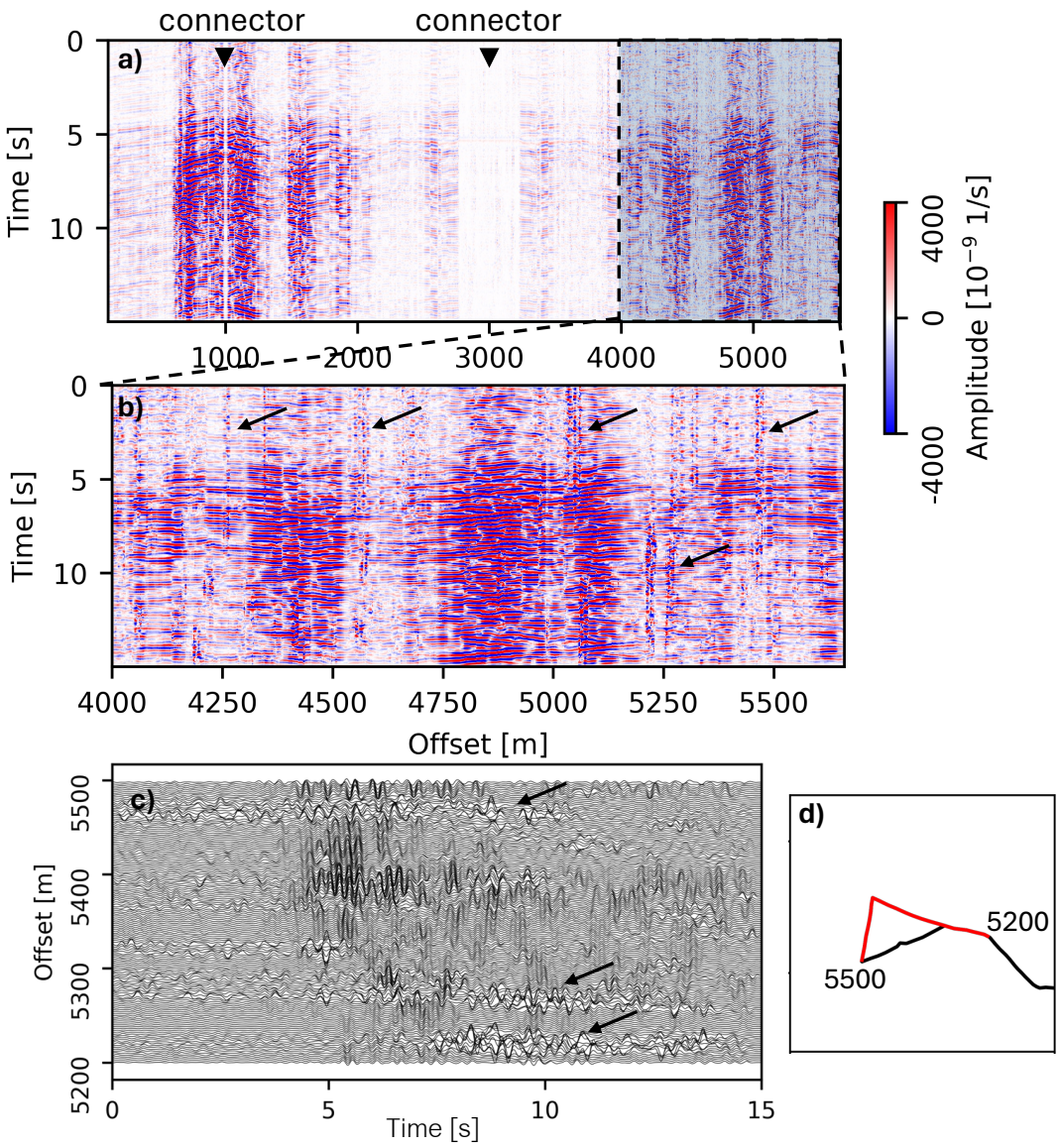

Figure S6.5: (a) 15-second strain rate traces of the explosion occurred at 07:05 UTC on 2022/10/09 (same as Supplementary Figs. S6.2, S6.7, S6.6) recorded along the entire fibre-optic cable. (b) Zoom on the last portion of the fibre between offsets 4000 and 5600 (comprising the D-NT array). Several spurious signals due to high noise levels are visible at different (and varying) offsets as vertical features. (c) Individual strain rate traces between offsets 5200-5500 m. We observe the same features due to high noise levels. (d) Map of the fibre location of D-NT with offsets 5200-5500 m highlighted in red. Arrows in (b) and (c) indicate the spurious signals.

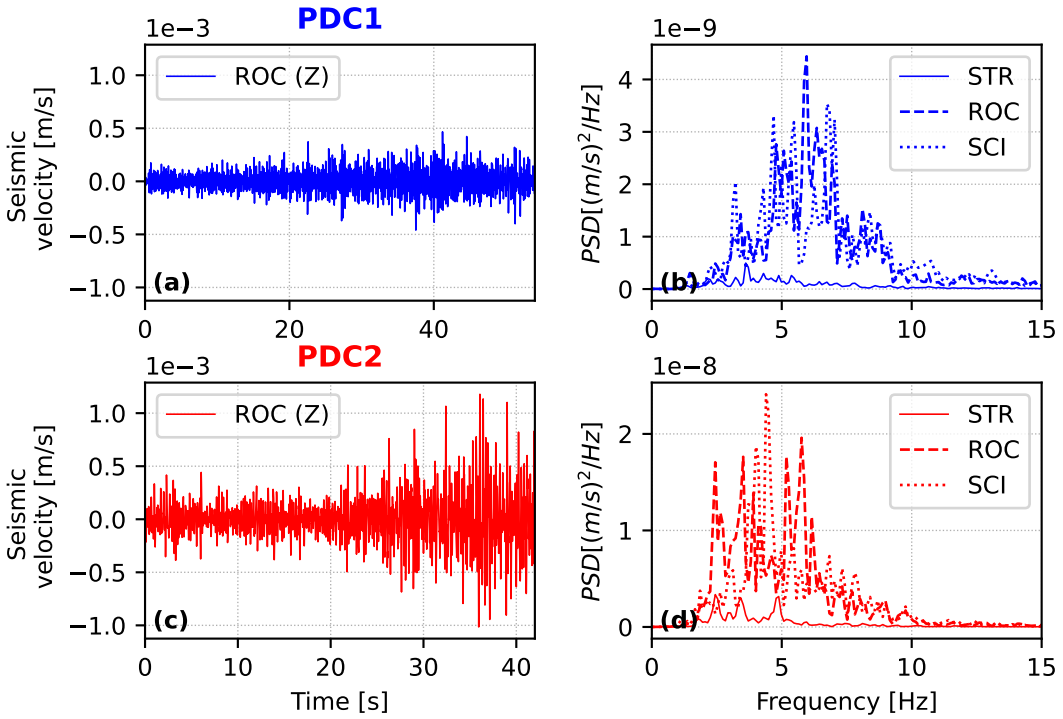

Figure S6.6: (left column) Seismic velocity traces of ROC broadband seismometer (Z component) of PDC1 (a) and PDC2 (b) used to compute seismic energies. The onsets correspond to t_{s1} and t_{s2}, respectively. Signals are truncated 4 s after the entrance of the PDCs in the sea (at t_{e1} and t_{e2}. (right column) Power spectral densities of PDC signals recorded by STR, ROC and SCI broadband seismometers (Z components).

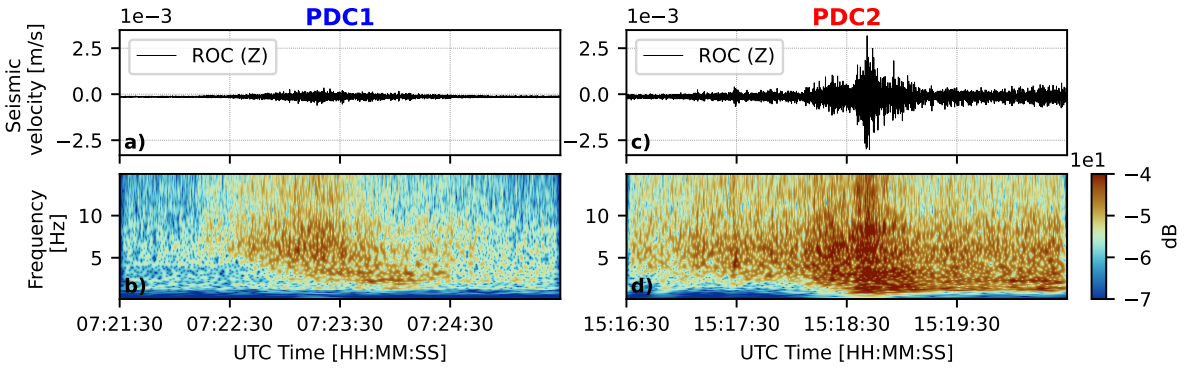

Figure S6.7: Seismic velocity traces of ROC Z component (top row) and spectrograms (bottom row) for both PDC1 and PDC2. Same as Fig. 2b,e, but maintaining ROC as station for both PDCs for a better comparison.

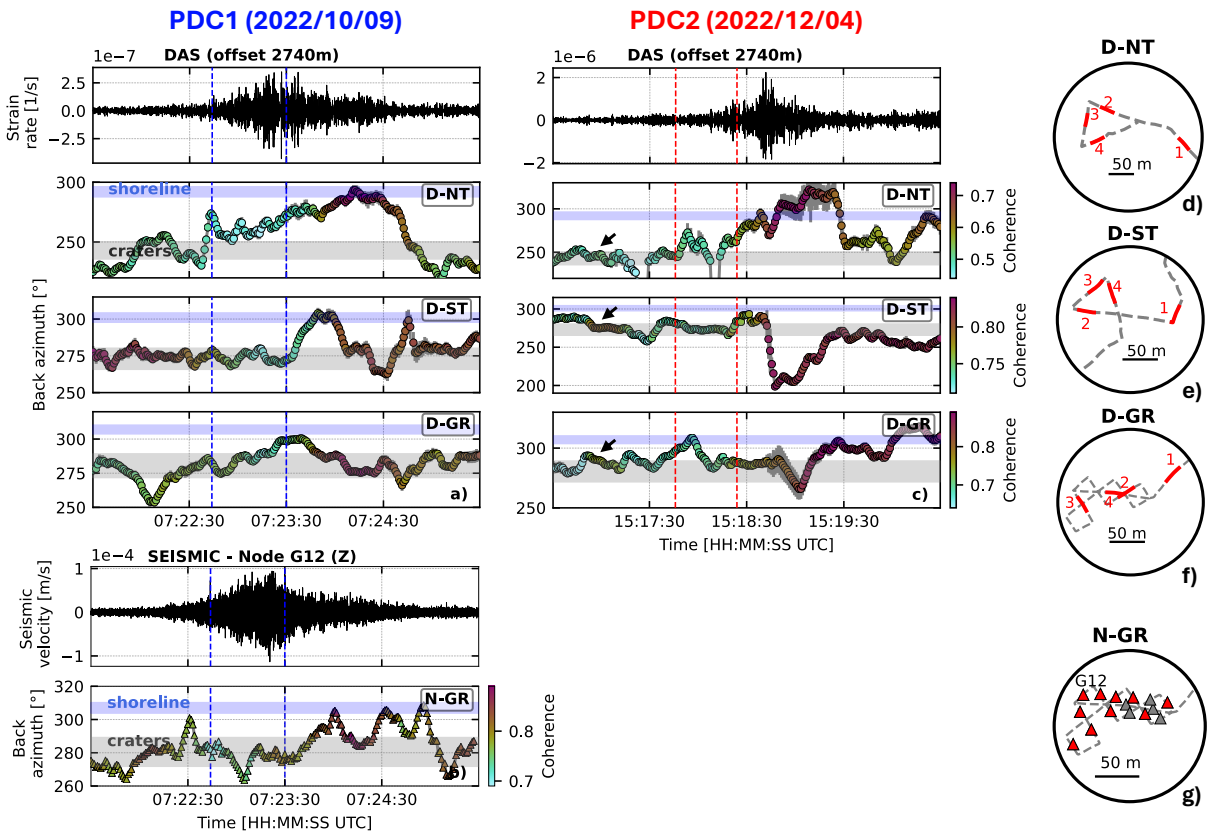

Figure S6.8: 4-minutes-long traces and corresponding back-azimuths of PDC1 (left column) and PDC2 (right column) of the DAS strain rate (a,c), the seismic velocity (b). Blue and red vertical dotted lines indicate the onsets (t_{s1} and t_{s2}) and arrival at sea (t_{e1} and t_{e2}) of PDC1 and PDC2, respectively, as observed by the thermal and visible cameras (Supplementary Fig. S6.1, Supplementary Movies 1,2). Back-azimuths are calculated using D-NT, D-ST, D-GR (a,c) and N-GR (b) arrays. Back-azimuths are filtered for coherencies> 0.4 and smoothed with a 3 s-long window. Black arrows in (c) indicate the back-azimuths obtained for an explosion that occurred at the NECs at 15:16:45 UTC (Fig. 2f). (d-g) Array geometries of DAS and nodal arrays. Red triangles in (g) indicate the nodes used for the analysis, while grey ones are unused.

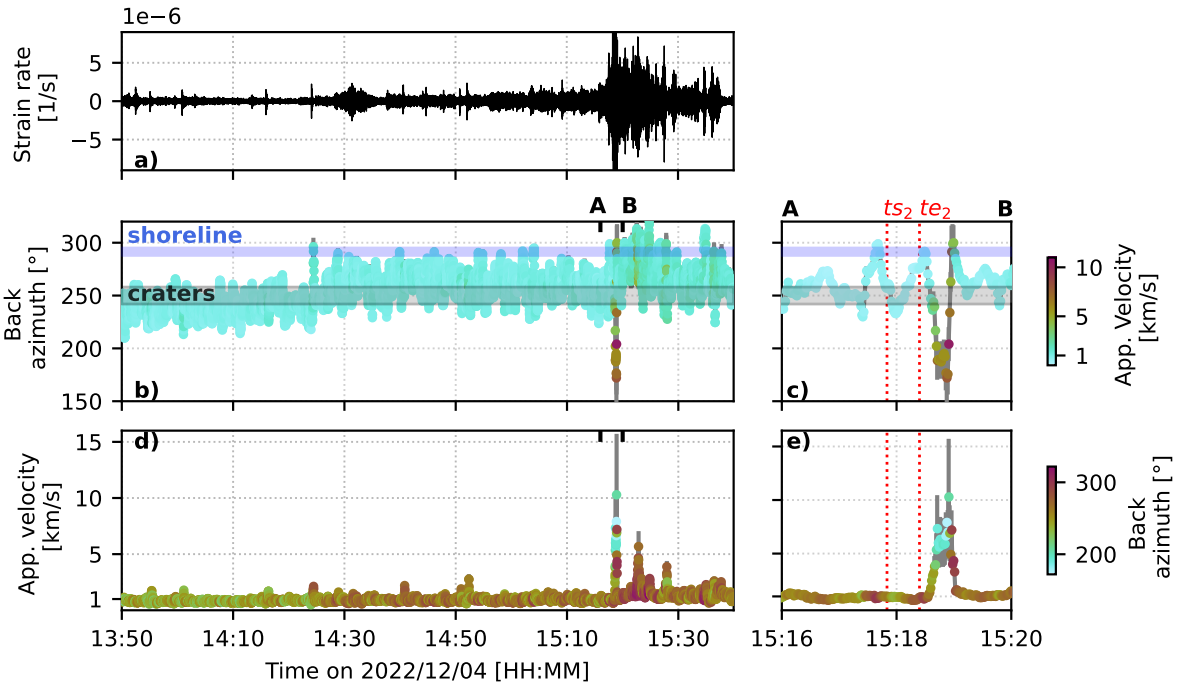

Figure S6.9: (a) Cumulative strain rate time series along offsets 890-910 between $13:50$ and $15:40$ UTC on 2022/12/04. (b) and (d) are the back-azimuths and apparent velocities obtained with D-CT during the entire time series. (c) and (e) are 4-minute zooms over PDC2. The colour grading of (b) and (c) is related to the apparent velocity, while that of (d) and (e) is concerning the back-azimuth. We observe that, right after PDC2, apparent velocities suddenly increase to ~ 6 km/s with errors up to ~ 3 km/s. Back-azimuths are further south than the craters with errors of up to $\sim 30°$. Horizontal bands in (b) and (c) mark the crater and coastline back-azimuths. Vertical dotted lines in (c) indicate the onset (ts_2 = 15:17:46 UTC) and the arrival at sea (te_2 = 15:18:24 UTC) of PDC2.

Node arrays										
N-NT										
Station	**T1**	**T2**	**T3**	**T4**	**T5**	**T6**	**T7**			
Serial number	453000501	453001435	453020881	453002041	453002301	453020908	453020933			
D-GR										
Station	**G1**	**G4**	**G5**	**G6**	**G7**	**G8**	**G9**	**G10**	**G11**	**G12**
Serial number	453001689	453020821	453000674	453000156	453002636	453002772	453002584	453005026	453020971	453002588
Infrasound arrays										
EAR										
Station	**MC1**	**STR**	**MC5**							
DAS arrays										
D-NT						**D-CT**				
Line	**1**	**2**	**3**	**4**		Line	**1**	**2**	**3**	**4**
Channels	5140	5330	5420	5530		Channels	832	878	1044	1090
	5144	5334	5424	5534			836	882	1048	1094
	5148	5338	5428	5538			840	886	1052	1098
	5152	5342	5432	5542			844	890	1056	1102
	5156	5346	5436	5546			848	894	1060	1106
	5160	5350	5440	5550			852	898	1064	1110
	5164	5354	5444	5554			856	902	1068	1114
	5168	5358	5448	5558			860	906	1072	1118
D-ST						**D-GR**				
Line	**1**	**2**	**3**	**4**		Line	**1**	**2**	**3**	**4**
Channels	1590	1750	1830	1880		Channels	2082	2194	2346	2680
	1594	1754	1834	1884			2086	2198	2350	2684
	1598	1758	1838	1888			2090	2202	2354	2688
	1602	1762	1842	1892			2094	2206	2358	2692
	1606	1766	1846	1896			2098	2210	2362	2696
	1610	1770	1850	1900			2102	2214	2366	2700
	1614	1774	1854	1904			2016	2218	2370	2704
	1618	1778	1858	1908			2010	2222	2374	2708

Table S6.1: Stations and channels used for array analyses considering node (N-NT, N-GR), infrasound (EAR) and DAS (D-NT, D-CT, D-ST and D-GR) arrays.

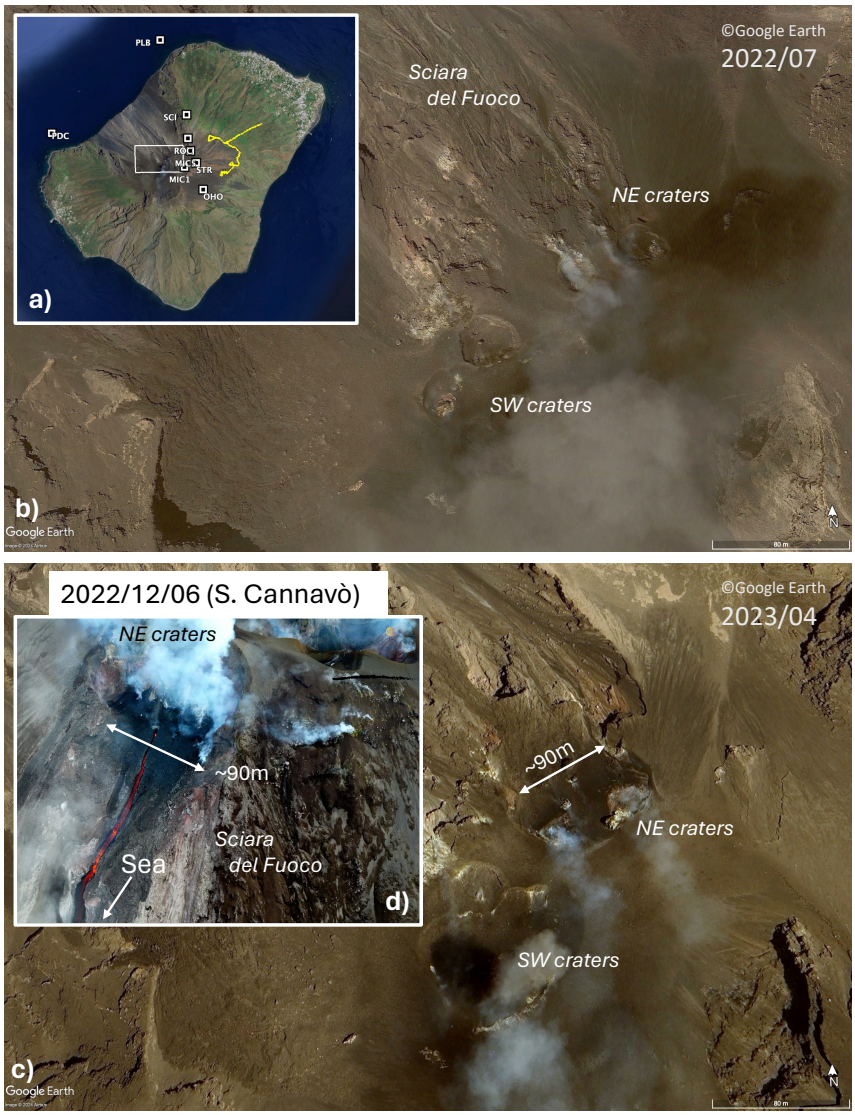

Figure S6.10: (a) GoogleEarth satellite imagery of Stromboli volcano showing the DAS cable (yellow) and UniFi monitoring stations (white squares). (b) Zoom on the Stromboli craters (satellite image dated 2022/07). (c) Same as (b), but with a satellite image taken about 9 months later (2023/04). We can observe traces of the partial collapse of the northeast crater rim, also clearly visible in drone images (d) immediately after PDC2 (2022/12/06). Drone image is courtesy of Sebastiano Cannavò.

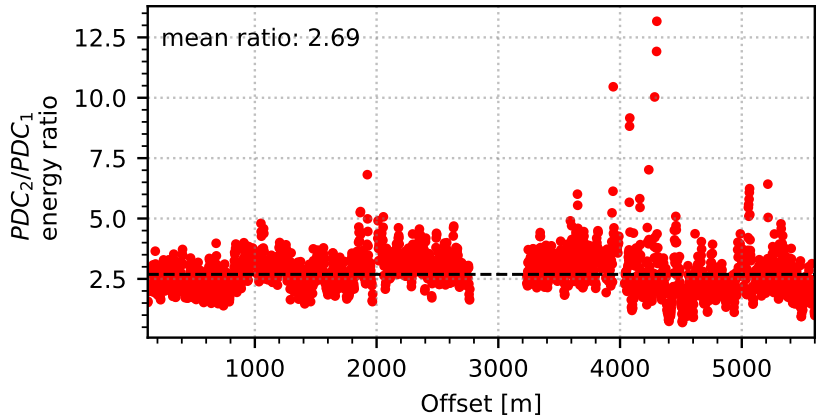

Figure S6.11: Ratios between seismic energies of PDC2 and PDC1 calculated using each DAS channel. Seismic energies are calculated via Eq. (6) (Methods, Estimating seismic energies) considering strain rate traces between $1 - 20$ Hz. Dashed line represent the mean value of the ratios.

Table S6.2: Seismic energies Es computed for PDC1 and PDC2 using Eq. (6) for the E, N and Z components of STR, ROC and SCI broadband seismometers (Fig. 1

Seismic energies Es PDC1 [MJ]	E	N	Z
STR	0.28	0.23	0.06
ROC	3.50	1.84	0.40
SCI	2.84	1.61	0.40
Seismic energies Es PDC2 [MJ]	E	N	Z
STR	1.04	1.19	0.34
ROC	18.92	12.11	1.80
SCI	17.08	9.08	1.64

Table S6.3: Ratios $R_{Es} = Es_{PDC2}/Es_{PDC1}$ between the seismic energies Es of PDC2 and PDC1 for the E, N and Z components of STR, ROC and SCI broadband seismometers (Fig. 1).

R_{Es} PDC2/PDC1	E	N	Z
STR	3.2	4.5	4.6
ROC	4.9	6.0	4.0
SCI	5.5	5.2	3.7
Mean	4.5	5.2	4.1

Acknowledgements

This study depends on the work done by S. Oliva and his team, who dug the trench for the fibre-optic cable. Furthermore, we acknowledge the help offered in the field by G. Diana, M.-P. Bouin, S. Kiel, R. Longo, M. Masini, J. P. Sepulveda Birke. We thank C. Jestin, G. Calbris and V. Lanticq of FEBUS Optics for their support. We processed differential GPS data with the RTKLIB software (https://rtklib.com), for which we thank J.-B. De Chabalier for his valuable support. We used the Interparc Matlab library (https://www.mathworks.com/matlabcentral/fileexchange/34874-interparc, John D'Errico, 2012, MATLAB Central File Exchange) to interpolate the fibre layout to geolocalise the DAS channel. This work is financially supported by the ANR-19-CE04-0011-01 MONIDAS (Natural Hazard Monitoring using Distributed Acoustic Sensing) Project.

Conclusions

The continuous monitoring of volcanic activity is crucial for understanding volcanic phenomena and forecasting eruptions. However, several factors may challenge such an aim, particularly in environments that require substantial logistical and financial resources. The relatively novel fibre-optic-based DAS technology is revolutionising seismological observations across various fields. DAS offers a cost-effective, high-resolution method for dense seismic wavefield sampling, making it a promising tool for monitoring volcanoes, especially in submarine or hard-to-reach areas (Jousset et al., 2024; Nakano et al., 2024). Numerous studies have demonstrated the potential of DAS for volcanic seismic monitoring, such as locating seismicity and characterising the wavefield generated by volcanic explosions (e.g., Currenti et al., 2021; Klaasen et al., 2021; Nishimura et al., 2021; Jousset et al., 2022).

We carried out multiple experiments at Stromboli volcano (Italy) to investigate the potential of DAS as a monitoring tool. Stromboli is well-known for its persistent and diverse activity ranging from frequent (~10 events/hr) and mild explosions to more intense eruptions and pyroclastic flows. This eruptive regime, together with extensive literature, makes Stromboli an ideal test site for DAS applications, allowing us to compare our findings with former studies. Below, we provide an exhaustive summary of the main results obtained in this thesis.

Most significant achievements

In this thesis, we analysed signals from volcanic activity recorded along a 4 km long dedicated fibre-optic cable that we deployed on the Stromboli northeastern flank. Together with the fibre, we installed nodal (5 Hz) and broadband (30 s) three-component seismometers to validate the DAS data and the results that we obtained. During four recording campaigns between 2020 and 2023, we gathered almost five months of DAS strain rate measurements of various volcanic phenomena, including mild and more intense explosions and pyroclastic flows.

This thesis aims to analyse these measurements and demonstrate how DAS can provide valuable information for volcano monitoring. In particular, we followed two main (and

interconnected) research tracks, which we briefly recap here.

- Understanding whether DAS is capable of accurately measuring the seismic signals generated by volcanic activity.
- Obtaining information about the location and dynamics of volcanic phenomena.

First track: assessing DAS data quality

Throughout this thesis, we calibrated DAS measurements by comparing them to records from co-located inertial sensors. We also examined the reasons for discrepancies between DAS and seismometer signals. In Chapter 3, we showed that DAS can effectively measure strain signals generated by several volcanic processes such as volcanic tremor, volcanic explosions and pyroclastic flows. To an initial comparison, DAS strain rate signals generally match those from traditional seismometers, though exhibiting lower resolution outside the 2.5–10 Hz frequency band and higher noise levels below ~2 Hz (as later shown in Section 5.4). However, to accurately compare DAS and node waveforms from various volcanic processes, we employed two methodologies that yielded valuable and similar outcomes.

The first approach is well-established in the literature (e.g., Bakku, 2015; Wang et al., 2018; Jousset et al., 2022) and enabled us to derive strain rate signals from the finite difference of seismic velocity traces captured by two nodes along a linear fibre segment. The results, detailed in Sections 4.3, 5.5, and 6.6.3, showed that DAS and node strain rate waveforms of volcanic tremor and explosions (both ordinary and major ones) exhibit nearly perfect phase matching, achieving cross-correlation coefficients of up to 0.99.

Nevertheless, DAS signals typically exhibit amplitudes ~1.5 to 5 times smaller than those recorded by nodes. This discrepancy probably arises from the coupling conditions between the cable and the ground, as the amplitude difference is not always constant along the fibre. Additionally, we argued that inefficient strain transfer from the cable to the single fibres may contribute to this issue. In Section 5.9.1, we explored (and quantified) how a loose bundle of fibres within the cable may hinder the strain transfer, causing some strain to be absorbed by the vertical compaction of the bundle instead of being transmitted as longitudinal elongation or compression of the fibres.

The second approach was developed through a collaboration between our research group, Université Côte d'Azur (France), and the University of Napoli Federico II (Italy). Some of the research presented in this thesis has also been included in the following publication: Trabattoni et al. (2023). This methodology allowed us to retrieve the longitudinal displacement (or velocity) along the fibre through numerical, spatial integration of DAS strain (or strain rate) waveforms without requiring co-located seismometers. Moreover, it can be applied promptly to the data, enhancing wavefield reconstruction under the assumption of sufficiently long and rectilinear fibre segments. Section 4.4 detailed the theoretical background and results obtained using this approach. We observed that DAS-derived particle velocity traces closely match those from co-located seismometers along the same direction, achieving maximum cross-correlation coefficients between ~0.7-0.9. However, DAS velocity waveforms exhibit lower amplitudes than those from the nodes, matching the previous findings.

Finally, we reported evidence (Section 3.7) of very long period (VLP, 0.04-0.1 Hz) signals produced by several volcanic explosions in November 2022 and effectively recorded by our DAS interrogator. The VLPs recorded by DAS resemble those from permanent

broadband seismometers (along the fibre directions) and display uniform features across different events, indicating a non-destructive and repetitive source.

Second track: locating and characterising volcanic phenomena

We applied array processing techniques to DAS strain rate waveforms to investigate volcanic activity and locate seismic sources for different signals. We used the array method of Métaxian et al. (2002), which consists of estimating time delays between all possible $N(N-1)/2$ pairs of N sensors composing an array with a coherence-weighted linear fit of the cross-spectrum phase (Poupinet et al., 1984) on subsequent sliding time windows. We considered different array configurations and analysed signals corresponding to volcanic tremor, explosions, and PDCs. The results were then validated against independent outcomes from co-located seismic arrays, infrasound arrays, and visual observations.

In Chapter 5, we gathered information about the apparent velocity and the back azimuth of incoming waves generated by ordinary activity. We focused on one hour of strain rate measurements, comprising volcanic tremor and several ordinary explosions. Results obtained from strain rate waveforms between 3-5 Hz indicate seismic waves propagating from the volcano summit area, approximately 200 m from the active craters. Apparent velocities of around 0.6 km/s (mainly representing surface waves) are consistent with literature findings (Chouet et al., 1997, 1998). These results, stable over the entire one-hour period, suggest a persistent source for both explosions and tremor and closely match those from a co-located nodal array.

In Chapter 6, we extended the array analysis to signals generated by two PDCs of different sizes, aiming to track their downslope propagation. These flows occurred in October and December 2022. Monitoring images show that the October flow (PDC1) was smaller and slower than the December flow (PDC2). Both flows generated tsunami waves, ranging from centimetres (PDC1) to metres (PDC2) in scale, upon reaching the sea. Back-azimuth analysis from DAS, node, and infrasound arrays show a clear shift in the seismo-acoustic source from the craters to the coastline, consistent with visual observations, allowing us to estimate flow velocities of 33-48 m/s (PDC1) and 50-73 m/s (PDC2).

Additionally, using thermal camera images, we estimated the volume of PDC2 at approximately 80×10^3 m^3. We then used DAS and seismic data to estimate the volume of PDC1 by comparing the seismic energy generated by both events. The ratio of the seismic energies between PDC2 and PDC1 of velocity and strain rate signals range from 2.7 to 4.6, leading to an estimated volume for PDC1 of 17-30$\times 10^3$ m^3. We incorporated these volumes into numerical simulations, which show that Coulomb friction angles decrease with increasing volume: 25° for PDC1 and 21° for PDC2. This pattern mirrors the behaviour of other gravitational processes on Earth and in extra-terrestrial environments. In addition, estimates of the rheological parameters of flows are of fundamental importance for better modelling their dynamics, velocities and run-out distances.

Ideas for further research

This thesis presents valuable insights into volcanic processes and expands the application of array techniques to DAS data from volcanic explosions and pyroclastic flows.

However, further research is necessary to refine the application of array processing techniques to DAS strain (or strain rate) data, particularly by considering the directivity patterns of DAS measurements. In particular, We must assess the stability of array methodologies results obtained with larger DAS arrays comprising a broader number of channels. Additionally, utilizing DAS-derived velocity traces obtained through spatial integration of strain rate waveforms (as discussed in Chapter 4) could enhance waveform coherence, reduce the impact of local effects and heterogeneity and provide improved outcomes.

Future work should also analyse broader periods and incorporate the entire fibre array to leverage the full capacities of DAS data. While this thesis focused on a limited number of events over five months of recorded data, a comprehensive analysis of the entire dataset could reveal further volcanic phenomena and provide additional knowledge about DAS capabilities as a volcano monitoring tool. Given the significant volume of our DAS dataset, big-data management approaches could extract additional insights from this rich dataset.

Finally, the varying site responses along the fibre highlight the significant influence of the shallow subsurface on DAS measurements. This observation could provide critical information for better and high-resolution mapping of the heterogeneous subsurface of Stromboli volcano beneath our fibre-optic deployment, potentially improving the comprehension of wave propagation in the volcanic structure and helping identify areas with varying structural characteristics for volcanic risk assessments.

DAS as a complementary volcano monitoring tool

This thesis demonstrates that fibre-optic cables probed with DAS technology can effectively complement traditional seismological tools for volcano monitoring. DAS measurements may offer reliable seismic wavefield sampling (including low frequencies) and provide insights into volcanic dynamics and detailed subsurface characterisation (Currenti et al., 2021; Nishimura et al., 2021; Jousset et al., 2022). Array processing of DAS strain rate waveforms enables pinpointing seismo-volcanic activity and tracking fast-moving pyroclastic flows. Additionally, these methodologies make it possible to investigate rapid mass movements in different environments, such as landslides or debris flow.

Stromboli volcano is intensively and real-time monitored by a broad network of multiparameter sensors. Integrating DAS with pre-existing and standard instruments such as seismometers and infrasound sensors offers a more complete view of volcanic activity, providing signal localisation and insights into the dynamics of several processes. Chapter 6 highlights how seismic and infrasonic data provide complementary information during eruptions, improving our understanding of complex, simultaneous volcanic events. While DAS technology proves valuable even in well-monitored areas, it may hold significant potential in less-instrumented environments, where dedicated fibre optics may need to be installed. These optical fibres could serve multiple purposes, including DAS other fibre-optic sensing applications, as well as transmitting data on weather conditions, volcanic activity, and infrastructure status (Nishimura et al., 2021; Jousset et al., 2022). Additionally, one key advantage of DAS is its ability to leverage existing fibre-optic networks, such as in urban or submarine environments, enabling continuous monitoring of strain and ground motion for the evaluation of natural hazards (e.g., Spica et al., 2020; Currenti et al., 2023; Jousset et al., 2024; Nakano et al., 2024).

One final point to highlight is the limitation of nodal arrays due to battery life. Our

seismic arrays in Stromboli did not capture the second pyroclastic flow in December 2022 due to battery depletion after one month. Conversely, DAS continued recording for nearly four months. Equipping seismometers in an array with solar panels could mitigate such issues. However, it presents logistical challenges, especially for networks comprising numerous sensors. Real-time signal processing would also require robust data transmission systems across various sensors.

On the other hand, DAS technologies offer key advantages compared to installations of similar numbers of sensors: they do not rely on batteries as long as a stable power source is available, allowing for continuous, real-time, and long-term monitoring from a safe distance. Such features make DAS especially useful for capturing densely sampled seismic measurements close to the source without endangering the equipment or technical/scientific personnel. These advantages make DAS a powerful tool for future recording campaigns and permanent monitoring installations to gain new insights into the characteristics of the shallow subsurface and volcanic dynamics (Jousset et al., 2018, 2022). However, the massive volume of DAS data requires innovative solutions for efficient analysis (Jousset et al., 2022).

However, while DAS measurements remain reliable, they involve certain limitations. Our findings indicate that DAS-based back-azimuth estimations exhibit broader dispersion and higher uncertainties than nodes. This effect is reduced with triangular array geometries but persists in analyses of explosive events and volcanic tremor phases. Similarly, DAS provides less precise results than nodes for PDCs, with increased uncertainty in source location and tracking source position changes during RGMM events along volcanic flanks. Such outcomes highlight the need for further research into applying array processing techniques to analyse emergent and complex volcanic signals.

Lower recorded amplitudes further limit applications requiring precise seismic amplitude measurements unless fibre-optic data is pre-calibrated. However, such a procedure would necessitate co-located seismometers. Our findings emphasise the need to understand ground-to-fibre strain transfer processes better. For widespread and reliable seismological applications, DAS technologies require well-characterised instrumental responses accounting for both the interrogator and the cable. Enhancements such as reduced self-noise and improved low-frequency sensitivity of DAS systems would provide valuable insights into fluid dynamics within magmatic pathways. Despite these challenges, our results confirm the strong potential of DAS as an advanced tool for volcanic monitoring.

References

Aiuppa, A., Bertagnini, A., Métrich, N., Moretti, R., Di Muro, A., Liuzzo, M., & Tamburello, G. (2010). A model of degassing for Stromboli volcano. *Earth and Planetary Science Letters*, *295*(1), 195–204. https://doi.org/10.1016/j.epsl.2010.03.040

Aiuppa, A., Bitetto, M., Delle Donne, D., La Monica, F. P., Tamburello, G., Coppola, D., Della Schiava, M., Innocenti, L., Lacanna, G., Laiolo, M., Massimetti, F., Pistolesi, M., Silengo, M. C., & Ripepe, M. (2021). Volcanic CO_2 tracks the incubation period of basaltic paroxysms. *Science Advances*, *7*(38), eabh0191. https://doi.org/10.1126/sciadv.abh0191

Ajo-Franklin, J. B., Dou, S., Lindsey, N. J., Monga, I., Tracy, C., Robertson, M., Rodriguez Tribaldos, V., Ulrich, C., Freifeld, B., Daley, T., & Li, X. (2019). Distributed Acoustic Sensing Using Dark Fiber for Near-Surface Characterization and Broadband Seismic Event Detection. *Scientific Reports*, *9*(1), 1328. https://doi.org/10.1038/s41598-018-36675-8

Aki, K., & Richards, P. G. (2002). *Quantitative Seismology*. University Science Books.

Al Hasani, M. (2024). *Distributed Acoustic Sensing using straight, sinusoidally and helically shaped fibres for seismic applications* [Dissertation (TU Delft)] [ISBN: 9789463845311]. https://doi.org/10.4233/uuid:3b23b63b-69be-4c0e-90c0-3312eae1d871

Allard, P. (2010). A CO2-rich gas trigger of explosive paroxysms at Stromboli basaltic volcano, Italy. *Journal of Volcanology and Geothermal Research*, *189*(3), 363–374. https://doi.org/10.1016/j.jvolgeores.2009.11.018

Allstadt, K. E., Matoza, R. S., Lockhart, A. B., Moran, S. C., Caplan-Auerbach, J., Haney, M. M., Thelen, W. A., & Malone, S. D. (2018). Seismic and acoustic signatures of surficial mass movements at volcanoes. *Journal of Volcanology and Geothermal Research*, *364*, 76–106. https://doi.org/10.1016/j.jvolgeores.2018.09.007

Almendros, J., Ibáñez, J. M., Alguacil, G., Del Pezzo, E., & Ortiz, R. (1997). Array tracking of the volcanic tremor source at Deception Island, Antarctica. *Geophysical Research Letters*, *24*(23), 3069–3072. https://doi.org/10.1029/97GL03096

Almendros, J., Chouet, B., Dawson, P., & Bond, T. (2002). Identifying elements of the plumbing system beneath Kilauea Volcano, Hawaii, from the source locations of very-long-period signals. *Geophysical Journal International*, *148*(2), 303–312. https://doi.org/10.1046/j.1365-246X.2002.01629.x

Andronico, D., Del Bello, E., D'Oriano, C., Landi, P., Pardini, F., Scarlato, P., de'Michieli Vitturi, M., Taddeucci, J., Cristaldi, A., Ciancitto, F., Pennacchia, F., Ricci, T., & Valentini, F. (2021). Uncovering the eruptive patterns of the 2019 double paroxysm eruption crisis of Stromboli volcano [Publisher: Nature Publishing Group]. *Nature Communications*, *12*(1), 4213. https://doi.org/10.1038/s41467-021-24420-1

Apuani, T., Corazzato, C., Cancelli, A., & Tibaldi, A. (2005). Stability of a collapsing volcano (Stromboli, Italy): Limit equilibrium analysis and numerical modelling. *Journal of Volcanology and Geothermal Research*, *144*(1), 191–210. https://doi.org/10.1016/j.jvolgeores.2004.11.028

Arran, M. I., Mangeney, A., De Rosny, J., Farin, M., Toussaint, R., & Roche, O. (2021). Laboratory Landquakes: Insights From Experiments Into the High-Frequency Seismic Signal Generated by Geophysical Granular Flows. *Journal of Geophysical Research: Earth Surface*, *126*(5), e2021JF006172. https://doi.org/10.1029/2021JF006172

Auker, M. R., Sparks, R. S. J., Siebert, L., Crosweller, H. S., & Ewert, J. (2013). A statistical analysis of the global historical volcanic fatalities record. *Journal of Applied Volcanology*, *2*(1), 2. https://doi.org/10.1186/2191-5040-2-2

Azzola, J., Thiemann, K., & Gaucher, E. (2023). Integration of distributed acoustic sensing for real-time seismic monitoring of a geothermal field. *Geothermal Energy*, *11*(1), 30. https://doi.org/10.1186/s40517-023-00272-4

Bai, Y., & Bai, Q. (2014, January). Chapter 7 - Fiber Optic Monitoring System. In Y. Bai & Q. Bai (Eds.), *Subsea Pipeline Integrity and Risk Management* (pp. 145–165). Gulf Professional Publishing. https://doi.org/10.1016/B978-0-12-394432-0.00007-X

Bakku, S. K. (2015). *Fracture characterization from seismic measurements in a borehole* [Thesis]. Massachusetts Institute of Technology [Accepted: 2015-06-10T19:10:27Z]. Retrieved July 14, 2024, from https://dspace.mit.edu/handle/1721.1/97331

Barberi, F., Civetta, L., Rosi, M., & Scandone, R. (2009). Chronology of the 2007 eruption of Stromboli and the activity of the Scientific Synthesis Group. *Journal of Volcanology and Geothermal Research*, *182*(3), 123–130. https://doi.org/10.1016/j.jvolgeores.2008.09.019

Barberi, F., Rosi, M., & Sodi, A. (1993). Volcanic hazard assessment at Stromboli based on review of historical data. *Acta Vulcanol.*, *3*, 173–187.

Battaglia, J., Aki, K., & Ferrazzini, V. (2005). Location of tremor sources and estimation of lava output using tremor source amplitude on the Piton de la Fournaise volcano: 1. Location of tremor sources. *Journal of Volcanology and Geothermal Research*, *147*(3), 268–290. https://doi.org/10.1016/j.jvolgeores.2005.04.005

Baxter, P. J., & Horwell, C. J. (2015, January). Chapter 60 - Impacts of Eruptions on Human Health. In H. Sigurdsson (Ed.), *The Encyclopedia of Volcanoes (Second Edition)* (pp. 1035–1047). Academic Press. https://doi.org/10.1016/B978-0-12-385938-9.00060-2

Bayarri, M. J., Berger, J. O., Calder, E. S., Dalbey, K., Lunagomez, S., Patra, A. K., Pitman, E. B., Spiller, E. T., & Wolpert, R. L. (2009). Using Statistical and Computer Models to Quantify Volcanic Hazards. *Technometrics*, *51*(4), 402–413. https://doi.org/10.1198/TECH.2009.08018

Bertagnini, A., Métrich, N., Landi, P., & Rosi, M. (2003). Stromboli volcano (Aeolian Archipelago, Italy): An open window on the deep-feeding system of a steady state basaltic volcano. *Journal of Geophysical Research: Solid Earth*, *108*(B7). https://doi.org/10.1029/2002JB002146

Bertagnini, A., Di Roberto, A., & Pompilio, M. (2011). Paroxysmal activity at Stromboli: Lessons from the past. *Bulletin of Volcanology*, *73*(9), 1229–1243. https://doi.org/10.1007/s00445-011-0470-3

Bevilacqua, A., Bertagnini, A., Pompilio, M., Landi, P., Del Carlo, P., Di Roberto, A., Aspinall, W., & Neri, A. (2020). Major explosions and paroxysms at Stromboli (Italy): A new historical catalog and temporal models of occurrence with uncertainty quantification [Publisher: Nature Publishing Group]. *Scientific Reports*, *10*(1), 17357. https://doi.org/10.1038/s41598-020-74301-8

Beyreuther, M., Barsch, R., Krischer, L., Megies, T., Behr, Y., & Wassermann, J. (2010). ObsPy: A Python Toolbox for Seismology. *Seismological Research Letters*, *81*(3), 530–533. https://doi.org/10.1785/gssrl.81.3.530

Biagioli, F., Métaxian, J.-P., Stutzmann, E., Ripepe, M., Bernard, P., Trabattoni, A., Longo, R., & Bouin, M.-P. (2024). Array analysis of seismo-volcanic activity with distributed

acoustic sensing. *Geophysical Journal International*, *236*(1), 607–620. https://doi.org/10.1093/gji/ggad427

Biondi, E., Wang, X., Williams, E. F., & Zhan, Z. (2022). Geolocalization of Large-Scale DAS Channels Using a GPS-Tracked Moving Vehicle. *Seismological Research Letters*, *94*(1), 318–330. https://doi.org/10.1785/0220220169

Biondi, E., Zhu, W., Li, J., Williams, E. F., & Zhan, Z. (2023). An upper-crust lid over the Long Valley magma chamber [Publisher: American Association for the Advancement of Science]. *Science Advances*, *9*(42), eadi9878. https://doi.org/10.1126/sciadv.adi9878

Blackburn, E. A., Wilson, L., & Sparks, R. S. J. (1976). Mechanisms and dynamics of strombolian activity. *Journal of the Geological Society*, *132*(4), 429–440. https://doi.org/10.1144/gsjgs.132.4.0429

Bona, A., Dean, T., Correa, J., Pevzner, R., Tertyshnikov, K. V., & Zaanen, L. V. (2017). Amplitude and Phase Response of DAS Receivers [ISSN: 2214-4609 Issue: 1], *2017*, 1–5. https://doi.org/10.3997/2214-4609.201701200

Bonaccorso, A., Gambino, S., Guglielmino, F., Mattia, M., Puglisi, G., & Boschi, E. (2008). Stromboli 2007 eruption: Deflation modeling to infer shallow-intermediate plumbing system. *Geophysical Research Letters*, *35*(6), 2007GL032921. https://doi.org/10.1029/2007GL032921

Bosman, A., Chiocci, F. L., & Romagnoli, C. (2009). Morpho-structural setting of Stromboli volcano revealed by high-resolution bathymetry and backscatter data of its submarine portions. *Bulletin of Volcanology*, *71*(9), 1007–1019. https://doi.org/10.1007/s00445-009-0279-5

Bouchut, F., & Westdickenberg, M. (2004). Gravity driven shallow water models for arbitrary topography [Publisher: International Press of Boston]. *Communications in Mathematical Sciences*, *2*(3), 359–389.

Bouchut, F., Mangeney-Castelnau, A., Perthame, B., & Vilotte, J.-P. (2003). A new model of Saint Venant and Savage–Hutter type for gravity driven shallow water flows. *Comptes Rendus Mathematique*, *336*(6), 531–536. https://doi.org/10.1016/S1631-073X(03)00117-1

Braun, T., & Ripepe, M. (1993). Interaction of seismic and air waves recorded at Stromboli Volcano. *Geophysical Research Letters*, *20*(1), 65–68. https://doi.org/10.1029/92GL02543

Brodsky, E. E., Gordeev, E., & Kanamori, H. (2003). Landslide basal friction as measured by seismic waves. *Geophysical Research Letters*, *30*(24). https://doi.org/10.1029/2003GL018485

Brosch, E., Lube, G., Cerminara, M., Esposti-Ongaro, T., Breard, E. C. P., Dufek, J., Sovilla, B., & Fullard, L. (2021). Destructiveness of pyroclastic surges controlled by turbulent fluctuations. *Nature Communications*, *12*(1), 7306. https://doi.org/10.1038/s41467-021-27517-9

Brown, S. K., Loughlin, S. C., Sparks, R. S. J., Vye-Brown, C., Barclay, J., Calder, E., Cottrell, E., Jolly, G., Komorowski, J. C., Mandeville, C., Newhall, C., Palma, J., Potter, S., & Valentine, G. (2015). *Global volcanic hazards and risk* [Pages: 81-173]. https://doi.org/10.1017/CBO9781316276273.004

Brown, S. K., Jenkins, S. F., Sparks, R. S. J., Odbert, H., & Auker, M. R. (2017). Volcanic fatalities database: Analysis of volcanic threat with distance and victim classification. *Journal of Applied Volcanology*, *6*(1), 15. https://doi.org/10.1186/s13617-017-0067-4

Bruno, P. P. G., Maraio, S., & Festa, G. (2017). The shallow structure of Solfatara Volcano, Italy, revealed by dense, wide-aperture seismic profiling. *Scientific Reports*, *7*(1), 17386. https://doi.org/10.1038/s41598-017-17589-3

Burton, M., Allard, P., Muré, F., & La Spina, A. (2007). Magmatic gas composition reveals the source depth of slug-driven strombolian explosive activity. *Science (New York, N.Y.)*, *317*(5835), 227–230. https://doi.org/10.1126/science.1141900

Cabral, T. (2016, November). *A First Approach to Structural Health Monitoring of Adhesive Bonded Joints in Pipelines Using Integrated Fiber Optic Sensors* [Doctoral dissertation]. https://doi.org/10.13140/RG.2.2.10258.25283

Calvari, S., Di Traglia, F., Ganci, G., Bruno, V., Ciancitto, F., Di Lieto, B., Gambino, S., Garcia, A., Giudicepietro, F., Inguaggiato, S., Vita, F., Cangemi, M., Inguaggiato, C., Macedonio, G., Mattia, M., Miraglia, L., Nolesini, T., Pompilio, M., Romano, P., … Belviso, P. (2022). Multi-parametric study of an eruptive phase comprising unrest, major explosions, crater failure, pyroclastic density currents and lava flows: Stromboli volcano, 1 December 2020–30 June 2021 [Publisher: Frontiers]. *Frontiers in Earth Science*, *10*. https://doi.org/10.3389/feart.2022.899635

Calvari, S., Spampinato, L., Bonaccorso, A., Oppenheimer, C., Rivalta, E., & Boschi, E. (2011). Lava effusion — A slow fuse for paroxysms at Stromboli volcano? *Earth and Planetary Science Letters*, *301*(1), 317–323. https://doi.org/10.1016/j.epsl.2010.11.015

Calvari, S., Di Traglia, F., Ganci, G., Giudicepietro, F., Macedonio, G., Cappello, A., Nolesini, T., Pecora, E., Bilotta, G., Centorrino, V., Corradino, C., Casagli, N., & Del Negro, C. (2020). Overflows and Pyroclastic Density Currents in March-April 2020 at Stromboli Volcano Detected by Remote Sensing and Seismic Monitoring Data [Number: 18 Publisher: Multidisciplinary Digital Publishing Institute]. *Remote Sensing*, *12*(18), 3010. https://doi.org/10.3390/rs12183010

Cansi, Y. (1995). An automatic seismic event processing for detection and location: The P.M.C.C. Method. *Geophysical Research Letters*, *22*(9), 1021–1024. https://doi.org/10.1029/95GL00468

Capdeville, Y., & Sladen, A. (2024). DAS sensitivity to heterogeneity scales much smaller than the minimum wavelength [Number: 1]. *Seismica*, *3*(1). https://doi.org/10.26443/seismica.v3i1.1007

Capon, J. (1969). High-resolution frequency-wavenumber spectrum analysis [Conference Name: Proceedings of the IEEE]. *Proceedings of the IEEE*, *57*(8), 1408–1418. https://doi.org/10.1109/PROC.1969.7278

Capon, J., Greenfield, R., & Kolker, R. (1967). Multidimensional maximum-likelihood processing of a large aperture seismic array [Conference Name: Proceedings of the IEEE]. *Proceedings of the IEEE*, *55*(2), 192–211. https://doi.org/10.1109/PROC.1967.5439

Casagli, N., Tibaldi, A., Merri, A., Del Ventisette, C., Apuani, T., Guerri, L., Fortuny-Guasch, J., & Tarchi, D. (2009). Deformation of Stromboli Volcano (Italy) during the 2007 eruption revealed by radar interferometry, numerical modelling and structural geological field data. *Journal of Volcanology and Geothermal Research*, *182*(3), 182–200. https://doi.org/10.1016/j.jvolgeores.2009.01.002

Celli, N. L., Bean, C. J., & O'Brien, G. S. (2024). Full-waveform simulation of DAS records, response and cable-ground coupling. *Geophysical Journal International*, *236*(1), 659–674. https://doi.org/10.1093/gji/ggad449

Cheng, F., Chi, B., Lindsey, N. J., Dawe, T. C., & Ajo-Franklin, J. B. (2021). Utilizing distributed acoustic sensing and ocean bottom fiber optic cables for submarine structural characterization [Publisher: Nature Publishing Group]. *Scientific Reports*, *11*(1), 5613. https://doi.org/10.1038/s41598-021-84845-y

Chiocci, F. L., Romagnoli, C., Tommasi, P., & Bosman, A. (2008). The Stromboli 2002 tsunamigenic submarine slide: Characteristics and possible failure mechanisms. *Journal of Geophysical Research: Solid Earth*, *113*(B10). https://doi.org/10.1029/2007JB005172

Chouet, B. (2003). Volcano Seismology. *pure and applied geophysics*, *160*(3), 739–788. https://doi.org/10.1007/PL00012556

Chouet, B., Saccorotti, G., Dawson, P., Martini, M., Scarpa, R., Gaetano, D. L., Milana, G., & Cattaneo, M. (1999). Broadband measurements of the sources of explosions at Stromboli Volcano, Italy. *Geophysical Research Letters*, *26*, 1937–1940. https://doi.org/10.1029/1999GL900400

Chouet, B. A. (1996a). New Methods and Future Trends in Seismological Volcano Monitoring. In R. Scarpa & R. I. Tilling (Eds.), *Monitoring and Mitigation of Volcano Hazards* (pp. 23–97). Springer. https://doi.org/10.1007/978-3-642-80087-0_2

Chouet, B., & Matoza, R. S. (2013). A multi-decadal view of seismic methods for detecting precursors of magma movement and eruption. *Journal of Volcanology and Geothermal Research*, *252*, 108–175. https://doi.org/10.1016/j.jvolgeores.2012.11.013

Chouet, B., Dawson, P., Ohminato, T., Martini, M., Saccorotti, G., Giudicepietro, F., De Luca, G., Milana, G., & Scarpa, R. (2003). Source mechanisms of explosions at Stromboli Volcano, Italy, determined from moment-tensor inversions of very-long-period data. *Journal of Geophysical Research: Solid Earth*, *108*(B1), ESE 7–1–ESE 7–25. https://doi.org/10.1029/2002JB001919

Chouet, B., De Luca, G., Milana, G., Dawson, P., Martini, M., & Scarpa, R. (1998). Shallow velocity structure of Stromboli volcano, Italy, derived from small-aperture array measurements of Strombolian tremor. *Bulletin of the Seismological Society of America*, *88*(3), 653–666. https://doi.org/10.1785/BSSA0880030653

Chouet, B., Saccorotti, G., Martini, M., Dawson, P., De Luca, G., Milana, G., & Scarpa, R. (1997). Source and path effects in the wave fields of tremor and explosions at Stromboli Volcano, Italy. *Journal of Geophysical Research: Solid Earth*, *102*(B7), 15129–15150. https://doi.org/10.1029/97JB00953

Chouet, B. A. (1996b). Long-period volcano seismicity: Its source and use in eruption forecasting [Publisher: Nature Publishing Group]. *Nature*, *380*(6572), 309–316. https://doi.org/10.1038/380309a0

Chouet, B. A., Dawson, P. B., James, M. R., & Lane, S. J. (2010). Seismic source mechanism of degassing bursts at Kilauea Volcano, Hawaii: Results from waveform inversion in the 10–50 s band. *Journal of Geophysical Research: Solid Earth*, *115*(B9). https://doi.org/10.1029/2009JB006661

Clarke, J., Adam, L., & van Wijk, K. (2021). LP or VT signals? How intrinsic attenuation influences volcano seismic signatures constrained by Whakaari volcano parameters. *Journal of Volcanology and Geothermal Research*, *418*, 107337. https://doi.org/10.1016/j.jvolgeores.2021.107337

Coppola, D., Piscopo, D., Laiolo, M., Cigolini, C., Delle Donne, D., & Ripepe, M. (2012). Radiative heat power at Stromboli volcano during 2000–2011: Twelve years of MODIS observations. *Journal of Volcanology and Geothermal Research*, *215-216*, 48–60. https://doi.org/10.1016/j.jvolgeores.2011.12.001

Corazzato, C., Francalanci, L., Menna, M., Petrone, C. M., Renzulli, A., Tibaldi, A., & Vezzoli, L. (2008). What controls sheet intrusion in volcanoes? Structure and petrology of the Stromboli sheet complex, Italy. *Journal of Volcanology and Geothermal Research*, *173*(1), 26–54. https://doi.org/10.1016/j.jvolgeores.2008.01.006

Cosentino, M., Lombardo, G., & Privitera, E. (1989). A model for internal dynamical processes on Mt Etna. *Geophysical Journal International*, *97*(3), 367–379. https://doi.org/10.1111/j.1365-246X.1989.tb00508.x

Currenti, G., Allegra, M., Cannavò, F., Jousset, P., Prestifilippo, M., Napoli, R., Sciotto, M., Di Grazia, G., Privitera, E., Palazzo, S., & Krawczyk, C. (2023). Distributed dynamic strain sensing of very long period and long period events on telecom fiber-optic cables

at Vulcano, Italy [Number: 1 Publisher: Nature Publishing Group]. *Scientific Reports*, *13*(1), 4641. https://doi.org/10.1038/s41598-023-31779-2

Currenti, G., Jousset, P., Napoli, R., Krawczyk, C., & Weber, M. (2021). On the comparison of strain measurements from fibre optics with a dense seismometer array at Etna volcano (Italy). *Solid Earth*, *12*(4), 993–1003. https://doi.org/10.5194/se-12-993-2021

Daley, T. M., Freifeld, B. M., Ajo-Franklin, J., Dou, S., Pevzner, R., Shulakova, V., Kashikar, S., Miller, D. E., Goetz, J., Henninges, J., & Lueth, S. (2013). Field testing of fiber-optic distributed acoustic sensing (DAS) for subsurface seismic monitoring. *The Leading Edge*, *32*(6), 699–706. https://doi.org/10.1190/tle32060699.1

Daley, T., Miller, D., Dodds, K., Cook, P., & Freifeld, B. (2016). Field testing of modular borehole monitoring with simultaneous distributed acoustic sensing and geophone vertical seismic profiles at Citronelle, Alabama. *Geophysical Prospecting*, *64*(5), 1318–1334. https://doi.org/10.1111/1365-2478.12324

D'Auria, L., Koulakov, I., Prudencio, J., Cabrera-Pérez, I., Ibáñez, J. M., Barrancos, J., García-Hernández, R., Martínez van Dorth, D., Padilla, G. D., Przeor, M., Ortega, V., Hernández, P., & Peréz, N. M. (2022). Rapid magma ascent beneath La Palma revealed by seismic tomography [Publisher: Nature Publishing Group]. *Scientific Reports*, *12*(1), 17654. https://doi.org/10.1038/s41598-022-21818-9

De Angelis, S., Bass, V., Hards, V., & Ryan, G. (2007). Seismic characterization of pyroclastic flow activity at Soufrière Hills Volcano, Montserrat, 8 January 2007 [Publisher: Copernicus GmbH]. *Natural Hazards and Earth System Sciences*, *7*(4), 467–472. https://doi.org/10.5194/nhess-7-467-2007

De Astis, G., Ventura, G., & Vilardo, G. (2003). Geodynamic significance of the Aeolian volcanism (Southern Tyrrhenian Sea, Italy) in light of structural, seismological, and geochemical data. *Tectonics*, *22*(4). https://doi.org/10.1029/2003TC001506

Dean, T., Cuny, T., & Hartog, A. H. (2017). The effect of gauge length on axially incident P-waves measured using fibre optic distributed vibration sensing. *Geophysical Prospecting*, *65*(1), 184–193. https://doi.org/10.1111/1365-2478.12419

Delannay, R., Valance, A., Mangeney, A., Roche, O., & Richard, P. (2017). Granular and particle-laden flows: From laboratory experiments to field observations [Publisher: IOP Publishing]. *Journal of Physics D: Applied Physics*, *50*(5), 053001. https://doi.org/10.1088/1361-6463/50/5/053001

Delle Donne, D., Ripepe, M., De Angelis, S., Cole, P. D., Lacanna, G., Poggi, P., & Stewart, R. (2014). Chapter 9 Thermal, acoustic and seismic signals from pyroclastic density currents and Vulcanian explosions at Soufrière Hills Volcano, Montserrat [Publisher: The Geological Society of London]. *Geological Society, London, Memoirs*, *39*(1), 169–178. https://doi.org/10.1144/M39.9

Delle Donne, D., Lacanna, G., Marchetti, E., Ripepe, M., & Ulivieri, G. (2006). Monitoring Explosive Volcanic Activity Using Thermal Images, Stromboli Volcano, Italy. *AGU Fall Meeting Abstracts*, *79*, 1795.

DeRoin, N., McNutt, S. R., Sentman, D. D., & Reyes, C. (2012). Seismicity of block-and-ash flows occurring during the 2006 eruption of Augustine Volcano, Alaska. *Journal of Volcanology and Geothermal Research*, *213-214*, 14–26. https://doi.org/10.1016/j.jvolgeores.2011.10.007

Di Lieto, B., Romano, P., Scarpa, R., & Linde, A. T. (2020). Strain Signals Before and During Paroxysmal Activity at Stromboli Volcano, Italy. *Geophysical Research Letters*, *47*(21), e2020GL088521. https://doi.org/10.1029/2020GL088521

Di Roberto, A., Bertagnini, A., Pompilio, M., & Bisson, M. (2014). Pyroclastic density currents at Stromboli volcano (Aeolian Islands, Italy): A case study of the 1930 eruption. *Bulletin of Volcanology*, *76*(6), 827. https://doi.org/10.1007/s00445-014-0827-5

Di Traglia, F., Calvari, S., Borselli, L., Cassanego, L., Giudicepietro, F., Macedonio, G., Nolesini, T., & Casagli, N. (2023). Assessing flank instability of Stromboli volcano (Italy) by reappraising the 30 December 2002 tsunamigenic landslides. *Landslides*, *20*(7), 1363–1380. https://doi.org/10.1007/s10346-023-02043-5

Di Traglia, F., Borselli, L., Nolesini, T., & Casagli, N. (2023). Crater-rim collapse at Stromboli volcano: Understanding the mechanisms leading from the failure of hot rocks to the development of glowing avalanches. *Natural Hazards*, *115*(3), 2051–2068. https://doi.org/10.1007/s11069-022-05626-y

Di Traglia, F., Nolesini, T., Intrieri, E., Mugnai, F., Leva, D., Rosi, M., & Casagli, N. (2014). Review of ten years of volcano deformations recorded by the ground-based InSAR monitoring system at Stromboli volcano: A tool to mitigate volcano flank dynamics and intense volcanic activity. *Earth-Science Reviews*, *139*, 317–335. https://doi.org/10.1016/j.earscirev.2014.09.011

Diaz-Meza, S., Jousset, P., Currenti, G., Wollin, C., Krawczyk, C., Clarke, A., & Chalari, A. (2023). On the Comparison of Records from Standard and Engineered Fiber Optic Cables at Etna Volcano (Italy) [Number: 7 Publisher: Multidisciplinary Digital Publishing Institute]. *Sensors*, *23*(7), 3735. https://doi.org/10.3390/s23073735

Dou, S., Lindsey, N., Wagner, A. M., Daley, T. M., Freifeld, B., Robertson, M., Peterson, J., Ulrich, C., Martin, E. R., & Ajo-Franklin, J. B. (2017). Distributed Acoustic Sensing for Seismic Monitoring of The Near Surface: A Traffic-Noise Interferometry Case Study [Publisher: Nature Publishing Group]. *Scientific Reports*, *7*(1), 11620. https://doi.org/10.1038/s41598-017-11986-4

Dufek, J. (2016). The Fluid Mechanics of Pyroclastic Density Currents [Publisher: Annual Reviews]. *Annual Review of Fluid Mechanics*, *48*(Volume 48, 2016), 459–485. https://doi.org/10.1146/annurev-fluid-122414-034252

Dufek, J., Esposti Ongaro, T., & Roche, O. (2015, January). Chapter 35 - Pyroclastic Density Currents: Processes and Models. In H. Sigurdsson (Ed.), *The Encyclopedia of Volcanoes (Second Edition)* (pp. 617–629). Academic Press. https://doi.org/10.1016/B978-0-12-385938-9.00035-3

Ehsaninezhad, L., Wollin, C., Rodríguez Tribaldos, V., Schwarz, B., & Krawczyk, C. M. (2024). Urban subsurface exploration improved by denoising of virtual shot gathers from distributed acoustic sensing ambient noise. *Geophysical Journal International*, *237*(3), 1751–1764. https://doi.org/10.1093/gji/ggae134

Eibl, E. P. S., Bean, C. J., Vogfjörd, K. S., Ying, Y., Lokmer, I., Möllhoff, M., O'Brien, G. S., & Pálsson, F. (2017). Tremor-rich shallow dyke formation followed by silent magma flow at Bárarbunga in Iceland [Publisher: Nature Publishing Group]. *Nature Geoscience*, *10*(4), 299–304. https://doi.org/10.1038/ngeo2906

Falsaperla, S., Neri, M., Pecora, E., & Spampinato, S. (2006). Multidisciplinary study of flank instability phenomena at Stromboli volcano, Italy. *Geophysical Research Letters*, *33*(9). https://doi.org/10.1029/2006GL025940

Fang, G., Li, Y. E., Zhao, Y., & Martin, E. R. (2020). Urban Near-Surface Seismic Monitoring Using Distributed Acoustic Sensing. *Geophysical Research Letters*, *47*(6), e2019GL086115. https://doi.org/10.1029/2019GL086115

Favreau, P., Mangeney, A., Lucas, A., Crosta, G., & Bouchut, F. (2010). Numerical modeling of landquakes. *Geophysical Research Letters*, *37*(15), 2010GL043512. https://doi.org/10.1029/2010GL043512

Fernández-Ruiz, M. R., Soto, M. A., Williams, E. F., Martin-Lopez, S., Zhan, Z., Gonzalez-Herraez, M., & Martins, H. F. (2020). Distributed acoustic sensing for seismic activity monitoring. *APL Photonics*, *5*(3), 030901. https://doi.org/10.1063/1.5139602

Fichtner, A., Bogris, A., Nikas, T., Bowden, D., Lentas, K., Melis, N. S., Simos, C., Simos, I., & Smolinski, K. (2022). Theory of phase transmission fibre-optic deformation sensing. *Geophysical Journal International*, *231*(2), 1031–1039. https://doi.org/10.1093/gji/ggac237

Fichtner, A., Edme, P., Paitz, P., Lindner, N., Hohl, M., Huguenin, P., Sovilla, B., Roig-Lafon, P., Surinach, E., & Walter, F. (2021, March). *Observing avalanche dynamics with Distributed Acoustic Sensing* (tech. rep. No. EGU21-16562) (Conference Name: EGU21). Copernicus Meetings. https://doi.org/10.5194/egusphere-egu21-16562

Fichtner, A., Klaasen, S., Thrastarson, S., Çubuk-Sabuncu, Y., Paitz, P., & Jónsdóttir, K. (2022). Fiber-Optic Observation of Volcanic Tremor through Floating Ice Sheet Resonance. *The Seismic Record*, *2*(3), 148–155. https://doi.org/10.1785/0320220010

Fossen, H. (2016, March). Structural Geology [ISBN: 9781107415096 Publisher: Cambridge University Press]. https://doi.org/10.1017/9781107415096

Francalanci, L., Lucchi, F., Keller, J., De Astis, G., & Tranne, C. A. (2013, January). Eruptive, volcano-tectonic and magmatic history of the Stromboli volcano (north-eastern Aeolian archipelago). In F. Lucchi, A. Peccerillo, J. Keller, C. A. Tranne, & P. L. Rossi (Eds.), *The Aeolian Islands Volcanoes* (p. 0, Vol. 37). Geological Society of London. https://doi.org/10.1144/M37.13

Francalanci, L., Davies, G. R., Lustenhouwer, W., Tommasini, S., Mason, P. R. D., & Conticelli, S. (2005). Intra-Grain Sr Isotope Evidence for Crystal Recycling and Multiple Magma Reservoirs in the Recent Activity of Stromboli Volcano, Southern Italy. *Journal of Petrology*, *46*(10), 1997–2021. https://doi.org/10.1093/petrology/egi045

Furumoto, M., Kunitomo, T., Inoue, H., Yamada, I., Yamaoka, K., Ikami, A., & Fukao, Y. (1990). Twin sources of high-frequency volcanic tremor of Izu-Oshima Volcano, Japan. *Geophysical Research Letters*, *17*(1), 25–27. https://doi.org/10.1029/GL017i001p00025

Genco, R., & Ripepe, M. (2010). Inflation-deflation cycles revealed by tilt and seismic records at Stromboli volcano. *Geophysical Research Letters*, *37*(12), 2010GL042925. https://doi.org/10.1029/2010GL042925

Giudicepietro, F., D'Auria, L., Martini, M., Caputo, T., Peluso, R., De Cesare, W., Orazi, M., & Scarpato, G. (2009). Changes in the VLP seismic source during the 2007 Stromboli eruption. *Journal of Volcanology and Geothermal Research*, *182*(3), 162–171. https://doi.org/10.1016/j.jvolgeores.2008.11.008

Giudicepietro, F., Calvari, S., De Cesare, W., Di Lieto, B., Di Traglia, F., Esposito, A. M., Orazi, M., Romano, P., Tramelli, A., Nolesini, T., Casagli, N., Calabria, P., & Macedonio, G. (2023). Seismic and thermal precursors of crater collapses and overflows at Stromboli volcano [Number: 1 Publisher: Nature Publishing Group]. *Scientific Reports*, *13*(1), 11115. https://doi.org/10.1038/s41598-023-38205-7

Glasgow, M. E., Schmandt, B., & Hansen, S. M. (2018). Upper crustal low-frequency seismicity at Mount St. Helens detected with a dense geophone array. *Journal of Volcanology and Geothermal Research*, *358*, 329–341. https://doi.org/10.1016/j.jvolgeores.2018.06.006

Goldstein, P., & Archuleta, R. J. (1987). Array analysis of seismic signals. *Geophysical Research Letters*, *14*(1), 13–16. https://doi.org/10.1029/GL014i001p00013

Hansen, S. M., & Schmandt, B. (2015). Automated detection and location of microseismicity at Mount St. Helens with a large-N geophone array. *Geophysical Research Letters*, *42*(18), 7390–7397. https://doi.org/10.1002/2015GL064848

Hartog, A. H. (2017, June). *An Introduction to Distributed Optical Fibre Sensors*. CRC Press. https://doi.org/10.1201/9781315119014

Heinrich, P., Boudon, G., Komorowski, J. C., Sparks, R. S. J., Herd, R., & Voight, B. (2001). Numerical simulation of the December 1997 Debris Avalanche in Montserrat, Lesser

Antilles. *Geophysical Research Letters*, *28*(13), 2529–2532. https://doi.org/10.1029/2001GL012968

Her, S.-C., & Huang, C.-Y. (2011). Effect of Coating on the Strain Transfer of Optical Fiber Sensors [Number: 7 Publisher: Molecular Diversity Preservation International]. *Sensors*, *11*(7), 6926–6941. https://doi.org/10.3390/s110706926

Hibert, C., Mangeney, A., Grandjean, G., Baillard, C., Rivet, D., Shapiro, N. M., Satriano, C., Maggi, A., Boissier, P., Ferrazzini, V., & Crawford, W. (2014). Automated identification, location, and volume estimation of rockfalls at Piton de la Fournaise volcano. *Journal of Geophysical Research: Earth Surface*, *119*(5), 1082–1105. https://doi.org/10.1002/2013JF002970

Hibert, C., Mangeney, A., Grandjean, G., & Shapiro, N. M. (2011). Slope instabilities in Dolomieu crater, Réunion Island: From seismic signals to rockfall characteristics. *Journal of Geophysical Research: Earth Surface*, *116*(F4). https://doi.org/10.1029/2011JF002038

Hidayat, D., Chouet, B., Voight, B., Dawson, P., & Ratdomopurbo, A. (2002). Source mechanism of very-long-period signals accompanying dome growth activity at Merapi volcano, Indonesia. *Geophysical Research Letters*, *29*(23), 33–1–33–4. https://doi.org/10.1029/2002GL015013

Hotovec, A. J., Prejean, S. G., Vidale, J. E., & Gomberg, J. (2013). Strongly gliding harmonic tremor during the 2009 eruption of Redoubt Volcano. *Journal of Volcanology and Geothermal Research*, *259*, 89–99. https://doi.org/10.1016/j.jvolgeores.2012.01.001

Hubbard, P. G., Vantassel, J. P., Cox, B. R., Rector, J. W., Yust, M. B. S., & Soga, K. (2022). Quantifying the Surface Strain Field Induced by Active Sources with Distributed Acoustic Sensing: Theory and Practice [Number: 12 Publisher: Multidisciplinary Digital Publishing Institute]. *Sensors*, *22*(12), 4589. https://doi.org/10.3390/s22124589

Hudson, T. S., Baird, A. F., Kendall, J. M., Kufner, S. K., Brisbourne, A. M., Smith, A. M., Butcher, A., Chalari, A., & Clarke, A. (2021). Distributed Acoustic Sensing (DAS) for Natural Microseismicity Studies: A Case Study From Antarctica. *Journal of Geophysical Research: Solid Earth*, *126*(7), e2020JB021493. https://doi.org/10.1029/2020JB021493

Inza, L. A., Mars, J. I., Métaxian, J. P., O'Brien, G. S., & Macedo, O. (2011). Seismo-volcano source localization with triaxial broad-band seismic array. *Geophysical Journal International*, *187*(1), 371–384. https://doi.org/10.1111/j.1365-246X.2011.05148.x

Inza, L. A., Métaxian, J. P., Mars, J. I., Bean, C. J., O'Brien, G. S., Macedo, O., & Zandomeneghi, D. (2014). Analysis of dynamics of vulcanian activity of Ubinas volcano, using multicomponent seismic antennas. *Journal of Volcanology and Geothermal Research*, *270*, 35–52. https://doi.org/10.1016/j.jvolgeores.2013.11.008

Ishikawa, A. (2023). *Pressurization process of shallow magma reservoir of Stromboli volcano (Italy) as inferred from analyses of ground deformation associated with different-type eruptions* [Doctoral dissertation, Tohoku University].

Iverson, R. M., & George, D. L. (2014). A depth-averaged debris-flow model that includes the effects of evolving dilatancy. I. Physical basis [Publisher: Royal Society]. *Proceedings of the Royal Society A: Mathematical, Physical and Engineering Sciences*, *470*(2170), 20130819. https://doi.org/10.1098/rspa.2013.0819

Iyer, H. M. (1992). Seismological Detection and Delineation of Magma Chambers: Present Status with Emphasis on the Western USA. In P. Gasparini, R. Scarpa, & K. Aki (Eds.), *Volcanic Seismology* (pp. 299–338). Springer. https://doi.org/10.1007/978-3-642-77008-1_22

Johnson, J. B., & Ronan, T. J. (2015). Infrasound from volcanic rockfalls. *Journal of Geophysical Research: Solid Earth*, *120*(12), 8223–8239. https://doi.org/10.1002/2015JB012436

Jolly, A. D., Thompson, G., & Norton, G. E. (2002). Locating pyroclastic flows on Soufriere Hills Volcano, Montserrat, West Indies, using amplitude signals from high dynamic range

instruments. *Journal of Volcanology and Geothermal Research*, *118*(3), 299–317. https://doi.org/10.1016/S0377-0273(02)00299-8

Jousset, P., Currenti, G., Murphy, S., Eibl, E., Caudron, C., Retailleau, L., Wollin, C., Klaasen, S., Nishimura, T., Fichtner, A., Spica, Z., Le Marchand, A., Krawczyk, C., Murphy, S., Eibl, E., Caudron, C., Retailleau, L., Wollin, C., Klaasen, S., ... Krawczyk, C. (2024). Fiber optic sensing for volcano monitoring and imaging volcanic processes. https://doi.org/10.31223/X5HM6J

Jousset, P., Currenti, G., Schwarz, B., Chalari, A., Tilmann, F., Reinsch, T., Zuccarello, L., Privitera, E., & Krawczyk, C. M. (2022). Fibre optic distributed acoustic sensing of volcanic events. *Nature Communications*, *13*(1), 1753. https://doi.org/10.1038/s41467-022-29184-w

Jousset, P., Reinsch, T., Ryberg, T., Blanck, H., Clarke, A., Aghayev, R., Hersir, G. P., Henninges, J., Weber, M., & Krawczyk, C. M. (2018). Dynamic strain determination using fibre-optic cables allows imaging of seismological and structural features [Publisher: Nature Publishing Group]. *Nature Communications*, *9*(1), 2509. https://doi.org/10.1038/s41467-018-04860-y

Kanamori, H. (2021). Transmission Loss of Optical Fibers; Achievements in Half a Century. *IEICE Transactions on Communications*, *E104.B*(8), 922–933. https://doi.org/10.1587/transcom.2020EBI0002

Kanamori, H., & Given, J. W. (1982). Analysis of long-period seismic waves excited by the May 18, 1980, eruption of Mount St. Helens—A terrestrial monopole? *Journal of Geophysical Research: Solid Earth*, *87*(B7), 5422–5432. https://doi.org/10.1029/JB087iB07p05422

Kanamori, H., Given, J. W., & Lay, T. (1984). Analysis of seismic body waves excited by the Mount St. Helens eruption of May 18, 1980. *Journal of Geophysical Research: Solid Earth*, *89*(B3), 1856–1866. https://doi.org/10.1029/JB089iB03p01856

Kirchdörfer, M. (1999). Analysis and quasistatic FE modeling of long period impulsive events associated with explosions at Stromboli volcano (Italy). *Annals of Geophysics*, *42*. https://doi.org/10.4401/ag-3728

Klaasen, S., Paitz, P., Lindner, N., Dettmer, J., & Fichtner, A. (2021). Distributed Acoustic Sensing in Volcano-Glacial Environments—Mount Meager, British Columbia. *Journal of Geophysical Research: Solid Earth*, *126*(11), e2021JB022358. https://doi.org/10.1029/2021JB022358

Konstantinou, K. I., & Schlindwein, V. (2003). Nature, wavefield properties and source mechanism of volcanic tremor: A review. *Journal of Volcanology and Geothermal Research*, *119*(1), 161–187. https://doi.org/10.1016/S0377-0273(02)00311-6

Koulakov, I., Gordeev, E. I., Dobretsov, N. L., Vernikovsky, V. A., Senyukov, S., & Jakovlev, A. (2011). Feeding volcanoes of the Kluchevskoy group from the results of local earthquake tomography. *Geophysical Research Letters*, *38*(9). https://doi.org/10.1029/2011GL046957

Koulakov, I., & Shapiro, N. (2014). Seismic Tomography of Volcanoes. In M. Beer, I. A. Kougioumtzoglou, E. Patelli, & I. S.-K. Au (Eds.), *Encyclopedia of Earthquake Engineering* (pp. 1–18). Springer. https://doi.org/10.1007/978-3-642-36197-5_51-1

Kuehnert, J., Mangeney, A., Capdeville, Y., Vilotte, J. P., Stutzmann, E., Chaljub, E., Aissaoui, E., Boissier, P., Brunet, C., Kowalski, P., & Lauret, F. (2021). Locating Rockfalls Using Inter-Station Ratios of Seismic Energy at Dolomieu Crater, Piton de la Fournaise Volcano. *Journal of Geophysical Research: Earth Surface*, *126*(4), e2020JF005715. https://doi.org/10.1029/2020JF005715

Kumagai, H. (2022). Source Quantification of Volcanic-Seismic Signals. In R. I. Tilling (Ed.), *Complexity in Tsunamis, Volcanoes, and their Hazards* (pp. 425–467). Springer US. https://doi.org/10.1007/978-1-0716-1705-2_583

La Rocca, M., Galluzzo, D., Saccorotti, G., Tinti, S., Cimini, G. B., & Del Pezzo, E. (2004). Seismic Signals Associated with Landslides and with a Tsunami at Stromboli Volcano, Italy. *Bulletin of the Seismological Society of America*, *94*(5), 1850–1867. https://doi.org/10.1785/012003238

La Rocca, M., Saccorotti, G., Del Pezzo, E., & Ibanez, J. (2004). Probabilistic source location of explosion quakes at Stromboli volcano estimated with double array data. *Journal of Volcanology and Geothermal Research*, *131*(1), 123–142. https://doi.org/10.1016/S0377-0273(03)00321-4

Lahr, J. C., Chouet, B. A., Stephens, C. D., Power, J. A., & Page, R. A. (1994). Earthquake classification, location, and error analysis in a volcanic environment: Implications for the magmatic system of the 1989–1990 eruptions at redoubt volcano, Alaska. *Journal of Volcanology and Geothermal Research*, *62*(1), 137–151. https://doi.org/10.1016/0377-0273(94)90031-0

Landi, P., Marchetti, E., La Felice, S., Ripepe, M., & Rosi, M. (2011). Integrated petrochemical and geophysical data reveals thermal distribution of the feeding conduits at Stromboli volcano, Italy. *Geophysical Research Letters*, *38*(8). https://doi.org/10.1029/2010GL046296

Langer, H., & Falsaperla, S. (1996). Long-term observation of volcanic tremor on Stromboli volcano (Italy): A synopsis. *pure and applied geophysics*, *147*(1), 57–82. https://doi.org/10.1007/BF00876436

Lay, T., & Wallace, T. (1995, January). Modern Global Seimology.

Lees, J. M. (2007). Seismic tomography of magmatic systems. *Journal of Volcanology and Geothermal Research*, *167*(1), 37–56. https://doi.org/10.1016/j.jvolgeores.2007.06.008

Legrand, D., & Perton, M. (2022). What are VLP signals at Stromboli volcano? *Journal of Volcanology and Geothermal Research*, *421*, 107438. https://doi.org/10.1016/j.jvolgeores.2021.107438

Leva, C., Rümpker, G., & Wölbern, I. (2022). Multi-array analysis of volcano-seismic signals at Fogo and Brava, Cape Verde [Publisher: Copernicus GmbH]. *Solid Earth*, *13*(8), 1243–1258. https://doi.org/10.5194/se-13-1243-2022

Levy, C., Mangeney, A., Bonilla, F., Hibert, C., Calder, E. S., & Smith, P. J. (2015). Friction weakening in granular flows deduced from seismic records at the Soufrière Hills Volcano, Montserrat. *Journal of Geophysical Research: Solid Earth*, *120*(11), 7536–7557. https://doi.org/10.1002/2015JB012151

Li, J., Zhu, W., Biondi, E., & Zhan, Z. (2023). Earthquake focal mechanisms with distributed acoustic sensing [Publisher: Nature Publishing Group]. *Nature Communications*, *14*(1), 4181. https://doi.org/10.1038/s41467-023-39639-3

Lindsey, N. J., Dawe, T. C., & Ajo-Franklin, J. B. (2019). Illuminating seafloor faults and ocean dynamics with dark fiber distributed acoustic sensing [Publisher: American Association for the Advancement of Science]. *Science*, *366*(6469), 1103–1107. https://doi.org/10.1126/science.aay5881

Lindsey, N. J., & Martin, E. R. (2021). Fiber-Optic Seismology [Publisher: Annual Reviews]. *Annual Review of Earth and Planetary Sciences*, *49*(Volume 49, 2021), 309–336. https://doi.org/10.1146/annurev-earth-072420-065213

Lindsey, N. J., Martin, E. R., Dreger, D. S., Freifeld, B., Cole, S., James, S. R., Biondi, B. L., & Ajo-Franklin, J. B. (2017). Fiber-Optic Network Observations of Earthquake Wavefields. *Geophysical Research Letters*, *44*(23), 11, 792–11, 799. https://doi.org/10.1002/2017GL075722

Lindsey, N. J., Rademacher, H., & Ajo-Franklin, J. B. (2020). On the Broadband Instrument Response of Fiber-Optic DAS Arrays. *Journal of Geophysical Research: Solid Earth*, *125*(2). https://doi.org/10.1029/2019JB018145

Lindsey, N. J., Yuan, S., Lellouch, A., Gualtieri, L., Lecocq, T., & Biondi, B. (2020). City-Scale Dark Fiber DAS Measurements of Infrastructure Use During the COVID-19 Pandemic. *Geophysical Research Letters*, *47*(16), e2020GL089931. https://doi.org/10.1029/2020GL089931

Lior, I., Sladen, A., Rivet, D., Ampuero, J.-P., Hello, Y., Becerril, C., Martins, H. F., Lamare, P., Jestin, C., Tsagkli, S., & Markou, C. (2021). On the Detection Capabilities of Underwater Distributed Acoustic Sensing. *Journal of Geophysical Research: Solid Earth*, *126*(3). https://doi.org/10.1029/2020JB020925

Lu, P., Lalam, N., Badar, M., Liu, B., Chorpening, B. T., Buric, M. P., & Ohodnicki, P. R. (2019). Distributed optical fiber sensing: Review and perspective. *Applied Physics Reviews*, *6*(4), 041302. https://doi.org/10.1063/1.5113955

Lube, G., Breard, E. C. P., Jones, J., Fullard, L., Dufek, J., Cronin, S. J., & Wang, T. (2019). Generation of air lubrication within pyroclastic density currents. *Nature Geoscience*, *12*(5), 381–386. https://doi.org/10.1038/s41561-019-0338-2

Lucas, A., Mangeney, A., & Ampuero, J. P. (2014). Frictional velocity-weakening in landslides on Earth and on other planetary bodies [Publisher: Nature Publishing Group]. *Nature Communications*, *5*(1), 3417. https://doi.org/10.1038/ncomms4417

Lucchi, F., Francalanci, L., De Astis, G., Tranne, C. A., Braschi, E., & Klaver, M. (2019). Geological evidence for recurrent collapse-driven phreatomagmatic pyroclastic density currents in the Holocene activity of Stromboli volcano, Italy. *Journal of Volcanology and Geothermal Research*, *385*, 81–102. https://doi.org/10.1016/j.jvolgeores.2018.10.024

Mangeney, A., Bouchut, F., Thomas, N., Vilotte, J. P., & Bristeau, M. O. (2007). Numerical modeling of self-channeling granular flows and of their levee-channel deposits. *Journal of Geophysical Research: Earth Surface*, *112*(F2). https://doi.org/10.1029/2006JF000469

Mangeney, A., Heinrich, P. H., Roche, R., Boudon, G., & Cheminée, J. L. (2000). Modeling of debris avalanche and generated water waves: Application to real and potential events in Montserrat. *Physics and Chemistry of the Earth, Part A: Solid Earth and Geodesy*, *25*(9), 741–745. https://doi.org/10.1016/S1464-1895(00)00115-0

Mangeney, A., Roche, O., Hungr, O., Mangold, N., Faccanoni, G., & Lucas, A. (2010). Erosion and mobility in granular collapse over sloping beds. *Journal of Geophysical Research: Earth Surface*, *115*(F3). https://doi.org/10.1029/2009JF001462

Mangeney-Castelnau, A., Bouchut, F., Vilotte, J. P., Lajeunesse, E., Aubertin, A., & Pirulli, M. (2005). On the use of Saint Venant equations to simulate the spreading of a granular mass. *Journal of Geophysical Research: Solid Earth*, *110*(B9). https://doi.org/10.1029/2004JB003161

Maramai, A., Graziani, L., & Tinti, S. (2005). Tsunamis in the Aeolian Islands (southern Italy): A review. *Marine Geology*, *215*(1), 11–21. https://doi.org/10.1016/j.margeo.2004.03.018

Marchetti, E., Walter, F., Barfucci, G., Genco, R., Wenner, M., Ripepe, M., McArdell, B., & Price, C. (2019). Infrasound Array Analysis of Debris Flow Activity and Implication for Early Warning. *Journal of Geophysical Research: Earth Surface*, *124*(2), 567–587. https://doi.org/10.1029/2018JF004785

Marchetti, E., & Ripepe, M. (2005). Stability of the seismic source during effusive and explosive activity at Stromboli Volcano. *Geophysical Research Letters*, *32*(3), 2004GL021406. https://doi.org/10.1029/2004GL021406

Martin, E. R. (2018). *Passive Imaging and Characterization of the Subsurface with Distributed Acoustic Sensing* [PhD thesis]. Department of Geophysics, Stanford Univ.

Martin, E. R., Biondi, B., Fabien-Ouellet, G., & Clapp, R. G. (2017). Sensitivity analysis of distributed acoustic sensing arrays.

Martini, M., Giudicepietro, F., DAuria, L., Esposito, A. M., Caputo, T., Curciotti, R., Cesare, W. D., Orazi, M., Scarpato, G., & Caputo, A. (2007). Seismological monitoring

of the February 2007 effusive eruption of the Stromboli volcano [Number: 6]. *Annals of Geophysics*, *50*(6). https://doi.org/10.4401/ag-3056

Masoudi, A., Belal, M., & Newson, T. P. (2013). A distributed optical fibre dynamic strain sensor based on phase-OTDR [Publisher: IOP Publishing]. *Measurement Science and Technology*, *24*(8), 085204. https://doi.org/10.1088/0957-0233/24/8/085204

Mateeva, A., Lopez, J., Potters, H., Mestayer, J., Cox, B., Kiyashchenko, D., Wills, P., Grandi, S., Hornman, K., Kuvshinov, B., Berlang, W., Yang, Z., & Detomo, R. (2014). Distributed acoustic sensing for reservoir monitoring with vertical seismic profiling. *Geophysical Prospecting*, *62*(4), 679–692. https://doi.org/10.1111/1365-2478.12116

McNutt, S., Tytgat, G., & Power, J. (1995). Preliminary Analyses of Volcanic Tremor Associated with 1992 Eruptions of Crater Peak, Mount Spurr Volcano, Alaska. *The 1992 Eruptions of Crater Peak Vent, Mount Spurr Volcano, Alaska*, *2139*, 161–177. https://doi.org/https://doi.org/10.3133/b2139

McNutt, S. R. (2005). VOLCANIC SEISMOLOGY [Publisher: Annual Reviews]. *Annual Review of Earth and Planetary Sciences*, *33*(Volume 33, 2005), 461–491. https://doi.org/10.1146/annurev.earth.33.092203.122459

McNutt, S. R., & Roman, D. C. (2015, January). Chapter 59 - Volcanic Seismicity. In H. Sigurdsson (Ed.), *The Encyclopedia of Volcanoes (Second Edition)* (pp. 1011–1034). Academic Press. https://doi.org/10.1016/B978-0-12-385938-9.00059-6

McNutt, S. R., Thompson, G., Johnson, J., Angelis, S. D., & Fee, D. (2015, January). Chapter 63 - Seismic and Infrasonic Monitoring. In H. Sigurdsson (Ed.), *The Encyclopedia of Volcanoes (Second Edition)* (pp. 1071–1099). Academic Press. https://doi.org/10.1016/B978-0-12-385938-9.00063-8

Mercalli, G. (1881). Natura delle eruzioni dello Stromboli e, in generale, delle attività sismovulcaniche nelle Eolie. *Atti della Società Italiana di Scienze Naturali*, *24*, 105–132.

Messerli, A., & Grinsted, A. (2015). Image georectification and feature tracking toolbox: ImGRAFT [Publisher: Copernicus GmbH]. *Geoscientific Instrumentation, Methods and Data Systems*, *4*(1), 23–34. https://doi.org/10.5194/gi-4-23-2015

Métaxian, J.-P., Lesage, P., & Dorel, J. (1997). Permanent tremor of Masaya Volcano, Nicaragua: Wave field analysis and source location. *Journal of Geophysical Research: Solid Earth*, *102*(B10), 22529–22545. https://doi.org/10.1029/97JB01141

Métaxian, J.-P., Lesage, P., & Valette, B. (2002). Locating sources of volcanic tremor and emergent events by seismic triangulation: Application to Arenal volcano, Costa Rica. *Journal of Geophysical Research: Solid Earth*, *107*(B10), ECV 10–1–ECV 10–18. https://doi.org/10.1029/2001JB000559

Métaxian, J.-P., Santoso, A. B., Caudron, C., Cholik, N., Labonne, C., Poiata, N., Beauducel, F., Monteiller, V., Fahmi, A. A., Rizal, M. H., & Nandaka, I. G. M. A. (2020). Migration of seismic activity associated with phreatic eruption at Merapi volcano, Indonesia. *Journal of Volcanology and Geothermal Research*, *396*, 106795. https://doi.org/10.1016/j.jvolgeores.2020.106795

Métrich, N., Bertagnini, A., & Di Muro, A. (2010). Conditions of Magma Storage, Degassing and Ascent at Stromboli: New Insights into the Volcano Plumbing System with Inferences on the Eruptive Dynamics. *Journal of Petrology*, *51*(3), 603–626. https://doi.org/10.1093/petrology/egp083

Métrich, N., Bertagnini, A., Landi, P., Rosi, M., & Belhadj, O. (2005). Triggering mechanism at the origin of paroxysms at Stromboli (Aeolian Archipelago, Italy): The 5 April 2003 eruption. *Geophysical Research Letters*, *32*(10). https://doi.org/10.1029/2004GL022257

Métrich, N., Bertagnini, A., & Pistolesi, M. (2021). Paroxysms at Stromboli Volcano (Italy): Source, Genesis and Dynamics [Publisher: Frontiers]. *Frontiers in Earth Science*, *9*. https://doi.org/10.3389/feart.2021.593339

Moretti, L., Allstadt, K., Mangeney, A., Capdeville, Y., Stutzmann, E., & Bouchut, F. (2015). Numerical modeling of the Mount Meager landslide constrained by its force history derived from seismic data. *Journal of Geophysical Research: Solid Earth*, *120*(4), 2579–2599. https://doi.org/10.1002/2014JB011426

Moretti, L., Mangeney, A., Capdeville, Y., Stutzmann, E., Huggel, C., Schneider, D., & Bouchut, F. (2012). Numerical modeling of the Mount Steller landslide flow history and of the generated long period seismic waves. *Geophysical Research Letters*, *39*(16). https://doi.org/10.1029/2012GL052511

Muanenda, Y., Oton, C. J., & Di Pasquale, F. (2019). Application of Raman and Brillouin Scattering Phenomena in Distributed Optical Fiber Sensing [Publisher: Frontiers]. *Frontiers in Physics*, *7*. https://doi.org/10.3389/fphy.2019.00155

Nakano, M., Ichihara, M., Suetsugu, D., Ohminato, T., Ono, S., Vaiomounga, R., Kula, T., & Shinohara, M. (2024). Monitoring volcanic activity with distributed acoustic sensing using the Tongan seafloor telecommunications cable. *Earth, Planets and Space*, *76*(1), 25. https://doi.org/10.1186/s40623-024-01972-2

Nappi, G. (1976). Recent activity of Stromboli [Number: 5556 Publisher: Nature Publishing Group]. *Nature*, *261*(5556), 119–120. https://doi.org/10.1038/261119a0

Näsholm, S. P., Iranpour, K., Wuestefeld, A., Dando, B. D. E., Baird, A. F., & Oye, V. (2022). Array Signal Processing on Distributed Acoustic Sensing Data: Directivity Effects in Slowness Space. *Journal of Geophysical Research: Solid Earth*, *127*(2), e2021JB023587. https://doi.org/10.1029/2021JB023587

Nayak, A., Ajo-Franklin, J., & the Imperial Valley Dark Fiber Team. (2021). Distributed Acoustic Sensing Using Dark Fiber for Array Detection of Regional Earthquakes. *Seismological Research Letters*, *92*(4), 2441–2452. https://doi.org/10.1785/0220200416

Neuberg, J., Luckett, R., Ripepe, M., & Braun, T. (1994). Highlights from a seismic broadband array on Stromboli Volcano. *Geophysical Research Letters*, *21*(9), 749–752. https://doi.org/10.1029/94GL00377

Nishimura, T. (1995). Source parameters of the volcanic eruption earthquakes at Mount Tokachi, Hokkaido, Japan, and a magma ascending model. *Journal of Geophysical Research: Solid Earth*, *100*(B7), 12465–12473. https://doi.org/10.1029/95JB00867

Nishimura, T., Emoto, K., Nakahara, H., Miura, S., Yamamoto, M., Sugimura, S., Ishikawa, A., & Kimura, T. (2021). Source location of volcanic earthquakes and subsurface characterization using fiber-optic cable and distributed acoustic sensing system [Number: 1 Publisher: Nature Publishing Group]. *Scientific Reports*, *11*(1), 6319. https://doi.org/10.1038/s41598-021-85621-8

Nishimura, T., Nakamichi, H., Tanaka, S., Sato, M., Kobayashi, T., Ueki, S., Hamaguchi, H., Ohtake, M., & Sato, H. (2000). Source process of very long period seismic events associated with the 1998 activity of Iwate Volcano, northeastern Japan. *Journal of Geophysical Research: Solid Earth*, *105*(B8), 19135–19147. https://doi.org/10.1029/2000JB900155

Norris, R. D. (1994). Seismicity of rockfalls and avalanches at three cascade range volcanoes: Implications for seismic detection of hazardous mass movements. *Bulletin of the Seismological Society of America*, *84*(6), 1925–1939. https://doi.org/10.1785/BSSA0840061925

O'Brien, G. S., & Bean, C. J. (2009). Volcano topography, structure and intrinsic attenuation: Their relative influences on a simulated 3D visco-elastic wavefield. *Journal of Volcanology and Geothermal Research*, *183*(1), 122–136. https://doi.org/10.1016/j.jvolgeores.2009.03.004

O'Brien, G. S., Bean, C. J., Meiland, H., & Witte, P. (2023). Imaging and seismic modelling inside volcanoes using machine learning [Publisher: Nature Publishing Group]. *Scientific Reports*, *13*(1), 630. https://doi.org/10.1038/s41598-023-27738-6

Ohminato, T., Chouet, B. A., Dawson, P., & Kedar, S. (1998). Waveform inversion of very long period impulsive signals associated with magmatic injection beneath Kilauea volcano, Hawaii. *Journal of Geophysical Research: Solid Earth*, *103*(B10), 23839–23862. https://doi.org/10.1029/98JB01122

Paitz, P. (2021). *Potentials of distributed acoustic sensing in seismic imaging / Patrick Paitz* [Doctoral dissertation, ETH Zürich] [Book Title: Potentials of distributed acoustic sensing in seismic imaging]. https://doi.org/urn:nbn:ch:bel-1888625,https://permalink.snl.ch/bib/sz991018137530703976,10.3929/ethz-b-000474545

Paitz, P., Edme, P., Gräff, D., Walter, F., Doetsch, J., Chalari, A., Schmelzbach, C., & Fichtner, A. (2020). Empirical Investigations of the Instrument Response for Distributed Acoustic Sensing (DAS) across 17 Octaves. *Bulletin of the Seismological Society of America*, *111*(1), 1–10. https://doi.org/10.1785/0120200185

Paitz, P., Lindner, N., Edme, P., Huguenin, P., Hohl, M., Sovilla, B., Walter, F., & Fichtner, A. (2023). Phenomenology of Avalanche Recordings From Distributed Acoustic Sensing. *Journal of Geophysical Research: Earth Surface*, *128*(5), e2022JF007011. https://doi.org/10.1029/2022JF007011

Parfitt, E. A. (2004). A discussion of the mechanisms of explosive basaltic eruptions. *Journal of Volcanology and Geothermal Research*, *134*(1), 77–107. https://doi.org/10.1016/j.jvolgeores.2004.01.002

Paschotta, R. (2010, January). *Field Guide to Optical Fiber Technology*. https://doi.org/10.1117/3.853722

Petersen, G. N., Bjornsson, H., & Arason, P. (2012). The impact of the atmosphere on the Eyjafjallajökull 2010 eruption plume. *Journal of Geophysical Research: Atmospheres*, *117*(D20). https://doi.org/10.1029/2011JD016762

Petrone, C. M., Mollo, S., Gertisser, R., Buret, Y., Scarlato, P., Del Bello, E., Andronico, D., Ellis, B., Pontesilli, A., De Astis, G., Giacomoni, P. P., Coltorti, M., & Reagan, M. (2022). Magma recharge and mush rejuvenation drive paroxysmal activity at Stromboli volcano [Publisher: Nature Publishing Group]. *Nature Communications*, *13*(1), 7717. https://doi.org/10.1038/s41467-022-35405-z

Petrosino, S., Cusano, P., Saccorotti, G., & Del Pezzo, E. (2002). Seismic Attenuation and Shallow Velocity Structures at Stromboli Volcano, Italy. *Bulletin of the Seismological Society of America*, *92*(3), 1102–1116. https://doi.org/10.1785/0120010147

Pichavant, M., Di Carlo, I., Pompilio, M., & Le Gall, N. (2022). Timescales and mechanisms of paroxysm initiation at Stromboli volcano, Aeolian Islands, Italy. *Bulletin of Volcanology*, *84*(4), 36. https://doi.org/10.1007/s00445-022-01545-9

Pistolesi, M., Delle Donne, D., Pioli, L., Rosi, M., & Ripepe, M. (2011). The 15 March 2007 explosive crisis at Stromboli volcano, Italy: Assessing physical parameters through a multidisciplinary approach. *Journal of Geophysical Research: Solid Earth*, *116*(B12). https://doi.org/10.1029/2011JB008527

Pistolesi, M., Bertagnini, A., Di Roberto, A., Ripepe, M., & Rosi, M. (2020). Tsunami and tephra deposits record interactions between past eruptive activity and landslides at Stromboli volcano, Italy. *Geology*, *48*(5), 436–440. https://doi.org/10.1130/G47331.1

Poupinet, G., Ellsworth, W. L., & Frechet, J. (1984). Monitoring velocity variations in the crust using earthquake doublets: An application to the Calaveras Fault, California. *Journal of Geophysical Research: Solid Earth*, *89*(B7), 5719–5731. https://doi.org/10.1029/JB089iB07p05719

Power, J. A., Lahr, J. C., Page, R. A., Chouet, B. A., Stephens, C. D., Harlow, D. H., Murray, T. L., & Davies, J. N. (1994). Seismic evolution of the 1989–1990 eruption sequence of Redoubt Volcano, Alaska. *Journal of Volcanology and Geothermal Research*, *62*(1), 69–94. https://doi.org/10.1016/0377-0273(94)90029-9

Pujol, J. (2003). *Elastic Wave Propagation and Generation in Seismology*. Cambridge University Press. https://doi.org/10.1017/CBO9780511610127

Rahman, M. A., Taheri, H., Dababneh, F., Karganroudi, S. S., & Arhamnamazi, S. (2024). A review of distributed acoustic sensing applications for railroad condition monitoring. *Mechanical Systems and Signal Processing*, *208*, 110983. https://doi.org/10.1016/j.ymssp.2023.110983

Reinsch, T., Thurley, T., & Jousset, P. (2017). On the mechanical coupling of a fiber optic cable used for distributed acoustic/vibration sensing applications—a theoretical consideration [Publisher: IOP Publishing]. *Measurement Science and Technology*, *28*(12), 127003. https://doi.org/10.1088/1361-6501/aa8ba4

Revil, A., Finizola, A., Johnson, T., Ricci, T., Gresse, M., Delcher, E., Barde-Cabusson, S., Duvillard, P. A., & Ripepe, M. (2023). The Thermal Plumbing System of Stromboli Volcano, Aeolian Islands (Italy) Inferred From Electrical Conductivity and Induced Polarization Tomography. *Journal of Geophysical Research: Solid Earth*, *128*(6), e2023JB026475. https://doi.org/10.1029/2023JB026475

Ripepe, M., Delle Donne, D., Lacanna, G., Marchetti, E., & Ulivieri, G. (2009). The onset of the 2007 Stromboli effusive eruption recorded by an integrated geophysical network. *Journal of Volcanology and Geothermal Research*, *182*(3), 131–136. https://doi.org/10.1016/j.jvolgeores.2009.02.011

Ripepe, M., Delle Donne, D., Legrand, D., Valade, S., & Lacanna, G. (2021). Magma pressure discharge induces very long period seismicity [Publisher: Nature Publishing Group]. *Scientific Reports*, *11*(1), 20065. https://doi.org/10.1038/s41598-021-99513-4

Ripepe, M., & Lacanna, G. (2024). Volcano generated tsunami recorded in the near source [Publisher: Nature Publishing Group]. *Nature Communications*, *15*(1), 1802. https://doi.org/10.1038/s41467-024-45937-1

Ripepe, M., Lacanna, G., Pistolesi, M., Silengo, M. C., Aiuppa, A., Laiolo, M., Massimetti, F., Innocenti, L., Della Schiava, M., Bitetto, M., La Monica, F. P., Nishimura, T., Rosi, M., Mangione, D., Ricciardi, A., Genco, R., Coppola, D., Marchetti, E., & Delle Donne, D. (2021). Ground deformation reveals the scale-invariant conduit dynamics driving explosive basaltic eruptions [Number: 1 Publisher: Nature Publishing Group]. *Nature Communications*, *12*(1), 1683. https://doi.org/10.1038/s41467-021-21722-2

Ripepe, M., Poggi, P., Braun, T., & Gordeev, E. (1996). Infrasonic waves and volcanic tremor at Stromboli. *Geophysical Research Letters*, *23*(2), 181–184. https://doi.org/10.1029/95GL03662

Ripepe, M., De Angelis, S., Lacanna, G., & Voight, B. (2010). Observation of infrasonic and gravity waves at Soufrière Hills Volcano, Montserrat. *Geophysical Research Letters*, *37*(19). https://doi.org/10.1029/2010GL042557

Ripepe, M., Donne, D. D., Genco, R., Maggio, G., Pistolesi, M., Marchetti, E., Lacanna, G., Ulivieri, G., & Poggi, P. (2015). Volcano seismicity and ground deformation unveil the gravity-driven magma discharge dynamics of a volcanic eruption [Publisher: Nature Publishing Group]. *Nature Communications*, *6*(1), 6998. https://doi.org/10.1038/ncomms7998

Ripepe, M., Donne, D. D., Harris, A., Marchetti, E., & Ulivieri, G. (2008). Dynamics of Strombolian Activity. In *The Stromboli Volcano: An Integrated Study of the 2002–2003 Eruption* (pp. 39–48). American Geophysical Union (AGU). Retrieved June 7, 2024, from https://onlinelibrary.wiley.com/doi/abs/10.1029/182GM05

Ripepe, M., & Gordeev, E. (1999). Gas bubble dynamics model for shallow volcanic tremor at Stromboli. *Journal of Geophysical Research: Solid Earth*, *104*(B5), 10639–10654. https://doi.org/10.1029/98JB02734

Ripepe, M., Pistolesi, M., Coppola, D., Delle Donne, D., Genco, R., Lacanna, G., Laiolo, M., Marchetti, E., Ulivieri, G., & Valade, S. (2017). Forecasting Effusive Dynamics and Decompression Rates by Magmastatic Model at Open-vent Volcanoes [Publisher: Nature Publishing Group]. *Scientific Reports*, *7*(1), 3885. https://doi.org/10.1038/s41598-017-03833-3

Risica, G., Rosi, M., Pistolesi, M., Speranza, F., & Branney, M. J. (2022). Deposit-Derived Block-and-Ash Flows: The Hazard Posed by Perched Temporary Tephra Accumulations on Volcanoes; 2018 Fuego Disaster, Guatemala. *Journal of Geophysical Research: Solid Earth*, *127*(6), e2021JB023699. https://doi.org/10.1029/2021JB023699

Roche, O., Attali, M., Mangeney, A., & Lucas, A. (2011). On the run-out distance of geophysical gravitational flows: Insight from fluidized granular collapse experiments. *Earth and Planetary Science Letters*, *311*(3), 375–385. https://doi.org/10.1016/j.epsl.2011.09.023

Rogers, A. (1999). Distributed optical-fibre sensing. *Measurement Science and Technology*, *10*(8), R75. https://doi.org/10.1088/0957-0233/10/8/201

Romagnoli, C., Casalbore, D., Chiocci, F. L., & Bosman, A. (2009). Offshore evidence of large-scale lateral collapses on the eastern flank of Stromboli, Italy, due to structurally-controlled, bilateral flank instability. *Marine Geology*, *262*(1), 1–13. https://doi.org/10.1016/j.margeo.2009.02.004

Rosi, M., Bertagnini, A., Harris, A. J. L., Pioli, L., Pistolesi, M., & Ripepe, M. (2006). A case history of paroxysmal explosion at Stromboli: Timing and dynamics of the April 5, 2003 event. *Earth and Planetary Science Letters*, *243*(3), 594–606. https://doi.org/10.1016/j.epsl.2006.01.035

Rosi, M., Bertagnini, A., & Landi, P. (2000). Onset of the persistent activity at Stromboli Volcano (Italy). *Bulletin of Volcanology*, *62*(4), 294–300. https://doi.org/10.1007/s004450000098

Rosi, M., Levi, S. T., Pistolesi, M., Bertagnini, A., Brunelli, D., Cannavò, V., Di Renzoni, A., Ferranti, F., Renzulli, A., & Yoon, D. (2019). Geoarchaeological Evidence of Middle-Age Tsunamis at Stromboli and Consequences for the Tsunami Hazard in the Southern Tyrrhenian Sea [Publisher: Nature Publishing Group]. *Scientific Reports*, *9*(1), 677. https://doi.org/10.1038/s41598-018-37050-3

Rosi, M., Pistolesi, M., Bertagnini, A., Landi, P., Pompilio, M., & Di Roberto, A. (2013). Chapter 14 Stromboli volcano, Aeolian Islands (Italy): Present eruptive activity and hazards [Publisher: The Geological Society of London]. *Geological Society, London, Memoirs*, *37*(1), 473–490. https://doi.org/10.1144/M37.14

Rost, S., & Thomas, C. (2002). Array Seismology: Methods and Applications. *Reviews of Geophysics*, *40*(3), 2–1–2–27. https://doi.org/10.1029/2000RG000100

Ryan, M. P., Koyanagi, R. Y., & Fiske, R. S. (1981). Modeling the three-dimensional structure of macroscopic magma transport systems: Application to Kilauea Volcano, Hawaii. *Journal of Geophysical Research: Solid Earth*, *86*(B8), 7111–7129. https://doi.org/10.1029/JB086iB08p07111

Saccorotti, G., Chouet, B., & Dawson, P. (2001). Wavefield properties of a shallow long-period event and tremor at Kilauea Volcano, Hawaii. *Journal of Volcanology and Geothermal Research*, *109*(1), 163–189. https://doi.org/10.1016/S0377-0273(00)00310-3

Saccorotti, G., Chouet, B., Martini, M., & Scarpa, R. (1998). Bayesian statistics applied to the location of the source of explosions at Stromboli Volcano, Italy. *Bulletin of the Seismological Society of America*, *88*(5), 1099–1111. https://doi.org/10.1785/BSSA0880051099

Saccorotti, G., & Lokmer, I. (2021, January). Chapter 2 - A review of seismic methods for monitoring and understanding active volcanoes. In P. Papale (Ed.), *Forecasting and Planning for Volcanic Hazards, Risks, and Disasters* (pp. 25–73, Vol. 2). Elsevier. https://doi.org/10.1016/B978-0-12-818082-2.00002-0

Schmidt, R. (1986). Multiple emitter location and signal parameter estimation [Conference Name: IEEE Transactions on Antennas and Propagation]. *IEEE Transactions on Antennas and Propagation*, *34*(3), 276–280. https://doi.org/10.1109/TAP.1986.1143830

Schneider, D., Bartelt, P., Caplan-Auerbach, J., Christen, M., Huggel, C., & McArdell, B. W. (2010). Insights into rock-ice avalanche dynamics by combined analysis of seismic recordings and a numerical avalanche model. *Journal of Geophysical Research: Earth Surface*, *115*(F4). https://doi.org/10.1029/2010JF001734

Schöpa, A., Chao, W.-A., Lipovsky, B. P., Hovius, N., White, R. S., Green, R. G., & Turowski, J. M. (2018). Dynamics of the Askja caldera July 2014 landslide, Iceland, from seismic signal analysis: Precursor, motion and aftermath [Publisher: Copernicus GmbH]. *Earth Surface Dynamics*, *6*(2), 467–485. https://doi.org/10.5194/esurf-6-467-2018

Schweitzer, J., Fyen, J., Mykkeltveit, S., Gibbons, S. J., Pirli, M., Kühn, D., & Kværna, T. (2012). Seismic Arrays. In: New Manual of Seismological Observatory Practice 2 (NMSOP-2).

Shen, Z., & Wu, W. (2024). Ocean Bottom Distributed Acoustic Sensing for Oceanic Seismicity Detection and Seismic Ocean Thermometry. *Journal of Geophysical Research: Solid Earth*, *129*(3), e2023JB027799. https://doi.org/10.1029/2023JB027799

Sladen, A., Rivet, D., Ampuero, J. P., De Barros, L., Hello, Y., Calbris, G., & Lamare, P. (2019). Distributed sensing of earthquakes and ocean-solid Earth interactions on seafloor telecom cables [Number: 1 Publisher: Nature Publishing Group]. *Nature Communications*, *10*(1), 5777. https://doi.org/10.1038/s41467-019-13793-z

Spica, Z. J., Perton, M., Martin, E. R., Beroza, G. C., & Biondi, B. (2020). Urban Seismic Site Characterization by Fiber-Optic Seismology. *Journal of Geophysical Research: Solid Earth*, *125*(3). https://doi.org/10.1029/2019JB018656

Strumia, C., Trabattoni, A., Supino, M., Baillet, M., Rivet, D., & Festa, G. (2024). Sensing Optical Fibers for Earthquake Source Characterization Using Raw DAS Records. *Journal of Geophysical Research: Solid Earth*, *129*(1), e2023JB027860. https://doi.org/10.1029/2023JB027860

Stutzmann, E., Schimmel, M., Patau, G., & Maggi, A. (2009). Global climate imprint on seismic noise. *Geochemistry, Geophysics, Geosystems*, *10*(11). https://doi.org/10.1029/2009GC002619

Sugimura, S., Nishimura, T., Lacanna, G., Legrand, D., Valade, S., & Ripepe, M. (2021). Seismic Source Migration During Strombolian Eruptions Inferred by Very-Near-Field Broadband Seismic Network. *Journal of Geophysical Research: Solid Earth*, *126*(12), e2021JB022623. https://doi.org/10.1029/2021JB022623

Tahira, K. T., Faruk, M. O., Ruma, T. A., Saha, T., & Rahman, M. M. (2019). Analysis of Fiber Loss Mechanisms in Communication System to Simulate Different Attenuation. *Journal of Engineering Research and Reports*, 1–15. https://doi.org/10.9734/jerr/2019/v8i116982

Takano, T., Brenguier, F., Campillo, M., Peltier, A., & Nishimura, T. (2020). Noise-based passive ballistic wave seismic monitoring on an active volcano. *Geophysical Journal International*, *220*(1), 501–507. https://doi.org/10.1093/gji/ggz466

Takebayashi, M., Onishi, M., & Iguchi, M. (2021). Large volcanic eruptions and their influence on air transport: The case of Japan. *Journal of Air Transport Management*, *97*, 102136. https://doi.org/10.1016/j.jairtraman.2021.102136

Tanguy, J.-C., Ribière, C., Scarth, A., & Tjetjep, W. S. (1998). Victims from volcanic eruptions: A revised database. *Bulletin of Volcanology*, *60*(2), 137–144. https://doi.org/10.1007/s004450050222

Taweesintananon, K., Landrø, M., Potter, J. R., Johansen, S. E., Rørstadbotnen, R. A., Bouffaut, L., Kriesell, H. J., Brenne, J. K., Haukanes, A., Schjelderup, O., & Storvik, F. (2023).

Distributed acoustic sensing of ocean-bottom seismo-acoustics and distant storms: A case study from Svalbard, Norway. *Geophysics*, *88*(3), B135–B150. https://doi.org/10.1190/geo2022-0435.1

Tibaldi, A. (2001). Multiple sector collapses at stromboli volcano, Italy: How they work. *Bulletin of Volcanology*, *63*(2), 112–125. https://doi.org/10.1007/s004450100129

Tinti, S., Zaniboni, F., Pagnoni, G., & Manucci, A. (2008). Stromboli Island (Italy): Scenarios of Tsunamis Generated by Submarine Landslides. *Pure and Applied Geophysics*, *165*(11), 2143–2167. https://doi.org/10.1007/s00024-008-0420-y

Trabattoni, A., Festa, G., Longo, R., Bernard, P., Plantier, G., Zollo, A., & Strollo, A. (2022). Microseismicity Monitoring and Site Characterization With Distributed Acoustic Sensing (DAS): The Case of the Irpinia Fault System (Southern Italy). *Journal of Geophysical Research: Solid Earth*, *127*(9), e2022JB024529. https://doi.org/10.1029/2022JB024529

Trabattoni, A., Biagioli, F., Strumia, C., Ende, M. v. d., Uccio, F. S. d., Festa, G., Rivet, D., Sladen, A., Ampuero, J. P., Metaxian, J. P., & Stutzmann, E. (2023). From strain to displacement: Using deformation to enhance distributed acoustic sensing applications [Publisher: EarthArXiv]. Retrieved August 1, 2023, from https://eartharxiv.org/repository/view/5292/

Ulivieri, G., Marchetti, E., Ripepe, M., Chiambretti, I., De Rosa, G., & Segor, V. (2011). Monitoring snow avalanches in Northwestern Italian Alps using an infrasound array. *Cold Regions Science and Technology*, *69*(2), 177–183. https://doi.org/10.1016/j.coldregions.2011.09.006

Valade, S., Lacanna, G., Coppola, D., Laiolo, M., Pistolesi, M., Donne, D. D., Genco, R., Marchetti, E., Ulivieri, G., Allocca, C., Cigolini, C., Nishimura, T., Poggi, P., & Ripepe, M. (2016). Tracking dynamics of magma migration in open-conduit systems. *Bulletin of Volcanology*, *78*(11), 78. https://doi.org/10.1007/s00445-016-1072-x

Valade, S., Ley, A., Massimetti, F., D'Hondt, O., Laiolo, M., Coppola, D., Loibl, D., Hellwich, O., & Walter, T. R. (2019). Towards Global Volcano Monitoring Using Multisensor Sentinel Missions and Artificial Intelligence: The MOUNTS Monitoring System [Number: 13 Publisher: Multidisciplinary Digital Publishing Institute]. *Remote Sensing*, *11*(13), 1528. https://doi.org/10.3390/rs11131528

van den Ende, M. P. A., & Ampuero, J.-P. (2021). Evaluating seismic beamforming capabilities of distributed acoustic sensing arrays [Publisher: Copernicus GmbH]. *Solid Earth*, *12*(4), 915–934. https://doi.org/10.5194/se-12-915-2021

Vergniolle, S., & Brandeis, G. (1996). Strombolian explosions: 1. A large bubble breaking at the surface of a lava column as a source of sound. *Journal of Geophysical Research: Solid Earth*, *101*(B9), 20433–20447. https://doi.org/10.1029/96JB01178

Vilajosana, I., Suriñach, E., Abellán, A., Khazaradze, G., Garcia, D., & Llosa, J. (2008). Rockfall induced seismic signals: Case study in Montserrat, Catalonia [Publisher: Copernicus GmbH]. *Natural Hazards and Earth System Sciences*, *8*(4), 805–812. https://doi.org/10.5194/nhess-8-805-2008

Voloschina, M., Métrich, N., Bertagnini, A., Marianelli, P., Aiuppa, A., Ripepe, M., & Pistolesi, M. (2023). Explosive eruptions at Stromboli volcano (Italy): A comprehensive geochemical view on magma sources and intensity range. *Bulletin of Volcanology*, *85*(6), 34. https://doi.org/10.1007/s00445-023-01647-y

Walter, F., Gräff, D., Lindner, F., Paitz, P., Köpfli, M., Chmiel, M., & Fichtner, A. (2020). Distributed acoustic sensing of microseismic sources and wave propagation in glaciated terrain [Publisher: Nature Publishing Group]. *Nature Communications*, *11*(1), 2436. https://doi.org/10.1038/s41467-020-15824-6

Wang, C., Huang, X., Li, Y., & Jensen, K. (2023). Removing multiple types of noise of distributed acoustic sensing seismic data using attention-guided denoising convolutional

neural network [Publisher: Frontiers]. *Frontiers in Earth Science*, *10*. https://doi.org/10.3389/feart.2022.986470

Wang, H. F., Zeng, X., Miller, D. E., Fratta, D., Feigl, K. L., Thurber, C. H., & Mellors, R. J. (2018). Ground motion response to an ML 4.3 earthquake using co-located distributed acoustic sensing and seismometer arrays. *Geophysical Journal International*, *213*(3), 2020–2036. https://doi.org/10.1093/gji/ggy102

Wassermann, J., Braun, T., Ripepe, M., Bernauer, F., Guattari, F., & Igel, H. (2022). The use of 6DOF measurement in volcano seismology – A first application to Stromboli volcano. *Journal of Volcanology and Geothermal Research*, *424*, 107499. https://doi.org/10.1016/j.jvolgeores.2022.107499

Wassermann, J. (1997). Locating the sources of volcanic explosions and volcanic tremor at Stromboli volcano (Italy) using beam-forming on diffraction hyperboloids. *Physics of the Earth and Planetary Interiors*, *104*(1), 271–281. https://doi.org/10.1016/S0031-9201(97)00041-1

Wassermann, J. (2012). Volcano Seismology. In *New Manual of Seismological Observatory Practice 2 (NMSOP-2)* (pp. 1–77). Deutsches GeoForschungsZentrum GFZ. https://doi.org/10.2312/GFZ.NMSOP-2_ch13

Watson, L. M., Cannata, A., & Andronico, D. (2023). Tracking a Pyroclastic Density Current With Seismic Signals at Mt. Etna (Italy). *Journal of Geophysical Research: Solid Earth*, *128*(3), e2022JB026114. https://doi.org/10.1029/2022JB026114

White, R., & McCausland, W. (2016). Volcano-tectonic earthquakes: A new tool for estimating intrusive volumes and forecasting eruptions. *Journal of Volcanology and Geothermal Research*, *309*, 139–155. https://doi.org/10.1016/j.jvolgeores.2015.10.020

Wielandt, E. (2012). Seismic Sensors and their Calibration. In *New Manual of Seismological Observatory Practice 2 (NMSOP-2)* (pp. 1–51). Deutsches GeoForschungsZentrum GFZ. https://doi.org/10.2312/GFZ.NMSOP-2_ch5

Wielandt, E., & Forbriger, T. (1999). Near-field seismic displacement and tilt associated with the explosive activity of Stromboli. *Ann. Geofis.*, *42*. https://doi.org/10.4401/ag-3723

Williams, E. F., Fernández-Ruiz, M. R., Magalhaes, R., Vanthillo, R., Zhan, Z., González-Herráez, M., & Martins, H. F. (2019). Distributed sensing of microseisms and teleseisms with submarine dark fibers [Number: 1 Publisher: Nature Publishing Group]. *Nature Communications*, *10*(1), 5778. https://doi.org/10.1038/s41467-019-13262-7

Williams, E. F. (2023). *Probing Solid-Earth, Ocean, and Structural Dynamics with Distributed Fiber-Optic Sensing* [phd]. California Institute of Technology. https://doi.org/10.7907/vehm-dd85

Witham, C. S. (2005). Volcanic disasters and incidents: A new database. *Journal of Volcanology and Geothermal Research*, *148*(3), 191–233. https://doi.org/10.1016/j.jvolgeores.2005.04.017

Wright, T. L., & Klein, F. W. (2006). Deep magma transport at Kilauea volcano, Hawaii. *Lithos*, *87*(1), 50–79. https://doi.org/10.1016/j.lithos.2005.05.004

Xie, T., Shi, B., Zhang, C.-C., Yin, J., Zhang, T.-Y., Li, J.-P., Wang, Z., & Chen, Z. (2021). Distributed acoustic sensing (DAS) for geomechanics characterization: A concise review [Publisher: IOP Publishing]. *IOP Conference Series: Earth and Environmental Science*, *861*(4), 042033. https://doi.org/10.1088/1755-1315/861/4/042033

Xie, T., Zhang, C.-C., Shi, B., Wang, Z., Zhang, S.-S., & Yin, J. (2023). Seismic monitoring of rockfalls using distributed acoustic sensing. *Engineering Geology*, *325*, 107285. https://doi.org/10.1016/j.enggeo.2023.107285

Yamasato, H. (1997). Quantitative Analysis of Pyroclastic Flows Using Infrasonic and Seismic Data at Unzen Volcano, Japan. *Journal of Physics of the Earth*, *45*(6), 397–416. https://doi.org/10.4294/jpe1952.45.397

Yang, J., Shragge, J., & Jin, G. (2022). Filtering Strategies for Deformation-Rate Distributed Acoustic Sensing [Number: 22 Publisher: Multidisciplinary Digital Publishing Institute]. *Sensors*, *22*(22), 8777. https://doi.org/10.3390/s22228777

Yeh, Y.-L., Wang, W.-H., & Wen, S. (2021). Dense seismic arrays deny a massive magma chamber beneath the Taipei metropolis, Taiwan [Publisher: Nature Publishing Group]. *Scientific Reports*, *11*(1), 1083. https://doi.org/10.1038/s41598-020-80051-4

Zhan, Z. (2019). Distributed Acoustic Sensing Turns Fiber-Optic Cables into Sensitive Seismic Antennas. *Seismological Research Letters*, *91*(1), 1–15. https://doi.org/10.1785/0220190112

Zhang, L., Costa, L. D., Yang, Z., Soto, M. A., Gonzalez-Herráez, M., & Thévenaz, L. (2019). Analysis and Reduction of Large Errors in Rayleigh-Based Distributed Sensor [Conference Name: Journal of Lightwave Technology]. *Journal of Lightwave Technology*, *37*(18), 4710–4719. https://doi.org/10.1109/JLT.2019.2917746

Zhou, J., Pan, Z., Ye, Q., Cai, H., Qu, R., & Fang, Z. (2013). Characteristics and Explanations of Interference Fading of a \phi -OTDR With a Multi-Frequency Source [Conference Name: Journal of Lightwave Technology]. *Journal of Lightwave Technology*, *31*(17), 2947–2954. https://doi.org/10.1109/JLT.2013.2275179

Zhu, H.-H., Liu, W., Wang, T., Su, J.-W., & Shi, B. (2022). Distributed Acoustic Sensing for Monitoring Linear Infrastructures: Current Status and Trends [Number: 19 Publisher: Multidisciplinary Digital Publishing Institute]. *Sensors*, *22*(19), 7550. https://doi.org/10.3390/s22197550

Zhu, T., Shen, J., & Martin, E. R. (2021). Sensing Earth and environment dynamics by telecommunication fiber-optic sensors: An urban experiment in Pennsylvania, USA [Publisher: Copernicus GmbH]. *Solid Earth*, *12*(1), 219–235. https://doi.org/10.5194/se-12-219-2021

Zobin, V. M. (2017, January). Chapter 3 - Fundamentals of Volcanic Seismology. In V. M. Zobin (Ed.), *Introduction to Volcanic Seismology (Third Edition)* (pp. 35–60). Elsevier. https://doi.org/10.1016/B978-0-444-63631-7.00003-0

Zobin, V. M., Plascencia, I., Reyes, G., & Navarro, C. (2009). The characteristics of seismic signals produced by lahars and pyroclastic flows: Volcán de Colima, México. *Journal of Volcanology and Geothermal Research*, *179*(1), 157–167. https://doi.org/10.1016/j.jvolgeores.2008.11.001

Acknowledgements

to complete after submission.